Titre: Title:	Innovative Traveling-Wave Optoelectronic Devices for Radio over Fiber and Terahertz Applications
Auteur: Author:	Ebrahim Mortazy
Date:	2010
Type:	Mémoire ou thèse / Dissertation or Thesis
Référence: Citation:	Mortazy, E. (2010). Innovative Traveling-Wave Optoelectronic Devices for Radio over Fiber and Terahertz Applications [Ph.D. thesis, École Polytechnique de Montréal]. PolyPublie. https://publications.polymtl.ca/413/

UNIVERSITÉ DE MONTRÉAL

INNOVATIVE TRAVELING-WAVE OPTOELECTRONIC DEVICES FOR RADIO OVER FIBER AND TERAHERTZ APPLICATIONS

EBRAHIM MORTAZY

DÉPARTEMENT DE GÉNIE ÉLECTRIQUE

ÉCOLE POLYTECHNIQUE DE MONTRÉAL

THÈSE PRÉSENTÉE EN VUE DE L'OBTENTION

DU DIPLÔME DE PHILOSOPHIÆ DOCTOR

(GÉNIE ÉLECTRIQUE)

OCTOBRE 2010

UNIVERSITÉ DE MONTRÉAL

ÉCOLE POLYTECHNIQUE DE MONTRÉAL

Cette thèse intitulée:

INNOVATIVE TRAVELING-WAVE OPTOELECTRONIC DEVICES FOR RADIO OVER FIBER AND TERAHERTZ APPLICATIONS

présentée par : MORTAZY Ebrahim

en vue de l'obtention du diplôme de : Philosophiae Doctor

a été dûment acceptée par le jury d'examen constitué de :

M. LAURIN Jean-Jacques, Ph.D., président

M. WU Ke, Ph. D., directeur de recherche

M. CALOZ Christophe, Ph.D., membre

M. LIU Hui Chun., Ph.D., membre

DEDICATION

To Parisa and my family

ACKNOWLEDGEMENT

I would like to thank:

- Prof. Ke WU, my PhD supervisor, for his support, his novel ideas in my research domains as well as introducing me to some research centers for device fabrications.
- Dr. H. C. LIU for his help in the design and fabrication of THz source generator in National Research Council (NRC), Ottawa.
- Prof. Michel MEUNIER who let me use the Excimer laser micromachining in physics department at Ecole Polytechnique.
- Prof. Mohamed CHAKER and Dr. Irina STATEIKINA from Institut National de la Recherche Scientifique (INRS), Varennes, to help me in the fabrication of optical waveguides.
- Mr. Jules GAUTHIER who fabricated my devices and gave me advices in the experimental parts.
- All of my friends in Montreal, specially Amirhossein TEHRANCHI, and members of Poly-Grames Research Center for their help and suggestions.
- My wife, Parisa, and my sister, brothers and parents who supported me during the PhD program.

RÉSUMÉ

La structure des composants conventionnels pour les applications optoélectroniques à haute fréquence ainsi que son intégration avec d'autres composants peuvent être modifiées en utilisant les guides d'ondes à faible perte. Par ailleurs le concept des circuits intégrés au substrat (*Substrate Integrated Circuits*: SICs), largement utilisé dans les structures des applications micro-ondes, peut être employé pour l'intégration de ces composantes dans les applications à ondes millimétriques (*millimetre Wave*: mmW) et sous-millimétriques.

Dans les systèmes de communication optique et systèmes optoélectroniques, photodétecteurs et modulateurs sont les éléments clés pour la conception des récepteurs et des émetteurs. Les photodétecteurs à ondes progressives (*Traveling-Wave*: TW) et les modulateurs conventionnels, dans leurs structures, utilisent les lignes microrubans (*Microstrip*: MS) et les guides coplanaires (*Coplanar Waveguide*: CPW). Les substrats majoritairement utilisés pour la fabrication des composantes optoélectroniques et électro-optiques, citées ci-dessus, sont en arséniure de gallium (GaAs) et niobate de lithium ($LiNbO_3$). Il faut bien noter que les pertes de micro-ondes/mmW dans les lignes microrubans et les guides coplanaires augmentent avec la fréquence. Ces pertes incluent les pertes ohmique, diélectrique et de rayonnement.

Le guide d'ondes rectangulaire ayant une faible perte après la fréquence de coupure sans grand changement, est un guide d'ondes de remplacement pour les composants mmW. Son inconvénient est qu'il n'est pas planaire et difficilement intégrable. Le guide d'ondes intégré au substrat (*Substrate Integrated Waveguide*: SIW) est une forme planaire du guide d'ondes rectangulaire. Dans ces guides d'ondes les trous métallisés remplacent les parois métalliques du guide rectangulaire. De nouveaux composants optoélectroniques peuvent être proposées avec l'intégration de la structure SIW pour les fréquences mmW. Les photodétecteurs et les modulateurs sont les candidats potentiels pour les nouveaux composants optoélectroniques.

Les pertes micro-ondes/mmW des photodétecteurs, en tant qu'un facteur important de limitation de bande passante, sont liées à la partie active de détection et à sa partie non-active de

transmission. Dans la pratique, la partie active est fabriquée en ligne microruban multicouche tandis que la partie non-active est réalisée en ligne microruban monocouche. La section non-active de la ligne microruban est généralement longue et occasionne des pertes importantes limitant considérablement la bande passante des photodétecteurs. Cette section peut être remplacée par une structure SIW à faible perte. La transition entre la ligne microruban du photodétecteur et la structure SIW est conçue et réalisée dans cette thèse. Pour séparer la polarisation DC des photodétecteurs et de la couche supérieure métallique en SIW, nous utilisons une structure SIW multicouche. Pour les modulateurs, nous considérons la structure en SIW afin de proposer de nouveaux types de modulateurs électro-optiques. Les modulateurs $LiNbO_3$ électro-optiques passe-bandes de phase et d'amplitude, en structures SIW et SIW-CPW, sont deux types de composant proposés dans la présente thèse. L'intégrale de recouvrement, la tension demi-onde, la profondeur de modulation et la bande passante sont les paramètres les plus importants à optimiser dans les modulateurs optiques.

Pour la conception du modulateur de phase SIW, l'interaction entre le signal micro-ondes/mmW et le signal optique dans SIW n'est pas considérable. Il est à noter que dans ces structures, les dimensions du SIW sont plus grandes que celles du guide d'ondes optiques et aussi le mode TE_{10} est plus distribué sur la section transversale du guide. Par conséquent, l'intégrale de recouvrement et la tension demi-onde ne donnent pas des résultats acceptables. Par ailleurs, une solution serait d'utiliser la structure en SIW mince pour augmenter l'intégrale de recouvrement. Cette solution n'est pas l'idéale car la perte micro-onde/mmW d'une structure en SIW mince est significativement haute affectant la profondeur de modulation et la bande passante. Pour améliorer l'intégrale de recouvrement et diminuer, en même temps, la perte mmW, les niobates de lithium sont utilisés comme substrat. Ces substrats sont coupés sur le plan X et Z de façons différentes. Nous déposons le substrat mince du plan X sur le substrat épais du plan Z avant de faire la conception des guides d'ondes optiques ainsi que les autres éléments du modulateur. Une matrice du guide optique est conçue sur la couche supérieure et diffusée en profondeur. Dans l'étape suivante, les paramètres du modulateur sont optimisés et les layouts de fabrications sont générés. Aussi le modulateur d'amplitude $LiNbO_3$ passe-bande est proposé sur la base du modulateur de phase SIW avec le mode TE_{10}. Au lieu d'utiliser le mode TE_{10}, le mode TE_{20} du SIW peut être utilisé pour le modulateur d'amplitude. L'excitation du mode TE_{20} du SIW est

conçue et optimisée pour le modulateur d'amplitude. La fabrication de la structure SIW en substrat $LiNbO_3$ transparent est réalisée en utilisant le micro-usinage par laser Excimer. En outre, pour valider nos structures, la transition de CPW à SIW est fabriquée et testée à 60 GHz pour le modulateur de phase SIW sur un substrat $LiNbO_3$. Les bonnes concordances entre les résultats simulés et mesurés sont obtenues.

Le modulateur SIW-CPW est un autre type de modulateurs d'amplitude électro-optique passe-bande proposé par la présente thèse. Il utilise le mécanisme du couplage entre CPW et SIW. Dans cette structure avec la perte fiable, il y a de fortes interactions entre les signaux optiques et micro-ondes. Le couplage entre le SIW et le CPW augmente de façon progressive dans la première moitié de la région de modulation et est à son maximum au milieu du modulateur proposé. Dans la seconde moitié, ce couplage se produit entre CPW et SIW. Dans ce modulateur, l'intégrale de recouvrement augmente progressivement pendant le transfert du signal micro-ondes vers la structure en CPW. Le mécanisme de couplage entre CPW et SIW de la structure proposée génère un modulateur d'amplitude passe-bande pour des applications mmW. Le modulateur SIW-CPW, avec les transitions de CPW à SIW pour la mesure, est conçu et réalisé dans cette thèse. Pour la validation, les mesures sous pointe sont effectuées et comparées avec les résultats simulées.

La génération des sources térahertz (THz) utilisant les photodétecteurs et les photo-mélangeurs est entreprise dans la seconde partie de cette thèse. Le photo-mélangeur en tant qu'un sous-ensemble des photoconducteurs de surface, est conçu et fabriqué aux fréquences sous-millimétriques avant d'être intégré à l'antenne spirale. Le signal optique de la diode laser à double longueur d'onde (dual-wavelength) est détecté par un photo-mélangeur en utilisant des doigts entrelacés. Ensuite, le signal THz est généré et rayonné avec l'antenne spirale à partir du bas du substrat. La conception et l'optimisation de photodétecteur et de l'antenne spirale, la conception de masques multicouches, la fabrication et la préparation de configuration expérimentale et les mesures de circuits intégrés sont présentées dans cette thèse. Finalement, pour générer du signal THz à la haute-puissance par la technique de photo-mélange, un photodétecteur TW intégré est conçu. Pour diminuer l'effet de la perte de CPW, une guide d'onde optique à faibles pertes est considérée. Ce guide d'onde optique et le photodétecteur sont intégrés avec une antenne log-périodique alimentée en CPW. Cette nouvelle composante possédant des

propriétés large-bande à haute-puissance en tant qu'un générateur THz est expliquée en détail dans cette thèse.

ABSTRACT

The structure of conventional optoelectronic devices for new high frequency applications as well as the integration with other devices may be modified by using low-loss microwave waveguides. Also the concept of substrate integrated circuits (SICs), which has widely been used in the microwave domain, can be utilized for the integration of optoelectronic devices at millimetre wave (mmW) and sub-mmW frequency ranges.

Photodetectors and modulators, as optoelectronic devices, are two key components of receivers and transmitters in optical communication systems. Conventional traveling-wave (TW) photodetectors and modulators make use of microstrip (MS) and coplanar waveguide (CPW) in their structures as transmission line electrodes. These electrode structures with high losses cannot be utilized in mmW devices. Microwave/mmW losses of MS and CPW, including ohmic, dielectric and radiative losses, in optoelectronic and electro-optical materials such as gallium arsenide (GaAs) and lithium niobate ($LiNbO_3$) are increased with frequency. Rectangular waveguide (RWG) with constant low loss in specific frequency range after its cut-off frequency is an alternative waveguide for mmW devices, although it is non planar and non integrable. Substrate integrated waveguide (SIW) derived from the general SICs concept is a planar form of RWG with some metalized via holes instead of metallic side walls of RWG. New optoelectronic devices and in particular TW photodetector and modulator can be proposed based on SIW structure for mmW frequency, terahertz (THz) photonics and electro-optical applications.

In the design of waveguide photodetectors, the microwave/mmW loss as an important factor for bandwidth limitation is related to two sections, namely, active MS multilayer detection and non-active MS single layer transmission. It is expected that the long section of lossy microstrip line after the detection would significantly limit the bandwidth of the photodetector and may be replaced by low-loss SIW structure. A transition of MS in the photodetector to the multilayer SIW, to separate the photodetector DC bias and SIW metallic plates, is designed and realised in this work.

SIW is considered to propose new types of TW electro-optical modulators. Band-pass $LiNbO_3$ electro-optical phase and amplitude SIW and hybrid SIW-CPW modulators are two types of the proposed devices in this work. The field overlap integral, half-wave voltage, modulation depth and bandwidth are the most important parameters in the design and characterisation of optical modulators which can be optimized for our proposed modulators. For the design of the SIW modulator, the field interaction between the microwave/mmW and optical signals in wide thick SIW and in narrow optical waveguide, respectively, is not considerable and thus low field overlap integral is obtained. This is also because of the half-sinusoidal field distribution of TE_{10} mode in the transverse cross-section of SIW. Furthermore, the microwave/mmW loss of a thin layer SIW to increase the overlap integral is significantly high which affects the modulation depth and bandwidth of the modulator. Therefore, to improve the overlap integral or half-wave voltage and to have simultaneously acceptable mmW loss or bandwidth of the new phase modulator, a structure with a thin $LiNbO_3$ layer including the use of an optical waveguide array in the top of a thick $LiNbO_3$ layer is designed and optimized. Different structures for array optical waveguides are designed and then modulator parameters are calculated. Also, an optical band-pass $LiNbO_3$ amplitude modulator is introduced based on the SIW phase modulator. Instead of utilizing the TE_{10} mode of SIW which is considered in the SIW phase modulator, the TE_{20} mode of SIW is used for this new amplitude modulator. Fabrication of the SIW structure based on a fragile transparent $LiNbO_3$ substrate is done by Excimer laser micromachining. Also, to validate our designed structures, the transition of CPW to SIW in $LiNbO_3$ substrate is designed, fabricated and tested at 60 GHz for the proposed SIW phase modulator and a good agreement between the simulated and measured results is obtained.

The hybrid SIW-CPW modulator is another type of our new designed band-pass electro-optical amplitude modulators using a special coupling mechanism between CPW and SIW for mmW frequencies. This structure preserves the advantages of high field interaction between the optical and microwave signals along CPW electrode structure as well as the advantages of low-loss SIW structure. This is in particular important for mmW packaging, which is critical for practical applications of electro-optical devices. Coupling from SIW to CPW is increased in the half first part of the modulation region and maximized in the middle of the proposed modulator. In the second half part, this coupling happens from CPW to SIW and the output microwave signal can

be used in the integrated systems. Overlap integral of this device increases gradually while the microwave signal is transferred to the CPW along the propagation path. The mode coupling mechanism between CPW and SIW in this structure results in a band-pass amplitude modulator for mmW applications. For the probing-station measurement and the validation of the simulated results, CPW to SIW transitions are designed and optimized.

THz source generation using photodetectors and photomixing techniques are also studied and realized in this thesis. Surface-type photoconductive as a photomixer as well as the integration of this photomixer with a spiral antenna are designed and fabricated for THz frequencies. Optical signal from dual-wavelength laser diode is detected by the photomixer with interdigitated fingers and the generated THz signal is then radiated from the back side of the substrate. Design and optimization of the photodetector and spiral antenna, design of multi-layer masks, fabrication and measurement of integrated circuits are presented in this work.

Furthermore, for high power THz source generation by photomixing techniques, a TWPD is designed and integrated with a CPW-fed log-periodic antenna. To decrease the effect of lossy CPW structure, a low-loss optical waveguide before the detection region is considered. This new device with the TWPD can be used as a high power and broadband THz source generator.

CONDENSÉ EN FRANÇAIS

Contexte des travaux de recherche

Le domaine de la radiofréquence optoélectronique ou micro-ondes photoniques est rapidement mis au point pour de nombreuses applications telles que la radio sur fibre (*Radio over Fiber:* RoF) et composants térahertz (*Terahertz:* THz). Ce domaine pluridisciplinaire de composants à systèmes, peux couvrir l'interaction entre le signal optique et le signal micro-ondes / ondes millimétriques (*millimetre Wave*: mmW) / sous-mmW dans le domaine de longueur d'onde, ou le signal en gigahertz (GHz) et THz dans le domaine fréquentiel.

Les composants optoélectroniques à ondes progressives (*Traveling-Wave*: TW), avec l'interaction distribuée entre les signaux optoélectroniques et micro-ondes, peuvent être des parties des composants principal d'émetteurs et de récepteurs dans les systèmes optiques qui sont important pour l'architecture RoF. Le guide microruban (*Microstrip*: MS) et le guide coplanaire (*Coplanar Waveguide*: CPW) présentent deux structures fondamentales pour la conception des électrodes des composants optoélectroniques à ondes progressives en micro-ondes et ondes millimétriques. Ces structures classiques peuvent présenter le problème de perte quand ils sont utilisés dans la conception de composants photoniques aux fréquences millimétriques.

Le photodétecteur et le modulateur, en tant que deux composants clés des récepteurs et émetteurs dans les systèmes optiques sont étudiés plus en détail. Selon l'illumination des signaux optique au photodétecteur, ils peuvent être divisés en deux types des structures de type de surface, et de type latéral. La bande passante de photodétecteur du type de surface telle que la photodiode PIN est limitée par la constante de temps RC ($BW = 1/2\pi RC$). Bien que sa fabrication soit simple, il ne peut pas être applicable pour les fréquences mmW.

Le guide d'onde photodétecteur (*Waveguide Photodetector*: WGPD) et photodétecteur à onde progressive (*Traveling-Wave Photodetector:* TWPD) sont des photodétecteurs de type latéral. Dans ces photodétecteurs, en raison des effets de propagation, la bande passante n'est pas limitée

par la constante de temps RC, donc, ces photodiodes peuvent être utilisées pour les fréquences millimétriques et sous- millimétriques.

Dans un WGPD microruban, l'absorption du signal optique dans la couche longue intrinsèque de la structure multicouche est convertie en signal micro-ondes et transmis par le guide microruban. Une limitation importante de la bande passante de WGPD est causée par les pertes micro-ondes et millimétriques. Les pertes peuvent être calculés sur la partie de la photodetection multicouches et la partie de la ligne microruban après la détection de la lumière. Il est prévu que la section longue de ligne microruban après la détection limite considérablement la bande passante du WGPD.

Un autre type de photodétecteur avec illumination latérale, TWPD, utilise la structure CPW pour le signal micro-onde et le signal millimétrique généré par l'absorption du signal optique. La géométrie CPW dans TWPD peut être conçue pour être adaptée aux circuits externes et résulter en une bande passante plus élevée comparée à celle du WGPD. Cependant la bande passante dans TWPD est limitée par les pertes micro-ondes dans les fréquences mmW et sous-mmW.

Un autre dispositif optoélectronique important est le modulateur optique. Deux catégories importantes des modulateurs optiques comme des composants optoélectroniques sont les modulateurs électro-optiques et modulateurs électro-absorption. La structure simple du modulateur électro-optique avec le niobate de lithium ($LiNbO_3$) rend ce modulateur plus général et avantageux, comparé au modulateur électro-absorption qui est d'une structure plus compliqué.

Le modulateur électro-optique conventionnel inclut le guide optique Mach-Zehnder (MZ) et le guide micro-onde coplanaire. Le signal optique est divisé dans la branche Y du MZ. Dans chaque bras du MZ, la phase du signal optique est changée par le signal micro-onde et à la sortie, les signaux de deux bras sont recombinés. Il y a des différentes techniques pour la fabrication de guide d'onde du MZ en substrat du niobate de lithium. Une méthode générale est la diffusion du Titane dans le substrat $LiNbO_3$ pour obtenir les différents indices de réfraction ordinaire et extraordinaire.

Toutes les études précédentes ont toujours considéré MS/CPW pour les composants optoélectroniques. Dans ces dispositifs, les pertes micro-ondes et mmW augmentent avec la fréquence. Ces pertes affectent les performances des composants optoélectroniques. Par conséquent, une nouvelle structure micro-ondes et mmW doit être envisagées pour des applications hautes fréquence.

Récemment, il y a un nouveau concept proposé pour la conception de circuits intégrés mmW qui s'appelle les circuits intégrés au substrat (*Substrate Integrated Circuits*: SICs). Les structures planaires et non planaires sont rassemblées en utilisant ce concept. Ces composants intégrés peuvent être réalisés par les trous périodiques de l'air et/ou métal qui peuvent créer l'équivalent des murs électriques ou des régions à faible diélectrique dans la même région diélectrique.

Après une introduction sur les dispositifs optoélectroniques classiques, la possibilité d'intégration des composants optoélectronique sur le SICs est étudiée.

De nouveaux composants optoélectroniques peuvent être conçus en choisissant des structures SICs appropriées, dont les SIWs (*Substrate Integrated Waveguides*) ou SINRDs (*Substrate Integrated Non-Radiative Dielectrics*), et aussi différents composants optoélectroniques comme les photodétecteurs et les modulateurs.

Des dispositifs optiques et SIW/SINRD intégrés au substrat (concept SIC) permettent de présenter de nouveaux dispositifs optoélectroniques à onde progressive. Dans les dispositifs proposés, le concept de SIC est appliqué aux photodétecteurs et modulateurs conventionnels afin de réaliser une nouvelle classe de dispositifs optoélectroniques fondées sur SICs avec une fréquence d'opération et une bande passante élevée. Ce qui est très important pour l'emballage de la structure, qui est plus compliquée dans les bandes mmW.

Deux types de dispositifs optoélectroniques sont considérés: les dispositifs optiques avec les guides d'ondes courts et longes. Pour les dispositifs de guide optiques courts, par exemple les photodétecteurs, le concept SICs peut être utilisé après la détection de la lumière comme une ligne de transmission à faibles pertes. La ligne MS/CPW conventionnelle est remplacée par un SIW pour augmenter la bande passante.

En considérant le SIW du concept SIC et le WGPD des dispositifs optoélectroniques, le SIW basé WGPD est proposé. Ce nouveau dispositif est conçu pour des fréquences spécifiques. C'est un nouveau photodétecteur passe-bande au lieu du photodétecteur conventionnel passe-bas.

Pour les dispositifs optique avec les guides d'ondes longe, comme modulateurs optique, les composants micro-ondes contrôlés optiquement et inversement, le concept SIC peut être appliqué directement au composant. Dans le modulateur optique, les signaux micro-ondes et optiques interagissent dans la range de centimètre et le SIW basé modulateur peut être proposé. Le SIW pur ou une combinaison de SIW et CPW sont utilisés dans les modulateurs SIW proposés au lieu d'utiliser le CPW conventionnel à hautes pertes micro-ondes.

Les Pertes Micro-ondes des Composants Optoélectroniques

Dans le premier chapitre de cette thèse, les caractéristiques mmW et micro-ondes des dispositifs optiques traditionnels y compris photodétecteurs et modulateurs sont couverts. Ensuite, le concept de SIW est appliqué à la structure des photodétecteurs et des modulateurs classiques avec GaAs, InP isotrope et $LiNbO_3$ anisotrope, respectivement. Dans les photodétecteurs conventionnels, la bande passante peut être limitée par la section multicouche courte pour d'absorption optique et la section longue pour de transmission micro-ondes. Par ailleurs, le facteur principal de limitation de la bande passante dans les hautes fréquences est lié à la partie de la ligne transmission microruban et de CPW.

Par conséquent, pour profiter des faibles pertes des SIWs dans la structure des dispositifs optoélectroniques, WGPD avec le guide microruban est remplacé par la structure SIW. Puis une transition du guide microruban à la structure multicouche SIW est conçue et fabriquée en considérant la tension continue du photodétecteur. Ce travail, théorique et expérimental, suggère que ces dispositifs optoélectroniques basés sur SIC sont des candidats très prometteurs pour les nouveaux systèmes photoniques micro-ondes / mmW à haute fréquence.

Les Modulateurs SIW Électro-optiques

Dans le deuxième chapitre, un modulateur électro-optique basé sur SIW est proposé pour les applications hautes fréquences. L'analyse optique et micro-ondes / mmW de ce modulateur passe-bande est présentée. L'intégrale de recouvrement, la tension demi-onde, la profondeur de modulation et la bande passante sont les principaux paramètres dans la conception de modulateurs optiques.

Les modulateurs classiques de phase et d'amplitude, avec le guide optique unique et le structure MZ, utilisent les CPW à hautes perte pour l'interaction des signaux optiques et micro-ondes. Bien que l'intégrale de recouvrement élevée et la basse tension peuvent être obtenus en utilisant les modifications dans les modulateurs électro-optiques classiques, la perte micro-onde limite la profondeur de modulation et aussi la bande passante de ces dispositifs conventionnels à hautes fréquences.

Dans ce chapitre, le SIW à faible perte est considéré comme ligne de transmission micro-ondes des modulateurs proposés et ensuite, certaines modifications sont appliquées à ces modulateurs passe-bande. L'utilisation d'un guide optique unique sur SIW à faible perte résulte en une intégrale de recouvrement très faible bien qu'il puisse être utilisé à haute fréquence avec une grande bande passante. Pour avoir une valeur élevée de l'interaction optique / mmW, le guide optique est remplacé par un réseau des guide optiques dans une mince couche de substrat $LiNbO_3$. Cette modification améliore l'intégrale de recouvrement, mais les pertes micro-ondes dans la structure mince de SIW sont sensiblement augmentés et affectent la bande passante du modulateur. Le substrat $LiNbO_3$ multicouches avec les réseaux de guides optiques dans la couche mince peut être une modification du modulateur SIW de phase avec à haute l'intégrale de recouvrement et basse perte micro-onde. L'idée d'un modulateur de phase SIW est considérée dans la structure du modulateur d'amplitude SIW. Une structure pour l'excitation de mode TE_{20} de SIW, qui peut être en interaction avec le signal optique, est présentée. La réalisation du modulateur SIW est faite en utilisant le micro-usinage laser Excimer et la conception de la cavité du résonateur et aussi de la transition de CPW à SIW dans le substrat $LiNbO_3$.

Les Modulateurs SIW-CPW Électro-optiques

Le troisième chapitre se concentre sur un nouveau type de modulateur d'amplitude électro-optique qui utilise le mécanisme de couplage entre les structures SIW et CPW.

Dans ce modulateur SIW-CPW hybride, nous gardons la structure CPW dans les modulateurs classiques avec intégrale de recouvrement élevée, et optimisons juste cette structure pour les applications hautes fréquences comme la radio sur fibre optique. Dans les modulateurs d'amplitude classiques, l'interaction entre les signaux micro-ondes et optiques est obtenu à partir de l'interaction croisée et cette interaction est constante sur la longueur du modulateur.

Dans le modulateur SIW-CPW proposé, le signal micro-onde change progressivement sur la longueur du modulateur et est maximisé dans le milieu du composant. En tant qu'un circuit intégré, le signal micro-onde vient du SIW et le couplage de SIW à CPW survient dans la première moitié de la partie de modulation. Dans la seconde partie, nous avons le couplage de CPW à SIW et à la fin, ce signal peut être utilisé dans d'autres parties du circuit intégré. La flexion du SIW et l'élimination de certains des trous du SIW sont considérés pour la séparation des ports optiques et micro-ondes et aussi pour le passage des guides optiques entre les trous du SIW. Finalement, la transition de CPW à SIW est considérée pour la mesure en mesures sous pointes.

Type de Surface Photodétecteur pour la source THz

Les conceptions et fabrications du photodétecteur de type de surface et d'antenne spirale à large bande pour le générateur THz intégré sont présentées dans le quatrième chapitre. Les différents photoconducteurs sont conçus pour les larges bandes générateurs THz. L'avantage de choisir ce photoconducteur/photo-mélangeur est la simplicité de conception et de fabrication. Le désavantage est un rayonnement de faible puissance en raison de la petite surface de seuil de dommage.

L'antenne spirale qui est une antenne indépendante de la fréquence est intégrée avec le photoconducteur pour rayonner le signal THz généré. Le taux de croissance de l'antenne spirale et le nombre des tours en spirale sont des paramètres optimisés dans la section de l'antenne de ce

chapitre. La fabrication de ce générateur THz est faite par la conception de trois masques y compris les doigts, mesa et spirale. En raison de certaines difficultés dans la gravure de la zone photoconducteur, le masque de mesa est conçu un peu plus grand que la taille désignée. Le wire-bonding et packaging avant la mesure sont présentés dans ce travail.

Générateur THz basé sur l'illumination de pointe

Un nouveau générateur de signal THz basé sur TWPD et son intégration avec une antenne THz log-périodiques alimentée en CPW est proposé dans le cinquième chapitre. La zone d'absorption optique dans le TWPD de générateurs THz est plus grande que celle des photoconducteur de type de surface. Par conséquent, la puissance d'illumination optique résultant de la haute puissance de rayonnement THz peut être augmentée. En changeant les pièces de métal et des pièces en métal gravé de l'antenne log-périodique classique, l'antenne alimentée en CPW peut être réalisée et intégré avec le TWPD pour le générateur THz.

Des travaux futurs peuvent être considérés pour les différents chapitres de cette thèse.

Pour l'intégration d'un photodétecteur et un guide d'ondes à faible pertes en utilisant les concepts de SIC comme discuté dans le premier chapitre, la transition de CPW (dans TWPD) à multicouche SIW peut être conçu. Aussi, le SIW peut être remplacé par le SINRD pour les applications sous- mmW.

Les modulateurs basés en SIW/SINRD peuvent être proposés sur le substrat de niobate de baryum et de calcium (*Calcium Barium Niobate:* CBN) avec un coefficient électro-optique élevé pour améliorer les performances des modulateurs proposés. En outre, pour la partie à branche longue Y dans la structure MZ présentée dans le Chapitre 2, certains techniques de couplage optique comme l'interférence multimode (*Multimode Interference:* MMI) peuvent être utilisés.

Dans le Chapitre 3, la seconde section du composant, qui est le couplage de CPW à SIW, peut être enlevée. L'intégrale de recouvrement est progressivement augmentée le long de la partie de modulation au lieu d'être maximum au milieu de la structure. L'utilisation de SINRD et des substrats multicouches pour augmenter le coefficient de couplage et la bande passante de ce nouveau modulateur pourraient être étudiées à l'avenir.

Pour le générateur THz de type de surface, une autre technique de fabrication comme low-temperature growing (LTG) peut être utilisé pour augmenter la bande passante du photoconducteur. Pour l'illumination de signal optique à haute puissance, un photoconducteur multicouche peut être conçu et fabriqué. Dans le dernier chapitre avec le photodétecteur de pointe, le concept SIC peut être utilisé dans la conception de certaines parties après la détection y compris la CPW et l'antenne. En outre, le concept SIC peut être appliqué à d'autres dispositifs optoélectroniques tels que des composants électriques/optiques, optiquement/électriquement contrôlés pour des applications mmW et sous- mmW.

TABLE OF CONTENTS

DEDICATION III

ACKNOWLEDGEMENT IV

RÉSUMÉ V

ABSTRACT IX

CONDENSÉ EN FRANÇAIS XII

TABLE OF CONTENTS XX

LIST OF TABLES XXIV

LIST OF FIGURES XXV

LIST OF ACRONYMS AND ABBREVIATIONS XXXIII

INTRODUCTION 1

CHAPTER 1. MICROWAVE AND MILLIMETRE LOSSES OF OPTOELECTRONIC DEVICES 11

1.1 Introduction 11

1.2 MS and CPW losses in conventional optoelectronic devices 12

1.2.1 MS/CPW in photodetectors 12

1.2.2 CPW in modulators 15

1.3 Loss comparison of conventional and SIW-based optical devices 18

1.3.1 SIW in photodetectors....20

1.3.2 SIW in modulators....20

1.4 Transition from MS to SIW in photodetector....22

1.4.1 Theoretical issues....22

1.4.2 Fabrication, measurement and validation....25

1.5 Conclusion....26

CHAPTER 2. SIW ELECTRO-OPTICAL MODULATORS....28

2.1 Introduction....28

2.2 TW conventional electro-optical modulators....29

2.2.1 Phase modulators....29

2.2.2 Amplitude modulators....31

2.3 Proposed SIW-based modulator....36

2.3.1 Design of single optical waveguide structure....37

2.3.2 Optical waveguide arrays in single $LiNbO_3$ layer....46

2.3.3 Multilayer structure with optical waveguide array....53

2.3.4 Transition of CPW to SIW in $LiNbO_3$....59

2.4 Exprimental issues and validation....65

2.4.1 Excimer laser micromachining....65

2.4.2 Wafer dicing and hole drilling....68

2.4.3 Applications and experimental results 73

2.5 Conclusion 77

CHAPTER 3. ELECTRO-OPTICAL SIW-CPW MODULATORS 79

3.1 Introduction 79

3.2 Newly proposed SIW-CPW based modulator 79

3.3 Microwave structure 82

3.3.1 Theoretical discussion 82

3.3.2 Experiments issues and validation 91

3.4 Optical waveguide 93

3.4.1 Theoretical discussion 93

3.4.2 Experimental issues 98

3.5 Conclusion 105

CHAPTER 4. SURFACE-TYPE PHOTODETECTOR FOR THZ SOURCE GENERATION 107

4.1 Introduction 107

4.2 Theoretical discussions 108

4.2.1 Photoconductive photomixer 109

4.2.2 Spiral antenna 114

4.2.3 Bandwidth and radiation power 118

4.3 Experimental issues 119

4.3.1 Multilayer mask 120

4.3.2 Fabrication and packaging 124

4.3.3 Measurements 128

4.4 Conclusion 132

CHAPTER 5. THZ GENERATOR BASED ON EDGE-ILLUMINATION 134

5.1 Introduction 134

5.2 Traveling-wave photodetector 137

5.2.1 Microwave and optical analysis 139

5.2.2 Bandwidth limitations 144

5.3 CPW-fed log-periodic antenna 148

5.4 Conclusion 152

CONCLUSIONS 153

REFERENCES 158

LIST OF TABLES

Table 1.1: Microwave design parameters for the new proposed device 24

Table 2.1: Microwave design parameters of CPW to SIW transition in SIW phase modulator at 60 GHz. 62

Table 3.1: Microwave design parameters of SIW-CPW amplitude modulator at 60 GHz. 90

Table 3.2: Design parameters for the optical waveguide of the newly proposed SIW-CPW modulator. 97

Table 4.1: Photoconductive capacitance and dimensions for three different structures. 112

Table 4.2: Photoconductor design parameters. 113

Table 5.1: Simulation parameters for microwave and optical analysis of TWPD. 140

Table 5.2: Simulation parameters for CPW-fed log-periodic antenna. 150

LIST OF FIGURES

Figure. 1: Different devices in terms of their inputs and outputs in optoelectronic devices. 2

Figure. 2: Combination of SIC concept and TW optoelectronic device to propose SICs-based TW optoelectronic devices. 6

Figure. 3: Applications of optoelectronic devices in the structure of a) RoF systems, and b) THz generator. 7

Figure 1.1: a) WGPD with MS line, b) MS loss versus frequency and conductor thickness as functions of MS width (W) and GaAs substrate thickness (H). 14

Figure 1.2: a) TWPD with CPW geometry, b) CPW loss versus frequency and conductor thickness as a function of strip (W)-to-slot width (S) ratio in GaAs substrate. 16

Figure 1.3: a) Optical intensity MZ modulator with CPW, b) CPW loss versus frequency and conductor thickness as a function of strip (W)-to-slot width (S) ratio in $LiNbO_3$ substrate. 17

Figure 1.4: a) SIW for new optoelectronic devices, b) Attenuation and phase constants versus frequency in SIW. 19

Figure 1.5: Comparison of attenuation constant versus frequency as functions of substrate thickness and width in MS, CPW and SIW for GaAs substrate. 21

Figure 1.6: Comparison of attenuation constant versus frequency as functions of substrate thickness and width in CPW and SIW in $LiNbO_3$ substrate. 21

Figure 1.7: Multilayer transition from WGPD to SIW. 23

Figure 1.8: Simulation results of microwave fields, a) MS mode in point A, b) MS and SIW modes in point B, c) SIW mode in point C of Figure 1.7. 25

Figure 1.9: Fabricated multilayer transition of MS to SIW with the device length of 11.8 mm. 27

Figure 1.10: Measured (dashed lines) and simulated (solid lines) insertion and return losses of SIW-based WGPD and MS conventional WGPD with the same length. 27

Figure 2.1: Phase modulator in a) X-cut and b) Z-cut $LiNbO_3$ substrates. 30

Figure 2.2: Cross-sectional view in the middle and 3D view of amplitude modulator in a) X-cut and b) Z-cut $LiNbO_3$ substrates. 33

Figure 2.3: Power transmittance factor in MZ amplitude modulator, (a) small-signal, (b) ON-OFF modulator. 34

Figure 2.4: Single optical waveguide in RWG for phase modulation in $LiNbO_3$. 37

Figure 2.5: RWG width versus cut-off frequency for different modes in the permittivity of a) 28 for Z-cut and b) 43 for X-cut $LiNbO_3$ substrates. 40

Figure 2.6: a) Cross-section view of RWG and its b) microwave loss and c) effective index, as bandwidth limitations for Z-cut $LiNbO_3$ substrate. 41

Figure 2.7: Modulation depth versus frequency for, a) lossy structure, b) mismatched velocity case and c) mismatched lossy case, of Z -cut $LiNbO_3$ with the device length of 1 cm. 42

Figure 2.8: a) New dimensions for RWG and b) microwave loss and c) effective index, to have symmetry behavior in modulation depth. 43

Figure 2.9: Optimized symmetric modulation depth versus frequency for 1 cm device length, a) lossy structure, b) mismatched velocity case, and c) mismatched lossy case, of Z -cut $LiNbO_3$. 44

Figure 2.10: Half-wave voltage versus modulation length for single optical waveguide phase modulator at 60 GHz. 46

Figure 2.11: Cross-section of RWG modulator with optical waveguide array. 47

Figure 2.12: a) Optical waveguide array in MZ structure as well as b) 20 μm and c) 30 μm spacing between the optical waveguides. 48

Figure 2.13: a) Optical waveguide array with four waveguides; spacing and length of the optical waveguide array respectively are b) 20 μm and 1 cm, c) 30 μm and 1 cm, and d) 30 μm and 2 cm. 50

Figure 2.14: a) Optical waveguide array with eight waveguides; b) spacing and length of the optical waveguide array respectively are 30 μm and 1 cm, respectively. 51

Figure 2.15: Half-wave voltage in single-mode optical waveguide array for different thicknesses of $LiNbO_3$ substrate. 52

Figure 2.16: a) Conversion of single-mode to multimode optical waveguide, and b) field distribution for multimode waveguide. 52

Figure 2.17: Half-wave voltage in multimode optical waveguide array for different thicknesses of $LiNbO_3$. 53

Figure 2.18: a) Schematic view of the proposed SIW phase modulator with an array of four optical waveguides, b) optical effective index (n_O), mmW effective index (n_M) and attenuation constant (α) versus frequency as a function of substrate thickness H. 55

Figure 2.19: Modulation depth in different cases, a) lossless, b) velocity-matched, and c) lossy unmatched case. 57

Figure 2.20: Half-wave voltage of the proposed modulator using two-layer substrate and optical waveguide array. 58

Figure 2.21: Transition of CPW to SIW for phase modulation. RF/optical ports and different regions of the device are shown. 59

Figure 2.22: Flowchart of the design procedure for transition of CPW to substrate integrated electro-optical waveguide. 61

Figure 2.23: Simulation result of microwave insertion and return loss of proposed SIW phase modulator. 63

Figure 2.24: SIW-based electro-optical amplitude modulator, a) using MZ structure, b) using waveguide array, and c) cross section of modulation part including TE_{20} mode of SIW. 64

Figure 2.25: Different lasers and their wavelength in micromachining. 66

Figure 2.26: Excimer laser micromachining system; (a) picture of the laser and control system, (b) beam profile of Excimer laser (c) optical beam schematics; circular and rectangular mask are shown. 67

Figure 2.27: Taper effect of Excimer laser. 68

Figure 2.28: a) X-Cut $LiNbO_3$ wafer with 76.2 mm diameter and 0.22 mm thickness, b) image of the cutting precision. 69

Figure 2.29: Flowchart for micromachining by Excimer laser. 71

Figure 2.30: Incomplete hole with 30 μm diameter and 3 μm depth. 72

Figure 2.31: SEM image of a) a complete 80 μm diameter hole and b) a series of holes in SIW 73

Figure 2.32: Laser micromachining of 10 μm $LiNbO_3$ optical ridge waveguides by scanning a 20 μm width line 74

Figure 2.33: a) Hole pattern by Excimer laser for microwave waveguide applications, and b) fabricated device. 75

Figure 2.34: Probing-station for the measurement of scattering parameters of the fabricated devices with CPW transition. 75

Figure 2.35: Return and insertion losses for fabricated devices with, a) short-length SIW and b) long-length SIW, and also c) attenuation constant and microwave effective index. 77

Figure 3.1: a) Proposed SIW-CPW electro-optical amplitude modulator and schematic top views of b) optical section and c) microwave section. 81

Figure 3.2: a) CPW, b) RWG and c) combination of CPW/RWG for coupling mechanism. 83

Figure 3.3: Normalized wave amplitude versus the length-coupling coefficient as a function of phase constant difference. 84

Figure 3.4: a) Effective permittivity versus frequency for CPW (case1: TEM mode), RWG (case2: TE_{10} mode) and the hybrid structure of both CPW and RWG (case3: first normal

mode, case4: second normal mode), b) electrical fields in different frequencies for different modes. 86

Figure 3.5: Maximum power transfer ratio and length of CPW and RWG modes versus frequency. 88

Figure 3.6: RWG incorporating CPW in the middle of the structure for mode coupling mechanism in $LiNbO_3$ substrate. 89

Figure 3.7: Scattering parameters used to explain the coupling mechanism from RWG to CPW. 89

Figure 3.8: Fabricated circuit for the microwave part of SIW-CPW modulator on $LiNbO_3$; SIW holes and resistor pads are shown. 92

Figure 3.9: Simulated and measured insertion and return losses of SIW-CPW amplitude modulator. 92

Figure 3.10: MZ interferometer in $LiNbO_3$ substrate and design parameters. 93

Figure 3.11: a) Mode propagation of MZ optical waveguide; and cross-section of the normalized optical field in MZ optical waveguide, b) input look of the optical waveguide, c) middle section of the optical waveguide. 95

Figure 3.12: Optical field in MZ optical waveguides versus optical waveguide width and Y-splitter angle. Optical waveguide depth is 3 μm. 96

Figure 3.13: a) Proposed optical waveguides using electro-optical CBN thin film, (b) Field distribution in CBN waveguide with the effective index of 2.0899. 98

Figure 3.14: Layout of different optical waveguides using Y-branch for SIW-CPW amplitude modulator on $LiNbO_3$ substrate. 99

Figure 3.15: a) Y-branch part for one of the fabricated waveguides, b) reflection in the edge of waveguide for visible light illumination, c) optical path in Y-branch and d) SEM image of the waveguide edge roughness. 100

Figure 3.16: a) Edge polishing machine from Ultrapol Company and b) edge of $LiNbO_3$ substrate for optical waveguide after polishing. 101

Figure 3.17: Optical loss measurement of fiber to Ti:$LiNbO_3$ waveguide to fiber, a) Measurement setups, b) fiber to waveguide connection, c) waveguide to fiber connection using matching oil, and d) output of spectrum analyzer. 103

Figure 3.18: a) Fabricated thin-film CBN optical waveguides and SEM images of the waveguides with b) 4 μm width, 2.5 μm thickness and c) 8 μm width, 2.5 μm thickness. 104

Figure 3.19: a) Measurement setup for the CBN waveguide, b) fiber to waveguide connection, and field intensity of optical waveguides with c) 5 μm width and d) 10 μm width. 105

Figure 4.1: Surface-type illuminated photomixer and spiral antenna in different structures for THz source generator. 108

Figure 4.2: THz generation using photoconductive photomixer and spiral antenna. 109

Figure 4.3: a) InGaAs photomixer on InP substrate with interdigitated electrodes, b) circuit modeling of the photoconductor including resistance, capacitance and bias voltage. 110

Figure 4.4: Photocurrent of the photomixer versus bias voltage as functions of optical power and carrier lifetime. 114

Figure 4.5: a) 3D view of spiral antenna in InP substrate, b) packaging of the circuit, c) top view and excitation port by optical signal, d) radiation pattern from the back of substrate. 116

Figure 4.6: 4-turn spiral antenna with growing factor of 0.18 and optical excitation part of 18×18 μm^2 in InP substrate, a) return loss, and, b) radiation pattern without package and, c) radiation pattern from packaged circuit at 100 GHz; Dashed line is φ = 90 degree and solid line for φ = 0. 117

Figure 4.7: THz output power versus frequency as functions of photoconductive carrier lifetime and photocurrent. 118

Figure 4.8: Effects of different parameters on THz output power. 119

Figure 4.9: Interdigitated finger mask and alignments. 121

Figure 4.10: Mesa mask and alignments. 122

Figure 4.11: Spiral mask and alignments. 123

Figure 4.12: Alignments of the finger, mesa and spiral masks together. 124

Figure 4.13: Some of the fabricated samples a) five different dosage for the samples, b) numbering of samples, c) usable samples, d) damaged samples. 125

Figure 4.14: Packaging of the fabricated circuit in 14-pin standard package from the bottom. .. 126

Figure 4.15: Wire bonding of the fabricated circuit from the top. 127

Figure 4.16: Stands of the fabricated circuit for optical table, a) metallic rotating part and b) sample on plastic rotating part. 127

Figure 4.17: I-V curve for the samples without implantation. 128

Figure 4.18: Measurement setup using commercial photodetector. 129

Figure 4.19: Measured signals from electrical spectrum analyzer, a) 50 GHz range from commercial photodetector, b) 100 GHz range from commercial photodetector. 129

Figure 4.20: Measurement setup using fabricated photomixer and antenna. 130

Figure 4.21: Measured signals from electrical spectrum analyzer for 50 GHz range of our fabricated device. 131

Figure 4.22: Measurement setup using Bolometer for detecting low power high frequency signals. 132

Figure 5.1: Edge-illumination structure for the photomixer and CPW-fed log-period antenna in exploring different possible schemes for THz generator. 135

Figure 5.2: Top view of the proposed high power THz generator based on edge-illumination. . 137

Figure 5.3: TW photodetector connected to CPW. 139

Figure 5.4: Microwave loss versus frequency as functions of strip width (W=1.5 μm to 3 μm) and I-layer thickness (d=1 μm to 1.5 μm) for TWPD. 141

Figure 5.5: Electrical phase velocity versus frequency as functions of strip width (W=1.5 μm to 3 μm) and I-layer thickness (d=1 μm to 1.5 μm) for TWPD. 141

Figure 5.6: Characteristic impedance versus frequency as functions of (W=1.5 μm to 3 μm) and I-layer thickness (d=1 μm to 1.5 μm) for TWPD. 142

Figure 5.7: a) Electrical and b) optical field intensities in TWPD (I-layer thickness 1 μm, strip width 3 μm). 143

Figure 5.8: Overlap between optical and electrical field intensities in TWPD for 1μm thickness of absorbing layer. 144

Figure 5.9: TWPD bandwidth limitation by the ratio of electrical to optical phase velocity as functions of optical absorption (α) and reflection coefficient in the input termination (γ). 146

Figure 5.10: Carrier drifts bandwidth limitation versus electrical field as a function of absorbing layer thickness. 147

Figure 5.11: Normalized velocity-mismatch and carrier drift bandwidth versus I-layer thickness. 148

Figure 5.12: a) 3D view of the complementary CPW-fed log-periodic antenna, b) top view of the antenna with dimensions. 149

Figure 5.13: a) Return loss versus frequency for CPW-fed log-periodic antenna, b) Radiation pattern at 100 GHz for φ = 0 (Solid line) and φ = 90 degree (Dashed line). 151

LIST OF ACRONYMS AND ABBREVIATIONS

CBN	Calcium Barium Niobate
CO_2	Carbon dioxide
CPS	Coplanar Strip
CPW	Coplanar Waveguide
FDFD	Finite Difference Frequency Domain
FEM	Finite Element Method
GaAs	Gallium Arsenide
HFSS	High Frequency Structure Simulator
InGaAs	Indium Gallium Arsenide
InGaAsP	Indium Gallium Arsenide Phosphate
InP	Indium Phosphate
KrF	Krypton Fluoride
$LiNbO_3$	Lithium Niobate
LTG	Low-Temperature Growing
MMI	Multimode Interference
MMT	Mode Matching Technique

mmW	millimetre Wave
MS	Microstrip
MSM	Metal Semiconductor Metal
MZ	Mach-Zehnder
Nd:YAG	Neodymium-doped Yttrium Aluminum Garnet
RF	Radiofrequency
RoF	Radio over Fiber
RWG	Rectangular Waveguide
SEM	Scanning Electron Microscope
Si	Silicon
SIC	Substrate Integrated Circuit
SiO_2	Silicon Dioxide
SINRD	Substrate Integrated Non-Radiative Dielectric
SIW	Substrate Integrated waveguide
TE	Transverse Electric
THz	Terahertz
Ti	Titanium
Ti:$LiNbO_3$	Titanium diffused Lithium Niobate
TLM	Transmission Line Method

TM	Transverse Magnetic
TW	Traveling-Wave
TWM	Traveling-Wave Modulator
TWPD	Traveling-Wave Photodetector
WGPD	Waveguide Photodetector

INTRODUCTION

The field of radiofrequency (RF) optoelectronics or microwave photonics including fibre wireless technologies is rapidly developed for many different applications such as radio over fiber (RoF) systems and terahertz (THz) biomedical imaging devices. This multidisciplinary field ranging from devices and technologies to systems can cover the interaction between the optical signal and microwave / millimetre wave (mmW) / sub-mmW signals in wavelength domain or gigahertz (GHz) and THz signals in frequency domain.

Traveling-wave (TW) optoelectronic devices with distributed field interaction between traveling microwave and optical signals have been considered as principal constituents of transmitters and receivers in optical and electro-optical systems, which are in particular significant for mmW RoF architectures. Microstrip (MS) line and coplanar waveguide (CPW) present two fundamental building structures for the electrode design of microwave and mmW TW electro-optical or optoelectronic devices [1]. Such conventional structures may exhibit a number of hurdles when used in the design of mmW photonic devices, namely, transmission loss, impedance and velocity matching and device packaging issues. In Figure 1, a general structure for optoelectronic devices is illustrated. Two microwave/mmW and two optical ports as well as DC bias are specified in the main figure. Four different types of the optoelectronic devices including laser diode, photodetector, electronically-controlled optical devices and optically-controlled electronic devices, with different input and output ports are illustrated in this figure. TW Photodetectors and modulators, as two key components of receivers and transmitters in optical systems, can thus be studied in more details. Although, for a two-port photodetector, the optical input signal is converted to microwave output signal, all optical and RF ports can be presented for a four-port modulator. Optical and electronic modulators can be used as electronically controlled optical devices and vice versa.

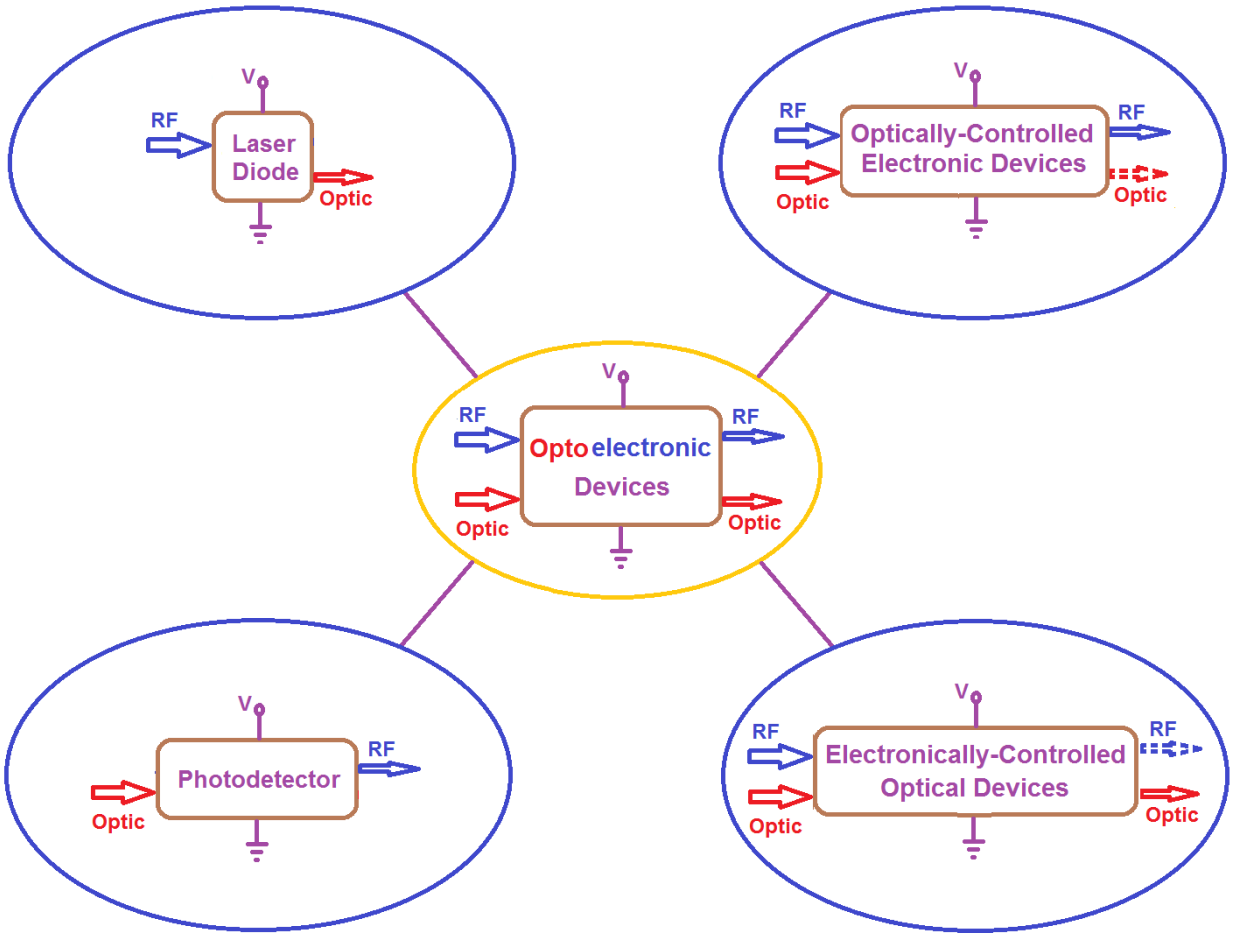

Figure. 1: Different devices in terms of their inputs and outputs in optoelectronic devices.

According to the illumination of optical input signals to the surface and the edge of photodetectors, they can be divided into surface-type and edge-type structures. Bandwidth of the surface-type photodetectors such as PIN photodiodes is limited by RC time constant (BW=1/2πRC). Although the fabrication of surface-type photodetectors is simple, they cannot be applicable for mmW frequencies. In the edge-type photodetectors, such as waveguide photodetector (WGPD) and TW photodetector (TWPD), because of TW effects, bandwidth is not limited by RC time constant and theses photodiodes can be used for mmW and sub-mmW frequencies [2].

In WGPD with edge-illumination and MS geometry, the optical signal absorbed into the long intrinsic layer of a multilayer structure is converted to the microwave signal and transmitted by

the MS waveguide. One of the important bandwidth limitations of WGPD is related to microwave and mmW losses because of the lossy MS geometry in its structure. The loss can be calculated over the multilayered photodetection region and MS line after the detection of light. It is expected that the long section of lossy MS line after the detection as a part of WGPD would significantly limit the bandwidth of WGPD. In [3], a bandwidth of 40 GHz for an edge-illuminated waveguide PIN photodetector was obtained. Also, the microwave losses of MS line used in WGPD were analyzed and measured in [4]-[7]. For gallium arsenide (GaAs) and indium phosphate (InP) substrates, high microwave losses were observed by increasing frequency. In another type of the edge-illuminated photodetectors, namely TWPD, CPW structure is used to support microwave and mmW signals generated by the absorption of optical signal. Although the CPW geometry in TWPD can be designed to be matched to the external circuit and results in a higher bandwidth compared to that of WGPDs, the bandwidth is still limited by loss in mmW and sub-mmW frequencies. Microwave characteristics of a long TWPD for high-power operation were discussed in [7]-[8]. In these works, the attenuation constant increases with frequency and therefore they are not applicable for high frequencies. Also, in [9]-[11], the microwave losses of CPW structure in GaAs and InP substrates were studied, suggesting that the bandwidth of TWPD is affected by the microwave loss of CPW transmission line.

The optical modulator is another important optoelectronic device. Two important categories of optical modulators as optoelectronic devices are electro-optical and electro-absorption modulators. Simple structure of electro-optical modulators in a single electro-optical substrate, such as lithium niobate ($LiNbO_3$), makes them more applicable compared to complicated multilayer electro-absorption modulators [12]. CPW-based conventional amplitude $LiNbO_3$ electro-optical modulators include Mach-Zehnder (MZ) optical waveguide and CPW structure for the microwave modulation signal. Generally, optical signal is split and separated in the Y-branch of MZ and after being subject to the phase change of optical signals in the two arms of MZ by microwave signal, they are recombined at the output. The MZ optical waveguide can be fabricated with various methods in different cuts of $LiNbO_3$ wafers [13]. One of the general methods requires performing in-diffusion of titanium (Ti) in X-cut or Z-cut $LiNbO_3$ substrates [14]-[15] to have both of ordinary and extraordinary refractive index changes. In $LiNbO_3$ optical modulator compared to the photodetector, microwave loss effect becomes more pronounced

because of a long field interaction section between microwave and optical signals. In [16]-[17], the microwave loss of $LiNbO_3$ modulator was discussed with reference to the bandwidth.

All of the previous studies have considered conventional MS/CPW in the development of optoelectronic devices. In such devices, microwave and mmW losses increase with frequency which adversely affects the performances of these devices. Therefore, a new microwave and mmW structure should be developed if higher frequency applications are considered.

Recently, there is an emerging concept proposed and demonstrated for the design of mmW integrated circuits and systems, namely, substrate integrated circuits (SICs), in which planar and non-planar structures are made together owing to the technique of synthesis that transforms the non-planar structures into planar form. In this case, technical and structural features are still retained as compared to their original counterparts. This is made possible through artificial periodic air-hole and/or metalized via arrays that can create equivalent electrical walls or low-dielectric regions within the same dielectric region. The SIC concept is different from the well-documented photonic bandgap structure [18] in which the artificial wave-guiding channel is created on the basis of stopband effects or resonance phenomena along the unwanted directions.

In [19]-[20], state-of-the-art SICs design and implementation platforms were reviewed and discussed in detail. Also, different possibilities and numerous advantages of the SICs are shown for microwave and mmW optoelectronics applications. In [21]-[23], a planar platform was developed in which the MS line and rectangular waveguide (RWG) are fully integrated on the same substrate, and they are interconnected via a simple taper. The losses of integrated type RWG, substrate integrated waveguide (SIW), are obtained and discussed. Also, a technique for designing and realising substrate integrated non-radiative dielectric (SINRD) guide from SICs concept was proposed and demonstrated by drilling a pattern of air holes in a planar dielectric substrate [24].

After a brief review of the conventional optoelectronic devices with the lossy MS and CPW geometries as well as new SICs concept which is used for microwave and mmW devices, possibility of using the SICs concept for optoelectronic devices for a wide range of applications such as RoF systems is studied. New optoelectronic devices can be designed by selecting an appropriate SICs structure such as SIW or SINRD guide that can be combined with different types of optoelectronic devices including photodetectors and modulators. In Figure 2, two typical

types of TW optical devices including WGPD and TW modulator (TWM) as well as SIW and SINRD from the SICs concept are shown. In the proposed devices, the SICs concept is applied to the design of conventional TW photodetectors and modulators to realize a new SICs-based optoelectronic device configuration expected with high operation frequency and bandwidth. According to Figure 2, two types of optoelectronic devices can be considered. First, the optical devices with short optical waveguides such as photodetectors and the second, optical devices with long optical waveguide such as optical intensity modulator or some of optically controlled microwave devices and vice versa. For the short optical waveguide devices such as photodetector, SIC concept can be used after the detection of light as a low-loss transmission line, instead of conventional MS or CPW, to increase the part of bandwidth related to the microwave loss. By considering SIW from the SICs concept and WGPD from optoelectronic devices, the SIW-based WGPD can be proposed. In the proposed device, multilayer structure is needed to bias the photodetector as it will be discussed later. A new device may be designed for the specific frequency range and it is a new band-pass photodetector instead of conventional low-pass photodetector. For the long optical waveguide devices, SICs concept can be applied directly to the device. In the optical modulator, the microwave and optical signals interact in the range of centimetre and the SICs concept can be applied to the entire optical waveguide region. In the newly proposed SIW-based modulators, instead of using conventional CPW with the high microwave loss, pure SIW or hybrid SIW-CPW are considered.

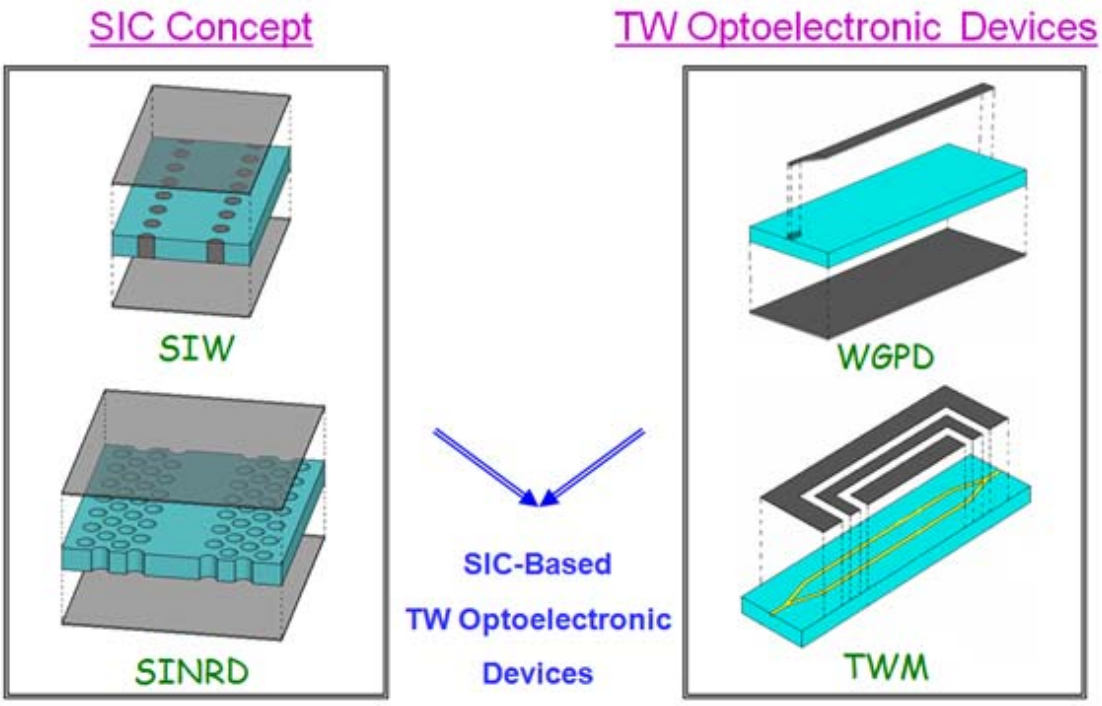

Figure. 2: Combination of SIC concept and TW optoelectronic device to propose SICs-based TW optoelectronic devices.

Applications of optoelectronic devices, photodetectors and modulators in RoF systems and THz generators are illustrated in Figure 3. All conventional optoelectronic devices may be replaced by new SICs-based optoelectronic devices to be used for mmW, sub-mmW and THz frequencies. As shown in Figure 3a, central and base stations are two main sections of the RoF systems. In these stations, some typical devices with different microwave waveguide geometries are illustrated. In the central station, the optical signal from a laser diode is modulated with the RF signal and transmitted on a low-loss optical fiber. On the other side in the base station, optical signal is detected by the MS-based photodetector and radiated by an antenna. Also, the microwave signal from the receiver antenna is used for the modulation of the optical signal and transmitted on optical fiber to the photodetector in the central station and then RF signal is detected.

In Figure 3b, THz source generator using a photodetector is illustrated. Optical signal with two different modes is generated and amplified by a laser diode and an optical amplifier. The wavelength difference between laser modes is in the range of THz in frequency domain and can

be detected by a high speed photodetector and transmitted for some applications such as biomedical imaging. Photodetectors and modulators in Figure 3 may be replaced by new SICs-based devices to improve the performance of these devices for mmW and THz frequencies.

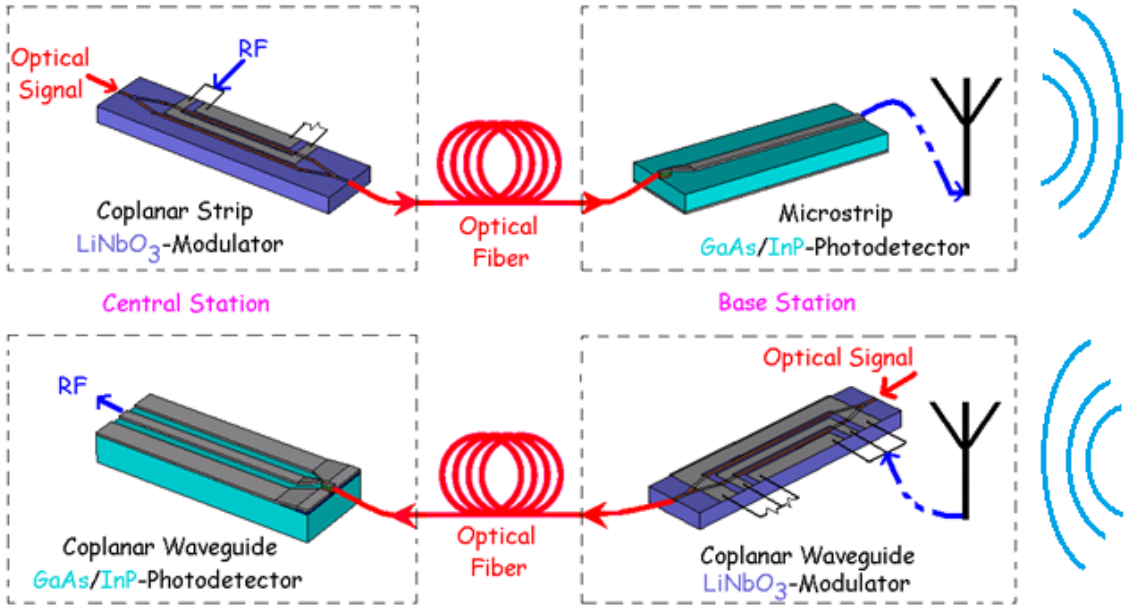

(a)

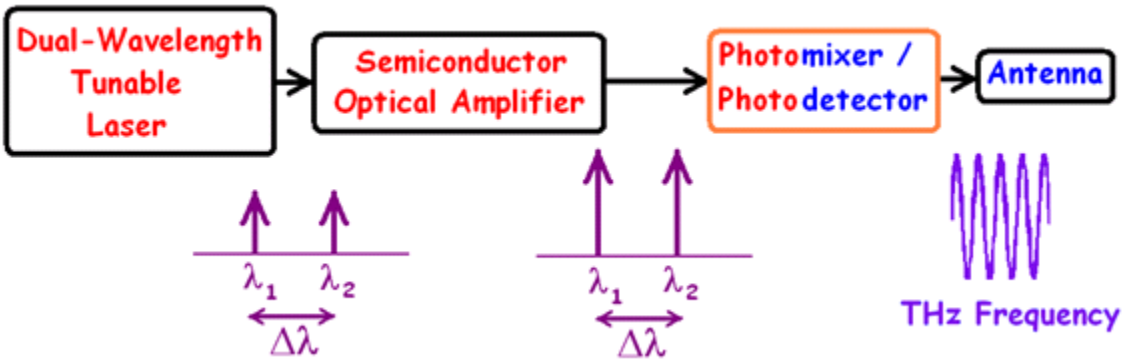

(b)

Figure. 3: Applications of optoelectronic devices in the structure of a) RoF systems, and b) THz generator.

In the first chapter of this thesis, mmW and microwave characteristics of conventional optical devices including WGPDs, TW photodetectors and modulators are presented. Then, the SIW concept is applied to the structure of conventional photodetectors and modulators with isotropic GaAs and InP substrates and anisotropic $LiNbO_3$ substrate, respectively. Afterwards, the mmW/microwave loss, as a principal bandwidth limitation factor, of the MS/CPW based optoelectronic devices and the new proposed SIW-based optoelectronic devices are compared. Although, in the conventional photodetector, bandwidth could be limited by the short-length multilayer optical absorbing section and long-length single layer microwave transmission part, the main bandwidth limitation factor in the high frequencies is related to the lossy MS/CPW transmission. Therefore, to realize the low-loss SIW in the structure of optoelectronic devices, MS of WGPD is replaced by SIW structure and a transition of MS to multilayer SIW structure by considering DC bias of the photodetector is designed and fabricated. The theoretical and experimental works suggest that the SICs-based optoelectronic devices are very promising candidates for new microwave/mmW photonic systems at high frequencies.

In the second chapter, newly proposed band-pass $LiNbO_3$ electro-optical SIW phase and amplitude modulators and their optical and microwave/mmW analysis are presented at 60 GHz frequency ranges. Overlap field integral, half-wave voltage, modulation depth and bandwidth are main parameters in the design of optical modulators. Conventional low-pass phase modulators with single optical waveguide and conventional amplitude modulators with MZ type optical waveguide use lossy coplanar strip (CPS) and CPW for the field interaction of optical and microwave signals. Although, the high overlap integral and low half-wave voltage can be achieved by using some geometrical modifications in the conventional electro-optical modulators, microwave/mmW loss still fundamentally limits the modulation depth and bandwidth of these conventional devices at high frequencies. In this chapter, low-loss SIW is considered as a microwave transmission line of the new proposed modulators and some modifications are applied to this band-pass modulator. Although using a single optical waveguide inside the low-loss SIW structure results a modulator with a large bandwidth at high frequency, a very low field overlap integral is obtained for this modulator. To have a high optical/mmW interaction, single optical waveguide is replaced with single optical waveguide array in a thin layer of $LiNbO_3$ substrate. This modification improves the overlap integral but the microwave/mmW loss in thin SIW structure is increased significantly, thus affecting the

bandwidth of the modulator. Multilayer $LiNbO_3$ substrates with the optical waveguide array in the thin layer could be a modified SIW phase modulator with high overlap integral and low microwave/mmW loss. The idea of the SIW phase modulator is directly considered in the structure of the SIW amplitude modulator using TE_{20} mode. The use of TE_{20} provides a common waveguide operation without creating a separate waveguide and differential field interactions are established with optical waveguides in this case. The realisation of SIW modulator is carried out by using Excimer laser micromachining and broadband cavity resonator design and transition from CPW to SIW in $LiNbO_3$ substrate.

The third chapter is dedicated to the investigation of a new type of our proposed electro-optical amplitude modulator that utilizes the mode coupling mechanism between the SIW and CPW structures. TE_{10} mode of the microwave signal which is transmitted through the SIW as a part of RoF system is coupled gradually to the quasi-TEM mode of the CPW which is placed on the top metallic SIW plate. The two structures share a common geometry. At the same time, the field interaction between optical and mmW signals is increased and maximized in the middle of the proposed device. This coupling mechanism is repeated in the second half part of the device in the vice versa manner and at the end of the device, the pure TE_{10} mode is transmitted to other parts of the system. With optimization of the device, the maximum coupling between the CPW and SIW can be obtained. Simulation and measurement parameters of this new SIW-CPW modulator are obtained and compared in chapter 3.

Design and fabrication of the surface-type photodetector and spiral broadband antenna for the integrated THz source generator are addressed in the fourth chapter. Photoconductors with different interdigitated finger types are designed for broadband THz source generators. Advantage of choosing this photoconductive photomixer is the simplicity of its design and fabrication and a disadvantage is its low power radiation because of a damaged small area threshold. Generally speaking, the power radiation through optical mixing techniques is inherent low because of the limited conversion efficiency. Spiral antenna which is almost a frequency independent antenna is integrated with the photoconductor to radiate THz generated signal. Growing rate of spiral antenna and the number of spiral turns are the optimized parameters in the antenna section of this chapter. Fabrication of this THz source generator is carried out by the design of three-layer mask including finger, mesa and spiral. Because of some difficulties in the etching of the photoconductive area, the mesa mask is designed a little bigger than the designed

size. Wire-bonding and packaging aspects before the measurements are important challenging issues that will be discussed.

A novel THz source generator based on the edge-illuminated TWPD and its integration with CPW-fed log-periodic broadband THz antenna is proposed in the fifth chapter. The optical absorbing area in the TWPD of THz source generators is larger than that of the surface-type photoconductors. Therefore, the optical illuminated power can be increased which results in high power THz radiation. By changing the metal and etched-metal segments of conventional log-periodic antennas, the CPW-fed antenna can be realised which is integrated with TWPD in the proposed THz generator.

CHAPTER 1. MICROWAVE AND MILLIMETRE LOSSES OF OPTOELECTRONIC DEVICES

1.1 Introduction

In this chapter, broadband characteristics including microwave and mmW properties of conventional optoelectronic devices with emphasis on WGPD, TW photodetector and modulator are discussed and compared with our subsequently proposed substrate integrated electro-optical devices.

In electro-optical devices, the bandwidth is limited by both optical and microwave characteristics of the device. From the optical perspective, the bandwidth can be related to structure parameters such as carrier lifetime and coupling loss. From the microwave point of view, the insertion and return losses have fundamental roles in the bandwidth limitation.

Microwave/mmW losses are one of the important bandwidth limitation factors for the microwave and mmW photonic devices. Microwave losses of MS line used in WGPD were analyzed and measured in [25]-[28] for GaAs and InP substrates. Higher microwave losses are observed with increasing frequencies. Coplanar waveguides are also used in the conventional TW photodetector and modulator as well. In [28]-[30], the microwave losses of CPW structure in GaAs and InP substrates were studied, which suggest that the bandwidth of TWPD is affected by the microwave loss of CPW transmission line. For the $LiNbO_3$ optical modulator, microwave loss effect becomes more pronounced because of a long interaction section between microwave and optical signals. In [31]-[32], the microwave loss of $LiNbO_3$ modulator was discussed with reference to the bandwidth. All of the previous studies have always considered conventional MS/CPW in the development of optoelectronic devices that in such devices, microwave loss inevitably increases with frequency.

In this chapter, different sources of loss including ohmic, dielectric and radiation losses in MS and CPW of the conventional electro-optical devices and SIW-based electro-optical devices are analyzed and compared. Isotropic and anisotropic substrates are used for the loss analysis. The

results show that the total microwave loss, which increases against frequency in the conventional MS and CPW structures, can be made almost constant in SICs-based devices. In addition, to use the SICs concept in the structure of electro-optical devices, microwave part of SIW-photodetector is fabricated and the results obtained from measurement are compared with simulation results.

1.2 MS and CPW losses in conventional optoelectronic devices

TW modulators and photodetectors are the key components of transmitter and receiver in optical systems, which are in particular critical for mmW RoF architecture. MS/CPW structures for the conventional photodetectors and CPW for the conventional modulators are considered for the microwave loss analysis.

1.2.1 MS/CPW in photodetectors

In Figure 1.1a, an edge-illuminated photodetector with MS geometry is shown. The optical signal, after being absorbed into the intrinsic layer of the multilayer structure, is converted into a microwave signal and transmitted by the MS waveguide. One of the important bandwidth limitations of this WGPD is related to microwave and mmW loss. The loss can be calculated over the multilayered photodetection region and MS line after the detection. It is expected that the long section of lossy MS line after the detection would significantly contribute to the bandwidth limitation of the photodetector. In Figure 1.1b, attenuation constant against frequency and conductor thickness as functions of MS width and substrate thickness are shown. Three different sources of the losses, including radiation (α_r), dielectric (α_d) and conductor (α_c) losses are considered in the simulations by commercial high frequency structure simulator (HFSS) software. The total loss is given by

$$\alpha_t = \alpha_r + \alpha_d + \alpha_c \qquad 1.1$$

To obtain the effects of different sources for microwave and mmW loss, analysis of the structure can be performed by using lossless dielectric and/or lossless conductor. To do this, the following steps can be considered in the analysis:

Step1) Radiative loss is obtained using infinite substrate resistivity and perfect conductor.

Step2) Summation of radiative and dielectric losses can be obtained by considering substrate conductivity and perfect conductor. Using the radiative loss from the previous step, dielectric loss is

$$\alpha_d = (\alpha_d + \alpha_r)\big|_{Step2} - \alpha_r\big|_{Step1} \qquad 1.2$$

Step3) Summation of radiative and conductor losses can be obtained by considering infinite substrate resistivity and conductor with specific conductivity. Using the radiative loss from the first step, conductor loss is given by

$$\alpha_c = (\alpha_c + \alpha_r)\big|_{Step3} - \alpha_r\big|_{Step1} \qquad 1.3$$

In Figure 1.1, the relative permittivity for GaAs substrate is 12.9 and the conductivity is considered to be 0.011 S/m. Conductor is Gold with the conductivity of 4.1×10^7 S/m and thickness of 3 μm. According to the figure, the relatively low dielectric loss is almost constant versus frequency and the role of the radiative loss is important for the total loss at higher frequencies. Conductor loss is the critical source for the total loss of the MS line in the WGPD. Increasing strip width and substrate thickness could decrease the loss. Increasing conductor thickness can decrease the loss; however, it is not so significant in most practical cases. To validate our simulation, experimental and theoretical results are shown in the Figure 1.1b and good agreements between our results and other published results are observed. Measurement results are extracted from [25] and [26], and results of mode-matching technique (MMT) are used from [27].

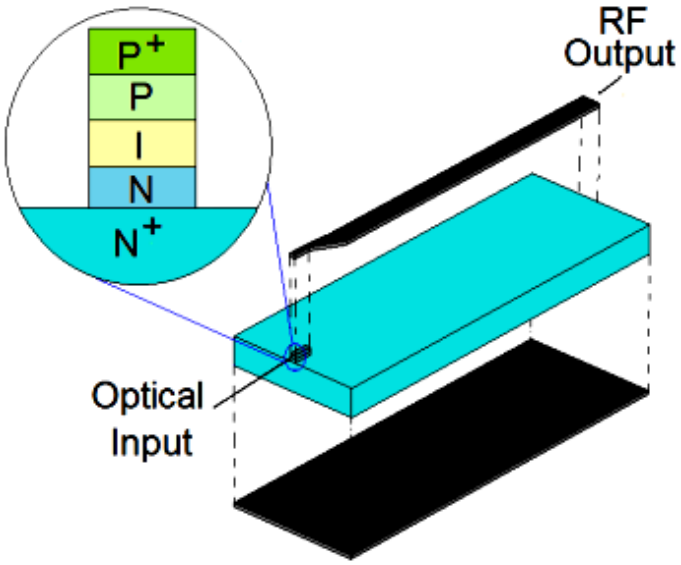

(a)

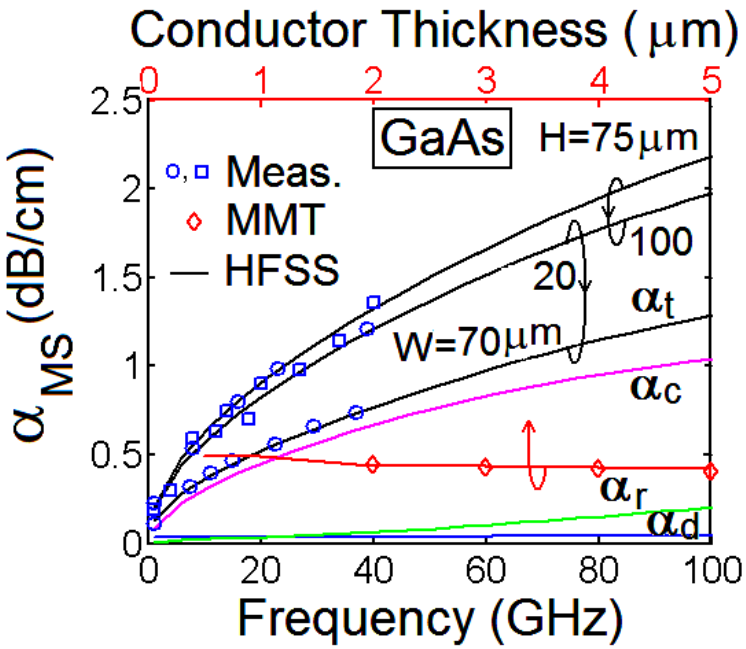

(b)

Figure 1.1: a) WGPD with MS line, b) MS loss versus frequency and conductor thickness as functions of MS width (W) and GaAs substrate thickness (H).

Figure 1.2a shows a TWPD with the CPW geometry. In the TWPD, electrical waveguide is a CPW, in support of microwave and mmW wave propagation generated by the absorption of optical wave, connected to the external circuits. In the TWPD similar to the WGPD, the bandwidth is limited by the microwave loss. In Figure 1.2b, the microwave loss of CPW structure against frequency and conductor thickness as a function of strip (W) to slot width (S) ratio is illustrated. GaAs and Gold are considered for the substrate and conductor, respectively. Strip and slot widths are 25 and 18 microns for the ratio of 1.3 and also they are selected to be 69 and 28 microns for the ratio of 2.4, respectively. The results again suggest that the attenuation constant increases with frequency and decreases with conductor thickness. Also, the microwave loss decreases by increasing the ratio of strip-to-slot width for 50 Ω systems. Good agreement between our results and those of mode-matching technique (MMT) from [27], measured results from [28] as well as those of finite difference – transmission line method (FD-TLM) from [29] are observed.

1.2.2 CPW in modulators

Another conventional optical device with the CPW geometry is TW modulator. In Figure 1.3a, a typical TW modulator is shown. As a four-port device, optical input and output and also microwave input and output can separately be considered in the modulator. Similar to the loss of the photodetector, the microwave loss in modulator is one of the important limitations for high frequency applications. CPW loss versus frequency and conductor thickness as functions of geometrical dimensions in anisotropic $LiNbO_3$ substrate is illustrated in Figure 1.3b. Dielectric constant of (28, 43, 43) with the loss tangent of 0.004 and substrate thickness of 500 μm are selected for the $LiNbO_3$ substrate. As expected, the microwave loss increases with frequency and decreases with conductor thickness and ratio of strip-to-slot width. The curve versus conductor thickness is generated at 60 GHz and strip width is 8 μm. Good agreements between the simulated results and other published results (measurements from [31] and finite element method (FEM) method from [32]) are obtained.

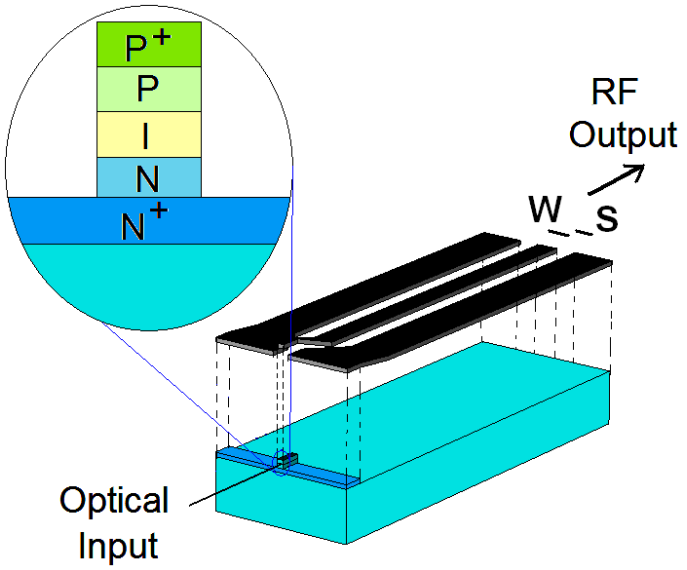

(a)

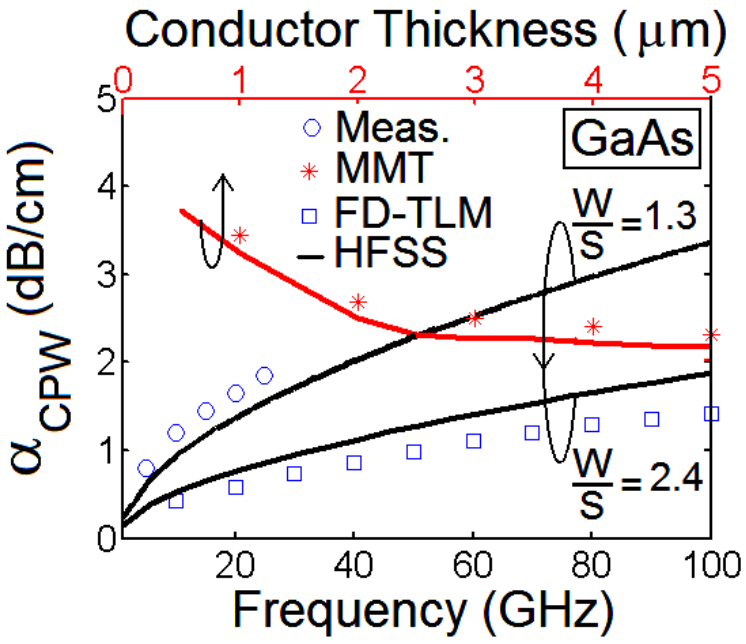

(b)

Figure 1.2: a) TWPD with CPW geometry, b) CPW loss versus frequency and conductor thickness as a function of strip (W)-to-slot width (S) ratio in GaAs substrate.

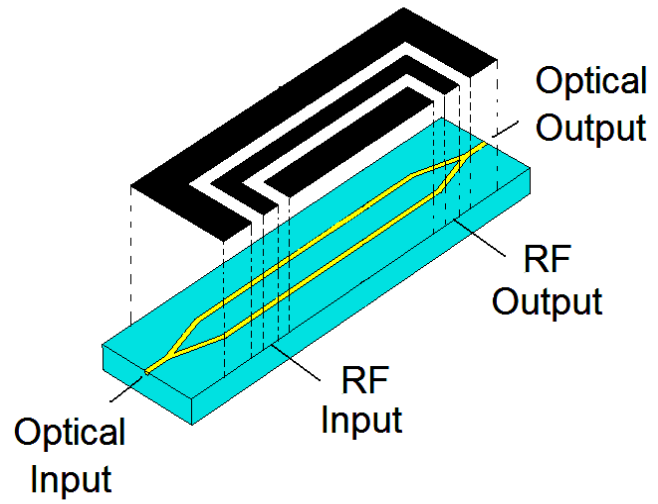

(a)

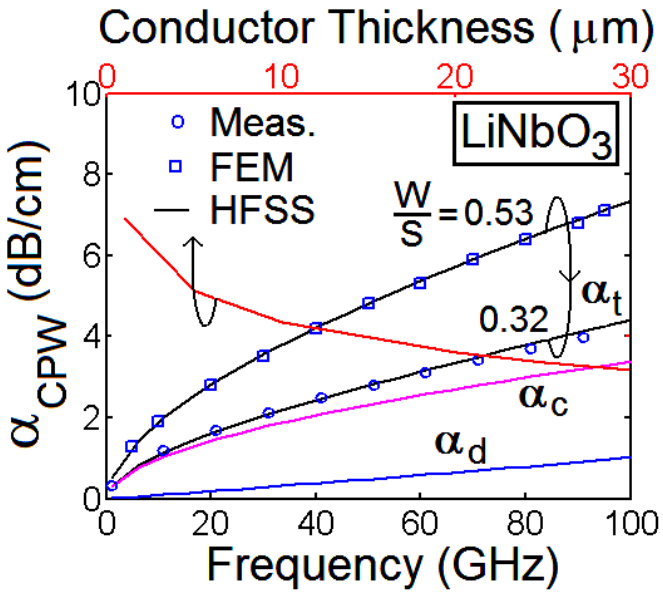

(b)

Figure 1.3: a) Optical intensity MZ modulator with CPW, b) CPW loss versus frequency and conductor thickness as a function of strip (W)-to-slot width (S) ratio in $LiNbO_3$ substrate.

From the results of this section, we could conclude that in the conventional optoelectronic devices, the microwave and mmW losses are much more pronounced at higher frequencies, which adversely affects the performances of these devices. Therefore, a new microwave and mmW structure with low loss transmission should be developed if higher frequency applications are considered.

1.3 Loss comparison of conventional and SIW-based optical devices

As it has been shown in the previous section, MS and CPW which are not suitable for the broadband applications at high frequencies should be replaced by low-loss waveguides. One of the candidates is the widely used RWG. For the integrated systems, two bilateral metallic walls of RWG are replaced by metalized via hole arrays that becomes SIW. To design the SIW structure, we consider $D<0.2\lambda$ and $G<2D$; where D is the diameter of the holes in the SIW structure, λ is the wavelength and G is the period of the holes. In Figure 1.4a, the SIW structure with parameters such as substrate thickness (H) and effective width (W_{eff}) is illustrated. For the validation of our following simulation results which are generated by the use of HFSS software, attenuation and phase constants for a typical structure are shown in Figure 1.4b and compared with the published experimental and numerical results. Substrate thickness, permittivity, loss tangent, effective width, via hole diameter and gap are considered 0.508 mm, 2.33, 0.0012, 6.9 mm, 0.8 mm and 2 mm, respectively for the simulation. Good agreement between the simulation and published results (measurements from [33] and finite difference frequency domain (FDFD) method from [34]) are obtained.

After the validation of our simulated results, we can deploy and design SIW structures for our photodetector and modulator substrates.

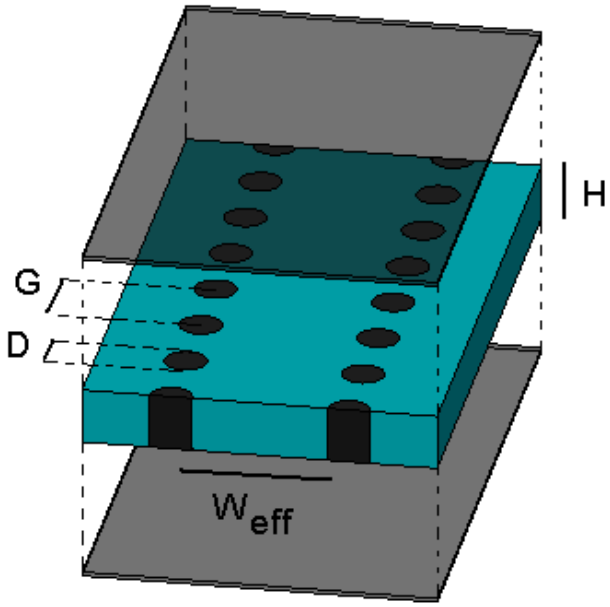

(a)

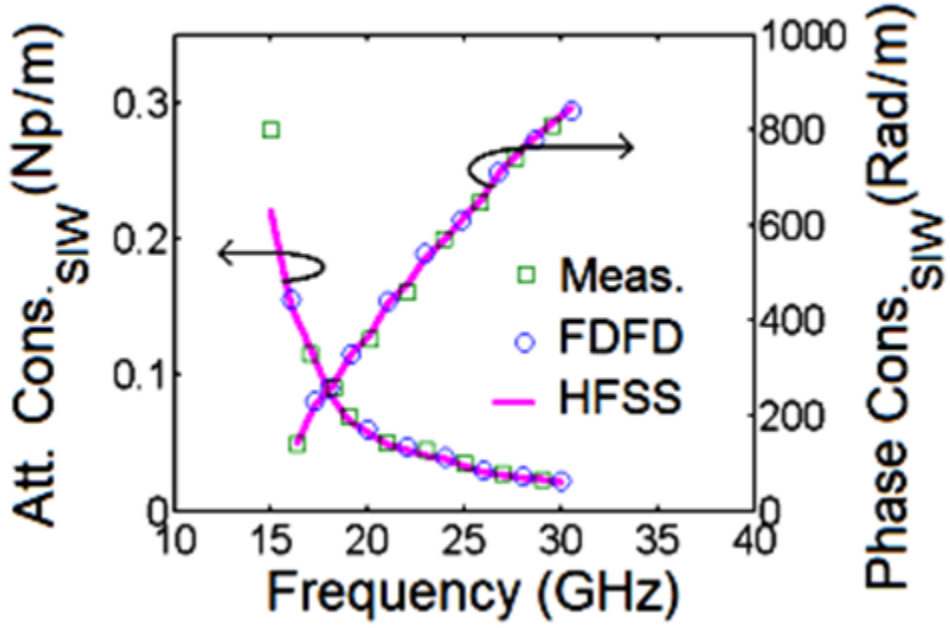

(b)

Figure 1.4: a) SIW for new optoelectronic devices, b) Attenuation and phase constants versus frequency in SIW.

1.3.1 SIW in photodetectors

In Figure 1.5, microwave loss for the conventional WGPD with MS geometry and CPW loss in TWPD are compared with the characteristics of SIW which can be deployed for our proposed SIC-based photodetectors. Strip width of the MS line is 20 μm in this case. Strip and slot widths of CPW are 25 and 18 μm, respectively. As it can be seen in the specific frequency band of interest, namely V-band and Ka-band, by increasing frequency, the SIW microwave loss decreases in a significant manner against the loss of MS and CPW. In addition, the SIW loss is decreased by increasing the substrate thickness and width.

1.3.2 SIW in modulators

In Figure 1.6, the $LiNbO_3$ substrate is considered for the comparison of loss for the conventional TW modulator with CPW structure and the new SIW modulators. For the CPW, the strip and slot widths are 8 and 25 μm, respectively. In this figure, over the specific range of frequency, the SIW loss is less than CPW loss, and it could be further reduced by increasing the substrate thickness and effective width.

In this section, microwave loss analyses suggest that SIW could be a very promising candidate for the new type of optoelectronic devices such as photodetector and modulator. In the following, low-loss SIW structure is considered and studied as the microwave transmission medium of the WGPD. Also, a transition of MS to SIW in photodetector with multilayer substrates is designed, fabricated and measured.

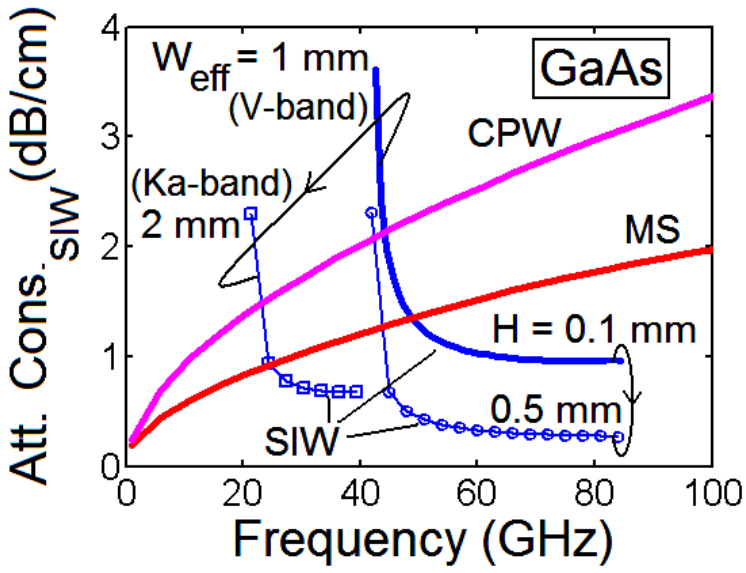

Figure 1.5: Comparison of attenuation constant versus frequency as functions of substrate thickness and width in MS, CPW and SIW for GaAs substrate.

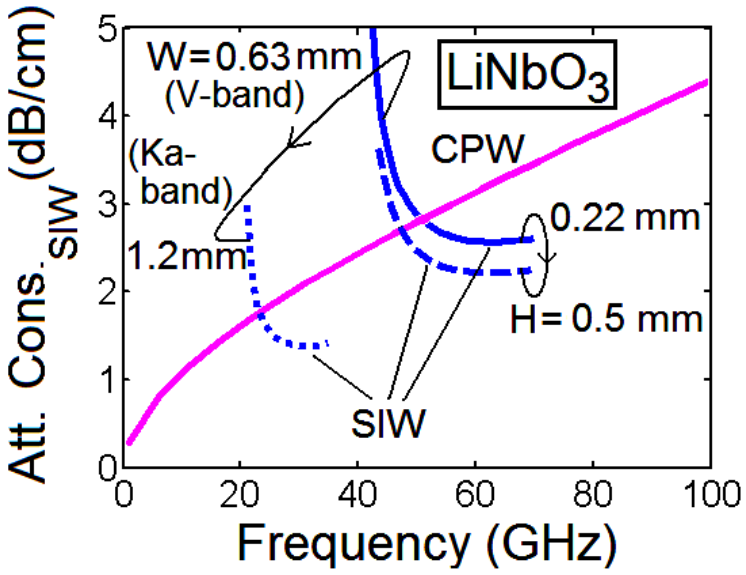

Figure 1.6: Comparison of attenuation constant versus frequency as functions of substrate thickness and width in CPW and SIW in $LiNbO_3$ substrate.

1.4 Transition from MS to SIW in photodetector

Long length of the MS transmission part of WGPD has a significant role in the bandwidth limitation of the detector and may be replaced by low-loss microwave waveguide such as SIW. For this replacement, transition of MS to SIW in the photodetector should be designed. MS can be used for the small length of the detection area and SIW can be used instead of long-length lossy MS transmission line. In this section, theory and design of integrated MS based WGPD and SIW are presented for the proposed SIW photodetector. Then, for the validation of our results, our measurements of insertion and return losses for the new fabricated device are presented.

1.4.1 Theoretical issues

Proposed SIW photodetector is the combination of conventional WGPD and SIW for high frequency applications.

Figure 1.7 illustrates an integration scheme between WGPD and SIW transmission line. The WGPD absorbs optical light and the generated microwave signal is then transmitted or carried by a low-loss multilayered SIW structure. By the integration of WGPD and band-pass SIW transmission line, the bandwidth of the new proposed device is dependent on the SIW cut-off frequency and the photodetector bandwidth. Long and thick bottom-substrate, short and thin top-substrate, metalized via holes in both substrates and metal plates in top and bottom of the structure are shown in the figure. In this structure, the top-dielectric layer is considered to separate DC bias and RF signal in the device. Thin top-substrate yields low loss transition. To obtain the microwave characteristics, we suppose that the absorbing layers thicknesses of WGPD are almost zero and only the transition from the MS to SIW is considered. Quasi-TEM mode of the MS line is transformed into the TE_{10} mode of SIW by a taper.

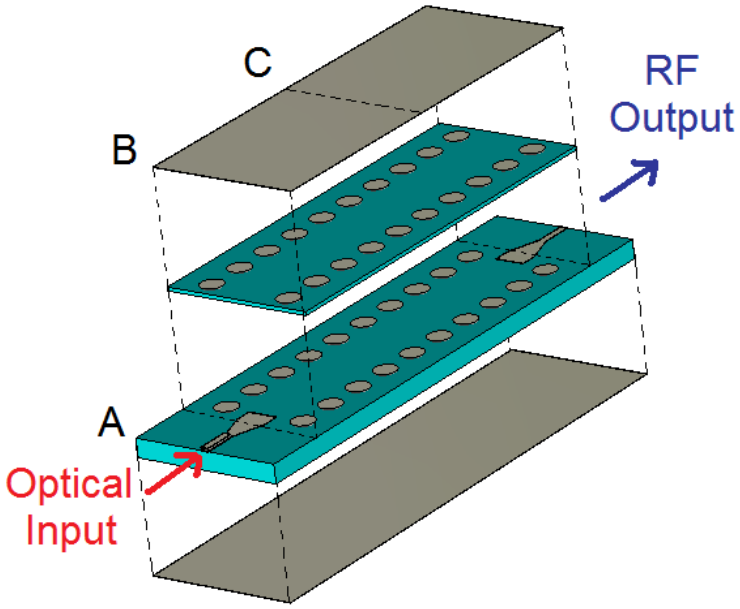

Figure 1.7: Multilayer transition from WGPD to SIW.

Design of the structure for the Ka-band includes the design of MS, SIW and a taper. In our work, design of the MS in the bottom-substrate is carried out by HFSS software. For a given substrate permittivity, the diameter of via holes and distance between the holes should be obtained. SIW width is another design parameter which specifies the cut-off frequency as in the case of RWG. This parameter can be changed to allow only the dominant mode in the desired frequency range. Although the propagation constant of TE_{10} mode is not related to the thickness of substrates, the thickness of the top substrate should be lower than that of the bottom substrate to have minimum insertion loss. Thickness of the bottom substrate is related to the design of the photodetector. The optimized simulation results show that the best excitation of SIW is obtained by $\lambda/4$ length after the taper. The length and width of the taper and MS excitation line are optimized by HFSS. In Table 1.1, the optimized parameters obtained for the new proposed device are presented.

Table 1.1: Microwave design parameters for the new proposed device

Parameter	Value (mm)
Bottom substrate thickness	0.635
Top substrate thickness	0.127
Dielectric constant	10.2
Hole diameter	0.787
Gap between the holes	0.584
SIW width	2.032
MS width	0.254
MS length	1.143
Taper length	1.143
Width of excited line	1.016

In Figure 1.8, electric fields inside of the structure are illustrated. Figure 1.8a illustrates the MS field in the point (A) of Figure 1.7. In Figure 1.8b, quasi-TEM mode is converted to TE_{10} mode in point (B) of Figure 1.7. In Figure 1.8c, microwave field which is now pure TE_{10} mode in the middle of structure is illustrated. As it is shown in Figure 1.8, the complete conversion from MS quasi-TEM mode to SIW TE_{10} mode is obtained. After the design and simulation of the proposed structure, the simulated results should be validated by the experimental results in the following part.

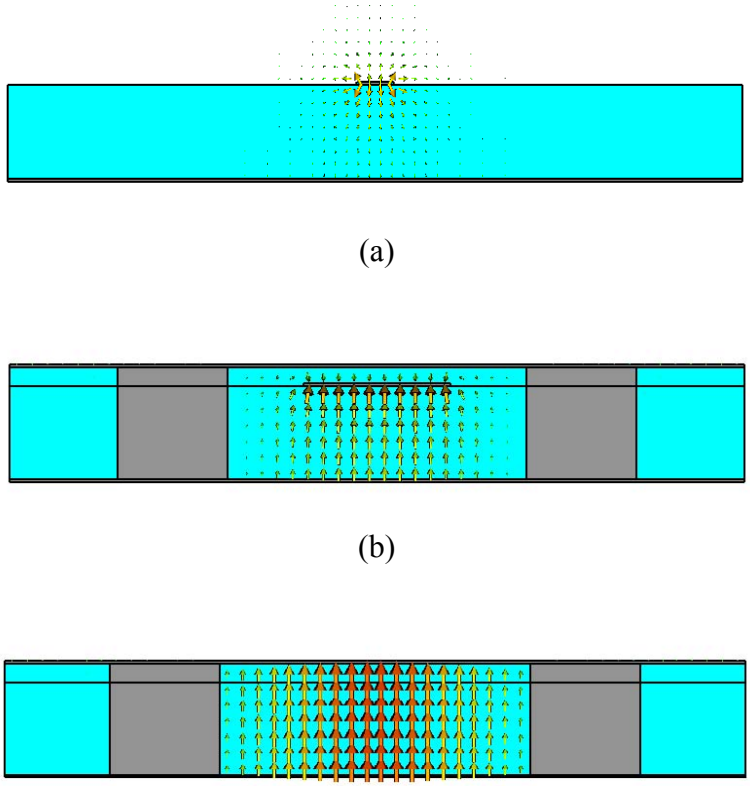

(a)

(b)

(c)

Figure 1.8: Simulation results of microwave fields, a) MS mode in point A, b) MS and SIW modes in point B, c) SIW mode in point C of Figure 1.7.

1.4.2 Fabrication, measurement and validation

In Figure 1.9, our early fabricated device for the transition of MS to SIW is shown. In the fabrication part, we have used a commercial substrate from the Rogers Company with the permittivity of 10.2 which is close to the permittivity of InP optical substrate. Main metalized via holes are specified in the middle of the structure and three alignment holes are observed as well. MS in the port can be used for the measurement purpose by test fixture.

Figure 1.10 shows measured and simulated results for two back-to-back transitions of the circuits shown in Figure 1.7 and Figure 1.9. For the measurement purpose, an HP8510 network analyzer and a Wiltron test fixture were used. Insertion loss of about 1 dB and 2 dB for the simulation and measurement were obtained, respectively. Also, less than -15 dB of return loss for the whole

frequency range was observed. As it is shown in the figures, a good agreement between the measured and simulated results is observed. The little difference between the results is related to the fabrication tolerance in connection with the SIW width. For the comparison of the insertion loss in our designed structure and conventional photodetector, microwave loss of the WGPD with MS structure (MS-WGPD) is shown in the figure, as well. In conventional MS-WGPD structure, the insertion loss increases by frequency and more than 5 dB of the loss is observed at the frequency range between 30 GHz and 40 GHz [4].

In this section, transition of the MS to SIW in WGPD structure in multilayer substrate for the DC bias separation has been designed, analyzed and fabricated. Simulation and measurement results have been obtained and compared to show the low microwave loss for SIW-based optical devices.

1.5 Conclusion

Microwave / mmW loss analysis has been developed for the conventional TW photodetector and modulator based on MS/CPW structures and for the new SIW-based optoelectronic devices as well.

SIW structure is applied to the GaAs and $LiNbO_3$ substrates to be used in the new photodetectors and modulators. It has been shown that SIW microwave and mmW losses at high frequencies are much lower than the MS and CPW counterparts in electro-optical substrates.

In the new SIC-based photodetector, a low-loss SIW structure and multilayer substrate to separate DC bias and microwave signal have been considered. Fabrication of the MS to SIW transition and comparison of simulation and measurement results have been carried out. This work suggests that the SICs-based electro-optical devices are very promising candidate for the new broadband applications of microwave and mmW photonic systems at high frequencies.

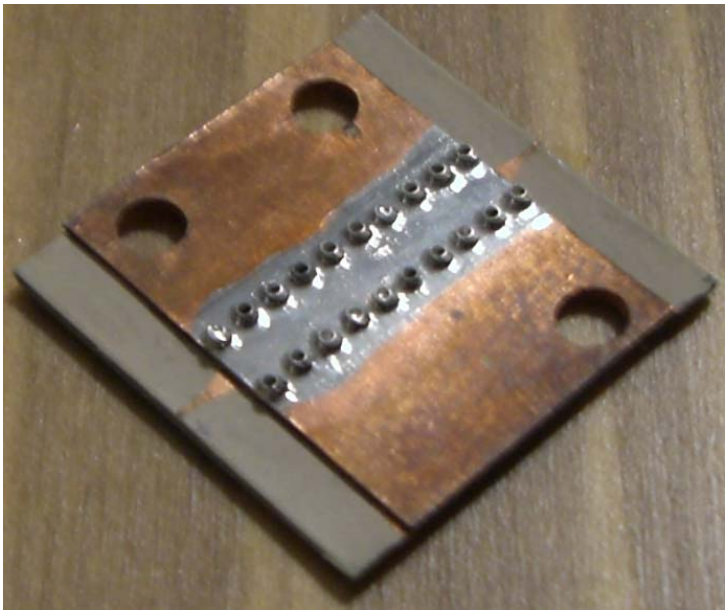

Figure 1.9: Fabricated multilayer transition of MS to SIW with the device length of 11.8 mm.

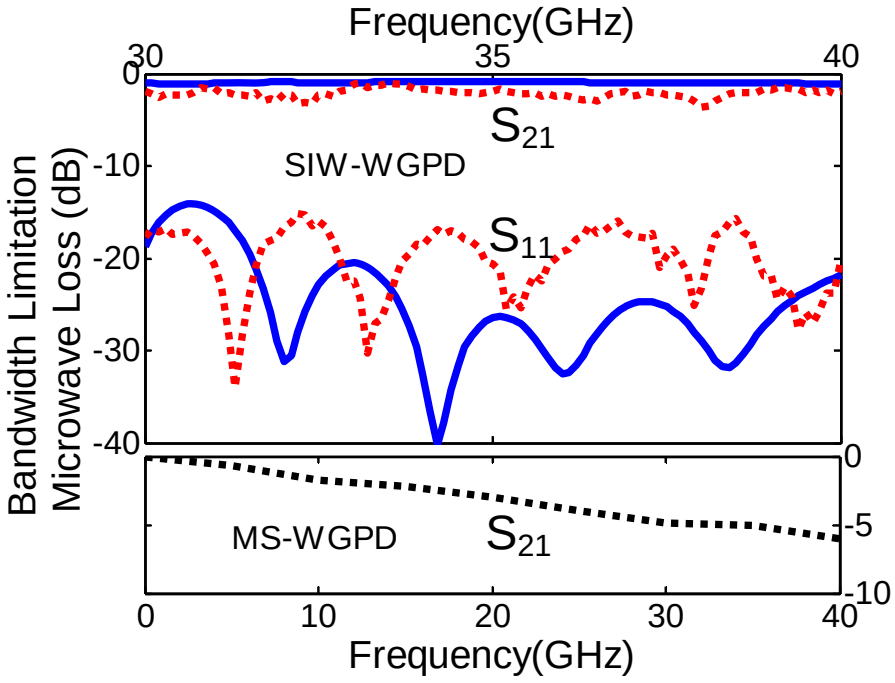

Figure 1.10: Measured (dashed lines) and simulated (solid lines) insertion and return losses of SIW-based WGPD and MS conventional WGPD with the same length.

CHAPTER 2. SIW ELECTRO-OPTICAL MODULATORS

2.1 Introduction

In this chapter, a brief review of electro-optical materials in conventional $LiNbO_3$ modulators, new proposed SIW modulators and modifications, fabrication techniques and experimental results are presented and discussed.

Phase or amplitude modulation can be obtained by changing the phase of optical signal with the variation of material refractive index. The refractive indices of electro-optical materials are a function of the applied electrical fields. Two effects including the linear (Pockels) effect and quadratic (Kerr) effect may be considered in the electro-optical materials.

The changes of refractive index by applying electrical field E and using Pockels coefficient r and Kerr coefficient ξ are given by [13]

$$n(E) = n - \frac{1}{2} r n^3 E \qquad 2.1$$

$$n(E) = n - \frac{1}{2} \xi n^3 E^2 \qquad 2.2$$

where r is typically between 1 and 100 pm/V and ξ is between 10^{-18} and 10^{-14} m^2/V^2.

The majority of $LiNbO_3$ modulators are based on the Pockels effect and the Pockels coefficients of the modulators according to the crystalline structure of their electro-optical substrates are given by

$$\begin{bmatrix} 0 & -r_{22} & r_{13} \\ 0 & r_{22} & r_{13} \\ 0 & 0 & r_{33} \\ 0 & r_{42} & 0 \\ r_{42} & 0 & 0 \\ -r_{22} & 0 & 0 \end{bmatrix}_{LN} = \begin{bmatrix} 0 & -3.4 & 8.6 \\ 0 & 3.4 & 8.6 \\ 0 & 0 & 30.8 \\ 0 & 28 & 0 \\ 28 & 0 & 0 \\ -3.4 & 0 & 0 \end{bmatrix} (pm/V) \qquad 2.3$$

The anisotropic $LiNbO_3$ indices of refraction for the ordinary (n_o) and extraordinary (n_e) waves at room temperature as a function of optical wavelength (λ) in micrometer are given by the following Sellmeier equations:

$$n_o^2 = 4.9130 + \frac{0.1188}{\lambda^2 - 0.04597} - 0.0278\lambda^2 \qquad 2.4$$

$$n_e^2 = 4.5798 + \frac{0.0994}{\lambda^2 - 0.04235} - 0.0224\lambda^2 \qquad 2.5$$

n_o and n_e are obtained 2.2218 and 2.1449 for optical wavelength of 1330 nm and 2.2128 and 2.1373 for optical wavelength of 1550 nm, respectively. Different changes are obtained for these refractive indices in optical waveguide region by different fabrication methods. For example, using Ti in-diffusion technique, the refractive index change of about 0.015 is expected for the optical waveguide region [35].

2.2 TW conventional electro-optical modulators

In this section, electro-optical phase and amplitude modulators will be introduced and discussed.

2.2.1 Phase modulators

In Figure 2.1, a simple structure for the electro-optical $LiNbO_3$ phase modulator is shown. Optical signal can be linearly polarized in transverse magnetic (TM) mode (X direction in X-cut and Z direction in Z-cut) or transverse electric (TE) mode (Z direction in X-cut and X direction in Z-cut) and propagated in the Y direction. We suppose that the only electric field component is

E_z and it is concentrated in the optical waveguide area. For the Z-polarized optical signal (TE mode in X-cut or TM mode in Z-cut), the phase shift is [36]

$$\phi_Z = k_Z L = \frac{\omega}{c} n_Z L = \frac{\omega}{c}\left(n_e - \frac{n_e^3}{2} r_{33} \frac{V}{G} \right) L \qquad 2.6$$

where k_Z is the propagation of light, L is the length of device, ω is angular frequency, c is the speed of light in free space, n_Z is the refractive index in Z direction, V is applied voltage and G is the space between the electrodes.

For the X-polarized optical signal (TM mode in X-cut or TE mode in Z-cut), the phase shift is

$$\phi_X = k_X L = \frac{\omega}{c} n_X L = \frac{\omega}{c}\left(n_o - \frac{n_o^3}{2} r_{13} \frac{V}{G} \right) L \qquad 2.7$$

According to the phase shift for X-cut and Z-cut $LiNbO_3$ substrate, since $n_e \approx n_o$ and $r_{33} = 3.6 r_{13}$, the modulation voltage required for the Z-polarized optical signal is 3.6 times less than modulation voltage for the X-polarized optical wave. Therefore, in X-cut Y-propagation structure for the phase modulation, it is preferred to use optical TE mode. TM mode may be used for the Z-cut substrate.

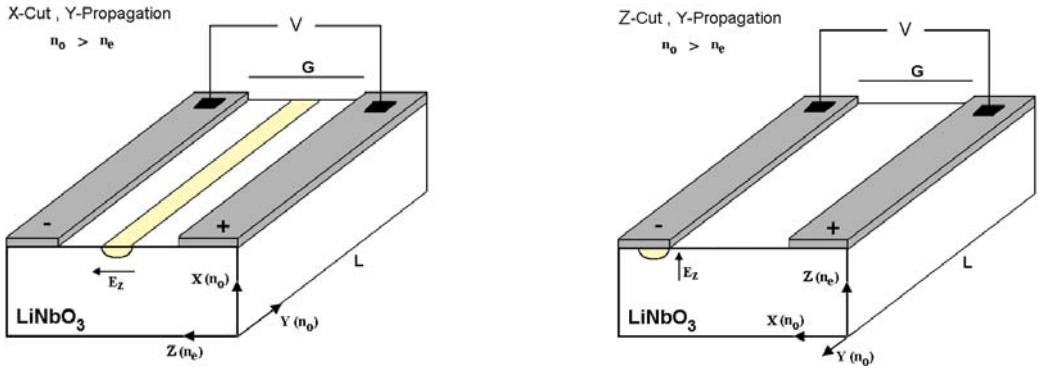

(a) (b)

Figure 2.1: Phase modulator in a) X-cut and b) Z-cut $LiNbO_3$ substrates.

To consider the exact model for the phase modulators presented in Figure 2.1, a new factor for the interaction between the optical and electrical signals which is called overlap integral should be defined [13]

$$\Gamma = \frac{G}{V} \frac{\int_{-\infty}^{+\infty}\int_{-\infty}^{+\infty} E_z^{el}(x,z).\left[E_z^{op}(x,z)\right]^2 dxdz}{\int_{-\infty}^{+\infty}\int_{-\infty}^{+\infty} \left[E_z^{op}(x,z)\right]^2 dxdz} \qquad 2.8$$

where V is the drive voltage of the modulator, G is the distance between the electrodes, E_z^{op} is the optical field which can be related to optical TE or TM modes, and E_z^{el} is the z component of the electrical fields. In the coplanar conventional type modulators, electrical fields in the propagation direction y are constant and are not considered in overlap integral. By changing the microwave waveguide structure, variation in y direction should be calculated.

The change of the phase for TM mode in Z-cut, or TE mode in X-cut, Y-propagating structure is [36]

$$\Delta\phi_Z = -\frac{\pi}{\lambda} n_e^3 r_{33} E_{eff} L \qquad 2.9$$

and for TE mode in Z-cut, or TM mode in X-cut, Y-propagating structure is

$$\Delta\phi_X = -\frac{\pi}{\lambda} n_o^3 r_{13} E_{eff} L \qquad 2.10$$

where $E_{eff} = \frac{V}{G}\Gamma$. As it is shown in equation 2.9 and equation 2.10, changing of the phase is related to the optical wavelength, electro-optical coefficient, refractive index, length of the device and applied electrical field.

2.2.2 Amplitude modulators

The concept of phase modulation can be applied to the amplitude modulator. In Figure 2.2, an MZ waveguide interferometer is shown. The optical signal is split equally and propagated in

different optical paths. The two paths are recombined after few centimetres, causing the optical waves to interfere with each other. In each arm, the phase of optical signal is changed by applied electrical field. If the phase difference of the signal between two arms is π, destructive interference occurs at the end of MZ interferometer and no optical output signal can be observed. Zero or 2π phase difference in two arms presents a constructive interference case and total power of optical signal appears at the end of interferometer. According to the push-pull structure for the microwave signal in CPW geometry, as it is shown in Figure 2.2, opposite phase difference in each arm is obtained and the total phase shift is twice the phase shift in each arm. Using the optical TE and TM modes in X-cut and Z-cut structures, respectively, the total phase shift is given by [13]

$$\Delta\phi = -\frac{\pi}{\lambda} n_e^3 r_{33} \frac{V}{G} (\Gamma_1 + \Gamma_2) L = \pi \frac{V}{V_\pi} \qquad 2.11$$

where Γ_1 and Γ_2 are the overlap integral in each arm . The half-wave voltage correspond to the phase difference of π between the two arms is given by

$$V_\pi = \frac{\lambda}{n_e^3 r_{33} (\Gamma_1 + \Gamma_2)} \frac{G}{L} \qquad 2.12$$

In the Z-cut structure of Figure 2.2, although the CPS with two electrodes can be used, CPW is more applicable for the TW applications in high frequencies.

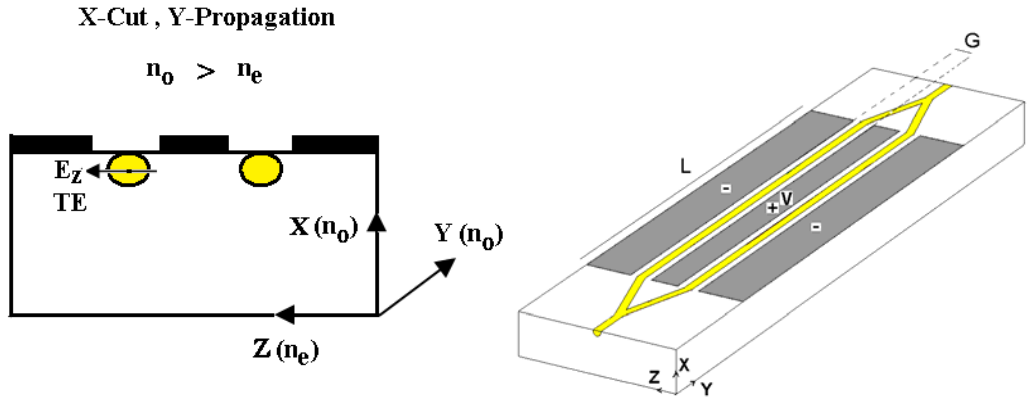

(a)

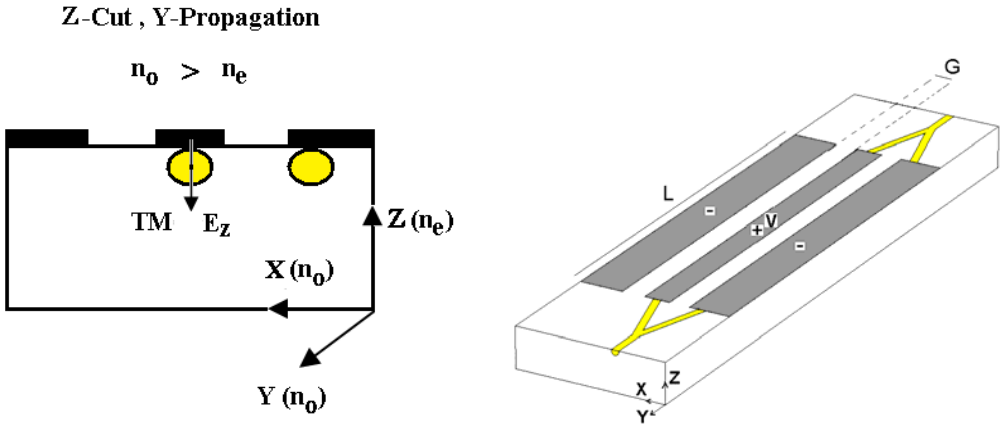

(b)

Figure 2.2: Cross-sectional view in the middle and 3D view of amplitude modulator in a) X-cut and b) Z-cut $LiNbO_3$ substrates.

The power transmittance versus total phase shift for the MZ with ideal 3dB input/output coupler is given by [13]

$$T = \frac{1}{2}(1+\cos\Delta\phi) = \frac{1}{2}(1+\cos\frac{\pi V}{V_\pi}) \qquad 2.13$$

For small-signal amplitude modulators with linear response, shown in Figure 2.3a, the working point for bias voltage should be placed in

$$V_b = \pm \frac{V_\pi}{2} \qquad 2.14$$

and modulation depth is defined as

$$\Gamma_m = \frac{2V_{\mathrm{m}}}{V_\pi} \qquad 2.15$$

where V_{m} is the amplitude of modulating.

For the ON-OFF state modulator, shown in Figure 2.3b, no bias is needed and extinction ratio is defined by

$$ER = -10 \log \frac{T_{\min}}{T_{\max}} \quad (dB) \qquad 2.16$$

where T_{min} and T_{max} are minimum transmittance in OFF state and maximum transmittance in ON state, respectively.

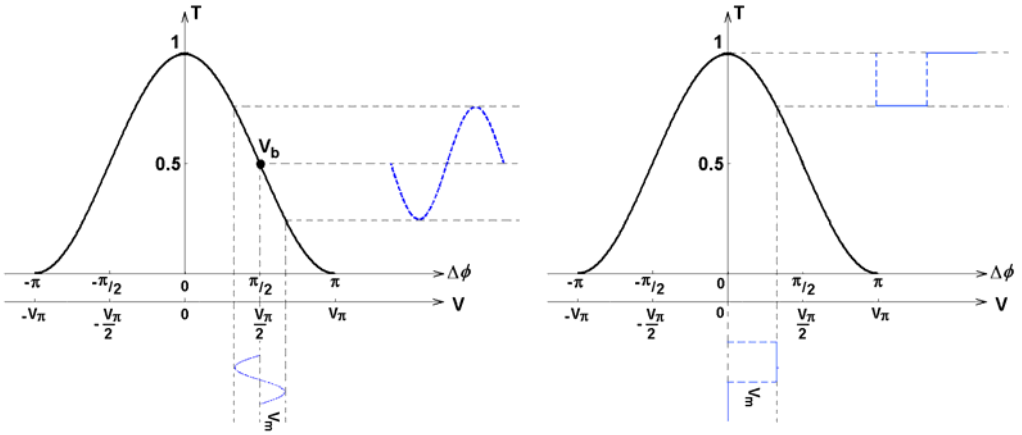

(a) (b)

Figure 2.3: Power transmittance factor in MZ amplitude modulator, (a) small-signal, (b) ON-OFF modulator.

As a brief literature review of previous researches on optical modulators, $LiNbO_3$ electro-optical MZ type amplitude modulator is discussed in the following. Bandwidth, modulation depth, half-

wave voltage, overlap integral, microwave and optical loss are the modulator parameters which have been subject to design and optimization in the previous researches.

The characteristics of high-speed $LiNbO_3$ electro-optical MZ modulator are discussed from the viewpoint of optimization of device performance in [37]-[38]. Specific calculations of the impedance, effective microwave index, and microwave attenuation parameter are presented as functions of the microwave electrode and buffer layer thicknesses. Microwave insertion loss of about 10 dB is measured at 20 GHz. In [39], the fabrication of the device with a shielding plane was made. As a result, a 3 dB optical bandwidth of 40 GHz with a driving voltage of 3.6 V is achieved at 1550 nm optical wavelength. In [40], a 5V half-wave voltage electro-optical Titanium diffused $LiNbO_3$ (Ti:$LiNbO_3$) MZ modulator with a 7.5 dB optical response at 40 GHz was demonstrated at 1.3 μm. A thick electrode structure was used in conjunction with a thin substrate to achieve a near optical-microwave phase match and a broadband electrical response. The microwave insertion loss is about 12 dB in 40 GHz.

MZ ridge waveguide modulators on $LiNbO_3$ by proton-exchange wet etch and nickel in-diffusion were fabricated in [41]. Modulators operating at 0.633 μm and 1.31 μm were both produced, and the half-wave voltages were measured to be 4V and 22.5V, respectively, for an electrode length of 6 mm. The finite element method was used to model a Ti:$LiNbO_3$ electro-optical modulator in [42]. Parameters such as the refractive index profile, the optical field profile, the applied electric field profile and the overlap between the applied electric and optical fields for a variety of electrode positions were included. By adjusting the position of the electrodes, it is possible to obtain the maximum value of the overlap. In [43], analysis and fabrication of Z-Cut $LiNbO_3$ modulator to achieve the velocity and impedance matching, low driving voltage and high bandwidth were carried out in the wavelength of 1.55 micron. The modulator made use of a ridge structure and CPW electrodes. Microwave transmission was obtained about -12 dB for 75 GHz. In [44], different electrode configurations for $LiNbO_3$-based MZ TW electro-optical modulators were analyzed. It was found that the Z-cut CPW configuration provides the best compromise between the characteristic impedance, the half-wave voltage, and the driving power. To increase the bandwidth and simultaneously reduce the half-wave voltage, an optimum design of multi-section phase reversal electrode was proposed. The 3 dB bandwidths of five-section and single-section modulators were found to be 15 GHz and 3.6 GHz, respectively, and the corresponding half-wave voltages were measured to be 14V and 4V, respectively. In [45], a push-pull type Ti:

$LiNbO_3$ optical modulator with a ridge structure and two-stage CPW electrode was applied to a 40-Gb/s optical transmission system. In that work, the half-wave voltage and electrical bandwidth were obtained 1.5 V and 30 GHz, respectively. An analysis of x-cut Ti:$LiNbO_3$ TW modulator with a ridge structure was presented in [46]. Two configurations employing ridge structure were compared to a conventional one. The characteristics of both the optical waveguide and the CPW electrode were computed using a finite element method. A packaged X-cut $LiNbO_3$ optical single-sideband modulator was presented in [47], which successfully performed a carrier-suppression ratio over 25 dB with an RF driving voltage of 8 V peak to peak at 10 GHz. In [48], a large-bandwidth back-slot $LiNbO_3$ modulator with a wide center electrode of typically 50 μm and relatively thin electrodes was designed and fabricated. From the calculation, a modulator with a bandwidth of 34 GHz and a half-wave voltage of 2.0 V for a 50 Ω characteristic impedance system was realized theoretically.

According to the reviewed previous works, one of the important parameters of TW modulators is related to bandwidth. Two important parameters in bandwidth limitation of a TW modulator are microwave attenuation (loss) and microwave/optical phase velocity mismatch. The microwave attenuation from the coplanar structure is increased at high frequencies. The phase velocity for optical signal is almost constant and for microwave signal can be changed according to the structure of modulator. In velocity-matched structures, bandwidth limitation is only related to conductor, dielectric and radiating losses of CPW. To improve the performance of conventional modulators, new structures for phase and amplitude modulators based on SIW are proposed and presented in the present thesis work.

2.3 Proposed SIW-based modulator

According to the discussion in the previous chapters, MS and CPW are lossy structures for high frequency electro-optical modulators. Low-loss RWG in planar form (SIW) in electro-optical material such as $LiNbO_3$ can be used instead of lossy conventional structure. Low-loss SIW can be considered around optical waveguide in $LiNbO_3$ substrate to propose a new type of high frequency SIW-based modulator. Interaction of optical signal in simple diffused optical waveguide and microwave signal in RWG change the phase of optical signal at the end of proposed electro-optical modulator. In the first step, a single optical waveguide and a simple

RWG on $LiNbO_3$ substrate are designed and then some modifications such as multilayer structure and array optical waveguide to increase the performance of the new device are considered.

2.3.1 Design of single optical waveguide structure

In this section, microwave and optical aspects of the new devices for phase modulators are studied and discussed. In Figure 2.4, an SIW structure for phase modulator is illustrated. In this structure, the phase of optical signal can be modulated by the microwave signal passing through the SIW structure. For the design parameters of proposed phase modulator at 1550 nm, $LiNbO_3$ substrate with different thickness is used. Bandwidth, modulation depth, overlap integral and half-wave voltage as important parameters of modulators are studied in this section.

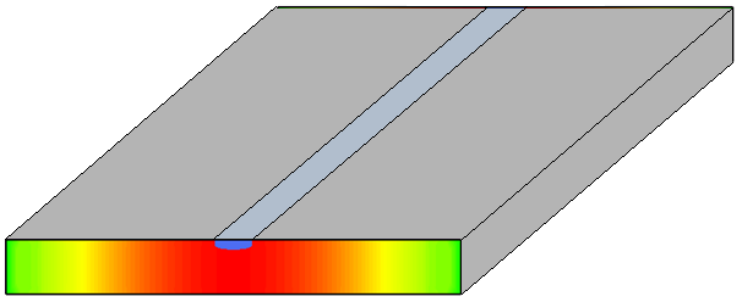

Figure 2.4: Single optical waveguide in RWG for phase modulation in $LiNbO_3$.

Bandwidth limitation caused by an optical and microwave phase velocity mismatch can be calculated in the following way. Modulation depth or efficiency is defined as [49]

$$m(f) = \frac{\Phi^2}{P} \qquad 2.17$$

where P is the input power and Φ is optical phase retardation given by

$$\Phi = \frac{\pi}{V_\pi} \int_0^L E_M \, dL \qquad 2.18$$

where L is the modulator length and V_π is the half-wave retardation voltage. E_M is the modulating wave with the phase velocity of v_M at $x=L$ and given by

$$E_M = E_{0M}\cos\left[(\omega-\omega_0).(t-\frac{L}{v_M})\right] \qquad 2.19$$

For the optical wave at $x=L$ with the phase velocity of v_0 with the initial time t_0, we have

$$t = \frac{L}{v_O} + t_0 \qquad 2.20$$

Inserting equation 2.20 in 2.19 and then in equation 2.18 yield

$$\Phi = \frac{\pi E_{0M} L}{V_\pi}\frac{\sin(U)}{U}\cos\left[(\omega-\omega_0)t_0 + U\right] \qquad 2.21$$

and

$$U = \frac{\pi(f-f_0)L}{c}\left(n_M - n_O\right) \qquad 2.22$$

where c is the speed of light in vacuum. $n_O = c/v_O$ and $n_M = c/v_M$ are optical and microwave effective indices, respectively. According to equation 2.21, phase retardation is reduced by the factor of $\sin(U)/U$. Bandwidth of the modulator can be defined when the modulation depth decreases to 70% from the maximum value. In this case, $U=1.4$ and we have [50]

$$\Delta f_{low-pass} = \frac{1.4c}{\pi L\left(n_M - n_O\right)} \qquad 2.23$$

and for the band-pass modulator at the center frequency f_0, we have

$$\Delta f_{band-pass} = 2\Delta f_{low-pass} = \frac{2.8c}{\pi L\left(n_M - n_O\right)} \qquad 2.24$$

Optical response or modulation depth can be related also to the microwave loss of the waveguide [51]

$$m(f) = \sqrt{\frac{1 - 2e^{-\alpha L}\cos(2U) + e^{-2\alpha L}}{(\alpha L)^2 + (2U)^2}} \quad 2.25$$

Modulation depth for the lossless case, $\alpha=0$, can be obtained by

$$m(f)_{Lossless} = \frac{\sin(U)}{U} \quad 2.26$$

and for the matched-velocity, $n_M=n_O$, is

$$m(f)_{Matched-Velocity} = \frac{1 - e^{-\alpha L}}{\alpha L} \quad 2.27$$

Now to obtain the modulation depth and bandwidth related to the microwave loss and optical/microwave effective indices, we need to design and analyze the proposed single optical waveguide rectangular based phase modulator.

First of all, the width of RWG which has important role in connection with the cut-off frequency should be calculated at desired frequency ranges. Figure 2.5 shows the width of RWG versus cut-off frequency for different modes. Permittivity of 28 and 43 is used in the different directions of anisotropic $LiNbO_3$. For example, the range of RWG width at the desired 60 GHz frequency for TE_{10} dominant mode can be obtained between 0.47 mm and 0.95 mm for the permittivity of 28 and between 0.38 mm and 0.76 mm for the permittivity of 43.

In Figure 2.6, cross-section view of the proposed RWG phase modulator as well as microwave loss and effective index for three different substrate thicknesses are shown. Z-cut $LiNbO_3$ is selected for TE_{10} mode of RWG which leads to maximum microwave signals. $LiNbO_3$ thickness of 220 μm is available on the market and surface polishing can be done to reach the thickness of 50 and 10 μm. Width of RWG with the center frequency of 60 GHz can be determined to be 665 μm to have maximum usable range of TE_{10} mode.

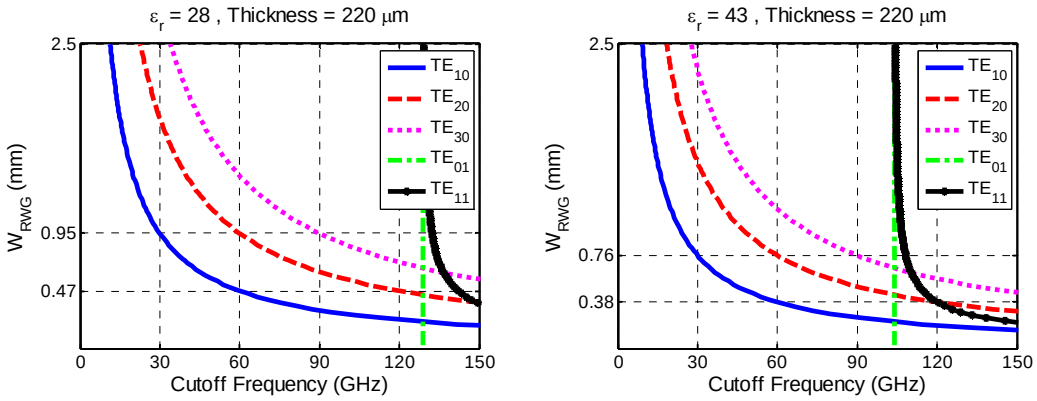

(a) (b)

Figure 2.5: RWG width versus cut-off frequency for different modes in the permittivity of a) 28 for Z-cut and b) 43 for X-cut $LiNbO_3$ substrates.

In Figure 2.6b, microwave loss versus frequency is illustrated. In general, after the cut-off frequency of RWG, microwave loss is decreased and it has almost constant value for the dominant mode, TE_{10}, region. Although these microwave losses are the summation of dielectric and conductor losses, the effect of dielectric loss is almost negligible in $LiNbO_3$ substrate. Minimum values of microwave losses are observed for the thick $LiNbO_3$ substrates. For example, in 10 μm thickness of z-cut $LiNbO_3$ substrate, high attenuation of 13 dB/cm cannot be acceptable for the new design at 60 GHz and this problem should be solved by using new structures. In Figure 2.6c, microwave effective indices are obtained. According to the figure, thickness of the substrate does not affect the effective index. According to the proposed RWG widths, microwave effective index of 3.8 is obtained at 60 GHz. From the Sellmeier equations, optical effective index is about 2.2 for the optical wavelength of 1.55 μm and the difference of optical and microwave effective index which is (*3.8-2.2*=) 1.6 in our structure can be the limiting factor of bandwidth.

After having obtained the microwave loss and effective index, we can use equations 2.25 to 2.27 to calculate modulation depths in the case of mismatched velocity, lossy waveguide and total modulation depth.

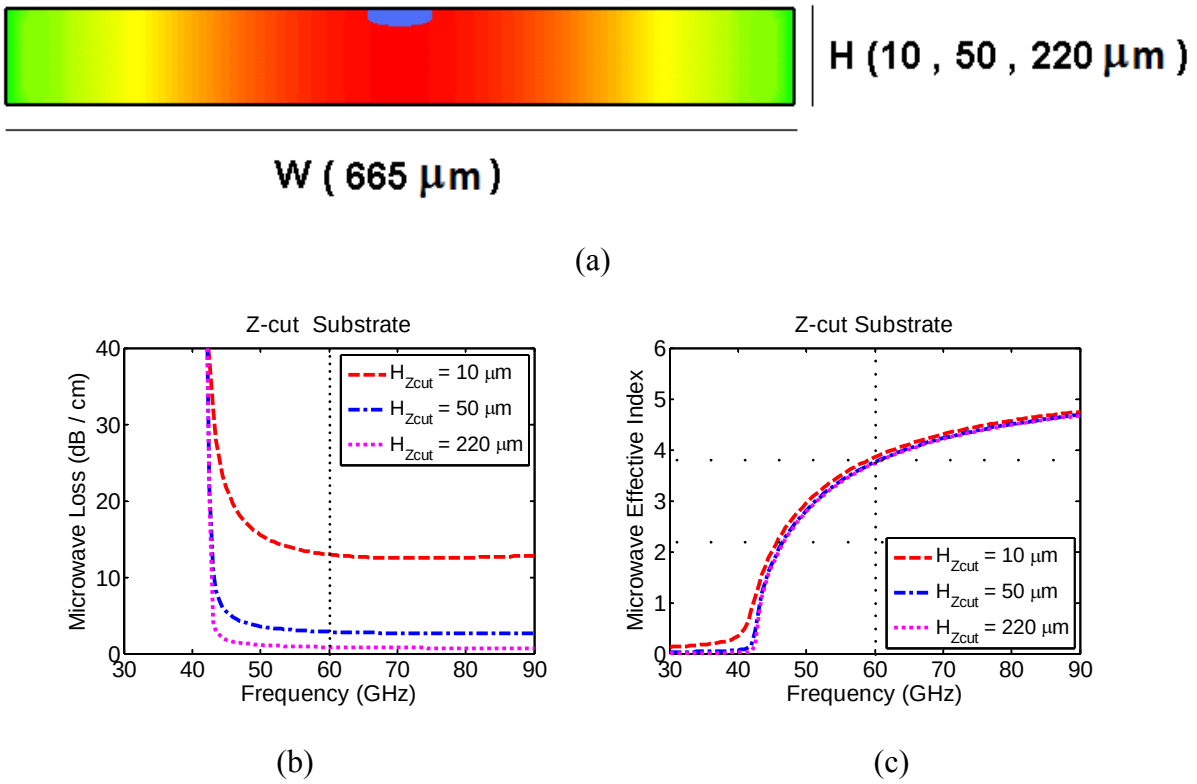

Figure 2.6: a) Cross-section view of RWG and its b) microwave loss and c) effective index, as bandwidth limitations for Z-cut $LiNbO_3$ substrate.

In Figure 2.7, modulation depths for different cases are shown. In Figure 2.7a, modulation depths for the lossy structures with an optical/microwave matched velocity are plotted. The modulation depth is almost constant after the RWG cut-off frequency and it can be explained according to the Figure 2.6b. In Figure 2.7b, a velocity mismatch of optical and microwave signals is assumed with the ideal case of zero microwave loss. In this figure, we can see the asymmetry curve for the modulation depth. For example, at 60 GHz, bandwidth is about 30 GHz between 40 and 70 GHz. This asymmetry can be explained in detail by refereeing to Figure 2.6c which is caused by increasing microwave effective index with reference to a constant optical effective index (2.2). In Figure 2.7c, total effect of mismatch velocity and lossy structure on modulation depth and bandwidth is observed. In this case, the asymmetric curve is related to the velocity mismatch. Also, decreasing of modulation depth amplitude is related to the microwave loss of the proposed phase modulator. The 3dB bandwidth, for which the modulation depth is more than 0.7, can be obtained from Figure 2.7c.

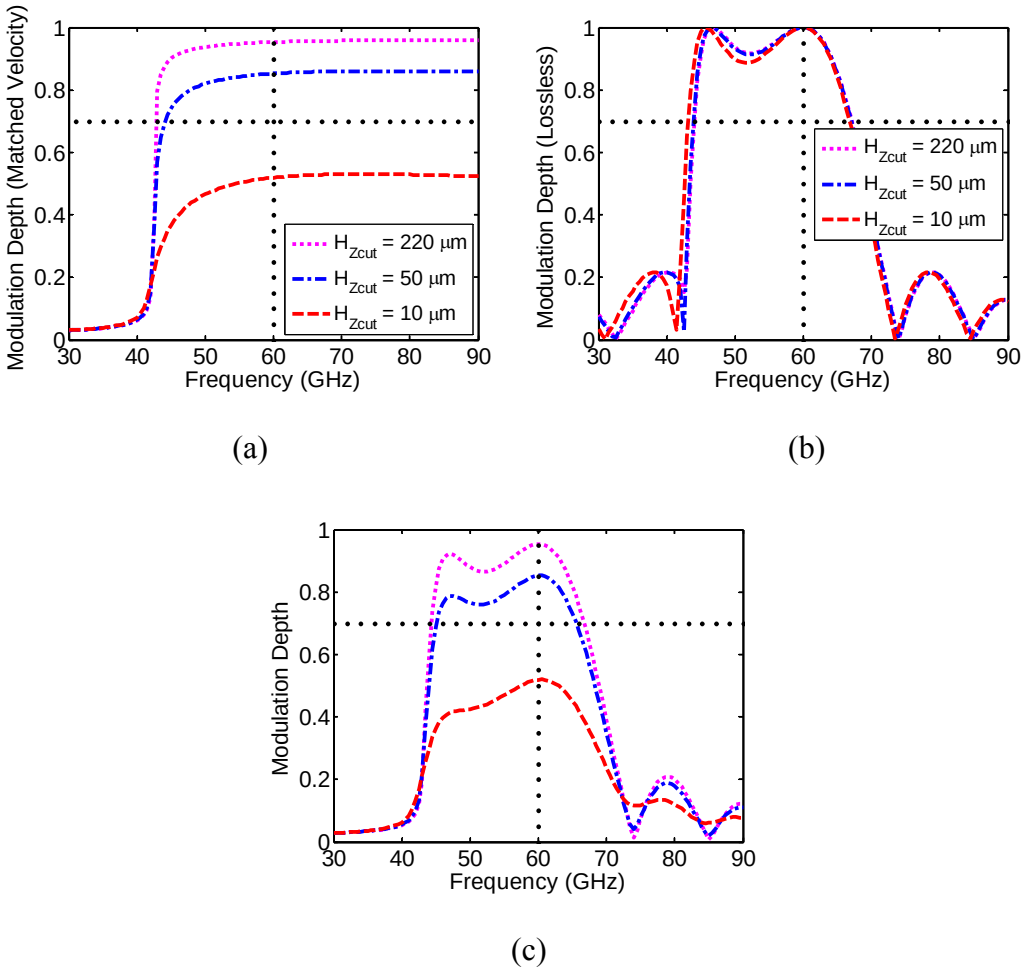

Figure 2.7: Modulation depth versus frequency for, a) lossy structure, b) mismatched velocity case and c) mismatched lossy case, of Z -cut $LiNbO_3$ with the device length of 1 cm.

In the first step of the device optimization, the asymmetry problem of RWG band-pass modulator should be solved. By changing the cut-off frequencies through the use of different width of RWG to have the almost same slope of microwave effective index before and after the point of 2.2 (optical effective index), we can effectively solve the asymmetry problem. In Figure 2.8, microwave losses and effective indices are plotted for the structure with the RWG width of 540 μm. In Figure 2.8b, 60 GHz working point is not in the middle of TE_{10} and TE_{20} cut-off frequencies and thus microwave losses are more than that in the structures shown in Figure 2.6b. In Figure 2.8c, microwave effective index is close to the optical effective index compared to the Figure 2.6c and it is expected to have symmetric curves for modulation depths.

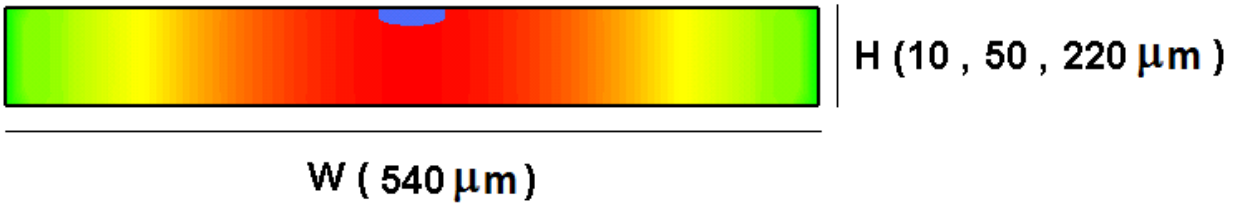

(a)

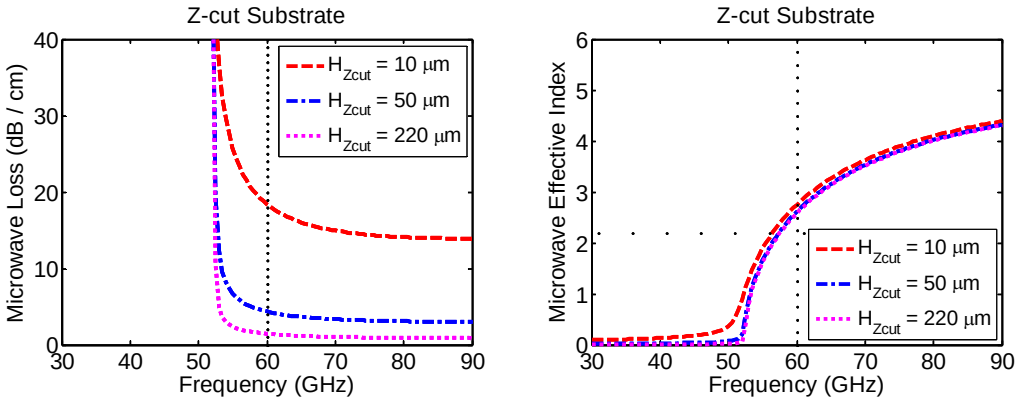

(b) (c)

Figure 2.8: a) New dimensions for RWG and b) microwave loss and c) effective index, to have symmetry behavior in modulation depth.

In Figure 2.9, optimized symmetric modulation depth for the matched velocities, lossless case and combined effects are illustrated. Comparison of these figures with Figure 2.7 shows the effect of microwave effective index on the increase of modulator bandwidth using a symmetric modulation depth. As an example, a bandwidth of about 20 GHz with the center frequency of 60 GHz is obtained for the Z-cut $LiNbO_3$ with the thickness of 50 µm and 220 µm.

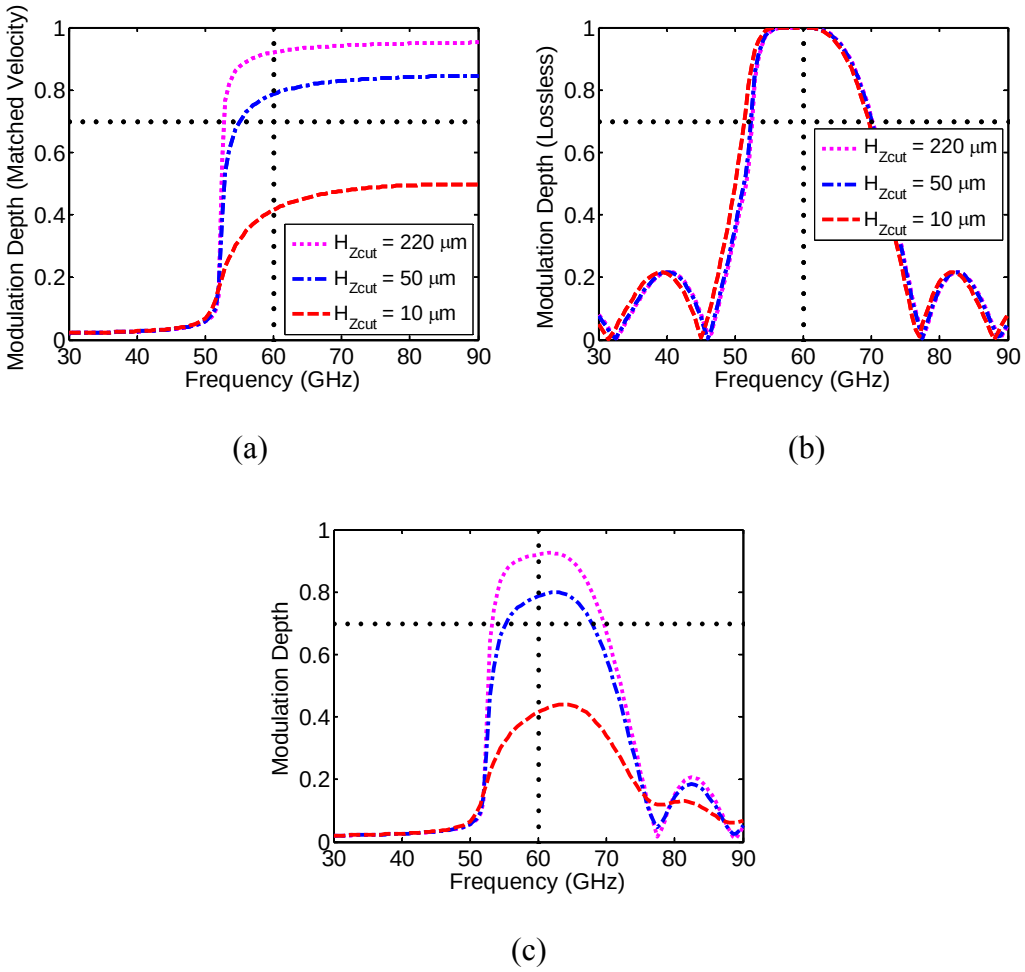

Figure 2.9: Optimized symmetric modulation depth versus frequency for 1 cm device length, a) lossy structure, b) mismatched velocity case, and c) mismatched lossy case, of Z - cut $LiNbO_3$.

Modulation depth and bandwidth are two important parameters of modulators that we have discussed so far. Overlap integral which is another important parameter for the optical modulators is related to the description of confinement between the optical and microwave fields. Considering the unique and flat optical field in the optical waveguide region (width W_O and Depth D_O), and also TE_{10} mode in RWG cross section region (width W_{RWG} and height H), the field overlap integral is

$$\Gamma = \frac{\int_{-DO}^{0}\int_{-WRWG/2}^{WO/2} E_M^Z(x,z)dxdz}{\int_{-H}^{0}\int_{-WRWG/2}^{WO/2} E_M(x,z)dxdz} \qquad 2.28$$

where E_M^Z is the Z-component of the electrical field E_M. Half-wave voltage V_π which is related to the field overlap integral of the modulator is given by

$$V_\pi = \frac{\lambda_0 H}{2n_e^3 r_{33} L\Gamma} \qquad 2.29$$

where $\lambda_0=1.55\mu m$ is the optical wavelength, H is the RWG (or SIW) height, $n_e=2.13$ is the extra ordinary refractive index of $LiNbO_3$, $r_{33}=30.8pV/m$ is the electro-optical coefficient, L is the modulation length and Γ is the overlap integral factor.

In the single optical waveguide phase modulator, the overlap integrals are obtained to be 0.36×10^{-3}, 1.6×10^{-3} and 7.4×10^{-3} for the thicknesses of 220 μm, 50 μm and 10 μm, respectively. These values are low compared to the conventional phase modulators and it should be increased by some modifications in the structure or other schemes.

In addition, for different RWG thicknesses, the half-wave voltages are calculated and shown in Figure 2.10. By increasing the length of the modulator, the required half-wave voltage is decreased. For example, the half-wave voltage of 69 V is obtained for the substrate thickness of 10 μm with the modulation length of 5 cm. Dimensions of the optical waveguide for single-mode propagation are designed to be 3 μm in depth and 6 μm in width.

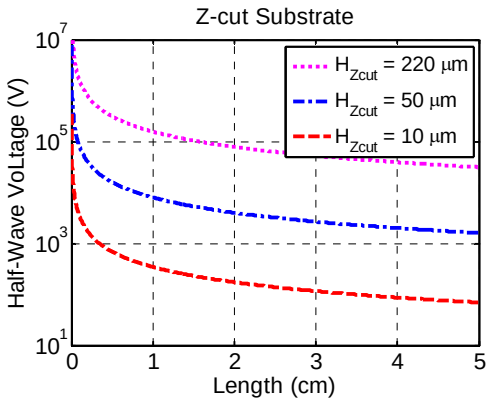

Figure 2.10: Half-wave voltage versus modulation length for single optical waveguide phase modulator at 60 GHz.

As a conclusion of the single optical waveguide analysis in the context of using a RWG phase modulator, by increasing the height of substrate to have a large bandwidth, overlap integral is decreased and then high half-wave voltage is needed. On the other hand, by considering long length of the device for low half-wave voltage, microwave loss is increased and then the bandwidth is limited. Therefore, some modifications in the proposed structure seem to be necessary.

2.3.2 Optical waveguide arrays in single $LiNbO_3$ layer

High applied or half-wave voltages are the important problem of the new proposed phase modulators involving single optical waveguide, as discussed in the previous section. To create a more field interaction between the optical and microwave signals and also to have a low applied voltage, optical waveguide array is suggested. In Figure 2.11, a cross-section view of the new RWG phase modulator using optical waveguide array is shown. In this structure, the field interaction between the optical and microwave signals can be increased to achieve a lower applied voltage.

As it is shown in the figure, optical and microwave field interaction in the middle of the RWG is maximal and decreases along the side-wall areas of RWG waveguide. If the optical waveguides in the array have the same dimensions, the phase difference obtained at the exit of the device for

each waveguide will be different because of the half-sinusoidal microwave field distribution for TE_{10} mode. The bandwidth of the device could be limited by combining the optical signals with certain phase changes. To maintain the same phase difference for the entire waveguide array, the length or propagation constant of the optical waveguides should be changed. For example, a low intensity of microwave fields can be compensated by using a long length of optical waveguide in the side wall area of the RWG. This can be done by using the arc shape of optical waveguides when going far away from the center of RWG. By using another method, the width of the optical waveguides can be changed gradually along the transverse direction of RWG width while their lengths are constant.

We suppose that optical waveguides are located in the middle of the RWG width and thus the effect of phase changes is almost negligible. The widths and lengths of optical waveguides are the same in our analysis. The number of optical waveguides is dependent on the RWG width and also on the distance between the optical waveguides. This distance can be obtained by optical analysis to have minimum optical coupling between the optical lines. Another limitation for the number of optical waveguides can be related to the Y-branch splitters and combiners. By using external commercial splitters/combiners, the maximum number of optical waveguides is specified by the RWG width and optical waveguide spacing. If Y-branch splitter/combiner are used on the same substrate in such a MZ type structure, the maximum number of optical waveguides should be 2^n *(n=1,2,3, ...)*. This limitation is added to the limitations coming from optical waveguide spacing and RWG width.

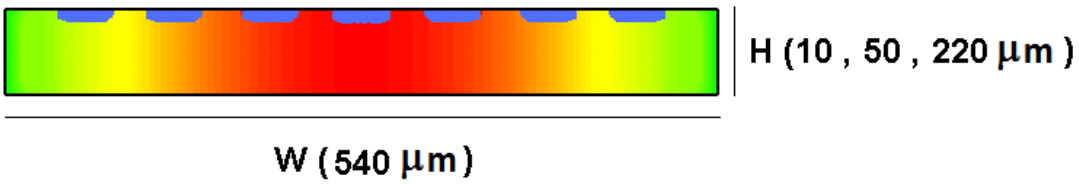

Figure 2.11: Cross-section of RWG modulator with optical waveguide array.

For analysis of the optical waveguide array, we consider 2^n *(n=1, 2 and 3)* optical waveguides with different optical waveguide spacing. In Figure 2.12, one MZ structure with two optical waveguides as an array is illustrated. The length of optical arms for the modulation purpose is 1 cm. The Y-branch lengths in this structure should be long enough to have about one degree of

separation in the Y-branches. This angle limitation comes from the simulation and fabrication criteria which will be discussed later. In the analysis, this length is considered to be 2 mm according to the spacing between the optical waveguides. Because of some limitation of fabrication, the minimum center to center spacing between the optical arms in MZ should be about 20 µm, although a careful consideration should be made about the optical coupling between the arms. In Figure 2.12b and Figure 2.12c, normalized intensities of optical fields for the optical waveguide spacing of 20 µm and 30 µm are shown, respectively. Because of the existence of two optical waveguides with large distance, no coupling between the optical waveguides is obtained. To see the effect of optical coupling, the optical waveguide array should be modeled with a large number of waveguides with tight spacing. According to the figures, less optical loss is observed for the optical array with 20 µm spacing because of low Y-branch angle in this case. The field distributions were obtained by using the beam propagation package of commercial Rsoft optical software.

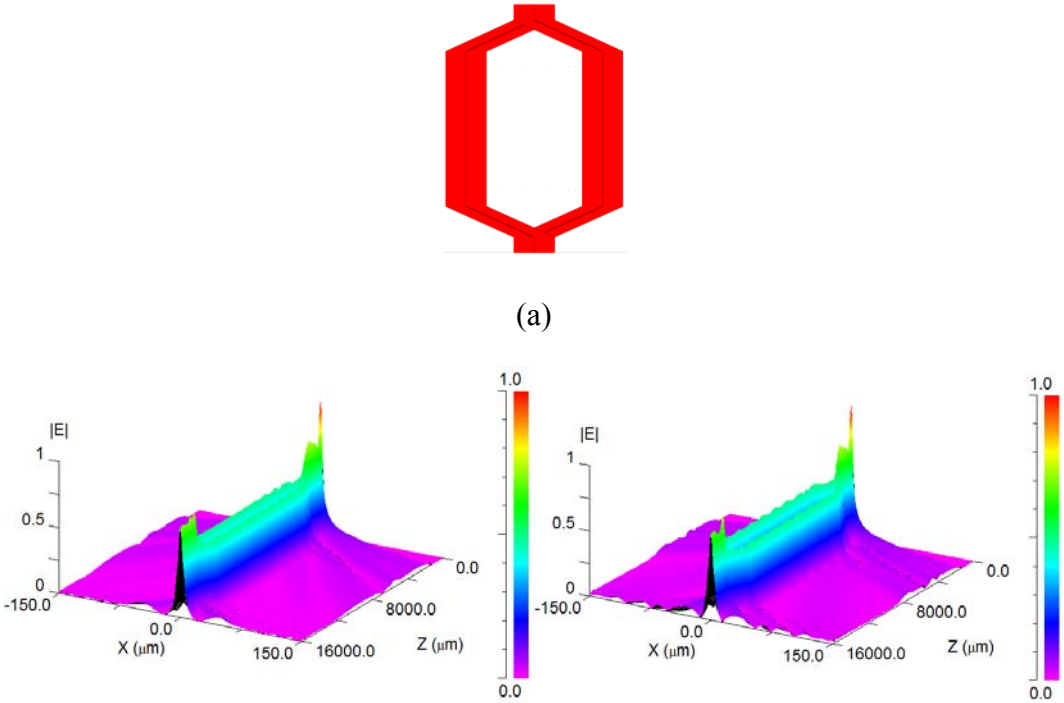

Figure 2.12: a) Optical waveguide array in MZ structure as well as b) 20 µm and c) 30 µm spacing between the optical waveguides.

In Figure 2.13a, optical waveguide array with four (2^2) waveguides is shown. Length of the optical waveguide array is considered to be 1 cm and 2 cm to observe the effect of optical coupling. The length of Y-branches is changed to have less than one degree Y-branch separation. Then, the outer and inner Y-branches have the length of 4 mm and 2 mm, respectively.

In Figure 2.13b, for 1 cm length of the array, optical coupling is observed in the 20 μm waveguide spacing. The amplitude of optical fields in two middle arms is increased with the length and then, about 60% of the power is coupled from outer arms to the inner arms after 1 cm. To diminish the optical coupling, as shown in Figure 2.13c, we need to increase the waveguide spacing. In this structure with 30 μm spacing, there is 25% of the input optical power in each arm and no optical coupling between the waveguides is observed. To be sure about the optical coupling, we have increased the length of optical array to 2 cm with the spacing of 30 μm between the waveguides in Figure 2.13d. no optical coupling is observed with this long length of the optical array.

To have an estimation of the Y-branch length in this MZ type of the optical waveguide array, an optical array with 8 (2^3) waveguides is illustrated in Figure 2.14a. The length of the Y-branches is increased while the spacing of the MZ arms is increased for less than one degree Y-branch separation which results in acceptable optical loss. These lengths in the simulated structure, shown in the figure from the input/output optical ports to the waveguide array, are 8 mm, 4 mm and 2 mm, respectively. In Figure 2.14b, 1/8 percentage of the input optical signal is transmitted through the waveguide array. In this structure, to have 1 cm of the optical waveguide array, a substrate with the minimum length of 4.4 cm is needed.

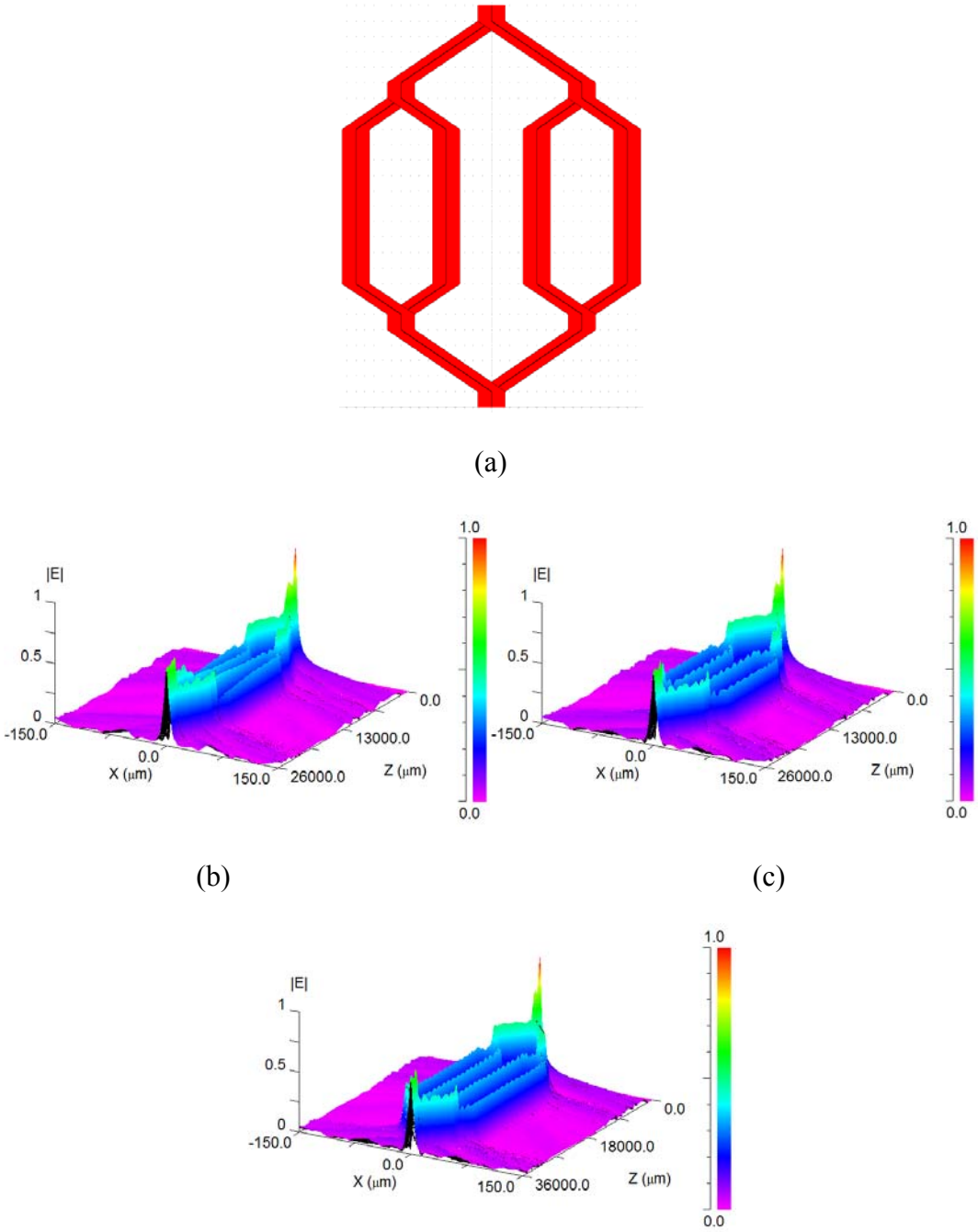

Figure 2.13: a) Optical waveguide array with four waveguides; spacing and length of the optical waveguide array respectively are b) 20 μm and 1 cm, c) 30 μm and 1 cm, and d) 30 μm and 2 cm.

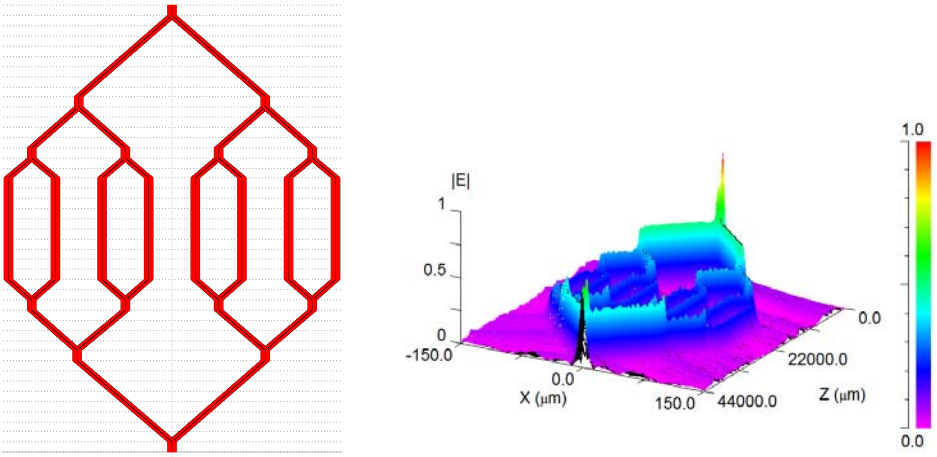

(a) (b)

Figure 2.14: a) Optical waveguide array with eight waveguides; b) spacing and length of the optical waveguide array respectively are 30 μm and 1 cm, respectively.

As it is shown in the optical analysis of the waveguide arrays with MZ structure, by increasing the number of optical waveguides, the total length of Y-branches is increased. Therefore, we need very long substrates for the dense optical arrays. To solve this important problem, the combining/splitting of optical signals can be arranged by external devices. In this case, the length of effective part of the device, modulation section, can be almost the same as the total length of the device.

For structures using optical waveguide array, the overlap integral can be increased which leads to a low applied voltage. In the phase modulator using an array with 2^4 optical waveguides, the overlap integrals are obtained to be 5.3×10^{-3}, 23.1×10^{-3} and 107.4×10^{-3} for the thicknesses of 220 μm, 50 μm and 10 μm, respectively. These values are significantly increased, about 15 times more, compared to the phase modulator with single optical waveguide. The spacing between the optical waveguides is 30 μm to avoid a potential optical coupling.

Half-wave voltage for the device with 16 waveguides versus the length of the modulator is plotted in Figure 2.15. This voltage is decreased by increasing the length of the device and has low values in the thin devices. For example, in 10 μm substrate thickness, the half-wave voltage of 4.7 V is required for 5 cm of the proposed phase modulator with 16 optical waveguides.

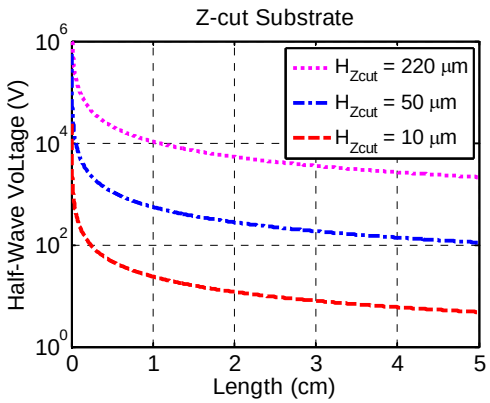

Figure 2.15: Half-wave voltage in single-mode optical waveguide array for different thicknesses of $LiNbO_3$ substrate.

Single-mode to multimode conversion is another method that can be used in the optical part of the proposed modulator. By using this structure, the field overlap between the optical and microwave signal can be increased. In Figure 2.16a, a single-mode to multimode optical waveguide is illustrated. The width of single-mode waveguide is 6 μm and the width of multimode waveguide is designed to be 50 μm. Taper length and multimode waveguide length are designed to be 2 mm and 10 mm, respectively. Normalized field as shown in Figure 2.16b has a uniform distribution in the multimode region.

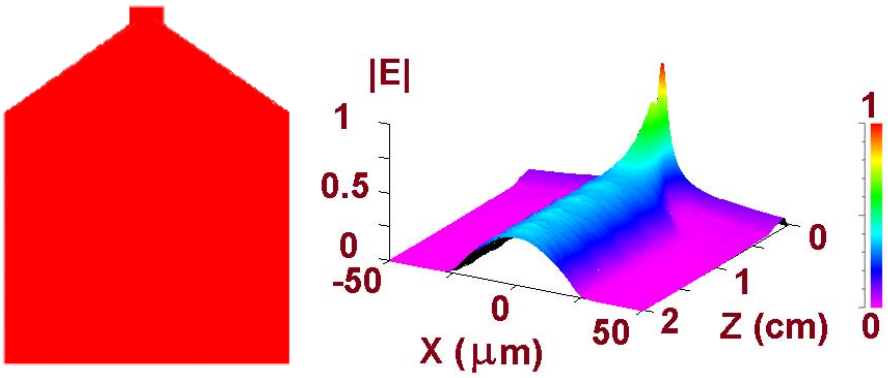

(a) (b)

Figure 2.16: a) Conversion of single-mode to multimode optical waveguide, and b) field distribution for multimode waveguide.

In the phase modulator using a multimode optical waveguide array, the overlap integrals are obtained to be 11×10^{-3}, 47.6×10^{-3} and 220.6×10^{-3} for the thicknesses of 220 µm, 50 µm and 10 µm, respectively. The width of multimode waveguides and spacing between the centers of optical waveguides are designed to be 50 µm and 75 µm, respectively. Seven multimode optical waveguides are located in the structure. These values are about 2 and 30 times more than those of the optical waveguide array and the single optical waveguide structures, respectively.

In Figure 2.17, the half-wave voltage obtained from the overlap integral is shown. According to the figure, the applied voltage of 2.3 V is required for the structure with the substrate thickness of 10 µm.

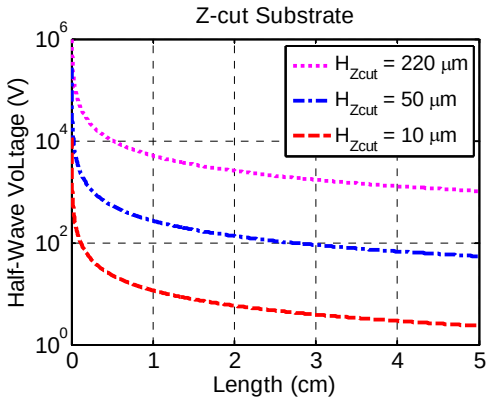

Figure 2.17: Half-wave voltage in multimode optical waveguide array for different thicknesses of $LiNbO_3$.

In this section, optical waveguide arrays are used in single-mode and multimode propagation to increase the field interaction of optical and microwave signals and decrease the half-wave voltage. Although the minimum values for the half-wave voltage is obtained in thin substrates, microwave loss that affects the bandwidth is still high and should be diminished by changing the structure. A thick multilayer substrate with microwave field confinement in the region of optical waveguide array is a suggestion to solve this problem.

2.3.3 Multilayer structure with optical waveguide array

The problem of a low overlap integral of the proposed phase modulator was solved by using an optical waveguide array. To solve the problem of high microwave loss in thin $LiNbO_3$ substrate,

a multilayer structure is proposed. Confinement of the microwave signal should be enhanced in the substrate which includes the optical waveguide array.

In Figure 2.18a, the proposed SIW band-pass phase modulator is illustrated with a synthesized microwave or millimetre-wave waveguide. In this structure, two $LiNbO_3$-layered substrates, two metallic plates, one optical waveguide array and two arrays of metalized via holes along the waveguide are used to build the structure of the proposed phase modulator.

Although the metalized via holes of the SIW instead of long and continuous metallic walls of the RWG are considered for the purpose of integration, the fabrication and packaging of the fragile $LiNbO_3$ with the metalized via hole arrays are much easier than those of the RWG with the metallic walls. It should be mentioned that in our analysis, RWG is considered instead of SIW structure because of the simulation time. At the end, to convert RWG to SIW structure, SIW effective width is designed to be the same as the RWG width.

Two layers of different $LiNbO_3$ cuts having respective thickness of h and H are utilized to confine the TE_{10} mode of SIW in the thin-layer substrate where the optical waveguides are located. To increase the modulation efficiency of the proposed structure, the optical waveguide array instead of a single optical waveguide channel is considered to create the maximum interaction between the mmW and optical field signals. The optical array is positioned in the inner side of the bottom substrate to minimize the optical loss that incurs in the presence of a metallic plate connecting to the optical waveguides.

Figure 2.18b shows the attenuation constant or mmW loss (α), mmW effective index (n_M) and optical effective index (n_O) versus frequency (f) as a function of the top substrate thickness H for a fixed bottom substrate thickness of h=10 μm. The optical effective index presents an almost constant value of 2.2 at 1550 nm. The mmW effective index is increased after the cut-off frequency of the SIW because of the SIW dispersion nature and it has a relatively low value in the case of considering a thin layer substrate. Over the 60 GHz range, the difference should be minimized between the optical and mmW propagation indices to achieve a large bandwidth. The mmW loss is significantly dropped off beyond the SIW cut-off frequency and it has almost a constant value over the operating frequency range. However, a high value of the mmW loss is observed for the thin SIW structures. The results obtained for the effective indices and mmW loss can be used in the calculation of the modulation depth and bandwidth.

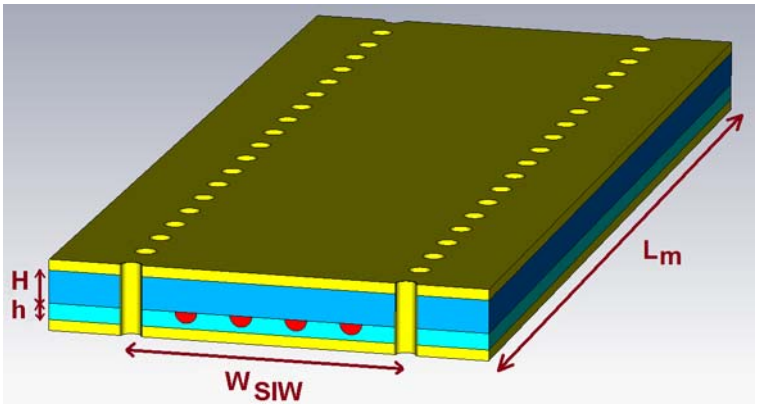

(a)

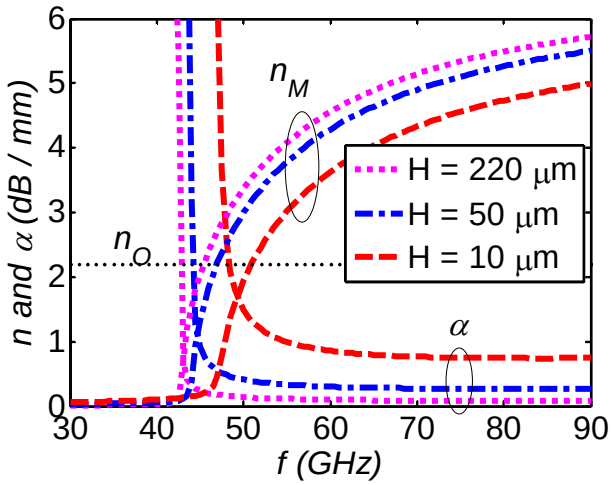

(b)

Figure 2.18: a) Schematic view of the proposed SIW phase modulator with an array of four optical waveguides, b) optical effective index (n_O), mmW effective index (n_M) and attenuation constant (α) versus frequency as a function of substrate thickness H.

Figure 2.19 shows the modulation depth (m) versus frequency (f) as a function of the substrate thickness H for lossless, velocity-matched and lossy unmatched cases.

In Figure 2.19a, the modulation depth for the lossless and unmatched-velocity case ($\alpha = 0, n_M \neq n_O$) of the proposed modulator is depicted. It can be seen that, by decreasing the substrate thickness, the lossless modulation depth becomes more symmetrical around the desired frequency.

Also in Figure 2.19a, two peaks for the lossless modulation depth are observed, one in the 60 GHz desired frequency and the other at the frequency corresponding to the point of n_M=n_O.

Although the point of n_M=n_O can be designed at the desired 60 GHz frequency for realizing a symmetrical modulation depth, the mmW loss at the velocity matched point, which is close to the cut-off frequency, is significant. According to the line *m=0.7*, the bandwidth of the modulator in the lossless case is obtained between 42 GHz and 70 GHz in our design.

In Figure 2.19b, the modulation depth for the lossy and matched-velocity case ($\alpha \neq 0, n_M = n_O$) of the SIW modulator is illustrated. In this figure, effects of the mmW loss because of high order modes of the SIW structure should be considered over high frequency range although the lossy modulation depth remains almost constant after the cut-off frequency of the TE_{10} dominant mode. It is worthwhile to mention that the TE_{20} is the second dominant mode of the SIW structure with its cut-off frequency twice that of the TE_{10} mode. In Fig. 5b, a high modulation depth and a broad bandwidth is obtained for the SIW modulator with thick substrate.

In Figure 2.19c, the modulation depth for the lossy unmatched-velocity case ($\alpha \neq 0, n_M \neq n_O$) is shown. It can be observed that the amplitude reduction and shape asymmetry of the modulation depth are caused by the mmW loss and the unmatched-velocity, respectively. Although the modulation depth or bandwidth is decreased for the use of a thin substrates in the band-pass SIW modulator, 20 GHz bandwidth can be obtained for the substrate thickness of H=10 μm.

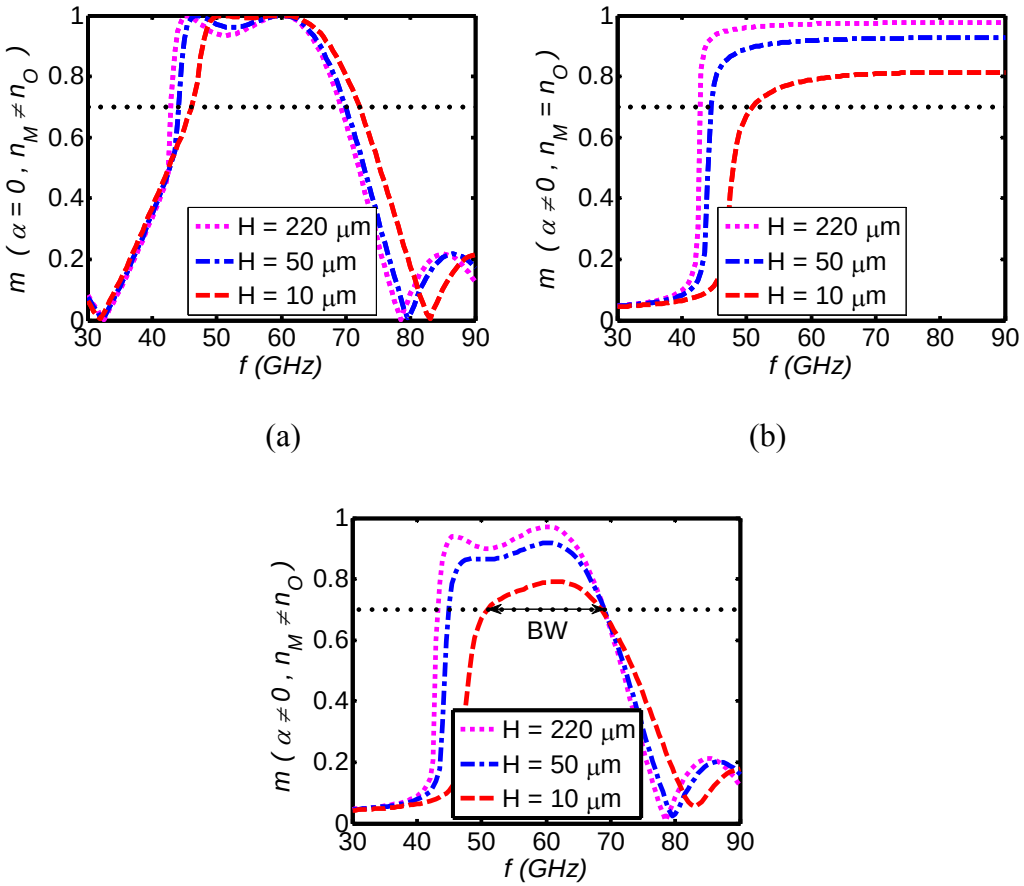

Figure 2.19: Modulation depth in different cases, a) lossless, b) velocity-matched, and c) lossy unmatched case.

Following the discussion about the microwave loss and velocity mismatch, the overlap integral and applied voltage can easily be obtained.

In the phase modulator using two-layer substrate and a single-mode optical waveguide array, the overlap integrals are obtained to be 5.7×10^{-3}, 20.5×10^{-3} and 52.2×10^{-3} for the thicknesses of 220 μm, 50 μm and 10 μm, respectively.

The half-wave voltages for the multi-layer proposed phase modulator are calculated and shown in Figure 2.20. For example, the half-wave voltage of 19.7 V is obtained for 5 cm of the device length with the substrate thickness of 10 μm.

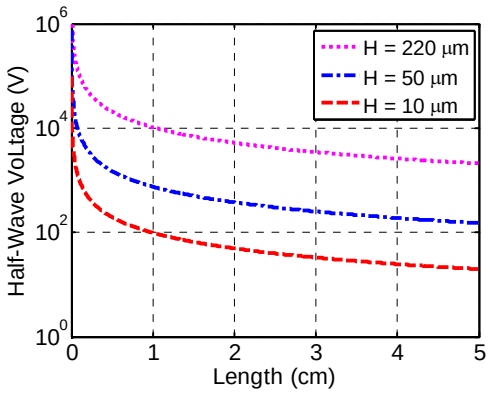

Figure 2.20: Half-wave voltage of the proposed modulator using two-layer substrate and optical waveguide array.

As a conclusion of this section, the two-layer phase modulator with optical waveguide array has been presented and studied to increase the overlap integral and bandwidth as well as decreasing the microwave loss. In the first step, RWG with single optical waveguide was proposed. The main problem of the proposed device was low overlap integral and then high applied voltage. To increase the overlap integral, the thickness of substrate could be decreased by surface polishing or other means, although this thin substrate results in high microwave loss in RWG. In addition, the value of overlap integral was not high enough in this single optical waveguide structure compared to the conventional phase modulators. In the next step, the waveguide array was proposed to have a high field interaction between microwave and optical signals. A long substrate has been used for this optical array using the MZ structure and the modulation could be done with a very small length. To solve this problem, the use of the external splitter/combiner was suggested. Another problem of the device was related to the microwave loss in thin waveguide array RWG phase modulator. As a potential solution for this limitation factor, a multilayer substrate was proposed. In two-layer RWG phase modulator with optical waveguide array, the microwave loss and applied voltage were decreased thanks to the use of thick substrate layer and optical waveguide array, respectively.

Following the proposition and design of the new RWG phase modulator, converting RWG to its integrated counterpart, namely SIW, and also transition of the conventional CPW to SIW will be studied.

2.3.4 Transition of CPW to SIW in $LiNbO_3$

In the previous sections, the RWG based phase modulator was presented and some modifications to increase the bandwidth and overlap integral were applied. To complete the structure of the proposed modulator, the transitions and also the procedure of converting RWG to SIW should be carried out.

The proposed structure for the transition of CPW to SIW for the electro-optical phase modulator is shown in Figure 2.21. In this structure, the SIW is realized by using circular-shaped holes instead of elliptical-shaped or square-shaped holes because of the difficulty in micromachining. Coplanar lines in two ports with metalized via holes to suppress undesired modes are shown in the figure. Two CPW structures may be used for the probing-station measurement purpose. The middle part, region (1), is the main waveguide section used for the phase modulator while the other two sections between the coplanar lines, regions (3), and main waveguide are cavity resonators, regions (2), designed to increase bandwidth of the device [52]-[53].

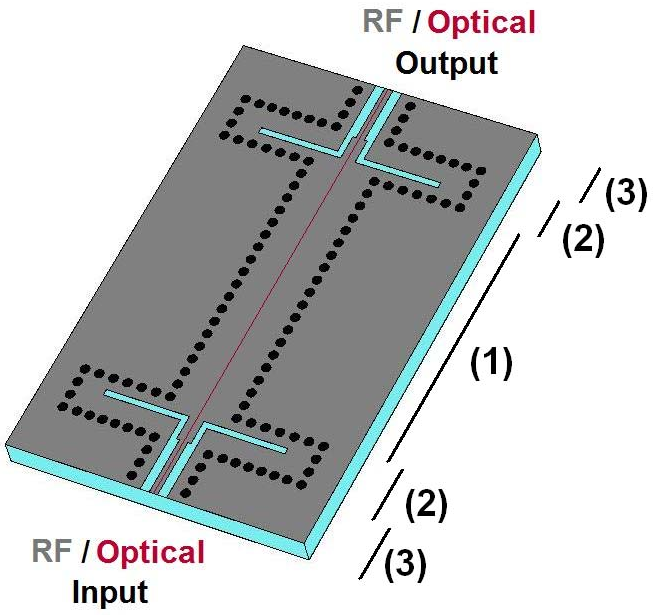

Figure 2.21: Transition of CPW to SIW for phase modulation. RF/optical ports and different regions of the device are shown.

In Figure 2.22, details of the proposed transition design in $LiNbO_3$ substrate are illustrated in a flowchart. The first design step is to consider input parameters.

By referring to the design curves plotted in Figure 2.5, the width of RWG can be specified. To enable substrate integration with other microwave devices, the RWG will be converted into its planar integrated type with some metalized via hole arrays for SIW. The following equation for the width of SIW can be used to convert the structure from non-planar RWG to planar SIW [54]

$$W_{SIW} = W_{RWG} + 4.2R_H^2 / G \qquad 2.30$$

where W_{RWG} is the width of RWG, R_H is the hole radius and G is the gap between the centers of hole in each row.

Once the RWG width is determined, the cavity resonators should be designed. The resonant frequency of dominant mode TE_{101} can be calculated by [55]

$$f_{101}(GHz) = \frac{0.15}{\sqrt{\varepsilon_r}}\sqrt{W_C^{-2} + L_C^{-2}} \qquad 2.31$$

where ε_r is substrate permittivity, and L_c and W_c are length and width of the cavity resonator, respectively.

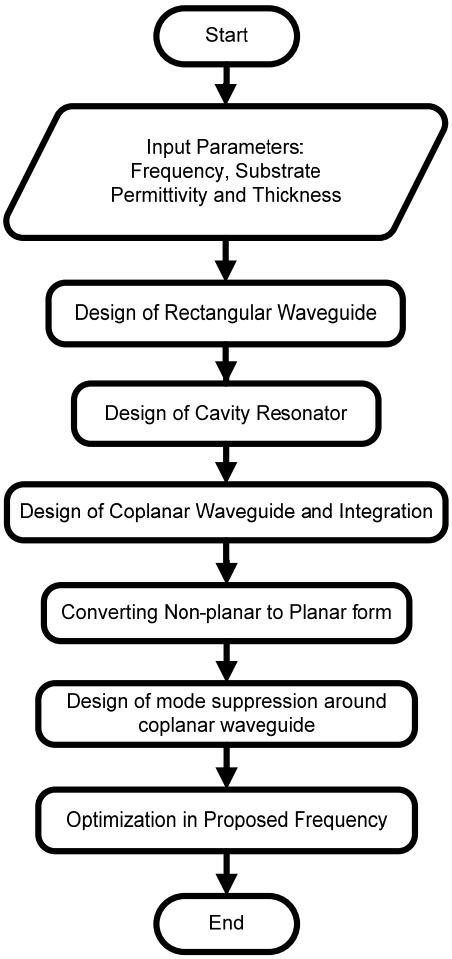

Figure 2.22: Flowchart of the design procedure for transition of CPW to substrate integrated electro-optical waveguide.

Next, the coplanar line should be designed. For our design example, 50 Ω matching condition and 0.15 mm pitch spacing of our probing-station are imposed. Then, the structure integration of coplanar lines, cavity resonators and RWG will be made. In this case, the size of coplanar strip in the transition can be changed to have maximum efficiency. Metalized via holes can be used to suppress undesired modes around the coplanar lines. These holes should be close to the coplanar line as much as possible and of course experimental limitations should be considered. Optimization of the structure for the desired frequency range is the last step of our design. The optimized designed parameters are presented in Table 2.1. In this table, two different lengths for the main SIW section in the middle of the structure are considered for the measurement purpose.

Table 2.1: Microwave design parameters of CPW to SIW transition in SIW phase modulator at 60 GHz.

Symbol	Quantity	Value (μm)
H	Substrate thickness	220
W_{MSIW}	Main SIW width	566
L_{MSIW}	Main SIW length	2400/4800
L_{CSIW}	Cavity length	430
W_{CSIW}	Cavity width	2000
R_H	Hole radius	40
G	Spacing between the holes	120
W_{ST}	Coplanar strip width	70
W_{SL}	Coplanar slot width	76

Figure 2.23 shows simulation results of the microwave losses for the SIW-based band-pass modulator with two different lengths. In these SIW modulators, more than 5 GHz of bandwidth for about -1 dB insertion loss and less than -10 dB return loss are obtained. It is worthwhile mentioning that the cut-off frequency of the principal mode should be designed to be closer to the desired frequency so to have symmetric bandwidth and modulation depth around the desired frequency, which were observed in the previous sections, In this figure, short SIW and long SIW refer to the length of 2.4 and 4.8 mm for the main SIW section.

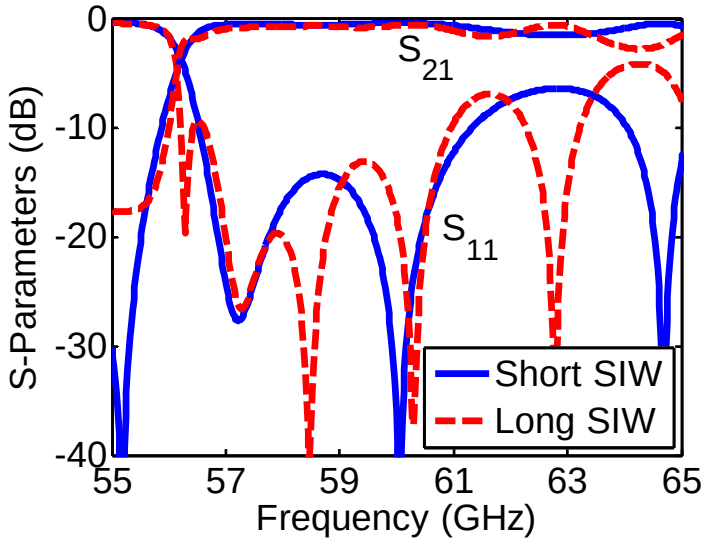

Figure 2.23: Simulation result of microwave insertion and return loss of proposed SIW phase modulator.

Following the above-discussed design procedure of phase modulators based on the SIW concept, SIW-based amplitude modulator can be developed on the same platform. In Figure 2.24, the proposed SIW-based electro-optical amplitude modulator is illustrated. In this proposed structure, there is no DC bias and it can be used as on-off state modulator. As it is shown in Figure 2.24a, the optical part of the device can be MZ type structure such as conventional amplitude modulators. This optical structure can be replaced by optical waveguide array and also splitting/combining of the optical signal can be realized in the substrate or by using external circuitry. In Figure 2.24b, optical part of the proposed modulator is replaced by waveguide array which can be connected to the external device for splitting or combining. For the microwave design, the TE_{20} mode of SIW is effectively used and the field interaction between optical and microwave signals is shown in Figure 2.24c. This figure shows the single optical waveguide in each arm of the MZ structure. Clearly, the required 180 degree phase difference between the arms of MZ optical waveguide is achieved, through the TE_{20} of SIW, which presents a special advantage of this type of structure. External splitter/combiner or multimode interference (MMI) technique [56] can be used for optical segment of the SIW amplitude modulator.

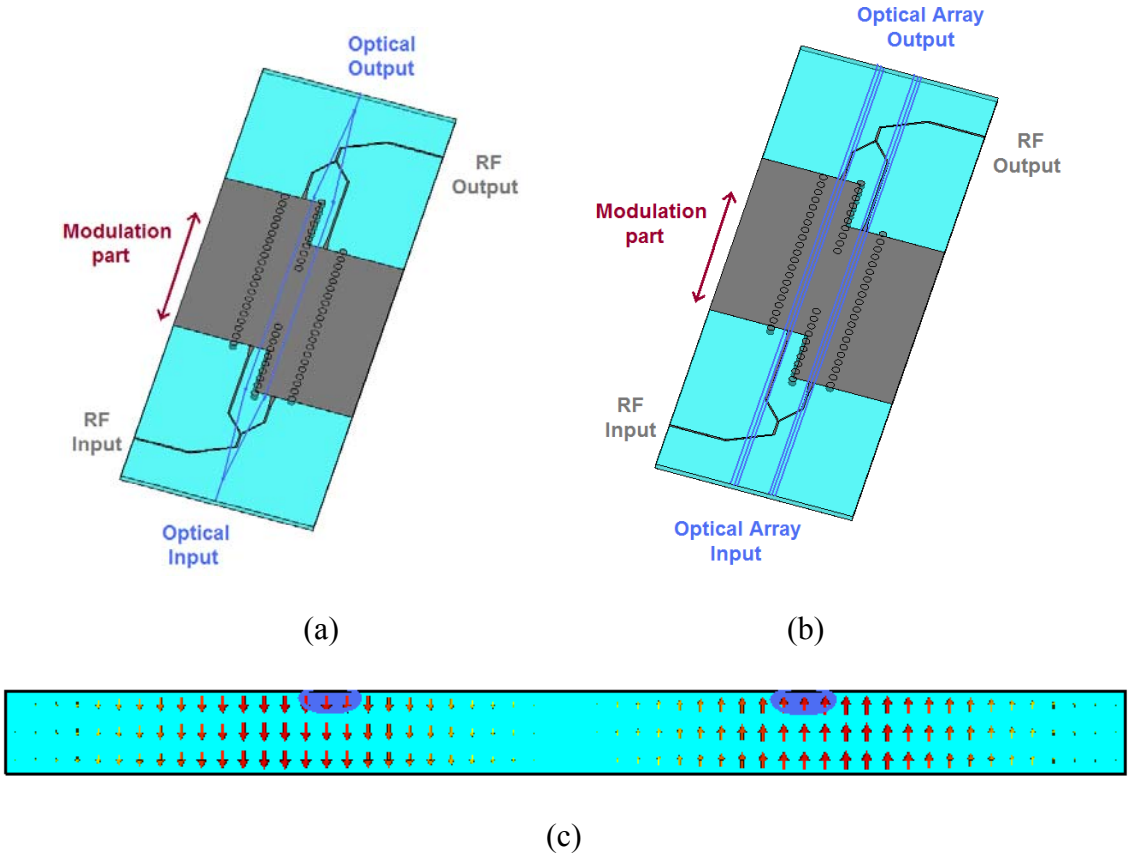

Figure 2.24: SIW-based electro-optical amplitude modulator, a) using MZ structure, b) using waveguide array, and c) cross section of modulation part including TE_{20} mode of SIW.

In this section, $LiNbO_3$ phase modulators based on the SIW structure were proposed. These modulators are band-pass with reference to the low-pass CPW conventional modulators. The proposed modulators in this section were optimized by changing the single optical waveguide to the optical waveguide array and also using the multilayer $LiNbO_3$ instead of single layer substrate. Transitions of conventional CPW to the SIW phase modulator were designed at 60 GHz frequency range. In addition, SIW amplitude modulator based on the TE_{20} mode of SIW is presented for future devices.

2.4 Exprimental issues and validation

In this section, a micromachining of the transparent $LiNbO_3$ by Excimer laser as well as methods for dicing and performing complete and incomplete holes of $LiNbO_3$ wafers are presented and discussed. Then, the applications of laser micromachining including optical ridge waveguides and new proposed SIW-based modulators are studied. At the end of this section, experimental results of the fabricated devices for the validation of simulated structures are presented.

2.4.1 Excimer laser micromachining

Drilling of via holes and fabrication are important issues for the new SIC-based optoelectronic devices. Although chemical etching and laser micromachining are two possibilities for the creation of the holes, conventional photolithography and liquid etch cannot be used because of low etching rate of 0.5 μm/hour [57] for the $LiNbO_3$ substrate. Lasers offer the possibility to micromachine in three dimensions with a high aspect ratio and also to rapidly fabricate prototypes without time-consuming mask design and fabrication. For telecommunication applications, Excimer lasers micromachining at 193 nm, 248 nm and 355 nm for Silicon (Si), InP and $LiNbO_3$ substrates was recently performed by Greuters and Rizvi [58]. Also, Femtosecond laser may be used to micro-fabricate semiconductors [59] and three dimensional optical waveguides [60]-[61].

As it is shown in Figure 2.25, the operation range of Excimer, Neodymium-doped Yttrium Aluminium Garnet (ND:YAG) and Carbon dioxide (CO_2) lasers are specified. For the optoelectronic substrates such as GaAs and InP, micromachining by commercial 532 nm green Nd:YAG laser can be done easily. Because of the transparency range of $LiNbO_3$ between 370 nm to 5000 nm, krypton fluoride (KrF) Excimer laser at 248 nm is one of the best options for micromachining. This laser was used in [62] to create a groove in the back side of $LiNbO_3$ substrate to increase the bandwidth of conventional modulators. By using the other types of lasers such as CO_2, some cracks may be created in the fragile $LiNbO_3$ substrate because of the thermal nature of this micromachining laser.

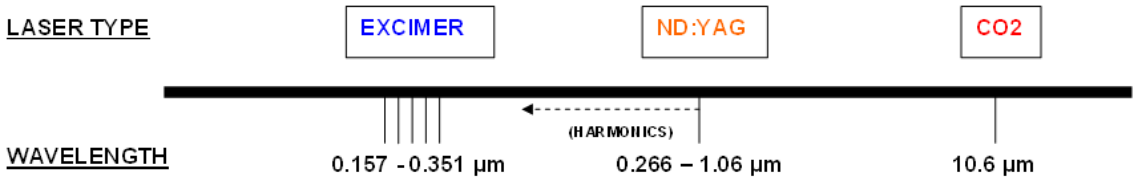

Figure 2.25: Different lasers and their wavelength in micromachining.

The system used for our fabrication is shown in Figure 2.26a. It consists of a Resonetics KrF laser micromachining system, X-Y stages and a mask controlled by user friendly software [63].

The beam profile of the Resonetics laser that is almost in elliptical shape is illustrated in Figure 2.26b. In Figure 2.26c, using the lens with a focal length (f) of 7.5 cm and the small variations of lens-stage distance (I), large variations in mask-lens distances (O) can be set while keeping the imaging condition $O^{-1} = f^{1} + I^{-1}$,to obtain different beam sizes and demagnification factor $F = O/I$ on the substrate. In all experiments, no particular care such as applying a gas flow was used to limit small debris accumulation on the surface.

(a)

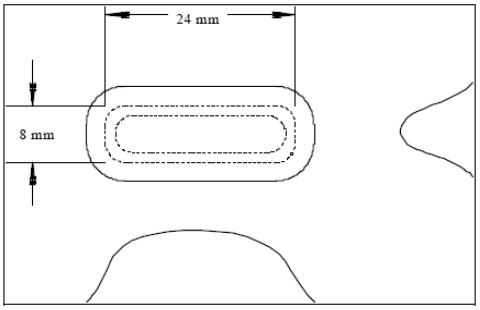

(b)

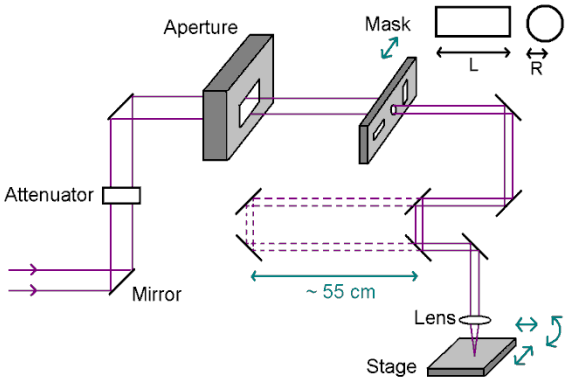

(c)

Figure 2.26: Excimer laser micromachining system; (a) picture of the laser and control system, (b) beam profile of Excimer laser (c) optical beam schematics; circular and rectangular mask are shown.

One of important problems of Excimer laser micromachining is taper effect which is illustrated in Figure 2.27. Taper angle is about 7° as the cutting depth penetrates into the substrate. This can be decreased by using low Fluence or other beam motion techniques. It can be reduced to approximately 2° in low aspect ratio applications by the use of high Fluence. The use of the double side micromachining to remove the taper effect because of the alignment could be difficult.

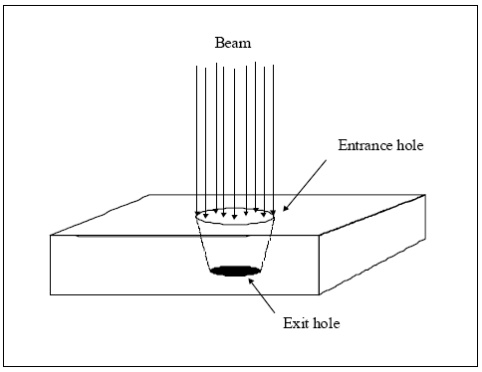

Figure 2.27: Taper effect of Excimer laser.

After a brief discussion on Excimer laser micromachining, $LiNbO_3$ wafer dicing and then via hole drilling are studied.

2.4.2 Wafer dicing and hole drilling

For the fabrication of the new electro-optical modulators based on SIW with the optical and microwave field interaction, large wafers are preferred for designing devices having both long and short waveguides. In the first step of wafer dicing, a 220 μm $LiNbO_3$ wafer was selected. Two methods for dicing the wafer by Excimer laser were tried. Single scan cutting of the wafer using circular or rectangular masks resulted into low quality cuts with a large edge roughness. Multiple scan of a rectangular mask scanned along the long edge L gave much better quality cuts. The scanning speed V of the target is determined by [63]

$$V = \frac{LD_p N_p}{FD_S} \qquad 2.32$$

where F is demagnification factor, D_p is the depth created by one pulse determined by the laser output energy, N_p is number of pulse per second and D_S is the desired slot depth. In Figure 2.28a, a 0.22 mm thick X-cut $LiNbO_3$ wafer was diced over a 76.2 mm length. High quality cutting was obtained by performing multiple scanning of a rectangular-mask over the substrate surface. By using N_p =100 pulses/s, L/F = 600 μm and D_p = 0.05 μm/pulse, etching about 5 μm at every scan was obtained and the wafer was cut by performing 44 scans at a speed of 0.6 mm/s. Figure 2.28a

shows also a 25 mm by 25 mm square cut. The cutting precision of the wafer is illustrated in Figure 2.28b.

(a) (b)

Figure 2.28: a) X-Cut $LiNbO_3$ wafer with 76.2 mm diameter and 0.22 mm thickness, b) image of the cutting precision.

For drilling a hole in $LiNbO_3$ substrate with a circle-mask, a flowchart shown in Figure 2.29 is presented. In this flowchart, output energy of the Excimer laser, hole diameter of the mask, demagnification factor and thickness of the substrate are the input parameters of the hole drilling process. The thickness of $LiNbO_3$ substrate which is diced in the previous step is constant although the other input parameters can be changed by desired hole diameter. The maximum energy and demagnification factor are 400 mJ and 35, respectively. As an example of drilling, a demagnification factor of 15.6 can be obtained to create a hole with 80 µm diameter and mask diameter of 1.25 mm. With the distance of 8 cm from the Lens in micromachining part to the substrate, a distance of 124.8 cm from mask to the Lens is obtained. The demagnification factor obtained in this work should satisfy required Fluence on the substrate for $LiNbO_3$ material.

The next step of the hole drilling process is finding the Fluence on the mask and then Fluence on the substrate considering the mask hole diameter and demagnification factor. Fluence on the Target or substrate is given by [63]

$$F_T = \eta . F_M . F \qquad 2.33$$

where coefficient of η is 0.5 for KrF Excimer micromachining laser, F_M is Fluence on the mask and F is demagnification factor. According to equation 2.33, Fluence of 1.75 J/cm^2 on the target is obtained for mask Fluence of 0.225 J/cm^2 and demagnification of 15.6. In the X-cut and Z-cut $LiNbO_3$ substrates, minimum required Fluence is about 1 J/cm^2. In the case less than this value, mask diameter and demagnification factor should be changed.

Finding the number of pulses for specific hole depth according to ablation rate is the next step after having prepared the setup. Two methods were used to calculate the ablation rate for X-cut $LiNbO_3$ substrate. In the first method, the data from the published papers can be used. The ablation rate for the $LiNbO_3$ substrate with 3J/cm^2 energy was obtained about 0.04 μm/pulse in [58]. To drill a complete hole in 0.22 mm $LiNbO_3$ substrate, 5500 pulses are needed. The second method, which is more accurate, the depth of hole created with specific number of pulses can be measured. Ablation rate is the created hole depth over the number of pulses. Using this method a table of ablation rates for different values of laser energy, demagnification factor and mask hole diameters can be obtained.

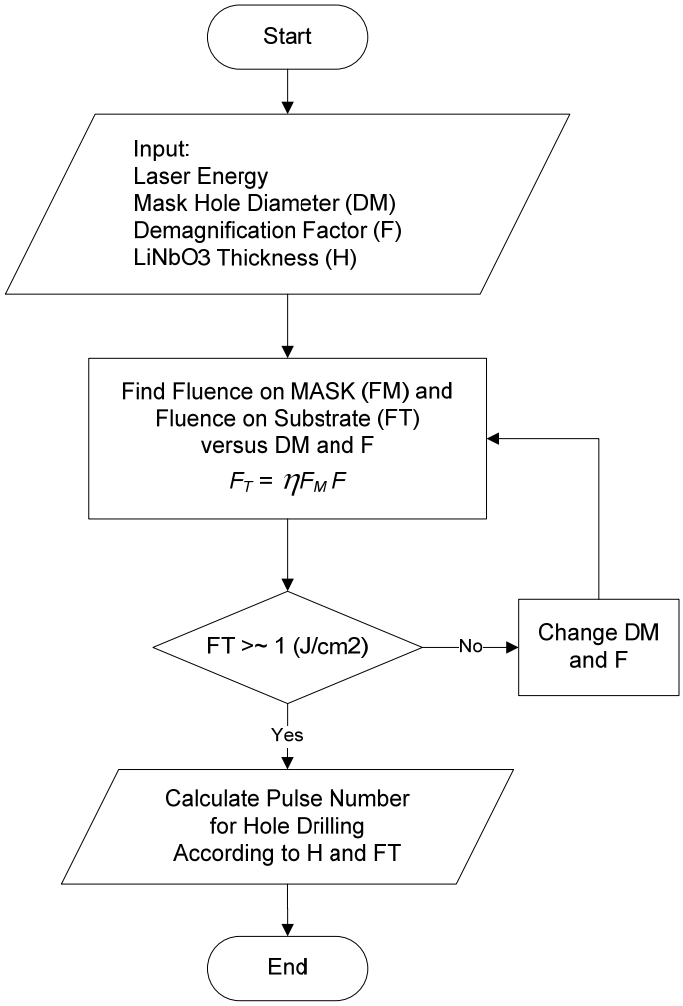

Figure 2.29: Flowchart for micromachining by Excimer laser.

Fabrication of the electro-optical modulator requires the drilling of two types of via holes into the wafer, namely, incomplete holes for ridge optical waveguide fabrication and complete ones for connecting the substrate surface to the bottom and for their use in the fabrication of microwave waveguides.

Figure 2.30 shows a typical incomplete hole of about 30 μm diameter micromachined with 75 pulses at the fluence on the target of 1.75 J/cm^2, as estimated by the demagnification factor of 15.6 and the fluence on the circular mask of 0.225 J/cm^2. An average ablation rate of 0.04 μm/pulse is deduced by measuring the depth of 3 μm.

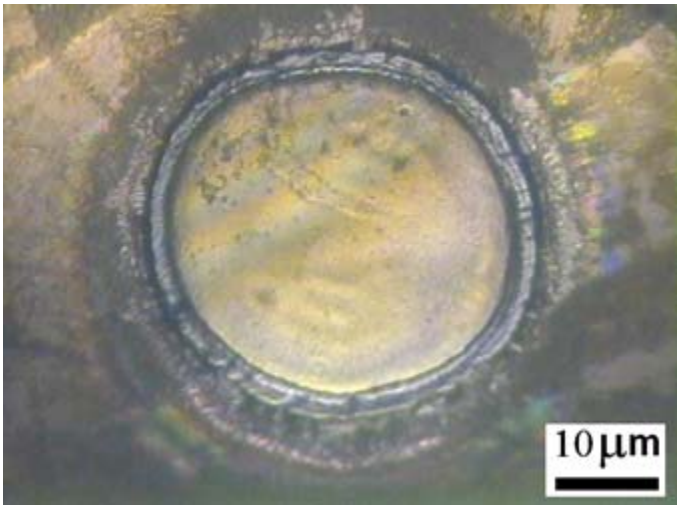

Figure 2.30: Incomplete hole with 30 µm diameter and 3 µm depth.

Figure 2.31 shows the scanning electron microscope (SEM) image of a complete 80 µm diameter hole throughout the whole wafer thickness of 220 µm and also a series of holes which can be used in SIW structure. At the fluence on the target of 3 J/cm^2, this hole takes 55 seconds at a repetition rate of 100 pulses per second. Even if some small debris are observed around the hole, their presence would not affect the device performance. The shape of this via hole is not perfectly circular, due to the elliptical shape of the laser output beam. In addition, the hole diameters at the entrance/top and exit/bottom of the substrate are not the same. This taper angle of about 4 degrees is due to a fix focal point during the process. In an optical image of the complete hole, a slight dark area surrounding the hole was observed. This area may be related to the light scattered by the small debris and to some bulk heating effects by the Excimer laser micromachining yielding an out diffusion of Lithium. Even if this last effect may alter the refractive index of $LiNbO_3$ surrounding the hole area by about +/- 0.001, we do not anticipate that it would affect the performance of the circuit used for our optical and microwave applications. Actually, in microwave applications using SIW, most of the main mode power is in the middle of the structure, that is far from the micro-machined sections. In the optical applications using a ridge waveguide, Ti in-diffusion can be used to have low-loss optical waveguides.

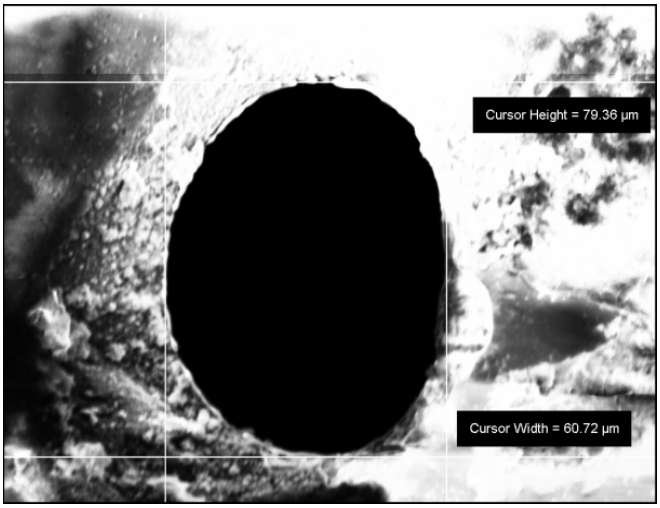

(a)

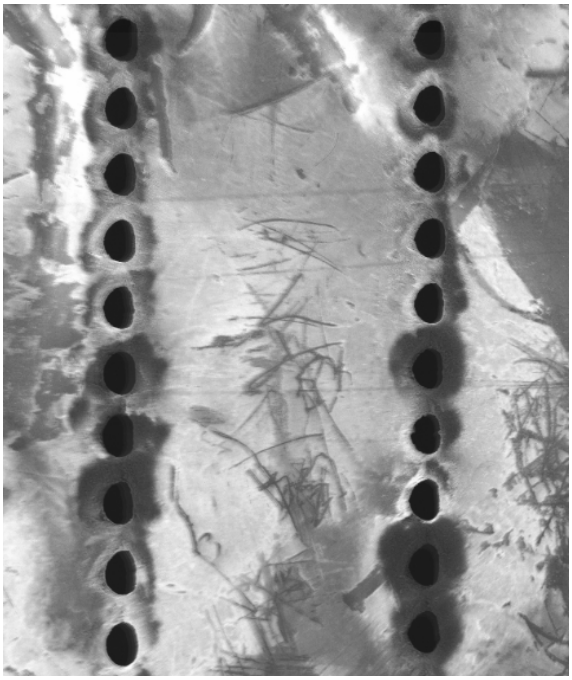

(b)

Figure 2.31: SEM image of a) a complete 80 µm diameter hole and b) a series of holes in SIW.

2.4.3 Applications and experimental results

After having prepared the Excimer laser, optical and microwave applications and also experimental results of this micromachining can be studied and realized.

Optical ridge waveguide opens the possibilities to design low driving voltage-oriented electro-optical modulators because of a relatively large field interaction between microwave and optical signals. Excimer laser micromachining offers the possibility to easily fabricate ridge waveguides with the desired geometry, width and etching depth. As an example, Figure 2.32 shows a 10 µm wide optical ridge waveguide fabricated using a rectangular mask. An attempt to make high quality ridge waveguide with circular masks of any dimensions failed, thus resulting in non uniform width which would eventually affect the optical propagation. Scanning speed of 450 µm/s, laser energy of 300 mJ and 100 pulses per second were programmed to obtain a high quality 10 µm ridge waveguide with a depth of about 5 µm. The ridge waveguide was fabricated by scanning a 20 µm width line in one direction and returning with the distance of 30 µm (from A to D in the figure). It is important to mention that to improve the quality of ridge waveguide just single-scan was applied instead of multiple-scan as it was used for cutting the wafer. The reasons of using single scan are because of the low edge roughness and low depth of the grooves around the ridge waveguide.

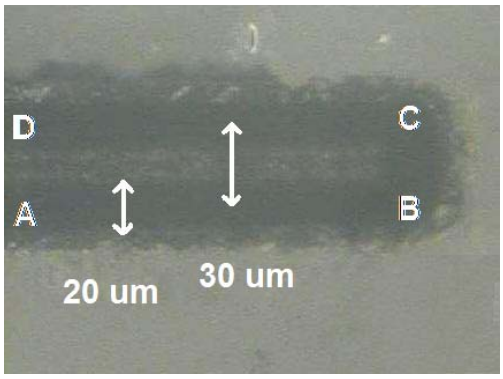

Figure 2.32: Laser micromachining of 10 µm $LiNbO_3$ optical ridge waveguides by scanning a 20 µm width line.

For the microwave application of Excimer laser, Figure 2.33a shows a pattern of holes designed to have an SIW in the middle of structure and CPWs on both sides of it over the top and bottom. The hole diameter is 85 µm on the front surface and this diameter decreases with a 4 degree angle to about 50 µm on the other side of the 220 µm thick substrate. This taper angle increases the effective waveguide width, although it is acceptable for our application at 60 GHz. The distance between the holes is about 120 µm. As noted in Figure 2.33, distances between the holes

in the horizontal direction is slightly greater by 5% than the ones between the holes in vertical direction. This difference, which is not critical for our design, comes from the elliptical shape of the focused beam. To complete the microwave waveguide, gold metallization of the top and bottom of substrate as well as in the inner parts of the holes was performed by sputtering method which is shown in Figure 2.33b. Probing-station including the probe pitch distance of 150 µm, user friendly software to control the positions, microscope and network analyzer is shown in Figure 2.34.

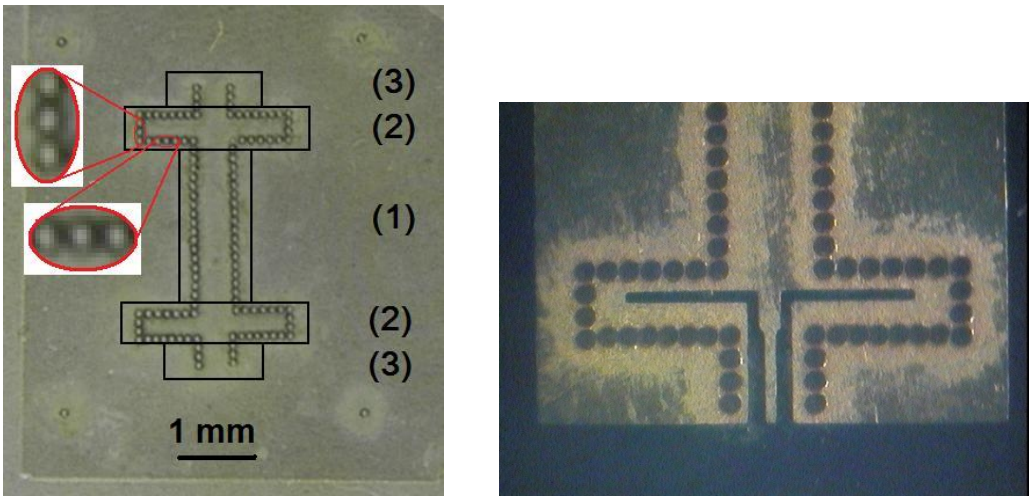

(a) (b)

Figure 2.33: a) Hole pattern by Excimer laser for microwave waveguide applications, and b) fabricated device.

Figure 2.34: Probing-station for the measurement of scattering parameters of the fabricated devices with CPW transition.

Figure 2.35 shows simulation and measurement results of the scattering parameters and attenuation constant and microwave effective index as well, for two fabricated devices designed in section (2.3.4). In Figure 2.35a and Figure 2.35b, the results for short-length and long-length SIW designed modulators are shown, respectively. In our SIW modulator, about 5 GHz of bandwidth can easily be obtained over 60 GHz operating frequency range. A small frequency shift because of an SIW width tolerance related to our micromachining process and metallization can be seen here. Nevertheless, good agreements between the simulated and measured results are observed for the new type of SIW-based phase modulators. In Figure 2.35c, attenuation constant and microwave effective index are extracted from the simulation and measurement scattering parameters for the devices with two different lengths [64] and a good agreement between the simulation and measurement is observed.

In this section, Excimer laser micromachining for $LiNbO_3$ substrate was explained for microwave and optical applications. Then, dicing the wafer and drilling the hole were discussed. Experimental results of the fabricated devices for the proposed SIW phase modulation have been presented.

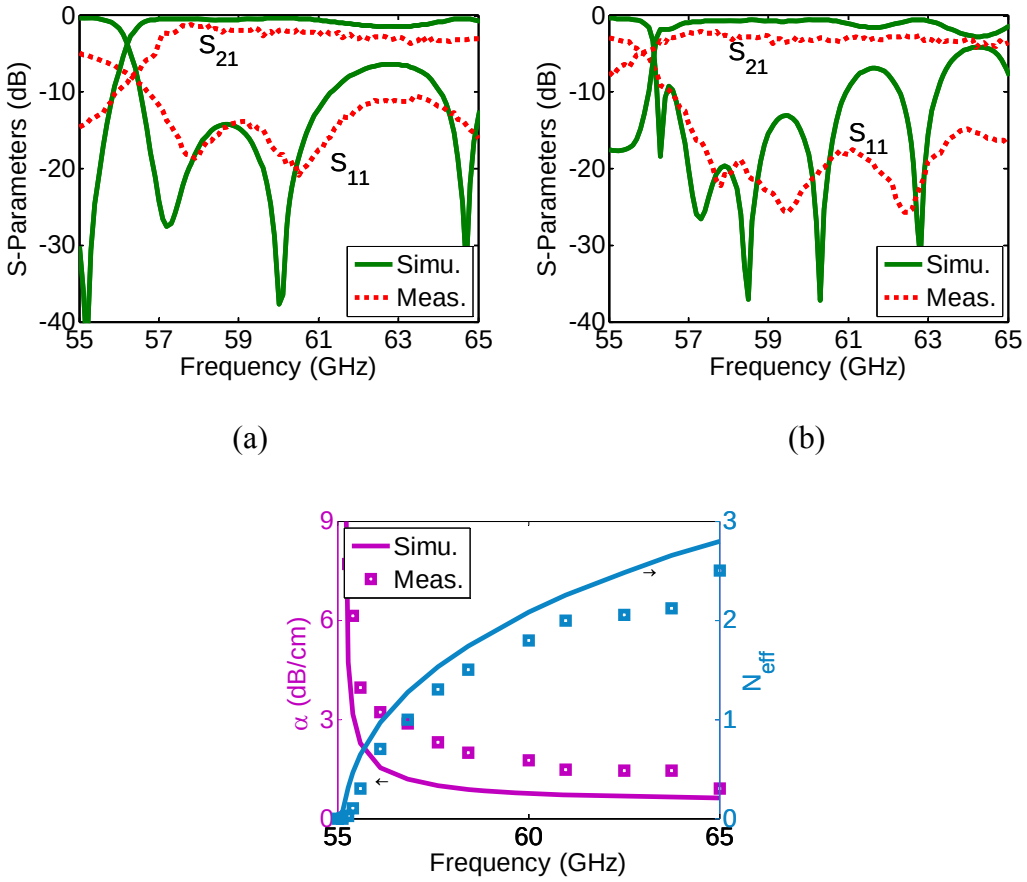

Figure 2.35: Return and insertion losses for fabricated devices with, a) short-length SIW and b) long-length SIW, and also c) attenuation constant and microwave effective index.

2.5 Conclusion

New types of electro-optical $LiNbO_3$ modulator based on SIW schemes have been proposed and studied. Conventional microwave structures in low-pass optical modulators are used CPS and CPW which are lossy in high frequency range. SIW with microwave loss less than conventional planar waveguides can be used to develop a class of new modulators over different frequency ranges. In this chapter, the proposed SIW phase modulator with single optical waveguide has been analyzed at first. Considering different width and thickness for $LiNbO_3$ substrate, the

overlap integral and microwave attenuation can be altered. In thin substrate with low microwave loss, the overlap integral is low and then we need to use a high half-wave voltage.

To increase the overlap integral, techniques of optical waveguide array have been proposed. Interaction of microwave signal with the optical signals in array structure can effectively decrease the applied voltage. Although the overlap integral of the SIW phase modulator with the optical waveguide array is much more than the structure with single optical waveguide, this value is still less than that observed in conventional CPW modulators. Multimode optical waveguide array is another method which has been used to increase the overlap integral. By converting narrow single-mode optical waveguide to wide multimode waveguide array, the overlap integral has been increased significantly.

Another limitation of the proposed SIW phase modulator, in addition to the overlap integral, was related to the high microwave loss in thin single layer $LiNbO_3$ substrates. To solve this problem, a structure with the multilayer substrates including a thin substrate for optical waveguides has been presented. By using this configuration, lower microwave loss has been obtained in total thick multilayer substrates while we have more field interaction between the microwave and optical fields in the thin substrate. Transitions of the conventional waveguides such as MS and CPW to SIW phase modulator at different frequencies have been designed as well.

In the next step, the design concept of SIW phase modulator has been used to propose the SIW amplitude modulators. The microwave part of this SIW amplitude modulator, which is based on the use of TE_{20} mode of the microwave RWG, can be excited by MS lines with different length to create a 180 degree microwave phase. The multimode waveguide array can be considered for the optical part of this SIW amplitude modulator in the same way as phase modulator.

At the end of this chapter, a laser micromachining technique with UV Excimer laser is used to fabricate the device. Optical and microwave applications of this micromachining and measurement results are also presented in this chapter. Scattering parameters of the fabricated and simulated results have been compared and good agreements were observed. In addition, for the validation of our analysis, bandwidth limitation factors of the fabricated phase modulator including the attenuation constant and microwave effective index have been obtained and compared with the simulation results.

CHAPTER 3. ELECTRO-OPTICAL SIW-CPW MODULATORS

3.1 Introduction

In the previous chapter, new type of the electro-optical modulator based on SIW platform were proposed, designed and realized. Difficulties of applying DC bias and also low overlap integral of the proposed SIW modulators present some of the important problems. In this chapter, the SIW structure is applied and integrated into the conventional CPW modulators. In this way, a low-pass low-frequency CPW modulator is converted to the band-pass high-frequency SIW-CPW modulator to solve the low overlap integral problem of pure SIW modulators.

In this chapter, the newly proposed SIW-CPW based modulator is introduced at first and then theoretical and experimental issues of the optical and microwave parts of this modulator are discussed.

3.2 Newly proposed SIW-CPW based modulator

Preserving the advantages of high overlap integral in CPW conventional modulators and modifying lossy microwave section of the modulator enable us to propose and design a class of new band-pass SIW-CPW electro-optical modulators for high frequency applications.

The microwave TE_{10} signal of the SIW structure at the entrance of the modulator is gradually transferred to the TEM mode in the CPW structure. Although this coupling mechanism has been demonstrated for other applications in [65], this is for the first time that it is effectively used for electro-optical structures.

Figure 3.1 shows the proposed SIW-CPW amplitude modulator and its optical and microwave sections. MZ interferometer can be used in the optical part of this modulator as shown a top view in Figure 3.1b. For the microwave part, SIW bending structure are used to separate microwave and optical ports, and also CPW and SIW cavity in the RF ports are used for probing-station measurements as well as for increasing the bandwidth (Figure 3.1c). The middle section of this

structure where we have CPW on the top metal plate of the SIW is used for modulation purpose. Microwave signal from a low-loss SIW structure is coupled to the CPW for modulation in the middle of the device. In the other side of the device, microwave signal from the SIW structure is transmitted to the other microwave devices such as antenna.

Overlap integral in the conventional CPW modulators can be obtained by the field interaction of the microwave and optical fields in the cross-section of the structure. In the proposed SIW-CPW structure, the microwave field is increased along the propagation path and it becomes maximized in the middle of structure. If we consider *y* axis as the propagation direction, E_z^{el} is tolerated to the microwave fields in *x*, *y* and *z* directions and we have [13]

$$\Gamma = \frac{G}{V} \frac{\int_{-\infty}^{+\infty}\int_{-\infty}^{+\infty}\int_{-\infty}^{+\infty} E_z^{el}(x,y,z).\left[E_z^{op}(x,z)\right]^2 dxdydz}{\int_{-\infty}^{+\infty}\int_{-\infty}^{+\infty}\left[E_z^{op}(x,z)\right]^2 dxdz} \qquad 3.1$$

where *G* is the distance between the CPW electrodes, *V* is the drive voltage of the modulator, E_z^{op} is the optical field and E_z^{el} is the *z* component of the electrical field.

Microwave and optical parts including theoretical and experimental issues of this structure will be explained more in the following sections.

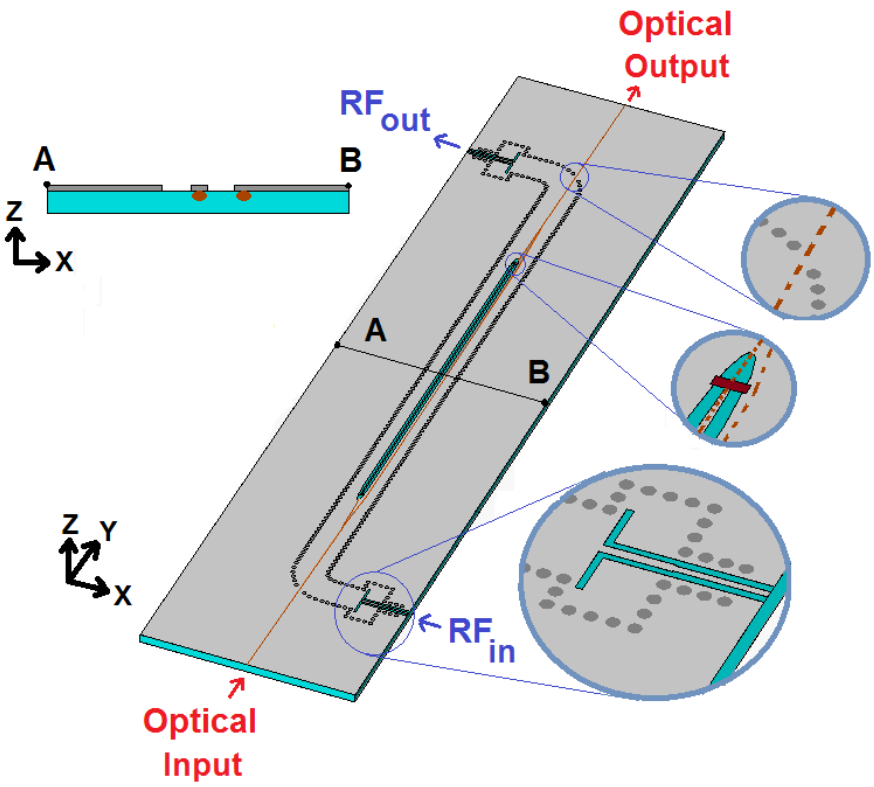

(a)

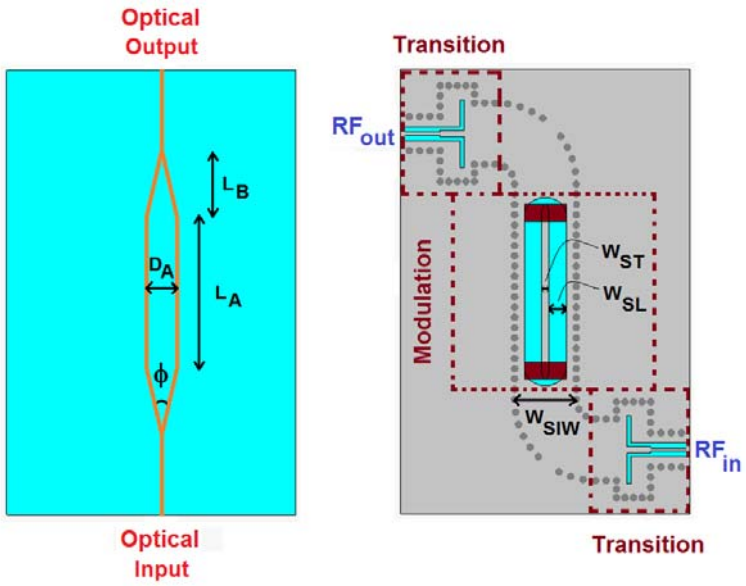

(b) (c)

Figure 3.1: a) Proposed SIW-CPW electro-optical amplitude modulator and schematic top views of b) optical section and c) microwave section.

3.3 Microwave structure

To design the proposed SIW-CPW modulator, certain important modification is applied to the microwave section of the conventional CPW modulator. In this case, the SIW is added to the conventional structures and a mode coupling between SIW and CPW is established as the special scheme of the microwave design for this new modulator.

Simulation and design for the entire microwave parts as well as fabrication and measurement are discussed in this section.

3.3.1 Theoretical discussion

Two different parts can be considered for the microwave section of the structure shown in Figure 3.1. The transition is the first part of the structure. The transition includes the circuits between the RF ports and SIW bending area. CPW is designed in the ports for the measurement purpose through a probing station. Some metalized holes around the CPW are used to suppress higher order modes of the CPW. These holes should have a minimum distance from the ports to avoid the top metal separation in the probing-station measurement. Also, there is an SIW cavity to increases the bandwidth of the transition from CPW to SIW. Details of this design were explained in the previous chapter. After this broadband transition, the SIW bending is used to separate microwave and optical ports. One or two holes should be removed from the external curves of the SIW bending to have enough space for passing the optical waveguide. The second and main part of the microwave section is related to the middle section of structure where we have mode coupling between SIW and CPW structures and also field interaction between the microwave and optical signals.

To design this coupling part, we start from the basic structures including pure CPW, pure RWG and also CPW designed on the top metallic plate of the RWG as shown in Figure 3.2.

RWG is considered instead of SIW to simplify the design procedure of coupling circuit, and it will be converted to SIW in the last steps.

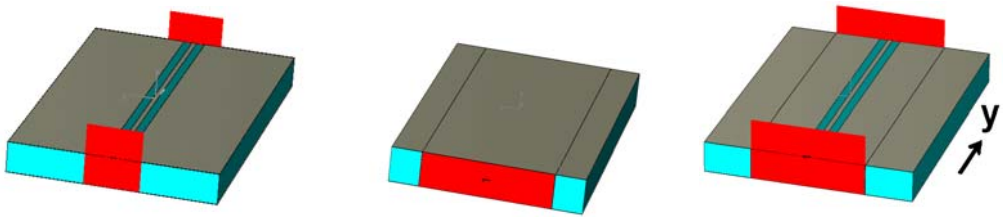

(a) (b) (c)

Figure 3.2: a) CPW, b) RWG and c) combination of CPW/RWG for coupling mechanism.

For the coupling mechanism, in the presence of CPW and RWG, electrical fields in the lossless case are given by [66]

$$\frac{dE_{RWG}}{dy} = -j\beta_{RWG}E_{RWG} + jCE_{CPW}$$
$$\frac{dE_{CPW}}{dy} = -j\beta_{CPW}E_{CPW} + jCE_{RWG} \qquad 3.2$$

where y is the propagation direction, C is the coupling coefficient and β_{CPW} and β_{RWG} are the phase constants of CPW and RWG modes, respectively. We suppose that the structure shown in Figure 3.2c is excited just by TE_{10} of RWG ($E_{RWG}\{y=0\} = 1$ and $E_{CPW}\{y=0\} = 0$).

From equation 3.2, electrical fields of TE_{10} in RWG and TEM in CPW can be obtained versus the length of structure [66].

$$E_{RWG}(y) = \exp\left[-jCy - j(\frac{\beta_{RWG}+\beta_{CPW}}{2})y\right].$$
$$\cos\left[Cy\sqrt{\left(\frac{\beta_{RWG}-\beta_{CPW}}{2C}\right)^2+1}\right] - \frac{j(\beta_{RWG}-\beta_{CPW})}{2C\sqrt{\left(\frac{\beta_{RWG}-\beta_{CPW}}{2C}\right)^2+1}}\sin\left[Cy\sqrt{\left(\frac{\beta_{RWG}-\beta_{CPW}}{2C}\right)^2+1}\right] \qquad 3.3$$

and

$$E_{CPW}(y) = \exp\left[-jCy - j\left(\frac{\beta_{RWG}+\beta_{CPW}}{2}\right)y\right].$$
$$\frac{j}{\sqrt{\left(\frac{\beta_{RWG}-\beta_{CPW}}{2C}\right)^2+1}}\sin\left[Cy\sqrt{\left(\frac{\beta_{RWG}-\beta_{CPW}}{2C}\right)^2+1}\right] \qquad 3.4$$

In Figure 3.3, these CPW and RWG fields versus the length-coupling coefficient are illustrated as a function of phase constant difference. According to the figure, in $Cy/\pi = 0$ only RWG wave appears. Maximum power transfer takes place from RWG to CPW in $Cy/\pi = 0.5$ with the condition of equal phase constants between the CPW and RWG waves ($\beta_{RWG} = \beta_{CPW}$). In the case of unequal values of the phase constants, the maximum power transfer cannot happen.

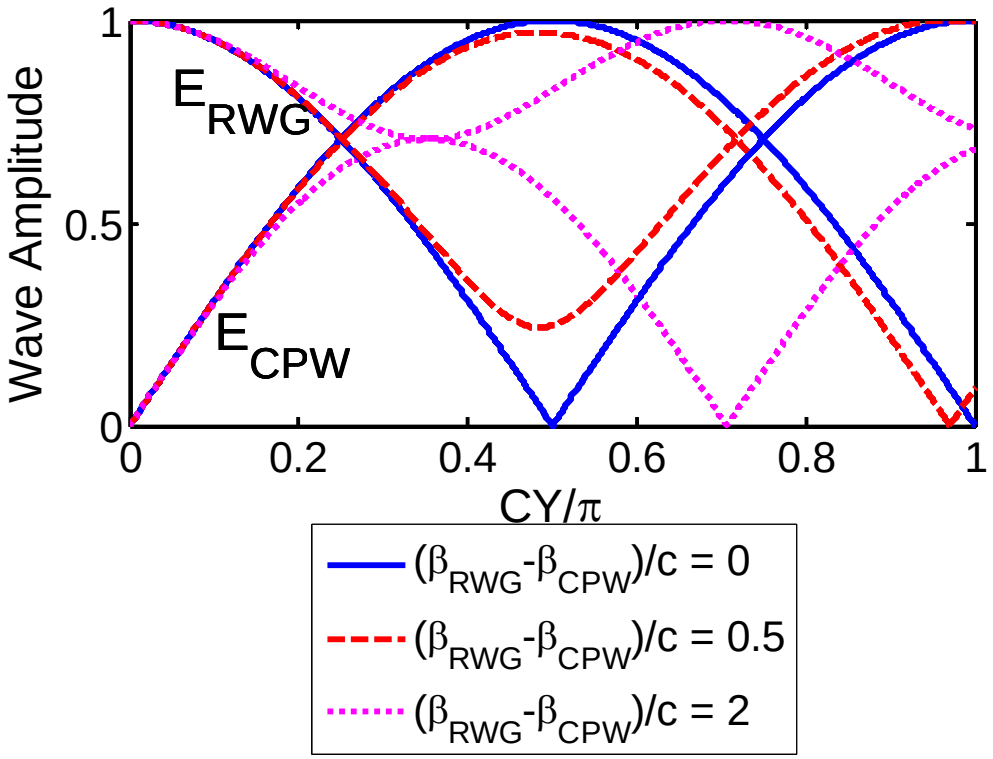

Figure 3.3: Normalized wave amplitude versus the length-coupling coefficient as a function of phase constant difference.

According to Figure 3.3, the phase constant or effective permittivity should be the same to have maximum coupling between the CPW and RWG. Now, we consider pure RWG for a desired frequency, 60 GHz, in the given $LiNbO_3$ substrate and then by changing dimensions of CPW, we are able to obtain the same effective permittivity of RWG for CPW around 60 GHz.

In Figure 3.4, effective permittivity and electrical fields versus frequency for CPW, RWG and the hybrid structure involving both CPW and RWG are shown. As it is shown in Figure 3.4a, effective permittivity of CPW (case 1: TEM mode) has small change versus frequency. In case 2 (TE_{10} mode), the effective index of the RWG increases after the cut-off frequency around 37 GHz. The permittivity of CPW and RWG is optimized to intercept with each other around 60 GHz. By combining these two structures, two different modes appear which can be called the first normal mode (case 3) and the second normal mode (case 4).

Although at low frequencies, the first normal mode (case 3) is completely TEM, it follows the TE_{10} mode of the RWG in the frequency range after the designated 60 GHz coupling frequency. For the second normal mode (case 4), it follows TE_{10} and TEM modes before and after the coupling frequency, respectively.

Figure 3.4b illustrates the coupling mechanism through electrical fields when the TEM mode is being converted to the TE_{10} mode and vice versa.

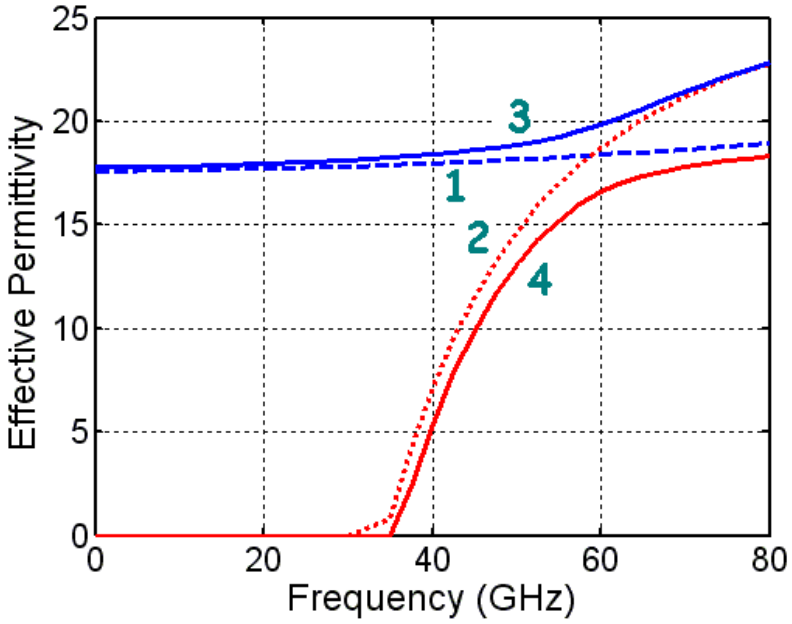

(a)

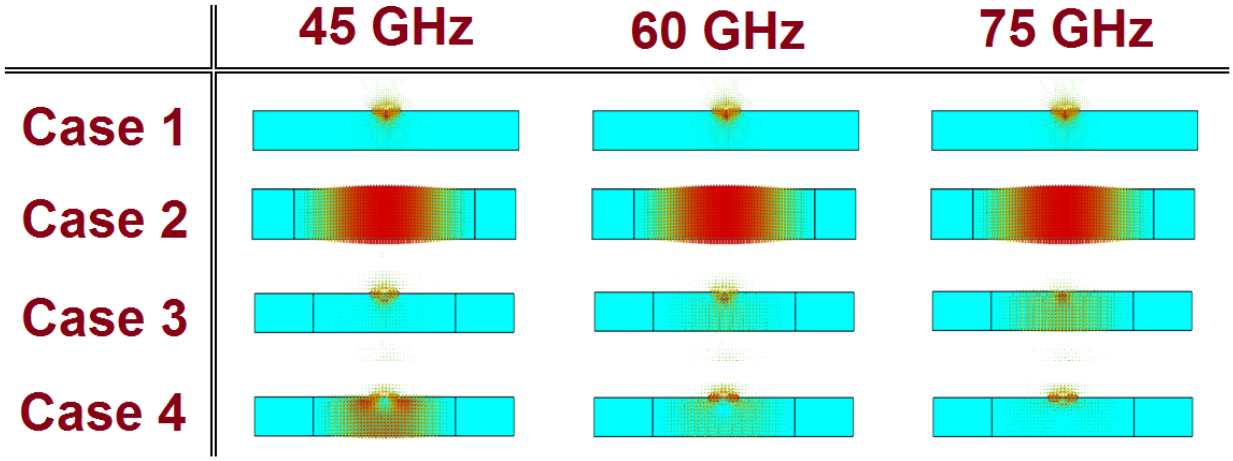

(b)

Figure 3.4: a) Effective permittivity versus frequency for CPW (case1: TEM mode), RWG (case2: TE_{10} mode) and the hybrid structure of both CPW and RWG (case3: first normal mode, case4: second normal mode), b) electrical fields in different frequencies for different modes.

The analysis of the coupling mechanism is completed by finding the coupling length so to yield the maximum power of mode transfer.

For uniform coupling structure, the phase difference of the two normal modes should be 180 degree and the coupling length is obtained by [66]

$$L_c(f) = \frac{\pi}{\beta_{CPW/RWG}(f) - \beta_{RWG/CPW}(f)} \qquad 3.5$$

where $\beta_{CPW/RWG}$ and $\beta_{RWG/CPW}$ are phase constants of first and second normal modes, respectively.

Considering the maximum power in equation 3.4 and given values of the coupling length and phase constants, coupling coefficient is obtained by [66]

$$C = \frac{\pi}{2L_c}\left[\left(\frac{\beta_{RWG} - \beta_{CPW}}{2C}\right)^2 + 1\right]^{-1/2} \qquad 3.6$$

By considering $P_{CPW} \propto |E_{CPW}|^2$ and $P_{RWG} \propto |E_{RWG}|^2$, power transfer ratio may be obtained.

In Figure 3.5, the maximum power transfer ratio and length of power transfer versus frequency are presented. The maximum power of the TE_{10} mode in RWG is converted to the TEM mode in CPW at 60 GHz and also the maximum value of transfer length is obtained at 60 GHz.

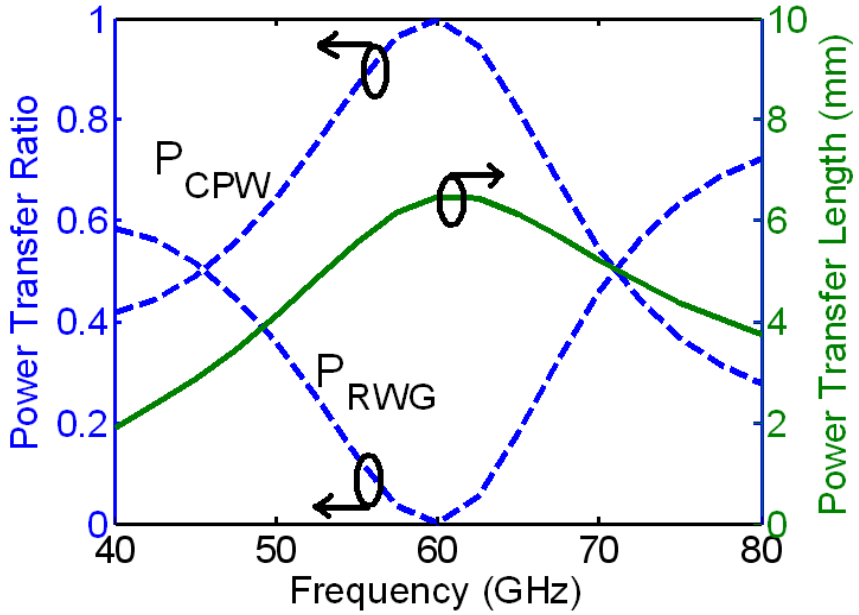

Figure 3.5: Maximum power transfer ratio and length of CPW and RWG modes versus frequency.

To design and optimize the complete coupling structure, it may be excited by TE_{10} mode of RWG at port 1, as shown in Figure 3.6. Some ports including lumped-element ports (ports 3 and 4) as well as waveguide ports (ports 1 and 2) are defined to optimize the structure dimensions. Between port 1 and port 3, the TE_{10} mode is guided. In port 3, the TE_{10} starts its conversion to the TEM mode and at the end of the CPW structure at port 4, the maximum converted power appears.

In Figure 3.7, scattering parameters that are used to explain the coupling mechanism is illustrated. There is a good transmission from port 1, which is related to the TE_{10} of RWG, to port 4, which is related to the TEM of CPW at 60 GHz.

Optimized dimensions obtained from the coupling mechanism between RWG and CPW are used for the design of SIW-CPW modulator including the metallized via holes of the SIW, bending structures for separation of optical and microwave ports as well as transitions for the measurement purpose.

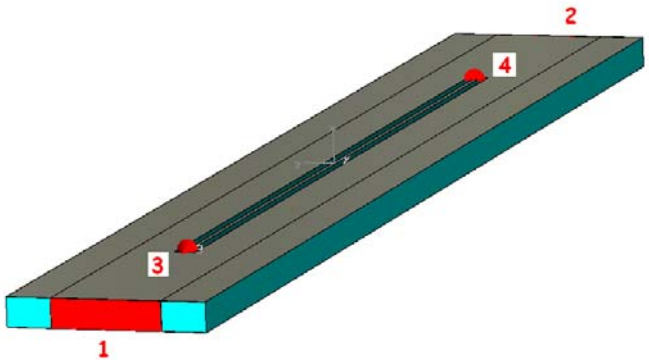

Figure 3.6: RWG incorporating CPW in the middle of the structure for mode coupling mechanism in $LiNbO_3$ substrate.

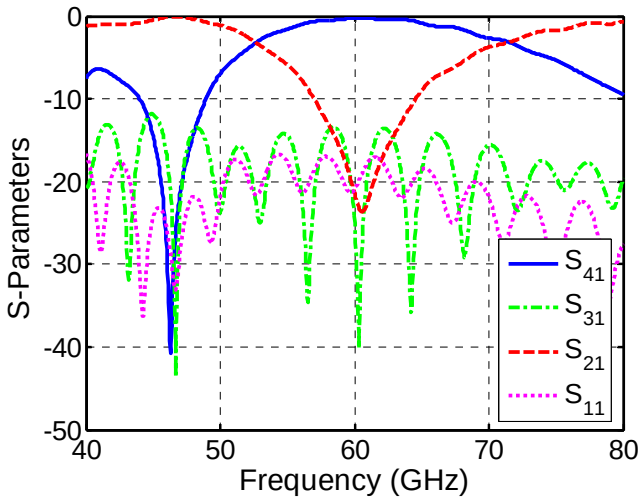

Figure 3.7: Scattering parameters used to explain the coupling mechanism from RWG to CPW.

After finding all of the parameters for coupling mechanism and converting RWG to SIW and design of transition parts as discussed in the previous chapter, the microwave part design of SIW-CPW amplitude modulator can be completed and optimized.

In Table 3.1, microwave design parameters of the new proposed SIW-CPW modulator are presented. Overlap integral of the proposed modulator is obtained 0.37 which is comparable with the conventional electro-optical modulators. Simulation results can be presented with the measurement results to have a comparison between them in the next section.

Table 3.1: Microwave design parameters of SIW-CPW amplitude modulator at 60 GHz.

Symbol	Quantity	Value (μm)
CL	Cavity length	650
ER_{slotM}	Elliptic radius of main slot	500
ER_{stripM}	Elliptic radius of main strip	300
Gap	Spacing between the via holes	150
L_{cpwM}	Length of main CPW	9500
L_{strip}	Strip length	450
$POCH$	Port offset from the center of hole	250
R_B	Hole radius in bottom side of substrate	40
R_T	Hole radius in top side of substrate	50
W_{SIWC}	Cavity SIW width	1470
W_{SIWM}	Main SIW width	820
W_{SIWP}	Port SIW width	400
W_{slot}	Slot width	65
W_{slotM}	Main slot width	60
W_{slotT}	Width of transition slot	55
W_{strip}	Strip width	60
W_{stripM}	Main Strip width	35

3.3.2 Experiments issues and validation

The next and important part of the fabrication is related to the microwave section of the proposed modulator. In Figure 3.8, the fabricated device is illustrated and one of the ports for the measurement by probing-station is zoomed in this figure.

In the first step of the fabrication, the pattern of SIW holes was drilled by using a micromachining technique. Because of different diameters of the holes in the entrance or over the top of the substrate and the exit or bottom of the substrate, the designed structure was optimized. In the next step of the fabrication, Ti was used as adhesion prior to gold metallization by sputtering method. This adhesion layer was unavoidable because of probing-station measurement with sharp probe tips.

In Figure 3.9, microwave analysis results including the insertion and return losses of the proposed SIW-CPW amplitude modulator are illustrated. This device is optimized for 60 GHz frequency range. It should be mentioned that in our analysis, only two microwave ports, including RF input and RF output are considered. Lumped element ports of the CPW in the middle of structure were replaced by resistor pads. Good agreement between the simulation and measurement results are observed.

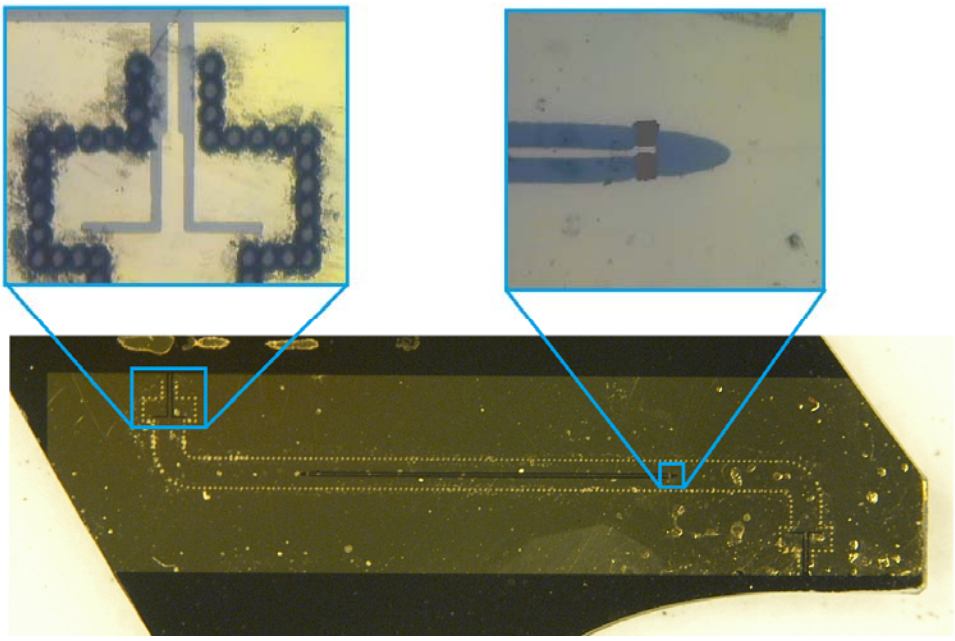

Figure 3.8: Fabricated circuit for the microwave part of SIW-CPW modulator on $LiNbO_3$; SIW holes and resistor pads are shown.

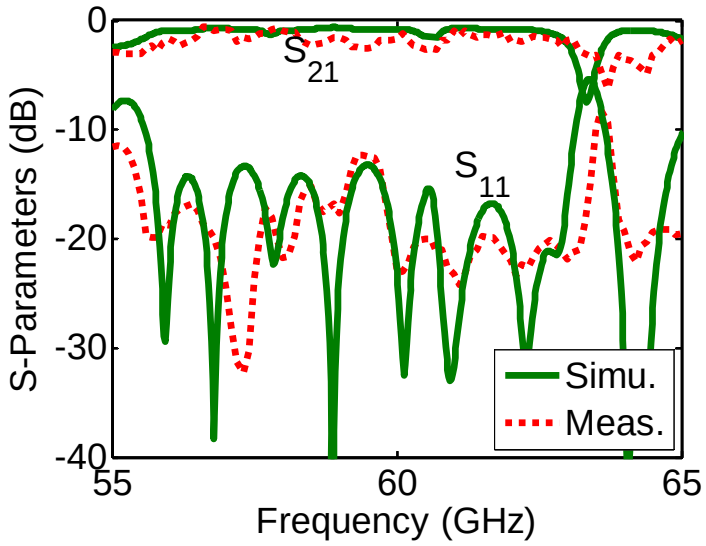

Figure 3.9: Simulated and measured insertion and return losses of SIW-CPW amplitude modulator.

3.4 Optical waveguide

In this section, two different electro-optical materials are considered for the optical part design of the new SIW-CPW modulator. The first material is $LiNbO_3$ which is the commonly used material for the electro-optical devices and the second with the electro-optical coefficient about three times higher than $LiNbO_3$ is called calcium barium niobate (CBN). For the $LiNbO_3$ substrate, a MZ interferometer is designed for the structure shown in Figure 3.1. For the thin-film CBN, a new configuration is designed and analyzed before investigating the MZ structure. Fabrication of these optical waveguides and measurement results are discussed in the experimental part of this section.

3.4.1 Theoretical discussion

For the MZ interferometer in $LiNbO_3$ substrate, just a brief review is presented and followed by a specific design. According to Figure 3.10, angle φ and length L_B of the Y-branch, distance D_A and length L_A of the arms, width W_o and depth T_o of the optical waveguide are considered as design parameters.

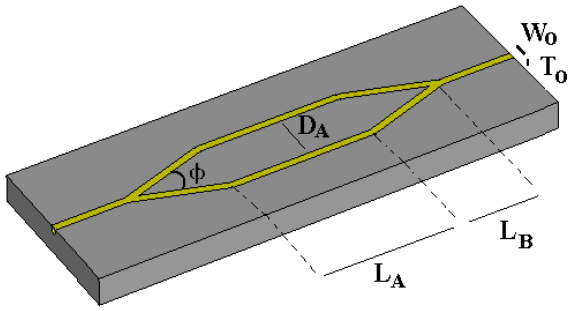

Figure 3.10: MZ interferometer in $LiNbO_3$ substrate and design parameters.

To design the MZ interferometer, dimensions of CPW obtained from the coupling design of the SIW-CPW modulator can be used to find L_A and D_A. The length of the MZ arms can be obtained by

$$L_A = 2L_C \qquad 3.7$$

where L_c is the SIW-CPW coupling length with which the maximum power is transferred from SIW to CPW.

Also, the distance between the MZ arms for the X-cut and Z-cut structures are obtained by

$$D_A \text{ (X-cut)} \sim W_{sl}/2+W_{st}+W_{sl}/2 \qquad 3.8$$

$$D_A \text{ (Z-cut)} \sim W_o/2+W_{sl}+W_o/2$$

where W_{sl} and W_{st} are CPW slot and strip width, respectively and W_o is the optical waveguide width.

Considering φ degree for the Y-branch angle, the length of the Y-branch is calculated by

$$L_B = D_A / (2\tan(\varphi/2)) \qquad 3.9$$

In Figure 3.11a, mode propagation of the MZ optical waveguide with steps of *2 mm* is shown. The optical waveguide is divided into two parts and at the end of MZ arms, the optical signals are recombined together. By changing the parameters such as angle, length, width and depth of the MZ waveguide, the power of optical transmission would be changed.

Figure 3.11b illustrates the optical field before the Y-branch and Figure 3.11c shows the optical field in the middle of structure. Distribution of the optical field can be used to obtain the overlap integral of the proposed optical modulator.

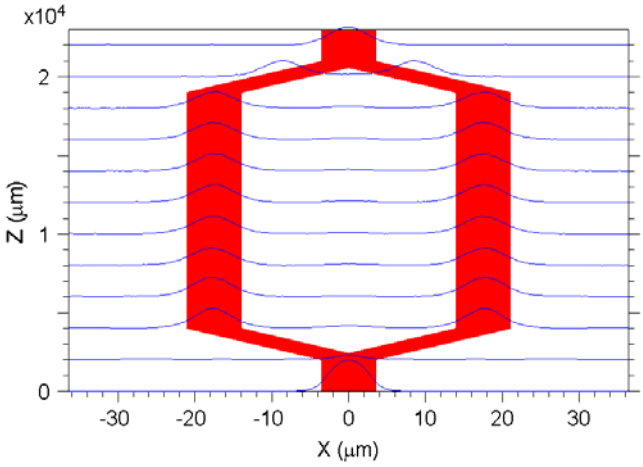

(a)

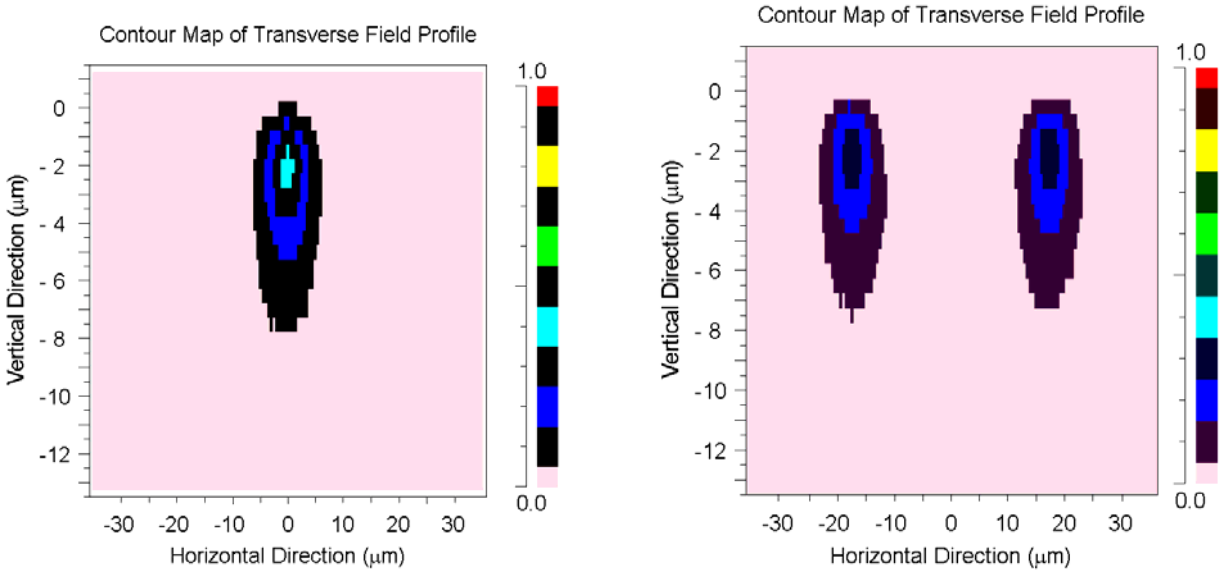

(b) (c)

Figure 3.11: a) Mode propagation of MZ optical waveguide; and cross-section of the normalized optical field in MZ optical waveguide, b) input look of the optical waveguide, c) middle section of the optical waveguide.

Obtaining the optical field distribution is the last step of the optical waveguide design. In Figure 3.12, optical fields are plotted for different values of Y-splitter angle and optical waveguide width. According to the figures, the maximum optical power transfer happens from the MZ interferometer by 1.2 degree of Y-splitter and 10 µm of optical waveguide width.

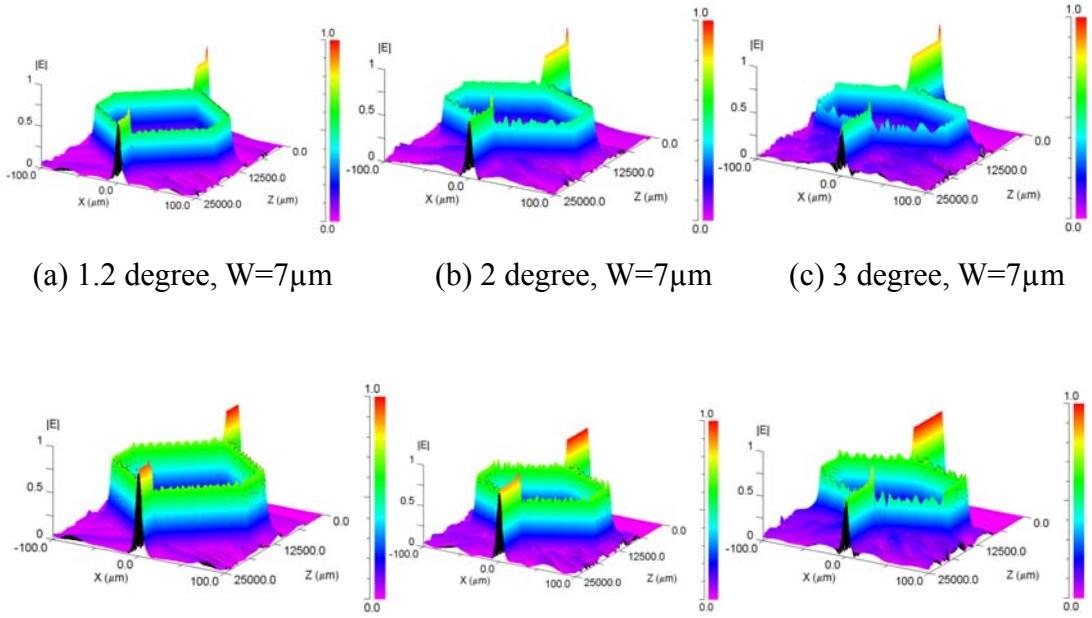

(a) 1.2 degree, W=7μm (b) 2 degree, W=7μm (c) 3 degree, W=7μm

(e) 1.2 degree, W=10μm (f) 2 degree, W=10μm (g) 3 degree, W=10μm

Figure 3.12: Optical field in MZ optical waveguides versus optical waveguide width and Y-splitter angle. Optical waveguide depth is 3 μm.

In Table 3.2, the design parameters for the optical waveguide of the newly proposed modulator are summarized.

Table 3.2: Design parameters for the optical waveguide of the newly proposed SIW-CPW modulator.

Symbol	Quantity	Value
λ_0	Optical Wavelength	1.55(μm)
n_e	Extra ordinary refractive index of $LiNbO_3$	2.14
n_o	Ordinary refractive index of $LiNbO_3$	2.21
L_A	length of MZ arms	1.5 (cm)
D_A	Distance between the MZ arms	35 (μm)
L_B	length of Y-branch	2 (mm)
W_o	Width of optical waveguide	7 (μm)
D_o	Depth of optical waveguide	3 (μm)

Another electro-optical material of interest which can be used in the design and fabrication of electro-optical modulators is CBN. The thin-film CBN can be grown on Si or silicon dioxide (SiO_2) to create optical waveguides. The electro-optical coefficient of CBN is about three times higher than that of $LiNbO_3$ so the half-wave voltages of modulators based on CBN are expected to get reduced significantly. In Figure 3.13, a proposed structure for this type of optical waveguide is presented. In Figure 3.13a, the main part of CBN for the optical waveguide is grown on the etched SiO_2. Because of some difficulty to remove CBN on Si substrate, these parts are considered in the simulation. In this figure, CBN is sandwiched between two SiO_2 layers and Si is used as a base substrate. Also, optical field distribution is obtained for the proposed CBN optical waveguide in Figure 3.13b and good confinements are observed.

Ordinary and extraordinary refractive indices for the CBN thin-film at 1550 nm are considered to be 2.09 and 2.18, respectively [67].

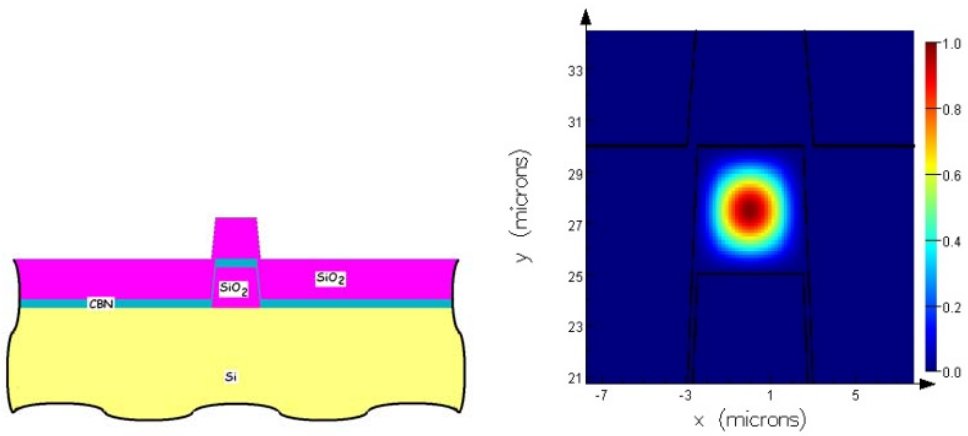

(a) (b)

Figure 3.13: a) Proposed optical waveguides using electro-optical CBN thin film, (b) Field distribution in CBN waveguide with the effective index of 2.0899.

3.4.2 Experimental issues

To complete the demonstration of the proposed electro-optical modulator, optical waveguide should be realised which may be fabricated by different techniques. Ion exchange and proton exchange, out-diffusion and in-diffusion are the common fabrication techniques to change extraordinary (n_e) and ordinary (n_o) refractive indices in the optical region.

For the ion exchange, silver/lithium ion exchange can occur in the optical waveguide regions by putting $LiNbO_3$ in silver nitrate at 360 degree Celsius for several hours. Using this fabrication method, optical loss of 6 dB/cm is obtained and only extraordinary refractive index change of 0.12 is observed.

In the proton exchange method, lithium ion is replaced by hydrogen by putting $LiNbO_3$ in benzoic acid at 120-250 ^oC. In this method both of the n_e and n_o are changed by about 0.1 and -0.05, respectively.

Using the out-diffusion technique, lithium oxide is out diffused from the optical waveguide area at high temperature (1000-1100 ^oC) and n_e is changed about 0.001.

In the in-diffusion technique, thin film (10-100nm) of Ti is deposited on the $LiNbO_3$ by a sputtering method and in-diffusion is occurred at high temperature (850-1100 ^oC). Using this technique, n_e and n_o are changed about 0.04 and 0.02, respectively.

In-diffusion technique is used for our fabrication of optical waveguide due to the change of both refractive indexes and easy fabrication. According to the simulation for different waveguide width and also the opening angle of Y-branch in MZ structure, a layout shown in Figure 3.14 was prepared.

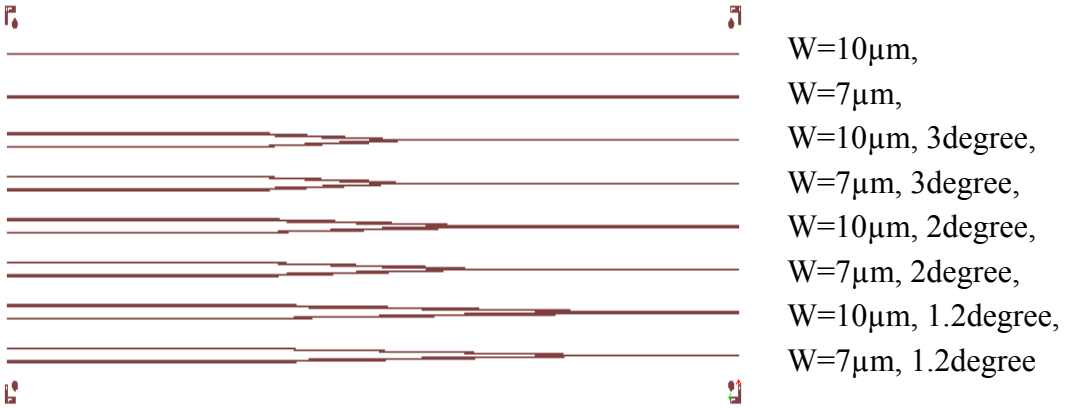

Figure 3.14: Layout of different optical waveguides using Y-branch for SIW-CPW amplitude modulator on $LiNbO_3$ substrate.

In Figure 3.15, one sample of the fabricated waveguides for the Y-branch area and launching of visible optical light and also SEM image of waveguide edge are illustrated. Figure 3.15a shows the fabricated Y-branch part of the waveguide with 3 µm width and 3 degree Y-branch angle. In Figure 3.15b, optical light is reflected from the edge of optical waveguide because of the edge roughness. In Figure 3.15c, an optical path in Y-branch is observed. SEM image of the waveguide edge roughness is shown in Figure 3.15d.

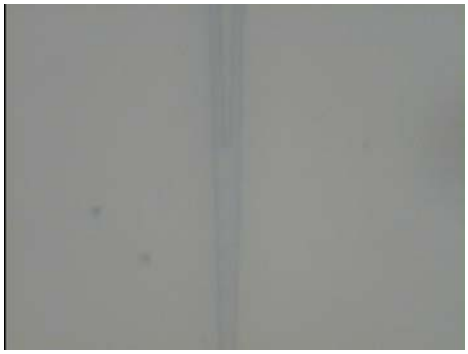

(a)

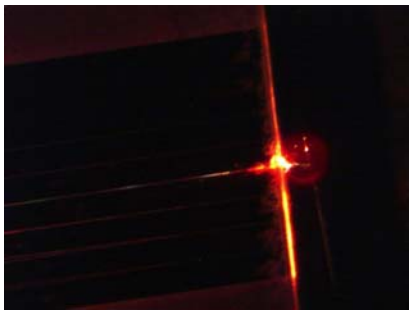

(b)

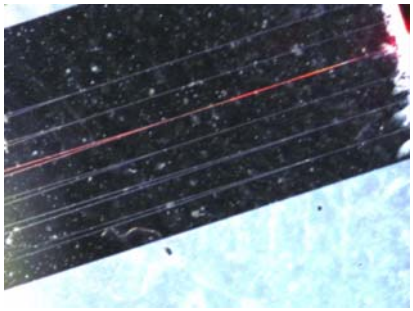

(c)

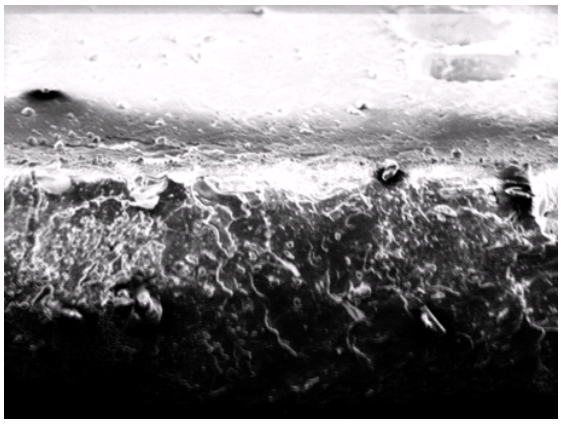

(d)

Figure 3.15: a) Y-branch part for one of the fabricated waveguides, b) reflection in the edge of waveguide for visible light illumination, c) optical path in Y-branch and d) SEM image of the waveguide edge roughness.

To minimize the reflection of optical signal, edge polishing may be done. Figure 3.16a illustrates an edge polishing machine that is used to polish the edge of $LiNbO_3$ waveguide. Using this

machine, the angle of the polishing and speed are variable and also different lapping pads may be used for the polishing process.

One of the problems to polish the edge of $LiNbO_3$ substrate is the substrate thickness which can be broken very easily. To prevent it from breaking, the substrate is sandwiches between two thick glasses which have almost the same roughness of $LiNbO_3$. Water is a good adhesion to prevent the substrate movement. Different diamond pads or Lapping films (30, 6, 1 and 0.1 μm) with different time periods were used for the polishing.

SEM image of the edge of substrate after polishing is shown in Figure 3.16b. According to this figure and compared it with the figure before polishing, removing the edge roughness is completely obvious.

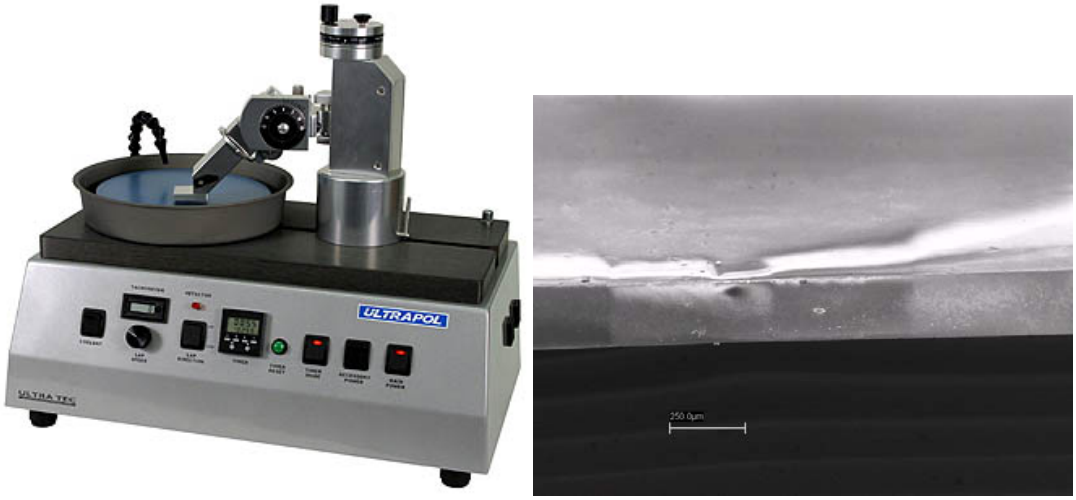

(a) (b)

Figure 3.16: a) Edge polishing machine from Ultrapol Company and b) edge of $LiNbO_3$ substrate for optical waveguide after polishing.

Launching an invisible optical signal at 1550 nm and preparing the measurement setup are the next step of the optical waveguide realisation. In Figure 3.17, measurement setup, fibre to Ti:$LiNbO_3$ waveguide connections and results are shown. Figure 3.17b shows the optical fiber to the input of the waveguide and Figure 3.17c shows one optical line from the Y-branch at the output side to optical fiber using the matching oil. In this setup, the optical output power comes from one branch of the 3-dB splitter, should be 3-dB less than the input optical power in the ideal

case without any optical loss in the Ti:$LiNbO_3$ waveguide. To improve the results of optical loss, considerations such as polishing about 200 μm of the edge of waveguide to remove the laser cutting effects and also polishing the fiber edges were carried out.

Fabrication of the thin-film CBN with a high electro-optical coefficient has been done as illustrated in Figure 3.18. SEM images of different types of the optical waveguides with different values of width are illustrated in Figure 3.18b and Figure 3.18c. These thin-film CBN waveguides have been covered by another SiO_2 layer on top as they are designed in the theoretical sections.

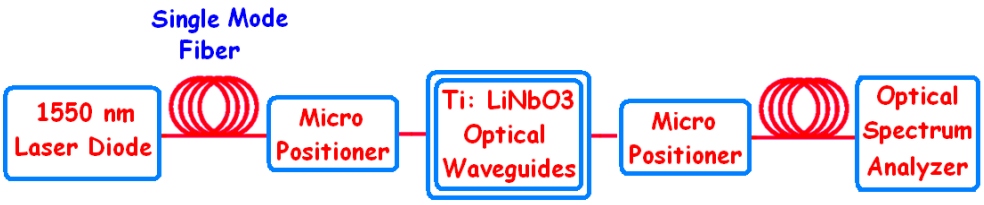

(a)

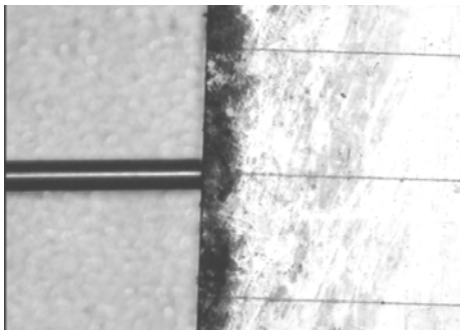

(b)

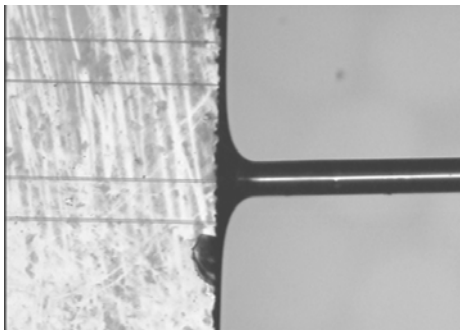

(c)

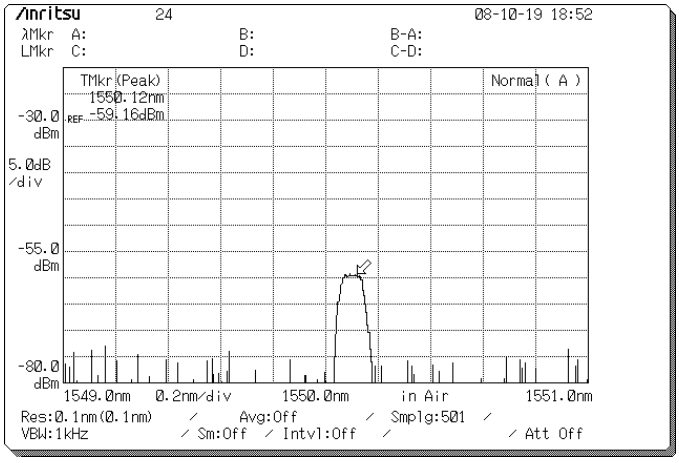

(d)

Figure 3.17: Optical loss measurement of fiber to Ti:$LiNbO_3$ waveguide to fiber, a) Measurement setups, b) fiber to waveguide connection, c) waveguide to fiber connection using matching oil, and d) output of spectrum analyzer.

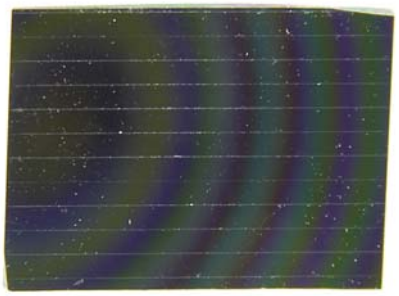

(a)

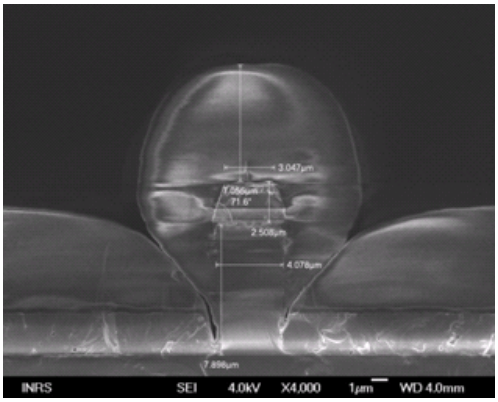

(b)

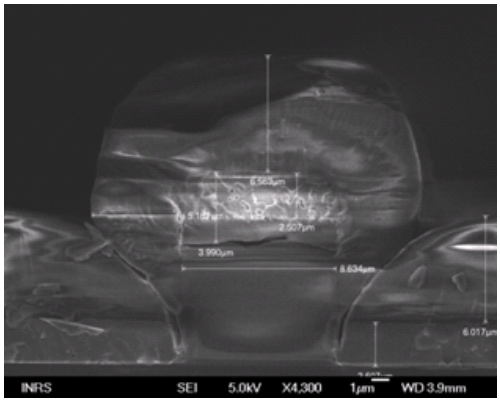

(c)

Figure 3.18: a) Fabricated thin-film CBN optical waveguides and SEM images of the waveguides with b) 4 μm width, 2.5 μm thickness and c) 8 μm width, 2.5 μm thickness.

In Figure 3.19a, the measurement setup for the CBN optical waveguide is shown. Using this setup, a good alignment for the position of the optical waveguides can be stablished and also the field intensity could be obtained. In Figure 3.19, optical fiber connection to one side of the fabricated waveguide after the edge polishing is shown. On the output side, the optical signal could be detected after confinement by a lens. In Figure 3.19c and Figure 3.19d, the field intensity of the CBN waveguide for 5 μm and 10 μm width waveguides are shown. As it is shown in the figure, the wide waveguide is concerned with the multimode waveguide. Optical loss less than 3.44 dB/cm was measured for this new optical waveguides. Although the loss of fabricated optical waveguides in conventional $LiNbO_3$ is less than that of CBN waveguide, it can be improved by optimization of the fabrication parameters of the new CBN waveguide.

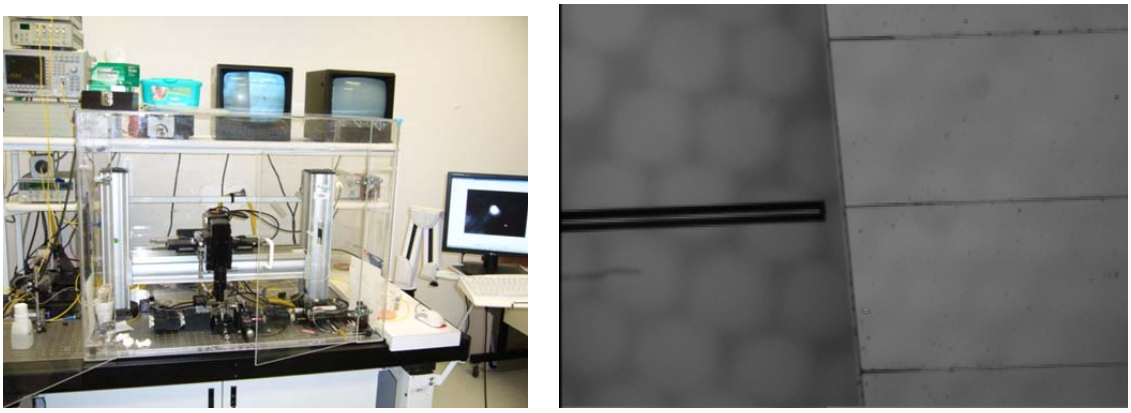

(a) (b)

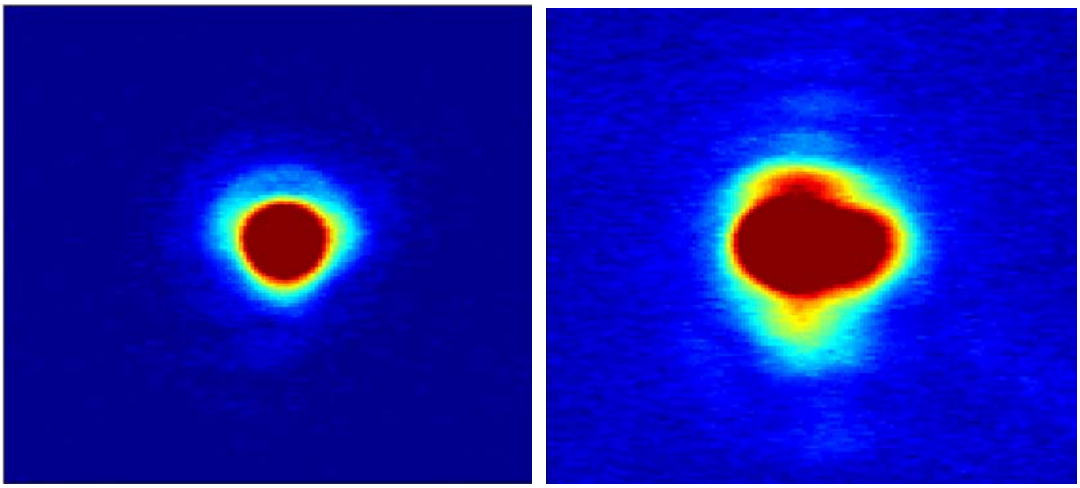

(c) (d)

Figure 3.19: a) Measurement setup for the CBN waveguide, b) fiber to waveguide connection, and field intensity of optical waveguides with c) 5 µm width and d) 10 µm width.

3.5 Conclusion

In this chapter, a newly proposed SIW-CPW amplitude modulator has been presented and studied. By changing the structure of conventional CPW modulators, we can apply microwave coupling from low-loss SIW to CPW for the modulation purpose. In this new 60 GHz band-pass modulator, the overlap integral becomes variable along the structure and maximized in the

middle of the device. In this proposed SIW-CPW modulator, the advantages of achieving a high overlap integral in CPW in addition to the advantages of low-loss SIW have been deployed.

For the microwave analysis of the new structure, mode coupling mechanism between CPW and SIW has been discussed on $LiNbO_3$ substrate at 60 GHz. Broadband transition of CPW to SIW has been designed with cavity resonators. Also, the bending structure for the SIW part has been considered to separate optical and microwave ports. Optical analysis of the device has been centered on MZ interferometer and new thin-film CBN waveguide. Different optical waveguides have been designed and optimized. Fabrication of the microwave and optical parts has been carried out by using $LiNbO_3$ substrate for MZ waveguide and Si substrate for CBN thin-film waveguide. Measurements of the optical and microwave parts have been done by a setup with Micropositioner on optical table and probing station, respectively.

CHAPTER 4. SURFACE-TYPE PHOTODETECTOR FOR THZ SOURCE GENERATION

4.1 Introduction

In this chapter, a surface-type of integrated THz source generators is studied, designed and realised. Our focus is especially on the photomixer of the THz generator. Also, the design of THz antenna could be studied because of its full integration with the photomixer. A review of the fabricated THz source generators was presented in [68].

Figure 4.1 shows different sections of possible structures for the design of integrated high power broadband THz generators. Two parts including photomixer and antenna are specified and should be integrated. Pulse laser, usually Femtosecond laser, and dual wavelength laser diode are used as optical sources for the photomixer.

In the design of the photomixer, surface-type illumination photodetector is considered in this chapter and edge-type illumination TWPD is studied in the following chapter. Our important advantage of using such a surface-type photomixer is related to its simplicity in design and fabrication process while the disadvantage is low-power THz generation because of the small area of the photo-detection section.

In the antenna design of the THz generator, different structures may be used. According to the conventional structures, spiral, log-period, dipole, slot and bow-tie antennas can be integrated with the surface-type photomixers and up to few THz can be handled using these broadband antennas. Our design and fabrication for the antenna in this chapter is concentrated on the spiral antenna because of its large bandwidth and simplicity of the design and fabrication. Silicon lens may be attached under the substrate to confine the radiated THz signal. Because of the integrated structure, DC bias pad and filter for the photomixer are considered after the antenna. DC bias is needed for the active component of the photomixer, and low pass filter can be used to separate THz signal and DC bias.

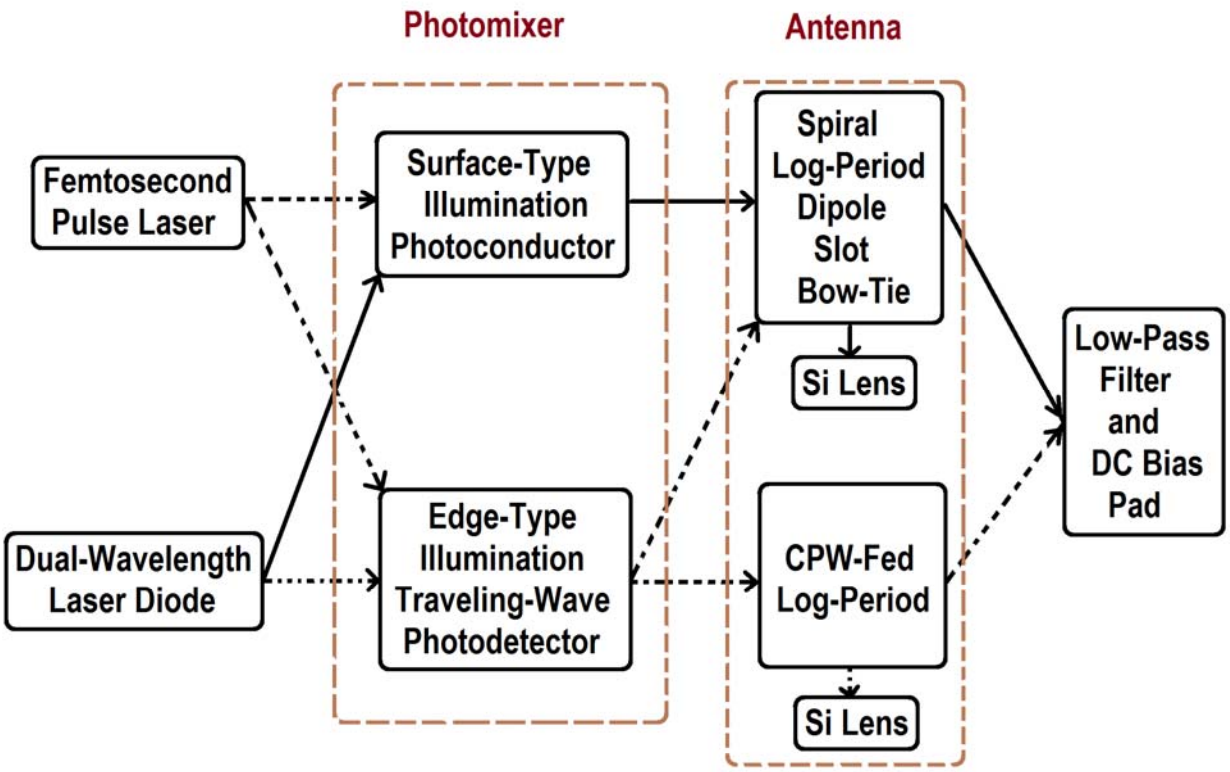

Figure 4.1: Surface-type illuminated photomixer and spiral antenna in different structures for THz source generator.

In this chapter, the structure using the surface-type photomixer and spiral antenna is designed at first and then experimental results are presented.

4.2 Theoretical discussions

The surface-type photoconductive photomixer and spiral antenna have been integrated for THz generation using two laser diodes, where they have fixed wavelength or they are tunable, with GaAs substrate [69]-[72] and InP substrate [73]-[74], which is compatible with 1550 nm optical communication systems. Also, using a dual wavelength laser diode, the photomixer antenna and laser diode could be integrated.

A surface-type photoconductive photomixer and spiral antenna is shown in Figure 4.2. A thin layer (about 2 μm) of indium gallium arsenide (InGaAs) is grown on InP substrate and a small

square part is etched for the detection purpose. Some interdigitated electrodes are used to increase the efficiency of the photoconductive section. This photoconductive photomixer is connected to the spiral antenna and DC bias pads. Optical signal from a dual wavelength laser diode or two different laser sources which are combined by optical coupler is illuminating on photoconductive area. On the back side of InP substrate, the THz radiation is confined by a Si lens. The InP substrate can be considered in all of the design and fabrication process because of the use of optical wavelength of 1550 nm. Circuit modeling of the THz generation including the resistor R_A for the antenna and capacitance C and resistor R_d for the photoconductive photomixer is shown in the figure. In the next sections, photoconductive photomixer and antenna are discussed in detail.

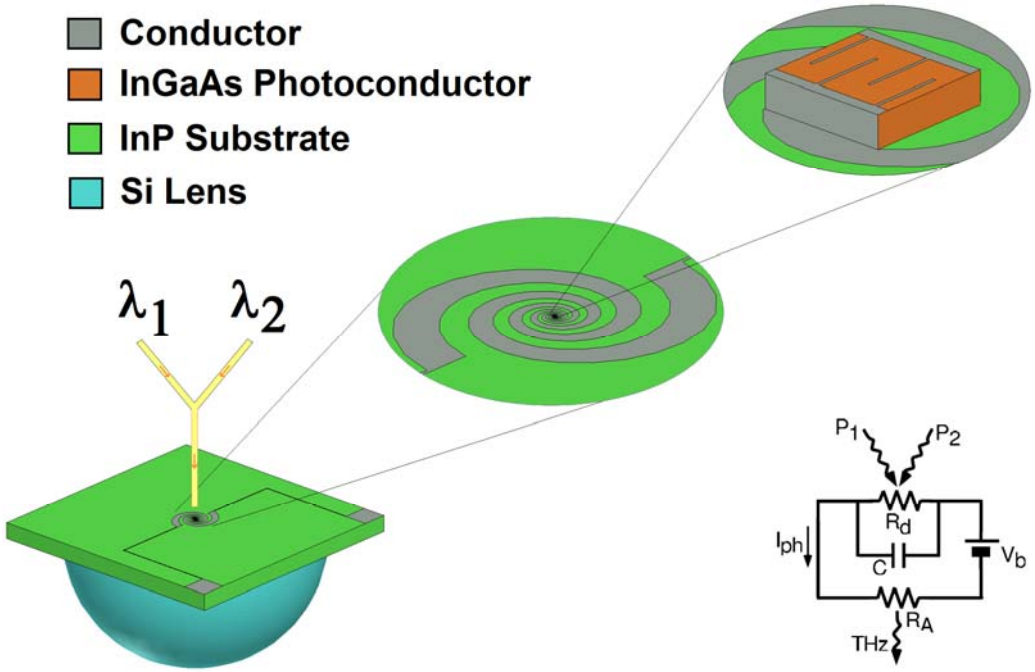

Figure 4.2: THz generation using photoconductive photomixer and spiral antenna.

4.2.1 Photoconductive photomixer

In the photomixer of a THz generator, the optical signal is converted to THz signal. The simple and commonly used device for the photomixing is a photoconductor. This photoconductor can be integrated with antenna to have THz radiation or can be connected to THz waveguides as transmission lines [75]-[76]. A thin layer of InGaAs in InP substrate can absorb optical light in

λ=1550 nm region as it is shown in Figure 4.3a. Interdigitated electrodes are used to maximize the efficiency of the photoconductor. Area of the photoconductor, number of the interdigitated fingers and their dimensions and also carrier lifetime are the parameters which determine the output photocurrent of the photomixer. These parameters are related to the growing techniques of the InGaAs layer as well as bias voltage and laser powers. Two sidewalls of the InGaAs layer are metalized for the connection of DC bias to the active photoconductor. A simple circuit model including the bias voltage, photo-resistance and capacitance of the photoconductor is illustrated in Figure 4.3b. Input photons from the laser are detected. Then generated photocurrent is transferred to the antenna for radiation. The illuminated laser powers are shown by P_1 and P_2.

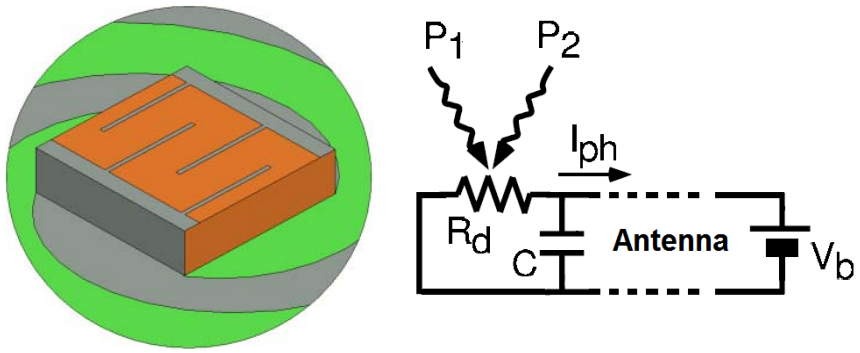

(a) (b)

Figure 4.3: a) InGaAs photomixer on InP substrate with interdigitated electrodes, b) circuit modeling of the photoconductor including resistance, capacitance and bias voltage.

To analyze the photomixer of the THz generator to investigate the effect of different parameters, capacitor and photo-resistor versus the dimensions of the photoconductor and material specifications should be calculated.

Photoconductance ($G_0=1/R_d$) of the device can be given by [77]

$$G_0 = \frac{\eta T_p \tau_{eh} q N_g^2 (\mu_e + \mu_h)}{hf (N_e W_e + N_g W_g)^2} P_0 \qquad 4.1$$

where η is internal quantum efficiency, T_p is the power transmissivity at the top air-InGaAs interface, N_g, W_g, N_e and W_e are number of gaps, gap width, number of electrodes and electrode

width in the interdigitated capacitance, respectively. P_0 is the total optical power averaged over a long time period, μ_e and μ_h are electron and hole mobilities, respectively.

Photoconductive capacitor is another element in the circuit model of the photoconductor and this capacitance is given by [69]

$$C \approx \frac{\pi(1+\varepsilon)\varepsilon_0 A}{2(W_g + W_e)Ln\left[2(1+\sqrt{\kappa})/(1-\sqrt{\kappa})\right]} \qquad 4.2$$

where A is photoconductance area and κ is obtained by

$$\kappa = \sqrt{1 - \tan^4\left[\frac{\pi W_e}{4(W_e + W_g)}\right]} \text{ for } W_e \prec W_g \qquad 4.3$$

In Table 4.1, photoconductor capacitances for three different structures with different photoconductive area and different dimensions of the interdigitated electrodes are presented. The minimum size of the electrodes is limited by the fabrication process. Also, mesa area is considered to be 2 μm wide in each side of the finger area because of the etching process.

Table 4.1: Photoconductive capacitance and dimensions for three different structures.

Parameter	N_g=2, W_g=2(µm) N_e=3, W_e=1(µm) 	N_g=4, W_g=2(µm) N_e=5, W_e=1.6(µm) 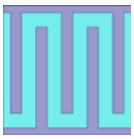	N_g=8, W_g=2(µm) N_e=9, W_e=2(µm) 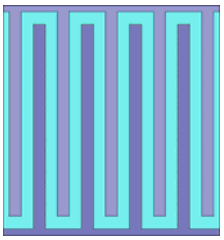
C (fF)	0.38	1.95	8.57
R_AC (pS)	0.027	0.14	0.62
$N_g.W_g+N_e.W_e$ (µm)	7	16	34
Finger area (µm^2)	9×9	18×18	36×36
Mesa area (µm^2)	13×13	22×22	40×40

To ensure a good connection between the fingers and antenna, the total dimension of finger area is considered more than the summation of gap and electrode widths. In this table, resistance of the spiral antenna is 72.8 Ω for InP substrate.

To obtain photocurrent variations versus the optical power and bias voltage in different structures, design parameters are presented in Table 4.2. As it is shown in this table, a thin Ti layer is used as an adhesion under the Gold layer.

Table 4.2: Photoconductor design parameters.

Parameter	Value
electron mobility (μ_e)	0.2 (m^2/V.S)
hole mobility (μ_h)	0.045 (m^2/V.S)
InP dielectric constant	12.4
Ti thickness	0.02 (μm)
Gold thickness	0.35 (μm)
Internal quantum efficiency (η_i)	0.68
Power transmissivity at top air-InGaAs interface (T_p)	0.59

Figure 4.4 shows the photocurrent of the photomixer ($I_{ph}=G_0 \times V_{bias}$) versus bias voltage as functions of photoconductive carrier lifetime and optical power. The photocurrent is increased by bias voltage and the maximum values of the photocurrent are obtained with the high values of the carrier lifetime and optical power. It should be mentioned that although maximum power is obtained with high value of the carrier lifetime but it may reduce THz bandwidth. For the validation of the simulated results, measurement results from [78] are plotted and a good agreement between our simulation and the measurement is observed.

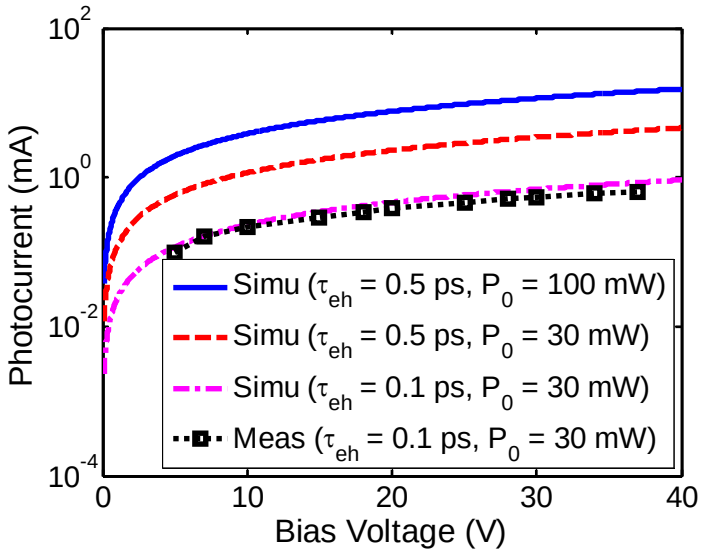

Figure 4.4: Photocurrent of the photomixer versus bias voltage as functions of optical power and carrier lifetime.

Following the analysis of the surface-type photomixer, this device should be integrated with spiral antenna for THz generation.

4.2.2 Spiral antenna

Spiral antenna is chosen for our structure because of its broadband radiation and simple integration with photoconductor. In Figure 4.5, spiral antenna with and without metallic package and its typical radiation pattern are illustrated. Figure 4.5a shows the 3D view of the spiral antenna on InP substrate. Because of the small size of the circuit and also for the DC bias connection using a standard package, a metallic part is designed around the InP and shown in Figure 4.5b. Also, in the middle of the antenna, a square feeding port for photomixer area is observed in Figure 4.5c. Radiation pattern from the backside of InP substrate is illustrated in Figure 4.5d. For the design of the spiral antenna, the number of spiral turns, size of optical feeding port, substrate thickness and growing rate of the spiral are considered as antenna design parameters.

Radiation resistance of the spiral antenna is given by [69]

$$R_A = \frac{60\pi}{\sqrt{\varepsilon_{eff}}} \quad \text{and} \quad \varepsilon_{eff} = \frac{1+\varepsilon}{2} \tag{4.4}$$

where ε_{eff} is the effective dielectric constant. For the InP substrate with ε=12.4, radiation resistance is obtained 72.8 Ω. Self-complementary spiral in cylindrical coordinates is given by the following equation

$$r = r_0 \exp(a.\phi) \tag{4.5}$$

where r_0 is the inner radius of the spiral for $\varphi=0$ and a is growing rate of the spiral.

In the design and parametric analysis of the spiral antenna, value r_0 can be obtained according to the size of optical beam and is related to the maximum operational frequency of the THz generator by

$$r_0 = \frac{\lambda}{4} = \frac{c}{4 f_{\max} \sqrt{\varepsilon_{eff}}} = 4\mu m \tag{4.6}$$

Let us consider 4.5 μm, 9 μm and 18 μm for value r_0, the maximum frequencies for InP substrate are obtained 6.4 THz, 3.2 THz and 1.6 THz, respectively. To increase the maximum operational frequency, the optical beam should be focused by lens in a small area of the photoconductor.

The variation of φ in the spiral antenna is used to specify the number of turns. For the spiral with n turns, we have $0 \le \phi \le 2\pi n$. On the other hand, the variation of a is related to the outer radius of the spiral and it is used to specify lower frequency range. Increasing the values of growing rate leads to the reduction of minimum operational frequency. For three different structures with the inner radius of (4.5, 9, 18 μm) and growing rate of (0.2, 0.18, 0.18) and spiral turn number of (4, 4, 3.25), the outer radius is (685, 829, 710 μm), respectively. These values of the outer radius specify the minimum frequency of 42 GHz, 35 GHz and 40 GHz, respectively.

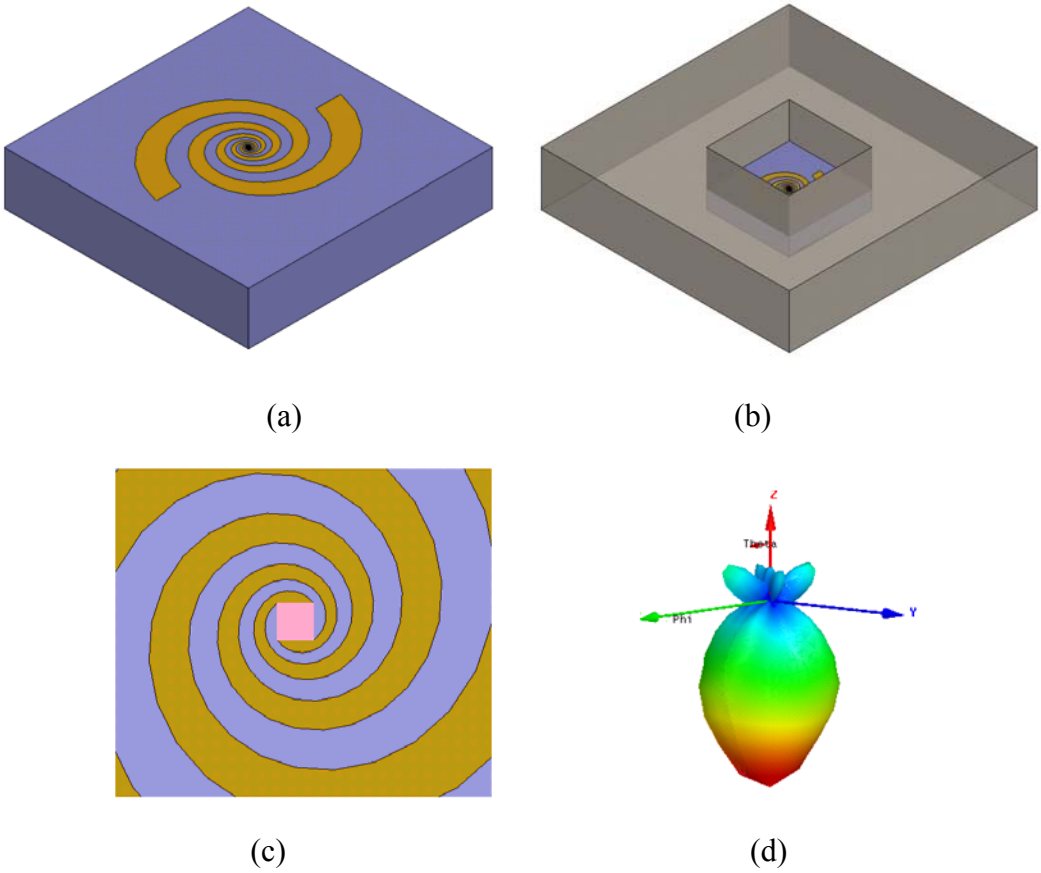

Figure 4.5: a) 3D view of spiral antenna in InP substrate, b) packaging of the circuit, c) top view and excitation port by optical signal, d) radiation pattern from the back of substrate.

In Figure 4.6, radiation pattern of the spiral antenna at 100 GHz and return loss up to one THz in InP substrate are shown. The radiation patterns are obtained for two structures, one structure without any packaging part and the other structure using metallic parts as shown in Figure 4.5. Growing rate of 0.18 for 4-turn spiral antenna with the excitation windows of 18×18 μm^2 is used in the analysis of antenna. Antenna gain of more than 6 dB and return loss of less than 10 dB are obtained for the designed antenna. Because of the simulation time, Si lens that could increase the gain of antenna is not considered in the backside of substrate.

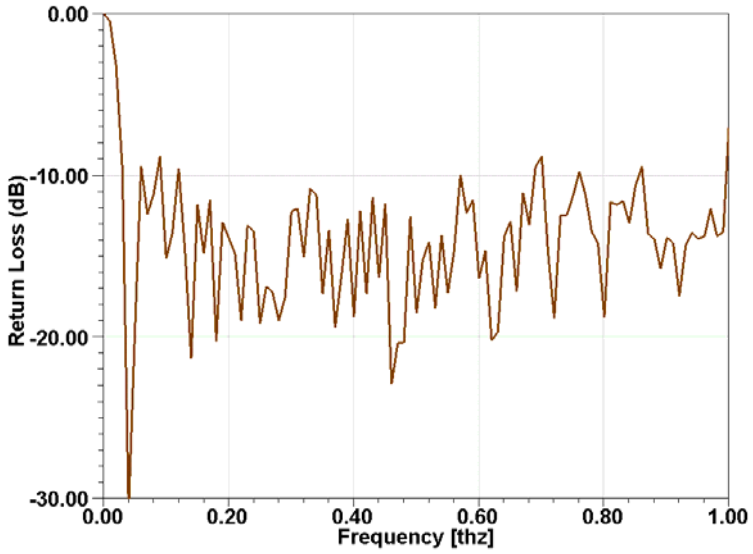

(a)

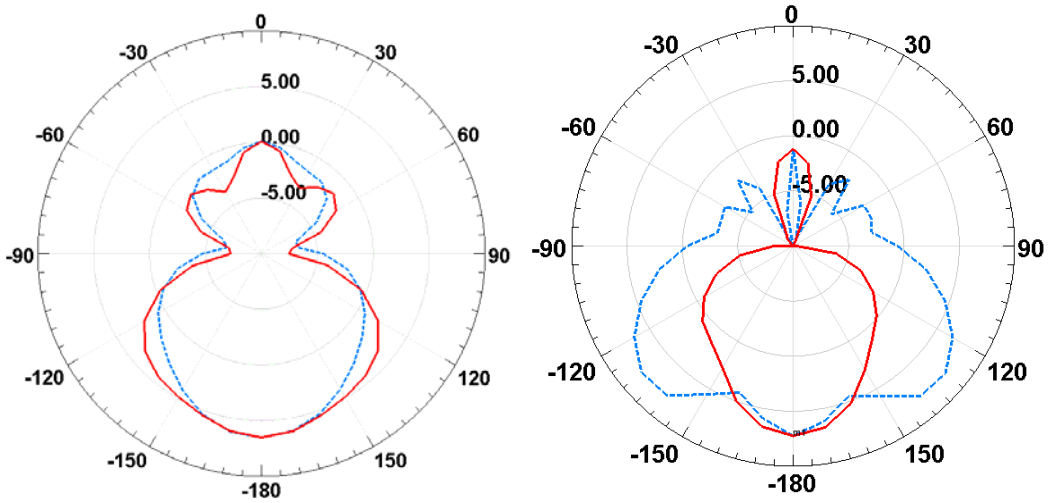

(b) (c)

Figure 4.6: 4-turn spiral antenna with growing factor of 0.18 and optical excitation part of 18×18 μm^2 in InP substrate, a) return loss, and, b) radiation pattern without package and, c) radiation pattern from packaged circuit at 100 GHz; Dashed line is φ = 90 degree and solid line for φ = 0.

After the design of the photoconductor and antenna for the THz source generator, bandwidth limitation of the structure and THz output power could be studied.

4.2.3 Bandwidth and radiation power

THz output power with the carrier lifetime limitation of the photoconductor and also RC limitation can be expressed by [68]

$$P_{THz} = \frac{I_{ph}^2 R_A}{2\left[1+(\omega\tau_{eh})^2\right]\left[1+(\omega R_A C)^2\right]} \qquad 4.7$$

where ω is angular frequency, τ_{eh} is the photoconductor carrier lifetime, R_A is the antenna resistance and I_{ph} is the generated photocurrent.

In Figure 4.7, THz output power versus frequency as functions of the photoconductive carrier lifetime and photocurrent in a given value of photoconductive capacitance that multiplies by antenna resistance is shown. In this figure, the maximum bandwidth and power are observed for high generated photocurrent and low carrier lifetime. Also, for the validation of our simulation results, the measurements from [69] are observed in the figure and a good agreement is obtained.

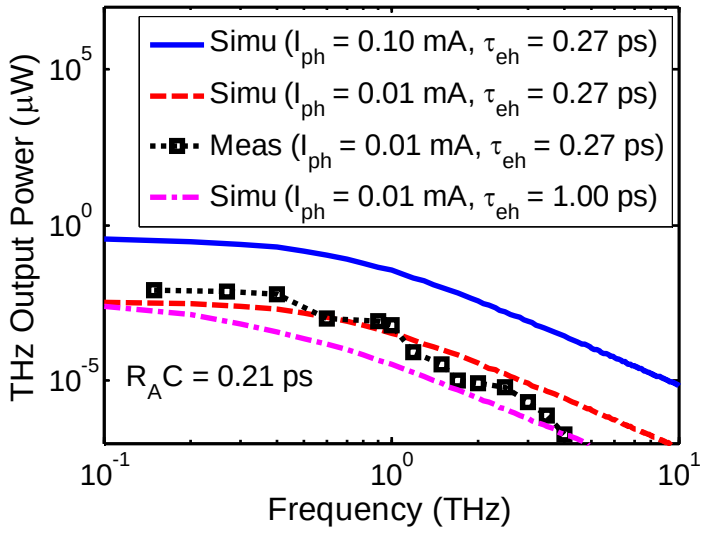

Figure 4.7: THz output power versus frequency as functions of photoconductive carrier lifetime and photocurrent.

In Figure 4.7, the photoconductive carrier lifetime is related to the fabrication process and the other parameters such as interdigitated size, bias voltage and optical power can be specified before the fabrication or during the measurements. In Figure 4.8, the effects of all parameters in

THz power and trade-off between them are observed. To generate a high THz output power, the capacitance of photoconductor and carrier life time should be reduced by the fabrication process and a proper design of the interdigitated fingers. Also, the photoconductive photocurrent should be increased. To have a high photocurrent, the optical input power and the bias voltage, as well as the carrier lifetime should be increased. Obviously, the carrier lifetime has an important role in the generation of THz output power. It can increase the photocurrent and therefore increase the THz power and on the other hand, it has a direct consequence of reducing the THz power. This challenging parameter is specified by fabrication methods.

$$P_{THz} = P_{THz}(I_{ph}, \tau_{eh}, C_j)$$

$$I_{ph} = I_{ph}(P_0, \tau_{eh}, V_{bias})$$

Figure 4.8: Effects of different parameters on THz output power.

In this section, the design and analysis of the photoconductive photomixer for 3 different structures with different photoconductive dimensions have been presented. Spiral antennas have been designed and optimized and the radiation power of the surface-type THz generator has been discussed.

4.3 Experimental issues

Following the design of the structure and the optimizing of the design parameters according to the fabrication limitations, the subsequent steps are concerned with the preparation of the related masks, fabrication, packaging and then measurements of the fabricated devices.

In the first step of the experimental part, growing 2 μm of InGaAs layer on InP substrates was carried out. These layers can be used as photoconductor in the final step of the fabrication. Among the five different samples with the InGaAs photoconductor on InP substrate, three of

them were irradiated by 1MeV proton at the dosages of 3×10^{10}, 3×10^{11}, and 3×10^{12} cm^{-2} and two other samples without irradiation. The carrier life time and bandwidth of the devices can be changed by irradiation of the samples.

Certain mesa parts should be etched from the growing InGaAs parts. Also, the interdigitated fingers on the InGaAs mesa parts as well as the spiral antenna on InP substrate should be fabricated. Therefore, a multilayer mask including the mesa, finger and spiral masks should be designed.

4.3.1 Multilayer mask

To use the maximum area of the mask, 9 circuits in 3 different dimensions are considered where the total dimension of the mask is 9×9 mm^2. To ensure the precision of the measurement results, three samples of each circuit are developed and complete circuits are fabricated by using 3 different masks.

The first mask is related to the interdigitated fingers on InGaAs photoconductive layers. In Figure 4.9, the finger mask with its alignments is shown. According to Table 4.2, three, five and nine fingers are considered for upper, middle and lower rows, respectively. The areas of the fingers are 9×9 μm^2, 18×18 μm^2 and 36×36 μm^2, from top to bottom, respectively. Some alignment marks are specified at the edge of each circuit.

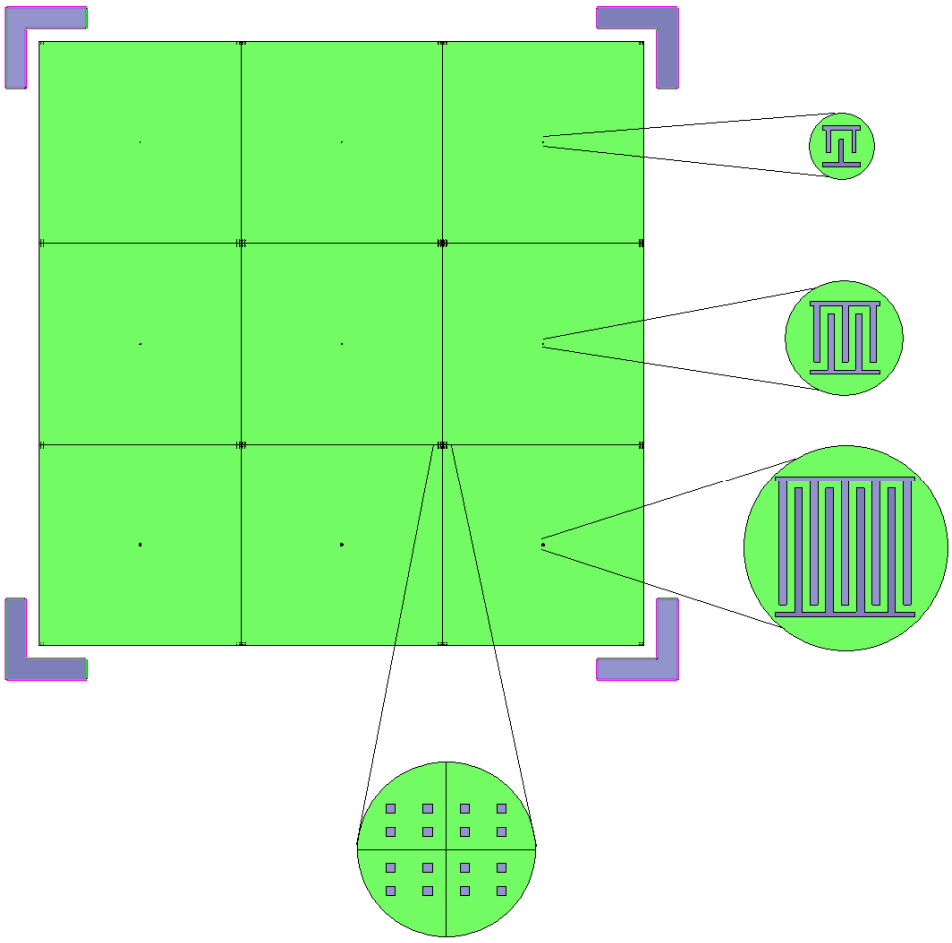

Figure 4.9: Interdigitated finger mask and alignments.

Etching process of the mesa areas is the second step of fabrication. Figure 4.10 shows the mesa mask and alignments. Compared with the finger dimensions, the mesa sizes are increased by 2 μm in all directions because of the etching process. The mesa areas are 13×13 μm^2, 22×22 μm^2 and 40×40 μm^2, for upper, middle and lower rows, respectively. We should mention that the alignments of this mask are to protect the finger mask alignments using big rectangles.

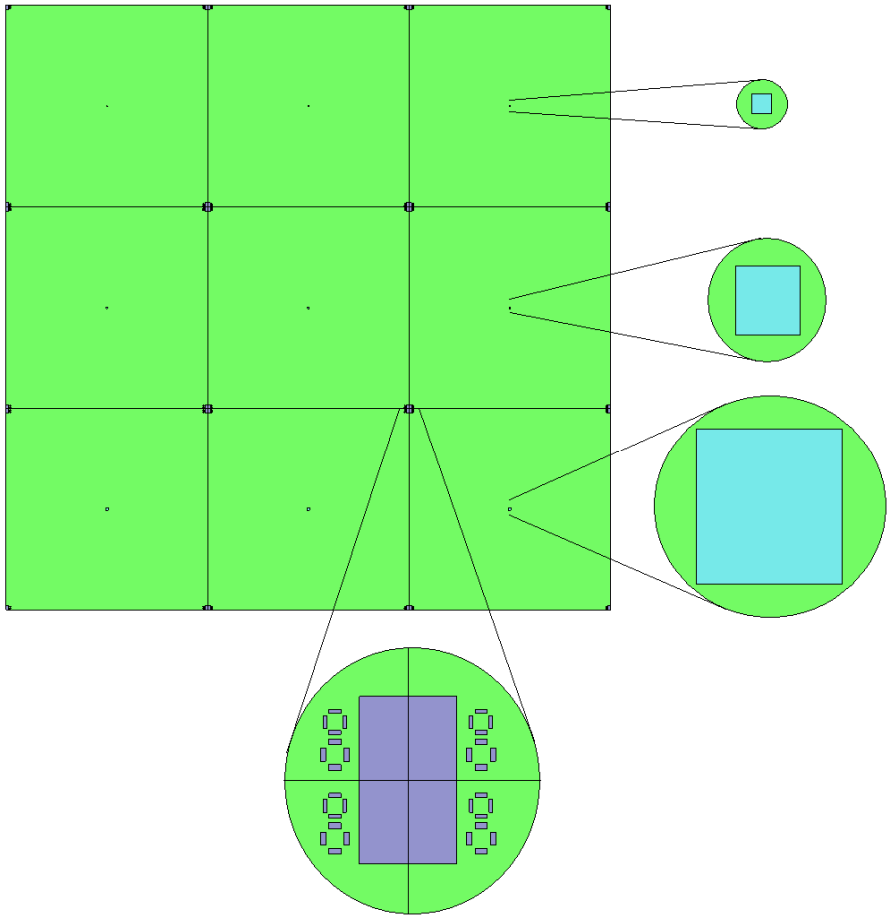

Figure 4.10: Mesa mask and alignments.

The last step is the fabrication of the spiral antenna. In Figure 4.11, the spiral mask with its alignments is shown. Photoconductive areas are considered in the middle of spiral antennas. To make sure that the photoconductors and antennas are connected together, the sizes of photoconductive area should be equal to the finger areas. In the upper row, the photoconductive area is 9×9 μm^2 with 4-turn spiral antenna using a growing factor of 0.20. In the middle row, photoconductive area is 18×18 μm^2 with 4-turn spiral antenna using growing factor of 0.18. In the lower row, the photoconductive area is 36×36 μm^2 with 3.25-turn spiral antenna using a growing factor of 0.18. The size of alignments used in the spiral mask is bigger than the alignments of the finger mask and mesa mask to protect them in the fabrication process.

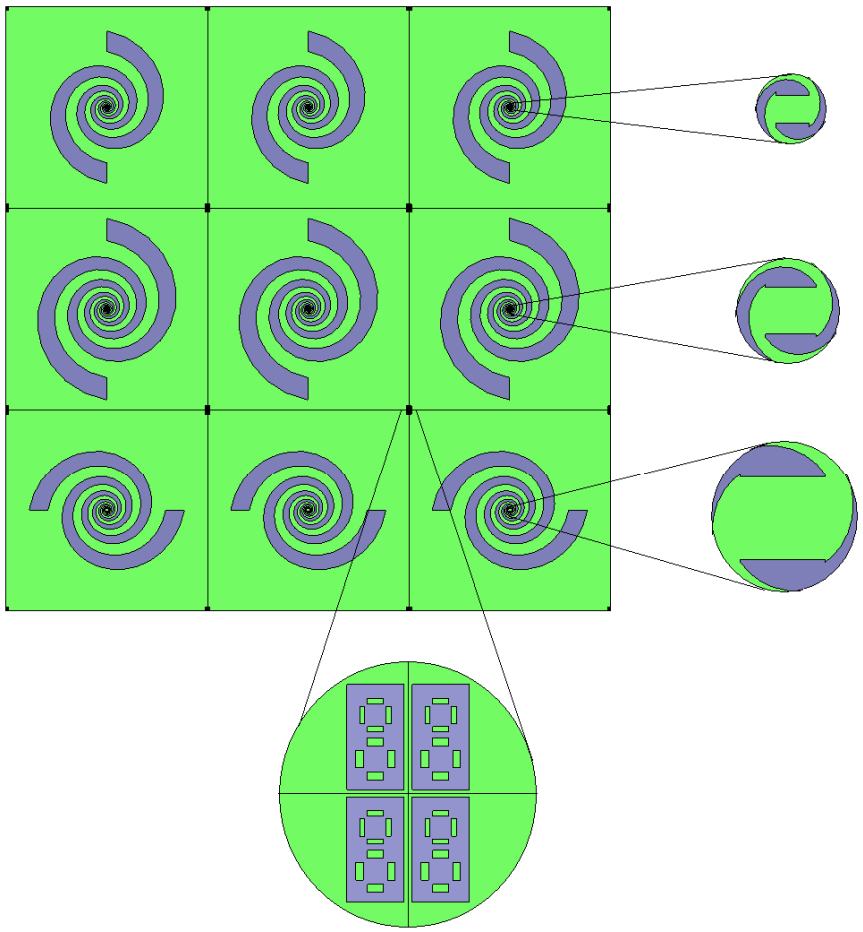

Figure 4.11: Spiral mask and alignments.

In Figure 4.12, the alignments of different masks including finger, mesa and spiral are plotted together at one edge of a circuit. After having prepared all of the masks, they are sent for fabrication by *HTA Photomask* Company.

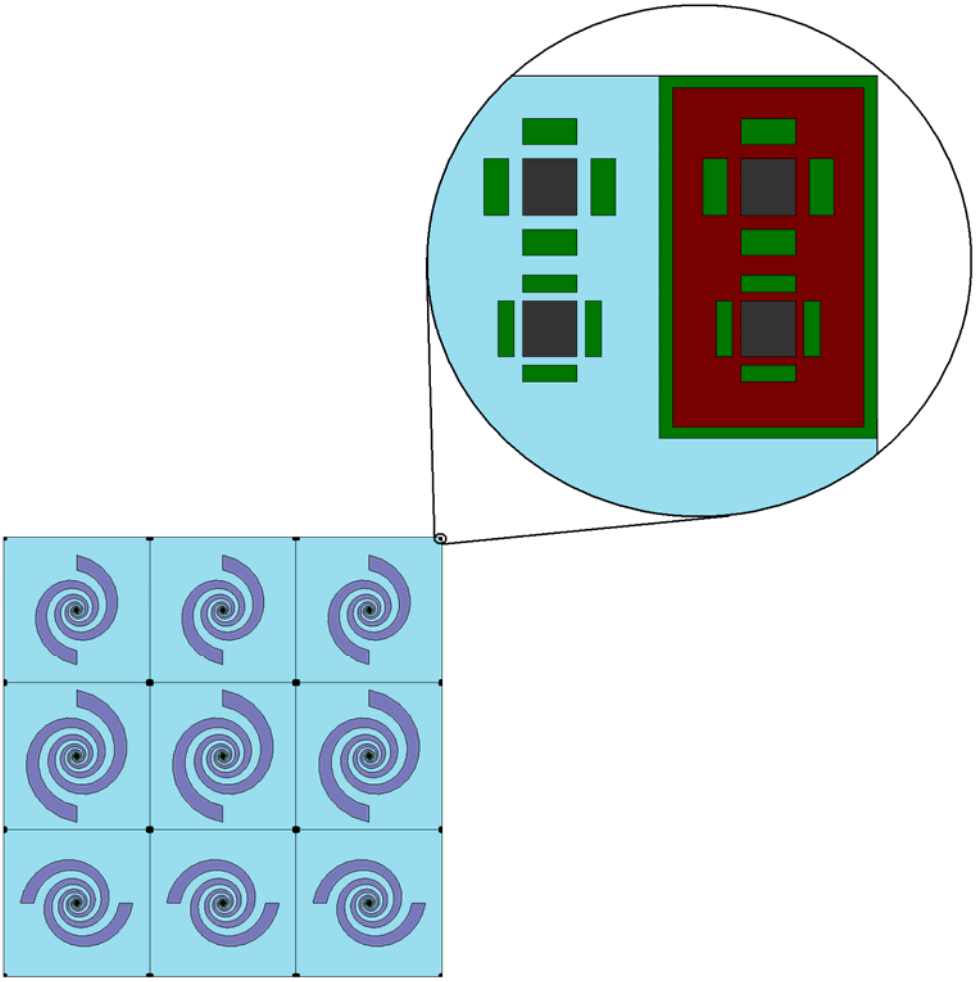

Figure 4.12: Alignments of the finger, mesa and spiral masks together.

4.3.2 Fabrication and packaging

Fabrication of the circuits was completed at National Research Council in Ottawa. Measurements on the precision of dimensions and also DC connections between the interdigitated parts can be done for the fabricated circuits. Taking high quality images from the photoconductive areas and spiral areas for the entire 45 samples (5 samples, each samples divided into 9 parts) has been done and we have numbered all of the samples according to their dosage, photomixer parameters and antenna parameters. Figure 4.13a and Figure 4.13b show the five fabricated samples and numbering of the typical sample, respectively. In Figure 4.13c and Figure 4.13d, some of the usable and damaged samples for three different designs are shown.

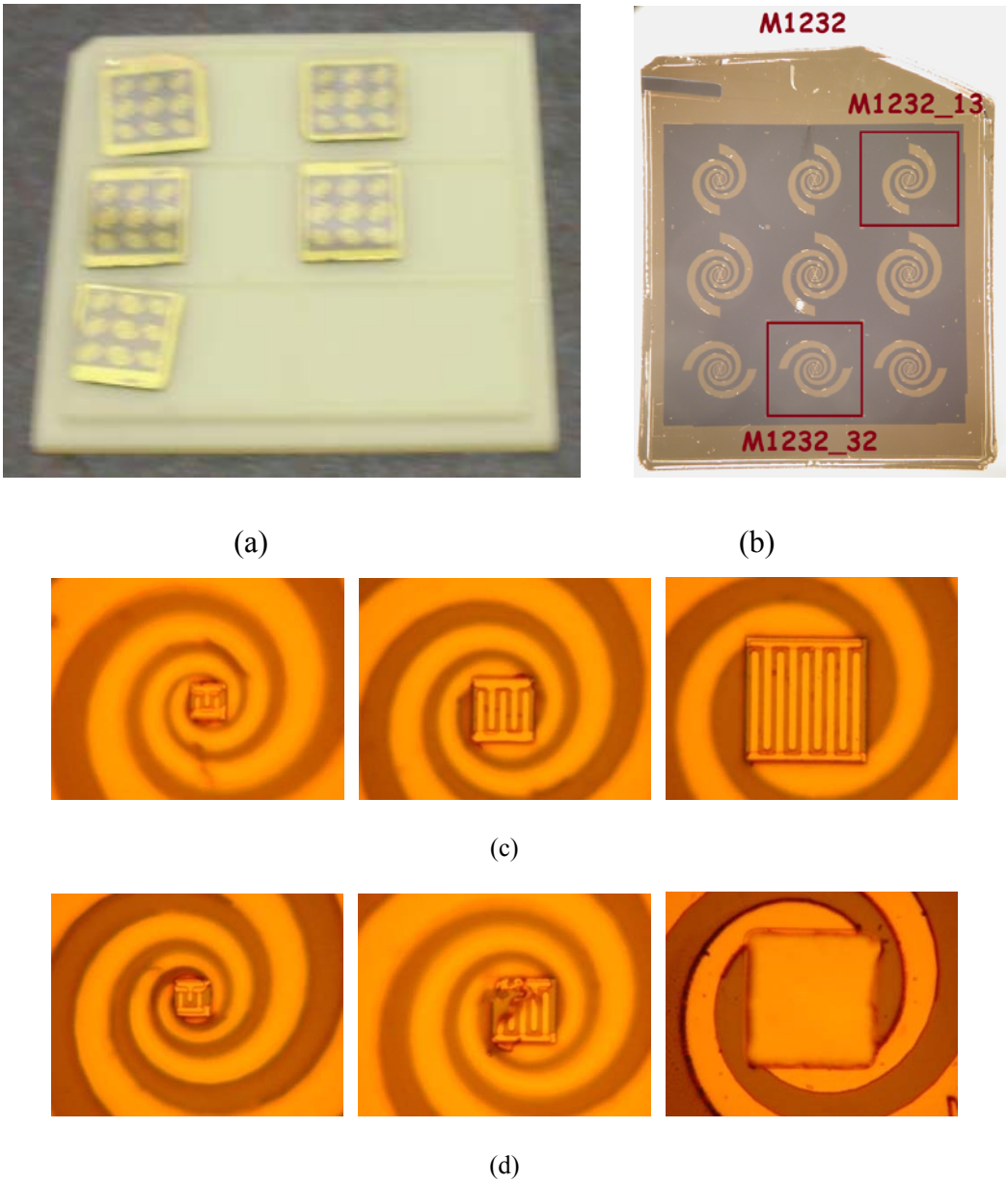

Figure 4.13: Some of the fabricated samples a) five different dosage for the samples, b) numbering of samples, c) usable samples, d) damaged samples.

Packaging of the small-sized devices (3mm by 3mm) for the measurements and wire bonding to apply the DC bias to the photoconductor are the next and important steps of the experimental task. Cleaving of the five big samples has been done to be able to install them in some standard packages. As a result of the cleaving, the samples are divided to 3 parts to put in the middle of 14-pin standard packages. Interaction between the radiations of the samples was not considerable

because of enough spaces between the circuits in the design. A slot with the dimension of 3×10 mm has been created in the standard package. The 14-pin standard package was thicker than our fabricated samples that could be at the same level of the top or bottom of the package. For the gloving of the cleaved circuits, the bottoms of circuits have been considered to be in the same level of the bottom side of the standard packages because of the minimum effect on the radiation pattern. In Figure 4.14, the packaging of a cleaved sample including 3 circuits was illustrated.

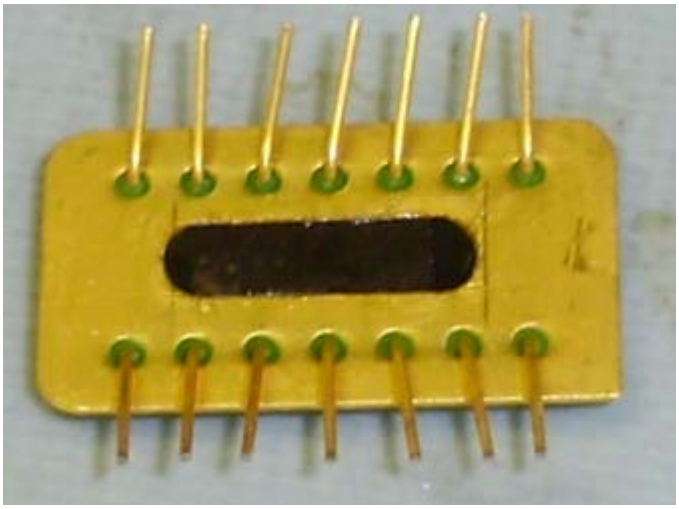

Figure 4.14: Packaging of the fabricated circuit in 14-pin standard package from the bottom.

The next step of the packaging is the wire-bonding for the DC bias connection of the photomixer. From the top side of the package as shown in Figure 4.15, the cleaved circuit and the metallic package are not in the same level and it could create some difficulty in wire bonding. As it is shown in the figure, the end of each spiral is not connected to the closest pin because of increasing the distance of the wires from the body of the package to prevent the wrong connection. Numbering of the pins for the DC bias connection of each circuit is specified in the figure.

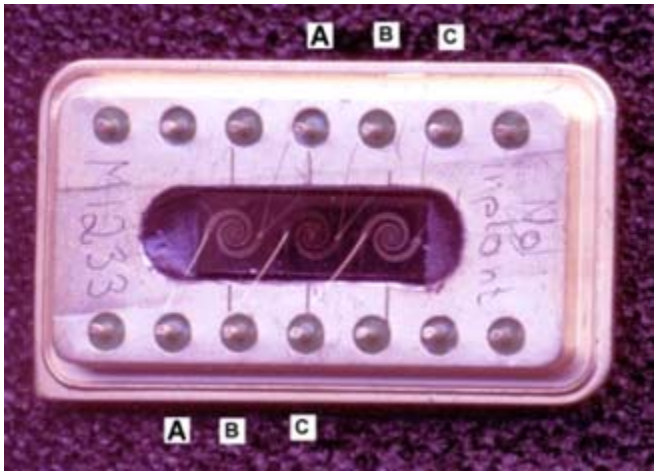

Figure 4.15: Wire bonding of the fabricated circuit from the top.

After the packaging and wire bonding of the fabricated circuits, they should be installed in a stand to connect to the optical table for the measurements. Also, the circuit should be able to be rotated for the measurements of the radiation pattern. In Figure 4.16, two stands with the metallic and plastic rotating parts are illustrated.

(a) (b)

Figure 4.16: Stands of the fabricated circuit for optical table, a) metallic rotating part and b) sample on plastic rotating part.

Now the samples are ready for the measurements of the I-V curve of the photoconductor and also the radiation pattern and power of the spiral antenna.

4.3.3 Measurements

In the first step of the measurements, we should make sure about the DC connection. Also the applied voltage and resistivity of the photoconductors should be measured. In Figure 4.17, I-V curve for the third circuits (36×36 μm^2 of the photoconductor area) of the sample *M1233*, which is a no-implantation sample, is observed. For the sample *M1233_32* and *M1233_33*, resistivity without any optical illumination is obtained about 300 Ω. Maximum applied voltage in our devices is obtained about 3 volts.

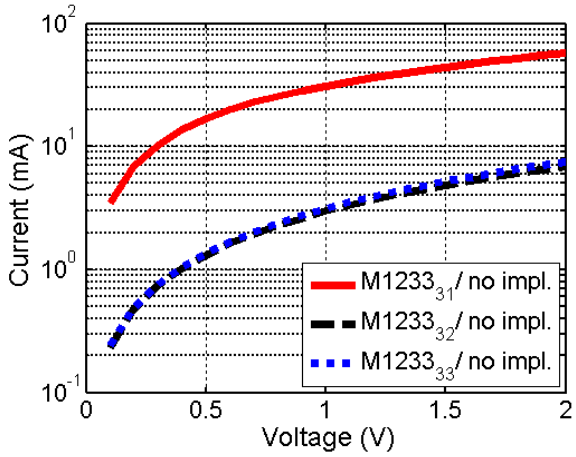

Figure 4.17: I-V curve for the samples without implantation.

Before obtaining the radiated power and pattern of our fabricated device, we should also make sure about the dual wavelength laser diode which can be used as a source for our circuits. Using the optical spectrum analyzer, spectrum of the multimode laser diode with the specific distance between the modes has been observed. The beating frequencies of this laser diode can generate microwave or THz signals at different frequencies.

In Figure 4.18, a measurement setup for 50 GHz and 100 GHz generation with the optical source and a commercial photodetector are described. Commercial photodetector used in this setup has a bandwidth of 110 GHz from *u2t Company*. To perform the measurements at 100 GHz, *W1* connector is used between the photodiode and harmonic mixer. Because we are using a 26 GHz spectrum analyzer, a harmonic mixer is utilized to down-convert the generated high frequency. The conversion losses of Agilent harmonic mixer used in the measurements are 34 dB and 42 dB for 50 GHz and 100 GHz, respectively.

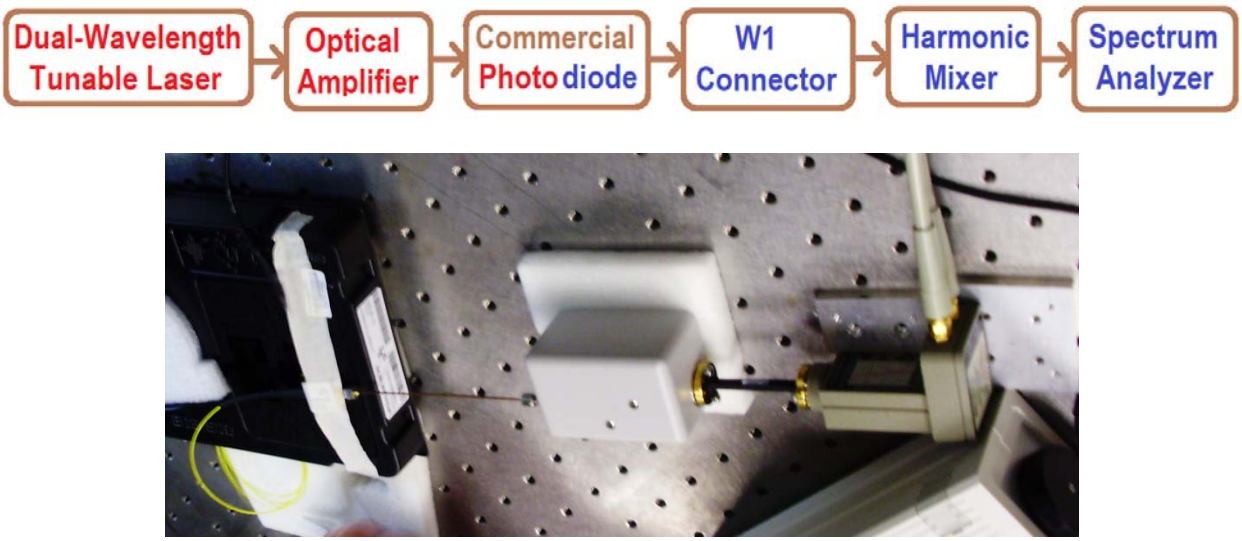

Figure 4.18: Measurement setup using commercial photodetector.

In Figure 4.19, measured signal from the electrical spectrum analyzer for the 50 GHz and 100 GHz frequency range is shown. The beating frequencies of the dual wavelength laser diode are about 45 GHz and 90 GHz with the maximum amplitude of -45 dB and -52 dB, respectively. Although the power of the laser diode is increased to about 80 mW by optical amplifier, the output generated power is still low because of the presence of lossy harmonic mixers.

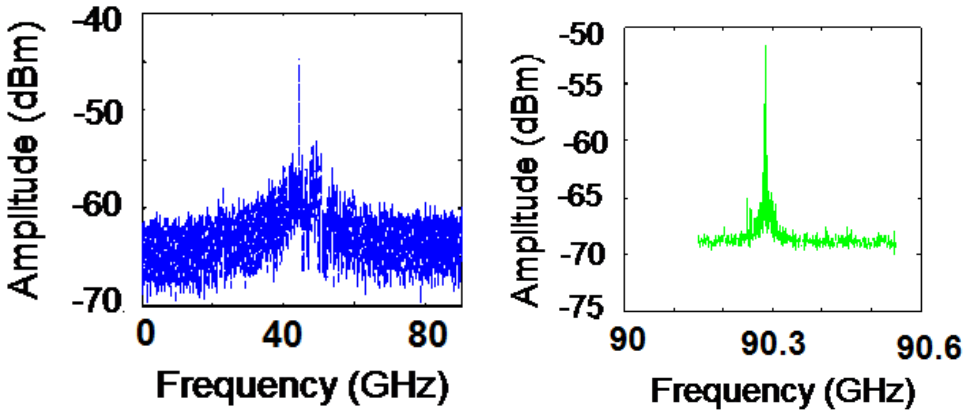

(a) (b)

Figure 4.19: Measured signals from electrical spectrum analyzer, a) 50 GHz range from commercial photodetector, b) 100 GHz range from commercial photodetector.

After having obtained the results from the dual wavelength laser diode and commercial photodiode, our circuit could be placed in the measurement setup. Commercial photodiode has been replaced by the fabricated photomixer antenna and then commercial horn antenna is added after the fabricated device in the receiver part. In this prepared measurement setup shown in Figure 4.20, the distance between the receiver horn antenna and the photomixer spiral antenna could be changed and also we could rotate the horn receiver antenna in different direction to obtain the radiation pattern. A microscope and a micropositioner are used to align the optical fiber in front of the photoconductive area of the fabricated device. The commercial horn antenna has been connected to the harmonic mixer and then the electrical spectrum analyzer.

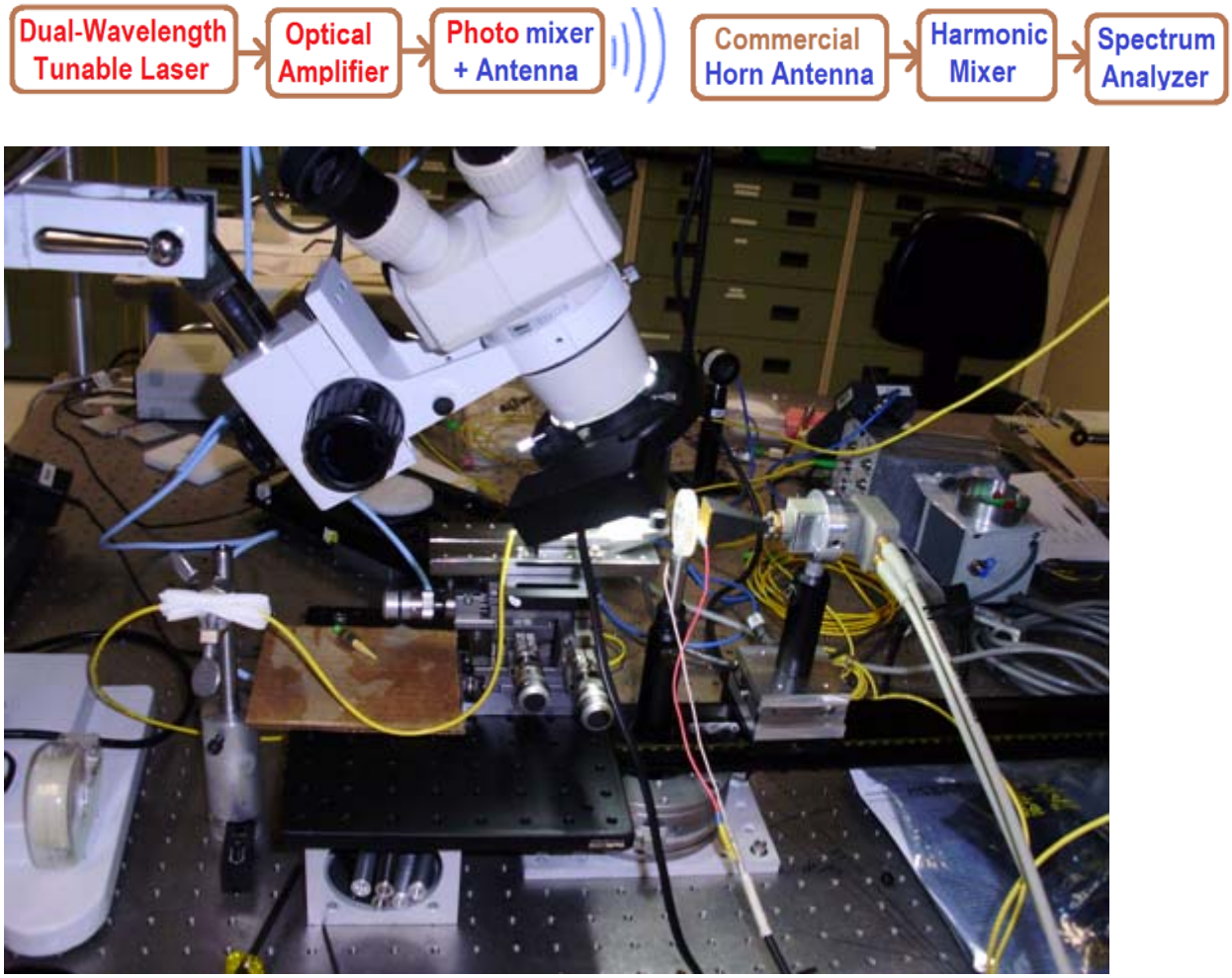

Figure 4.20: Measurement setup using fabricated photomixer and antenna.

After measurements, the results from a sample over 50 GHz frequency range have been obtained as shown in Figure 4.21. Because of low radiation power and lossy harmonic mixer, the measured power was obtained as low as -47 dBm.

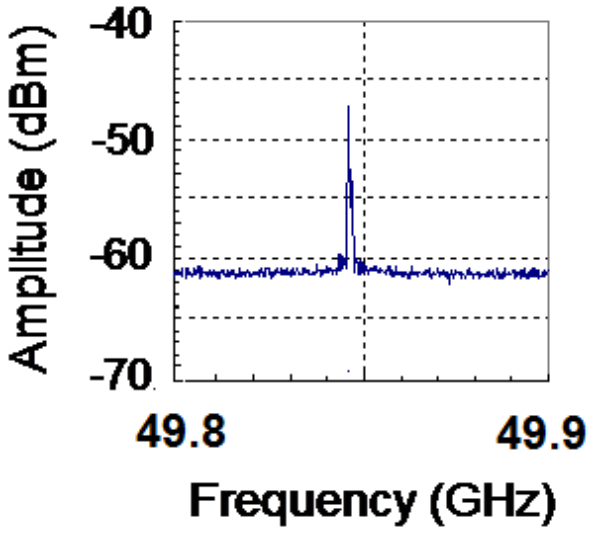

Figure 4.21: Measured signals from electrical spectrum analyzer for 50 GHz range of our fabricated device.

The observed low generated power could be related to the high conversion loss of the harmonic mixer and also the long carrier life time of the photoconductor. The fabrication of new high dosage devices, to improve the photoconductor carrier lifetime and increase the bandwidth of the devices, should be considered in the next steps. Also, for the high frequency measurements, the horn antenna and harmonic mixer and spectrum analyzer can be replaced by Golay cell or Bolometer to measure such low power signals. In the new setup shown in Figure 4.22, the generated low power THz signal after passing through the parabolic mirrors, concentrated on Bolometer. The measurements using Bolometer based on the thermal effects are obtained from the signal.

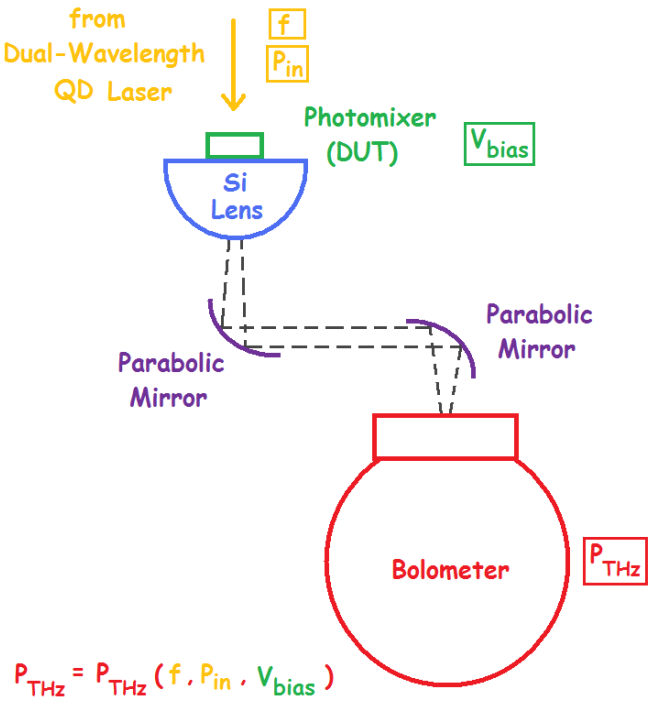

Figure 4.22: Measurement setup using Bolometer for detecting low power high frequency signals.

In this section, the experimental issues of the designed photoconductive photomixer and spiral antenna have been discussed. Multilayer masks were designed and then fabrication and packaging were carried out. Measurement results using commercial and fabricated devices have been obtained.

4.4 Conclusion

The design and analysis of the surface-type photomixer and the spiral antenna have been carried out and then the fabrication and measurements of the device have been done. In the design of the photoconductor, all of parameters are studied and related curves were extracted for three different types of structure with different photoconductive areas. In the design of antenna, a parametric analysis was carried out and radiation pattern and return loss are obtained. Results of the radiation patterns with metallic package were presented in this section as well. Parameters for the bandwidth limitation and also the radiation power limitation of the THz generator were

studied. It must be pointed out that the photodetectors located at the center of antennas have limited the high end working frequency.

In the experimental parts, the multilayer mask for the interdigitated fingers, mesa areas and spiral antennas were designed. In the mesa mask, some additional areas were considered because of the fabrication limitation in the etching process. Proper alignment marks for the multilayer mask were one of the important issues in the design. Fabrication of the masks and devices and then cleaving and packaging them were the following steps of the experiment. Two measurement setups, one for the commercial photodiode and the other for the fabricated device and spiral antenna were prepared on the optical table to use the dual wavelength laser diode. Results over 50 GHz frequency range have been obtained for our fabricated device. The obtained power was low and it can be related to the use of lossy harmonic mixer and also a small optical absorption area of the photoconductive photomixers. Lossy harmonic mixer could be replaced by Golay cell or Bolometer and also to solve the small photoconductive area problem, the type of photomixer should be changed.

In the following chapter, a photomixer with edge-type illumination is presented to increase the output power of the THz generator.

CHAPTER 5. THZ GENERATOR BASED ON EDGE-ILLUMINATION

5.1 Introduction

In the previous chapter, conventional types of the THz generators based on the photoconductive photomixer and the spiral antenna were studied and discussed. The important problem of such conventional surface-type generators is low power THz radiation because of the damage threshold of a small photoconductive area. This threshold limits the illuminated optical input power. Although by simply increasing the photoconductive area to have a large value of the damage threshold, the gain or bandwidth of the THz generator can be reduced. Therefore, the problem of the low power THz radiation can be solved by using a new type of photomixer with a large optical absorption area instead of the small photoconductor. TWPD with CPW electrode structure and edge-illumination is one of the large bandwidth photodetectors with a long absorption length which can be used as a photomixer in new THz generator. CPW in the structure of this photomixer should be connected to a broadband antenna. Because of the metallic structure of the antenna, integration of the large bandwidth spiral antenna and the CPW based photomixer is very difficult. Thus, the necessity of considering a new broadband antenna seems unavoidable. On the other hand, conventional CPS-fed log-periodic antenna is another candidate as a broadband antenna. Although a balun can be designed to connect CPW of TWPD to the conventional CPS fed log-periodic antenna, the design of such balun for the THz frequency range is difficult. Another solution, instead of using the balun, is the design of CPW-fed complementary log-period antenna. By changing the metal parts of a log-periodic antenna with the metal etched parts, a new structure of CPW-fed complementary log-periodic antenna can be proposed.

In Figure 5.1, the proposed high power THz generator including a dual wavelength laser diode, a TWPD and a CPW-fed log-period antenna are specified.

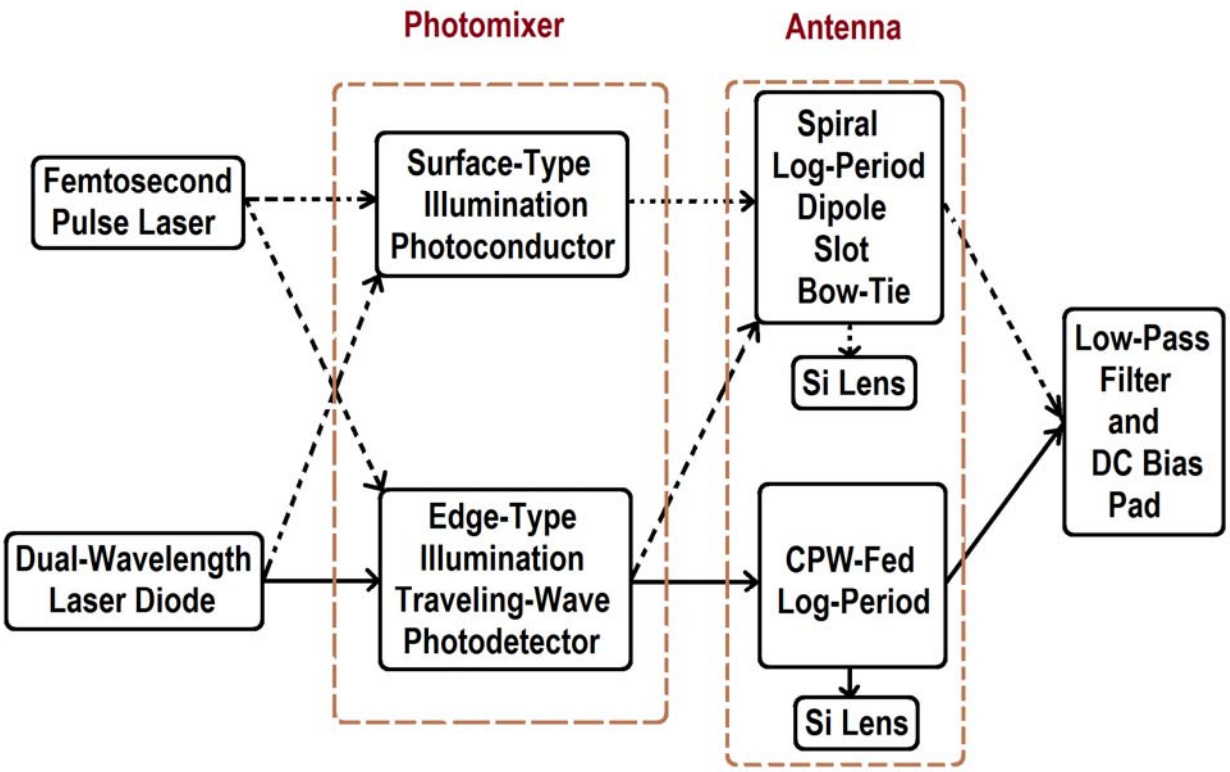

Figure 5.1: Edge-illumination structure for the photomixer and CPW-fed log-period antenna in exploring different possible schemes for THz generator.

Before explaining the detail of the proposed THz generator, a brief review of the published works on the edge-illuminated THz generator seems to be useful.

In [79]-[81], although the edge-illuminated THz generator using a metal semiconductor metal (MSM) and PIN TWPD integrated with a CPW-fed slot antenna has been presented, the slot antenna is not a broadband antenna and it is designed for the specific THz frequency. Furthermore, the integration of the log-periodic antenna and TWPD has been done by etching some metallic parts of the antenna in [82]; however the resulted bandwidth is obtained for the mmW applications. Also, in [83], a log-periodic slot antenna with a CPW-fed structure has been designed around 10 GHz. By a small modification of this antenna structure and integration of the photomixer, a newly broadband THz generator can be proposed which is sketched in Figure 5.2.

The integration of four different parts including optical waveguide, TWPD, CPW and complementary log-periodic antenna are shown in the figure. However, in a simple analysis, the

optical waveguide can be removed from the structure and the optical signals can be illuminated directly to the TWPD. InP substrate is considered in the proposed structure for the compatibility with 1.55 μm optical communication system.

Optical signal from a dual wavelength laser diode is illuminated from the edge of structure and passes through the optical waveguide. In TWPD, optical signal is converted gradually to the THz signal. Velocity matching between the optical and THz signals has an important role in the determination of the TWPD bandwidth. After the photomixing of the optical signals through a multi-layer TWPD, the CPW transfers the generated THz signal to the center of antenna for the radiation. The connection of the CPW to a large bandwidth THz log-periodic antenna is an important issue in the proposed THz source generator.

By changing the metalized area and etched area in the conventional log-periodic antenna, a new CPW-fed complementary log-periodic antenna is obtained which is shown in the figure. To minimize the CPW loss effect which is high in a long CPW, the length of a low-loss multilayer optical waveguide can be increased. The total length of the optical waveguide, TWPD and CPW is related to the size of antenna. As an example, for the 710 μm radius of the biggest curve of the log-period antenna, minimum radiated frequency is 40 GHz. In the proposed structure, two slots are considered in the top and bottom of the figure to separate the surface metallic parts for the DC connection of TWPD. Also, in the back of InP substrate, a Si lens can be considered to confine THz radiation.

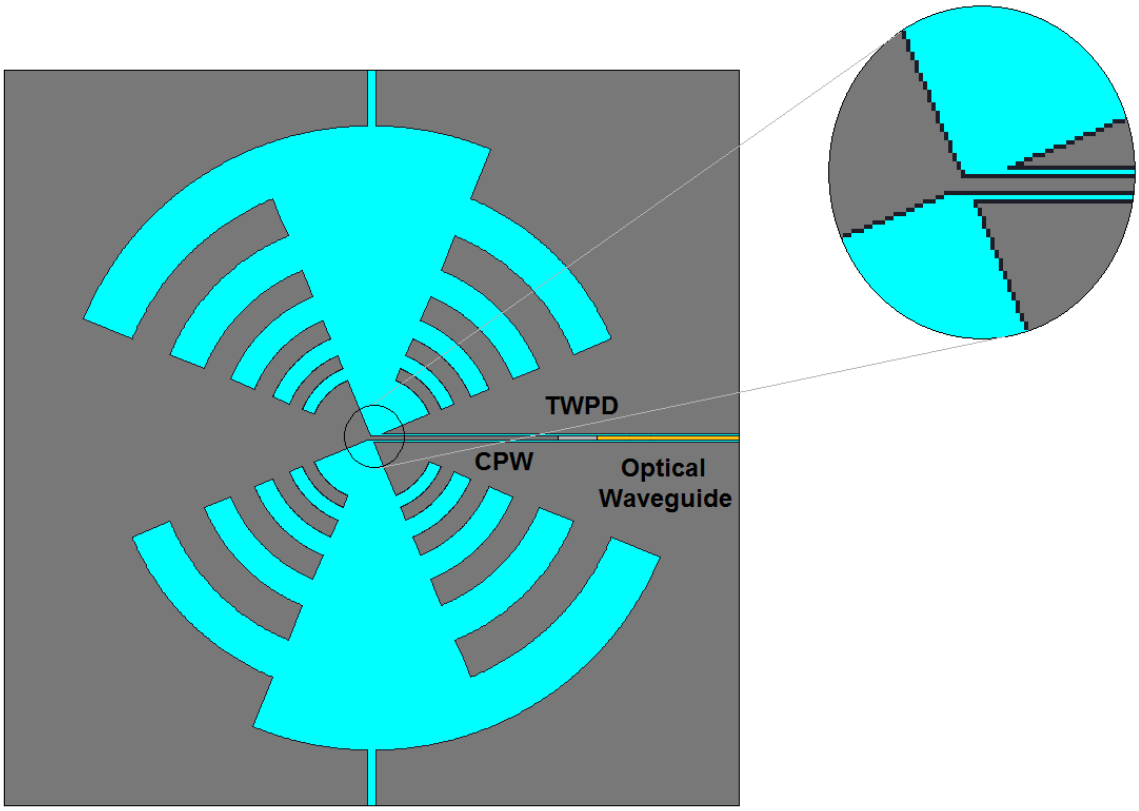

Figure 5.2: Top view of the proposed high power THz generator based on edge-illumination.

In this chapter, the design of two main sections of the proposed structure is discussed. First, the design and analysis of PIN-TWPD including the optical and microwave parts as well as the bandwidth limitations are presented. Then, the design of the CPW-fed complementary log-periodic antenna is presented and the resulted radiation pattern and return loss of the antenna are discussed.

5.2 Traveling-wave photodetector

A photodetector can be viewed as a two-port device with an optical input and an electrical output. TWPD is an edge-illuminated fully distributed photodetector and it has an electrode arrangement designed to support traveling electrical waves, as it is shown in Figure 5.3. Two different parts in this structure are presented. The first is the multilayer part for the detection and the second is a non-active part only for the transmission of a generated microwave signal. The

optical signal before detection can be coupled directly from a single-mode fiber or from a multilayer non-active optical waveguide to the active photodetection region. In the case of coupling from a multilayer optical waveguide, such types of photodetectors are called evanescently TWPD [84]-[89].

In the TWPD of Figure 5.3, by changing the dimensions of CPW, impedance matching can be obtained. According to the figure, the optical waveguide or I-layer is formed between two semiconductor cladding layers as the absorbing core of the optical wave. CPW is used to support RF waves, generated by the absorption of the optical wave, to the external circuits. N+ InP layer is on the substrate to transfer the generated electrons to the CPW grounded electrodes.

In the first part of the structure, the bandwidth is limited by the optical and microwave velocity mismatch, the carrier drift velocity from the intrinsic layer and the microwave loss. In the second part the bandwidth is only limited by the microwave loss of CPW geometry. Therefore, the use of a coplanar geometry with a high microwave loss is one of the important limitations for the TWPDs.

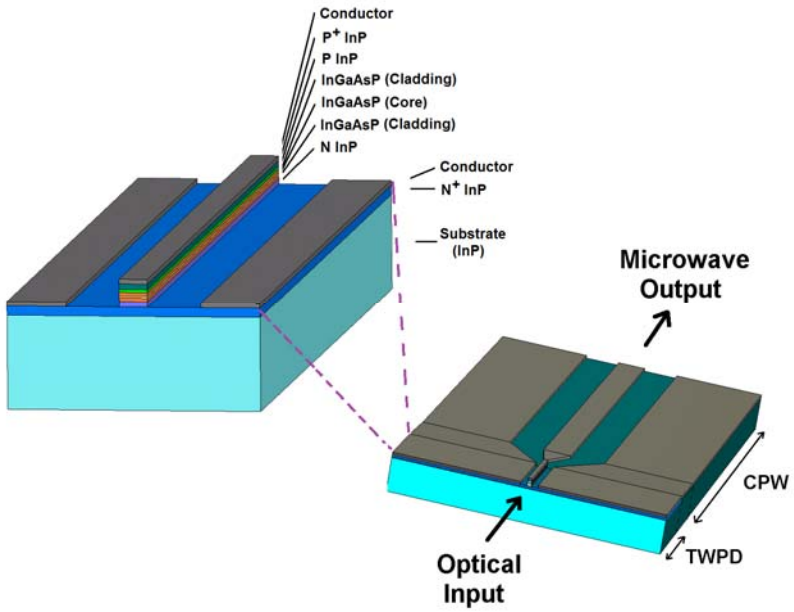

Figure 5.3: TW photodetector connected to CPW.

In this section, the microwave and optical analysis of TWPD, the bandwidth limitations and CPW analysis in the active multilayer detection region are discussed.

5.2.1 Microwave and optical analysis

The microwave/mmW analysis of CPW structure and the optical analysis of the multilayer structure in TWPD can be carried out separately and then, the results may be combined to obtain the overlap between the optical and millimetre/ microwave fields as well as the total bandwidth. In Table 5.1, simulation parameters for the optical and mmW/ μW analysis of TWPD are presented [90]-[91].

The microwave loss, electrical and optical phase velocities and characteristic impedance are some of the parameters which can be obtained through the microwave and optical analysis of TWPD. The electrical phase velocity is obtained by $v_e=\omega/\beta$, where β is the phase constant. Microwave loss is related to the attenuation constant by $-20\log(\alpha.l)\ (dB)$, where α is the field attenuation constant and l is the length of device.

Table 5.1: Simulation parameters for microwave and optical analysis of TWPD.

Layers	ε	σ (S/m)	n	Doping (cm^{-3})	d (μm)
P+ (InP)	12.4	20000	3.1	8.3e18	0.6
P (InP)	13.26	1980	3.15	0.82e18	0.3
I {active}, (InGaAsP)	12.4	0	3.55	0	0.2
I {cladding}, (InGaAsP)	11.5	0	3.54	0	0.4
N (InP)	13.26	24000	3.15	0.32e18	0.6
N+ (InP)	12.4	560000	3.1	7.6e18	1
Substrate (InP)	12.4	0	3.172	0	550

ε: Relative Permittivity ; σ : Conductivity ; n : Refractive index ; D : Doping ; d : Thickness

Width and thickness of the optical absorbing layer can be studied in the analysis. In Figure 5.4, the microwave loss versus frequency as functions of the photodiode width or strip width and absorbing / intrinsic layer thickness for TWPD is shown. It can be seen that microwave loss is increased with frequency and photodiode width and it is reduced with the I-layer thickness.

Figure 5.5 shows the electrical phase velocity versus frequency as functions of TWPD strip width and I-layer thickness. According to the figure, the electrical phase velocity increases with frequency and decreases with the photodiode width. Also, large electrical phase velocities are obtained in the thick absorbing layer.

The characteristic impedance versus frequency as functions of the thickness of absorbing layer and strip width is presented in Figure 5.6. Characteristic impedance tends to be constant at higher frequencies and goes up for narrow strips and thick absorbing layers. For the validation by HFSS, simulated results are compared with measured results from [92] which are obtained up to 40 GHz.

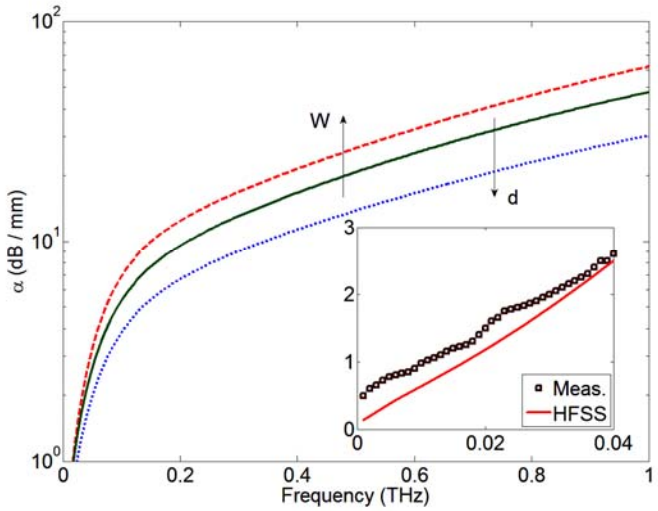

Figure 5.4: Microwave loss versus frequency as functions of strip width (W=1.5 μm to 3 μm) and I-layer thickness (d=1 μm to 1.5 μm) for TWPD.

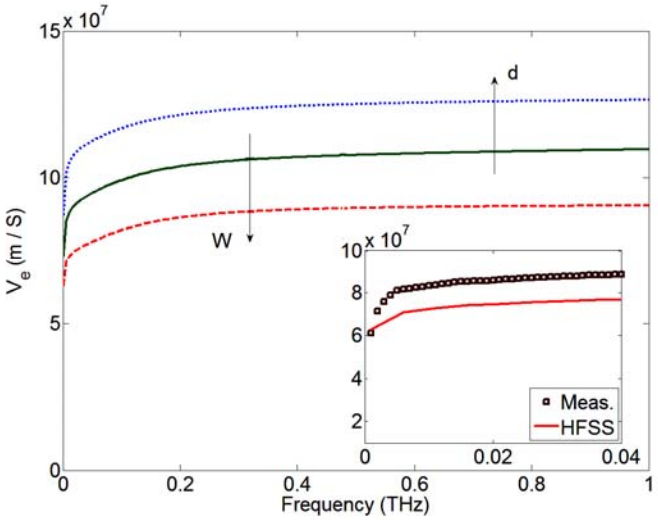

Figure 5.5: Electrical phase velocity versus frequency as functions of strip width (W=1.5 μm to 3 μm) and I-layer thickness (d=1 μm to 1.5 μm) for TWPD.

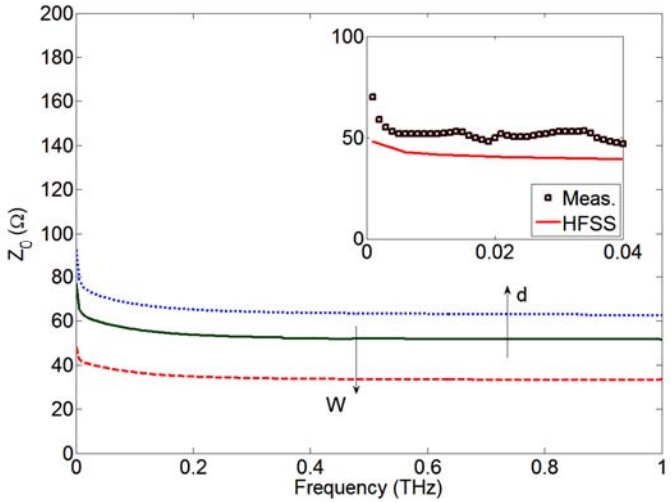

Figure 5.6: Characteristic impedance versus frequency as functions of (W=1.5 µm to 3 µm) and I-layer thickness (d=1 µm to 1.5 µm) for TWPD.

In Figure 5.7, the electrical and optical field intensities versus the dimension of TWPD are obtained. As it is shown in Figure 5.7a, the electrical field is confined in the intrinsic layer which is an optical waveguide. Also, as it is shown in Figure 5.7b, the optical field is confined in the intrinsic layers to form an optical waveguide.

The overlap between the electrical and optical fields points to the confinement factor of a TWPD.

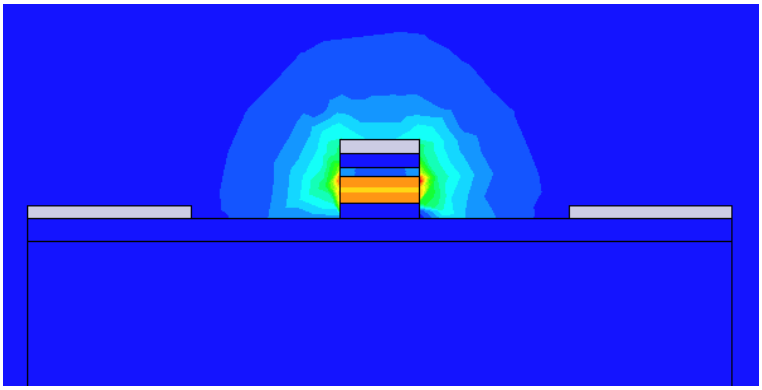

(a)

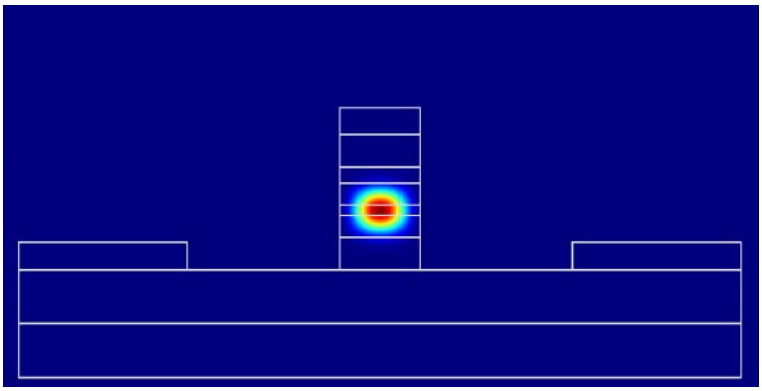

(b)

Figure 5.7: a) Electrical and b) optical field intensities in TWPD (I-layer thickness 1 µm, strip width 3 µm).

In Figure 5.8, the field overlap between optical and electrical fields in different layers of TWPD is illustrated. According to the figure and resulted fields values, the confinement factor for the proposed structure is given by [89]

$$\Gamma = \frac{\iint \left|E_x^{el}(x,y)\right|\left|E_y^{op}(x,y)\right|^2 dydx}{\iint \left|E_y^{op}(x,y)\right|^2 dydx} \qquad 5.1$$

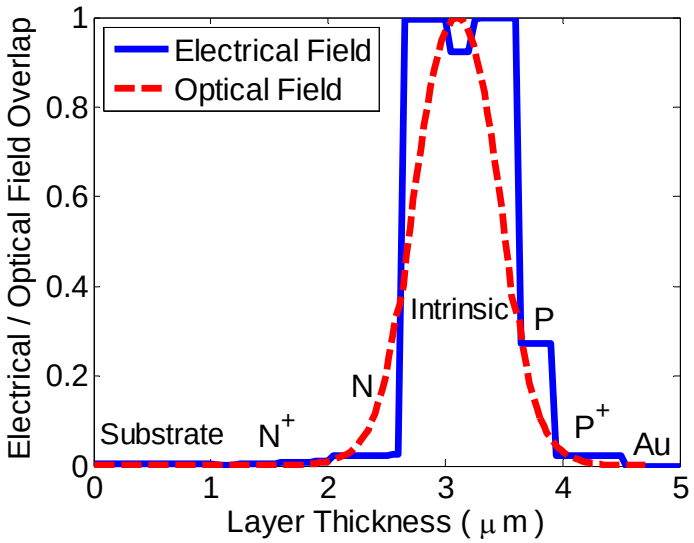

Figure 5.8: Overlap between optical and electrical field intensities in TWPD for 1μm thickness of absorbing layer.

The overlap integral is calculated to be 0.58 in the structure. Also from the optical analysis, effective index and optical phase velocity are obtained 3.48 and 8.6×107 (m/s), respectively.

5.2.2 Bandwidth limitations

After the analysis of the optical and mmW/μW parts of TWPD, the bandwidth limitations by electrical/optical phase velocity mismatch and carrier drift are studied.

The fractional photocurrent frequency response of TWPD is given by [89]

$$\left|\frac{i_{vm}(\omega)}{Q}\right|^2 = \frac{1}{4}\cdot\frac{(\omega_f-\gamma\omega_r)^2\omega^2+(1+\gamma)^2\omega_f^2\omega_r^2}{(\omega^2+\omega_f^2)(\omega^2+\omega_r^2)} \qquad 5.2$$

where $\omega_f = \frac{\Gamma\alpha v_e}{1-v_e/v_o}$, $\omega_r = \frac{\Gamma\alpha v_e}{1+v_e/v_o}$ and Q is the total charge available in the optical impulse. Γ is the optical waveguide confinement factor, α is the i-layer material optical absorption coefficient, v_o and v_e are the optical and electrical phase velocities, respectively.

The 3dB velocity-mismatch bandwidth limitation is obtained from equation 5.2 and we have

$$BW_{vm} = \frac{1}{2\pi}\sqrt{\left|\frac{-b \pm \sqrt{b^2 + 4\omega_f^2\omega_r^2}}{2}\right|} \qquad 5.3$$

where $b = \omega_f^2 + \omega_r^2 - \frac{1}{(1+\gamma)^2}(\omega_f - \gamma\omega_r)^2$

The velocity-mismatch bandwidth limitation in the matched input termination ($\gamma=0$) is

$$BW_{vm0} = \frac{\omega_f}{2\pi} \qquad 5.4$$

and in the open-circuit input termination ($\gamma=1$), the bandwidth limitation is approximated by

$$BW_{vm1} = \frac{\Gamma\alpha V_e}{3\pi} \qquad 5.5$$

Figure 5.9 illustrates the bandwidth limitation versus the ratio of the electrical to optical phase velocity as functions of the absorption coefficient and reflection coefficient in the input termination of TWPD. The bandwidth is increased in the matched electrical/optical phase velocity for the given values of the optical velocity, overlap factor and absorption coefficient. Also in the matched input termination ($\gamma=0$), the bandwidth is higher than the open-circuit input termination ($\gamma=1$).

Although the theoretical bandwidth goes to infinity in the case of $v_e=v_o$ and $\gamma=0$, the bandwidth is still limited by another factor which is the carrier drift velocity.

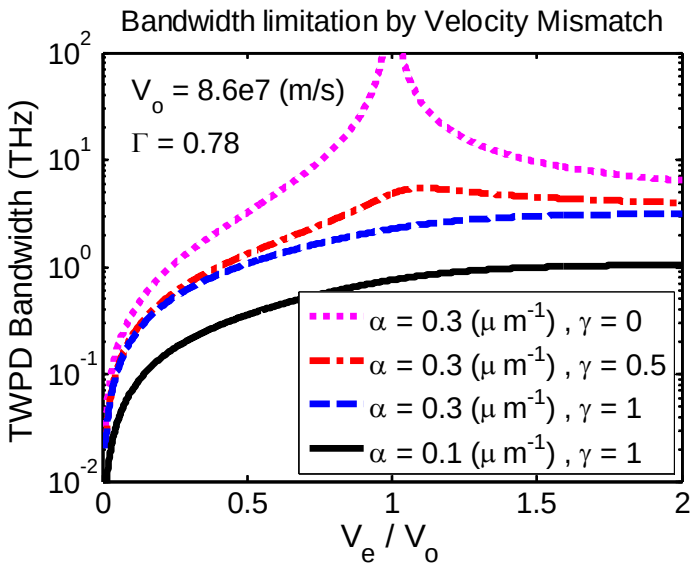

Figure 5.9: TWPD bandwidth limitation by the ratio of electrical to optical phase velocity as functions of optical absorption (α) and reflection coefficient in the input termination (γ).

Let us assume the carriers are uniformly generated across the intrinsic layer and the carrier drift velocities are constant and equal, the transit bandwidth limitation is given by

$$BW_t = 0.55\frac{V_{eh}}{d} = 0.55\frac{\mu.E}{d} \qquad 5.6$$

where V_{eh} is the electron and hole drift velocity, and d is the thickness of the intrinsic layer, μ is the mobility of electron and E is the electrical field applied to the photodiode. The carrier drift bandwidth versus applied electrical field to the photodiode is illustrated in Figure 5.10. The bandwidth increases in the case of high electric fields as it is shown in the figure. Also, a high carrier drift bandwidth is observed in the thin absorbing layer.

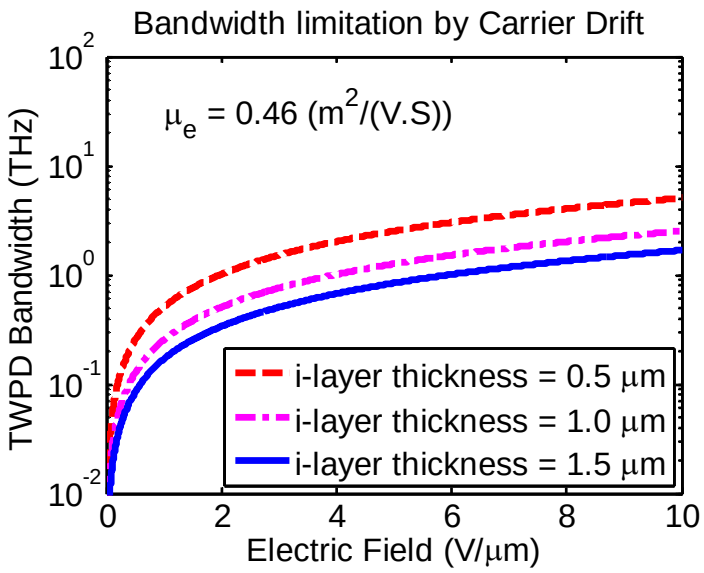

Figure 5.10: Carrier drifts bandwidth limitation versus electrical field as a function of absorbing layer thickness.

Normalized velocity-mismatch bandwidth and carrier drift bandwidth versus thickness of absorbing layer for TWPD are shown in Figure 5.11. The overall TWPD bandwidth from the velocity mismatch and carrier drift limitation is specified in the figure by arrows. While the thickness of the intrinsic layer is low, the dominant limitation factor is the bandwidth related to the velocity-mismatch and in the thick intrinsic layers, the effect of the carrier drift bandwidth is important.

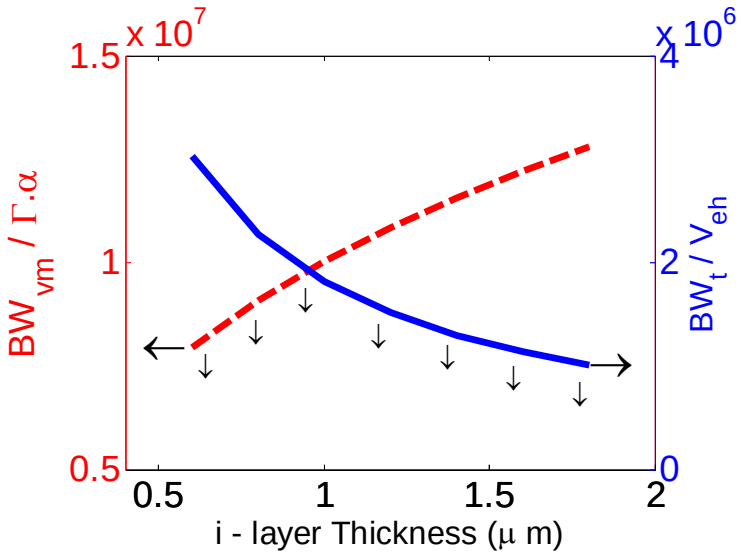

Figure 5.11: Normalized velocity-mismatch and carrier drift bandwidth versus I-layer thickness.

After the analysis of TWPD in the proposed THz generator, the next step is the design and analysis of the log-periodic antenna.

5.3 CPW-fed log-periodic antenna

The conventional log-periodic antennas make use of CPS in their structures which are not applicable for the CPW microwave output of the TWPD. Also, the design of a wideband balun to convert unbalanced to balanced structure for THz frequency range is very difficult.

In this section, a newly proposed complementary CPW-fed log-periodic antenna is designed and integrated to the new THz generator. In Figure 5.12, 3D and top view of the CPW-fed log-periodic antenna are illustrated. In this figure, two slots for the DC bias separation and also CPW-fed from the output of TWPD are shown. The growing rate of m and τ for the antenna is given by [93]

$$\tau = \frac{R_{i-1}}{R_i}; \quad m = \frac{r_i}{R_i} \qquad 5.7$$

where R_i, R_{i-1} and r_i are specified in Figure 5.12b.

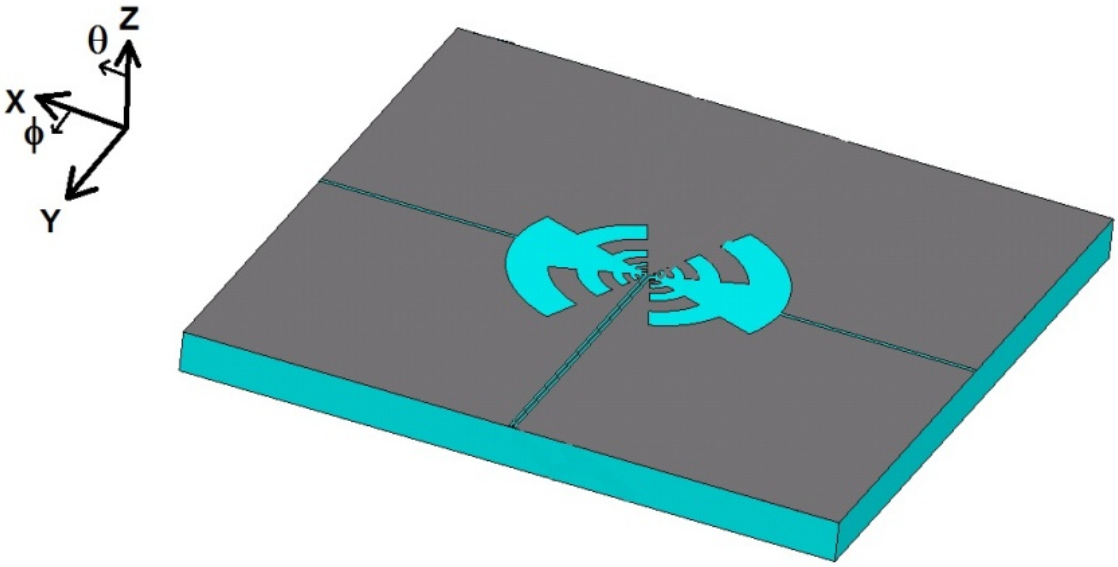

(a)

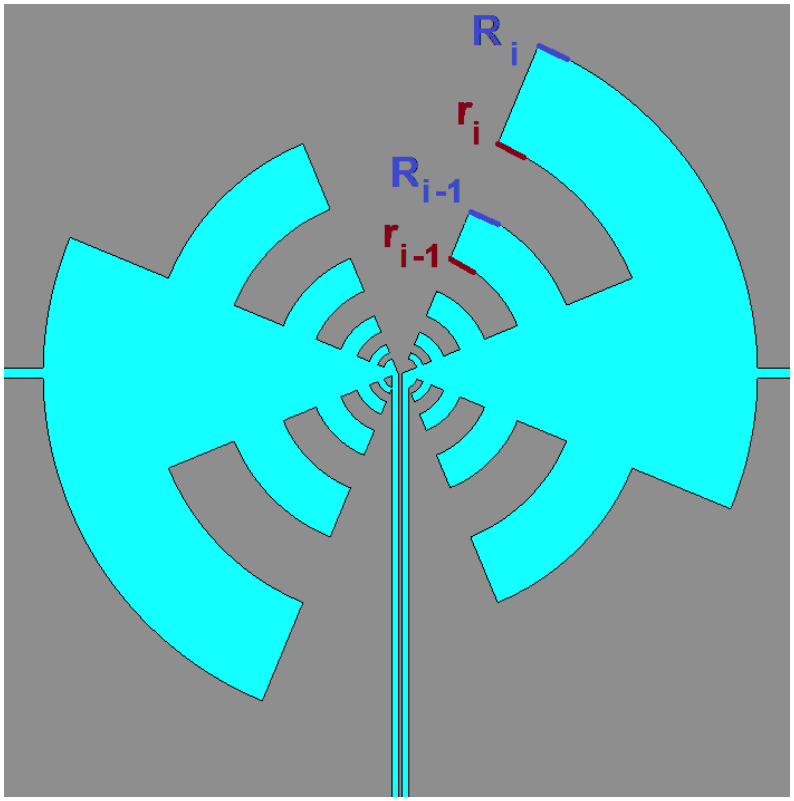

(b)

Figure 5.12: a) 3D view of the complementary CPW-fed log-periodic antenna, b) top view of the antenna with dimensions.

The optimized design parameters for the antenna are presented in Table 5.2.

Table 5.2: Simulation parameters for CPW-fed log-periodic antenna.

Symbol	Quantity	Value (μm)
R1	Radius of smallest curve	50
m	Growing factor	0.7
τ	Growing factor	0.5
H	Substrate thickness	250
Wcpw	Slot width of CPW	15
Scpw	Strip width of CPW	10
Wdc	Slot width of DC bias connection	25

In Figure 5.13a, the return loss versus frequency up to 1 THz, for the designed antenna is shown. Also, the radiation pattern at 100 GHz shows the maximum gain of about 1 dB.

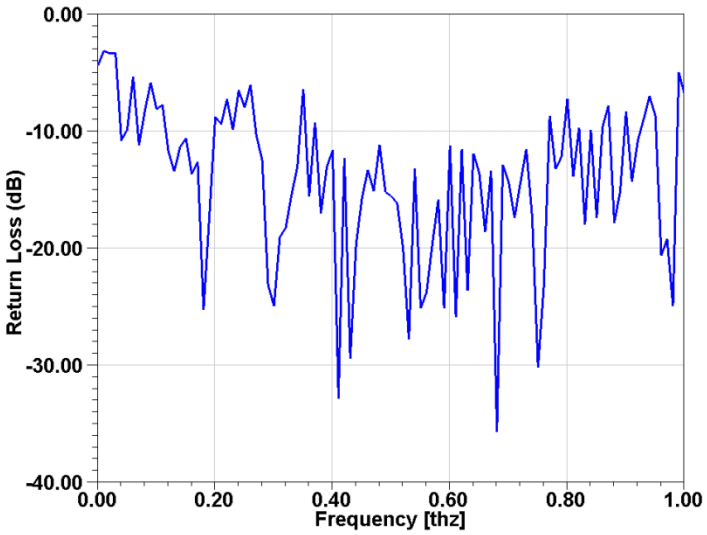

(a)

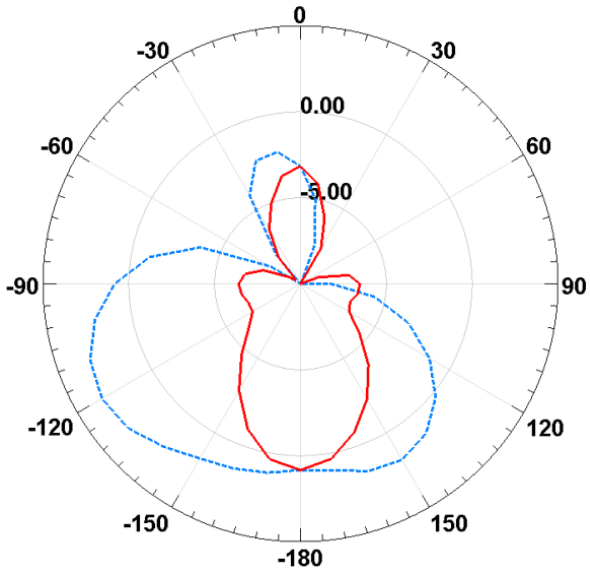

(b)

Figure 5.13: a) Return loss versus frequency for CPW-fed log-periodic antenna, b) Radiation pattern at 100 GHz for φ = 0 (Solid line) and φ = 90 degree (Dashed line).

As a conclusion of this section, the CPW-fed log-periodic antenna as a part of the integrated THz generator has been designed and analyzed.

5.4 Conclusion

The problem of a low power THz generation for the conventional surface-type generators because of the damage threshold of a small photoconductive area can be solved by the proposed new edge-type photomixer. TWPD with a long optical absorbing length was considered as an edge-type photomixer.

Four main parts are considered for the proposed generator. In the first, a long-length multilayer optical waveguide reduce the length of lossy CPW structure.

The second important part is related to TWPD. The design and analysis of this high power large bandwidth photodetector has been made in this chapter. Two bandwidth limitation factors including the velocity mismatch between the optical and microwave signals and the carrier drift time have been studied versus the dimensions of TWPD. The microwave loss of the active multilayer CPW in TWPD has been obtained.

In the third part of the proposed THz generator, a non-active single layer CPW can be considered to connect the TWPD to the antenna. As it has been presented in chapter one, the loss of CPW is increased by increasing frequency and CPW length, as well. In THz frequency range, the length of this lossy CPW should be decreased by increasing the length of low-loss optical waveguide.

In the last, a broadband antenna should be fed by the CPW structure. The newly proposed complementary log-periodic antenna has been designed and analyzed for this high power broadband THz generator. In this new antenna, the metal parts and metal etched parts of the conventional log-periodic antennas have been modified.

In the proposed structure, the size of the antenna which is excited from the center of the structure can be related to the minimum applicable frequency. Furthermore, the length of a low-loss optical waveguide can be increased to yield a short length of CPW because of the constant value for the summation of the length of multilayer optical waveguide, TWPD and CPW. In addition, the presented THz generator has the advantage of large bandwidth and high power radiation, because of using the log-periodic antenna and TWPD, respectively.

CONCLUSIONS

In the recent years, the fields of microwave photonics, mmW photonics and THz photonics are more interested for many different applications such as RoF systems and medical imaging. In all of these applications, the conversion of optical/electrical signal to electrical/optical signal and control of optical/electrical signal by electrical/optical signal present the fundamental function for microwave/mmW/THz photonic systems. High speed optoelectronic devices connecting to the optical fiber transmission lines with large capacity and low loss are instrumental for broadband communication systems. In particular, TW modulators and photodetectors are the key components of transmitter and receiver of these systems. Conventional TW photodetector and modulator have been using MS and CPW transmission lines in their structures. Although the fabrication and design of these planar electrode geometries are simple, microwave and mmW losses of MS and CPW increase with frequency and they cannot be used for very high frequency applications. RWG and NRD are two non-planar low-loss transmission lines which can be used in the design of mmW and sub-mmW device structure. The integration of RWG in planar form is simple compared to the NRD and it is more suitable for active optoelectronic devices, although the NRD can be designed into the structure of optoelectronic devices in the future. Non-planar problem of microwave low-loss waveguides which makes difficulty in integrated systems is solved using emerging SICs concept which utilizes some metallic and/or air via holes to synthesize the non-planar structures in planar form. Using this concept in microwave domain, non-planar RWG and NRD guide can be effectively converted to the planar and integrable SIW and SINRD guide, respectively. Therefore, we have optoelectronic devices with lossy MS and CPW electrode geometries for high frequencies in one hand and on the other hand, low-loss planar SIW and SINRD for mmW and sub-mmW applications. The proposition of SICs-based optoelectronic devices which is a completely novel approach for mmW and THz photonics has been presented in this thesis. In particular, lossy MS waveguide has been replaced by SIW after the detection by the WGPD. Also, two types of new electro-optical phase and amplitude modulators based on pure SIW structure and hybrid SIW-CPW structure have been studied and realised.

In the first chapter, different sources of loss including ohmic, dielectric and radiative losses have been studied at microwave and mmW frequency ranges. This study describes the loss mechanism of MS/CPW and SIW structures for GaAs isotropic substrate in photodetectors and anisotropic $LiNbO_3$ substrate in modulators. The results show that the microwave and mmW losses increase with frequency in MS and CPW; however these losses are almost constant after the cut-off frequency of SIW. Furthermore, in the specific frequency bands, such as Ka-band and V-band, the SIW loss is less than that of MS and CPW in GaAs and $LiNbO_3$ substrates. In the conventional WGPDs, the bandwidth limitation is related to the losses of short-length active multilayer detection region and non-active single layer MS transmission line following the detection. The results show that the effect of long-length non-active MS loss is more significant and this MS section should be replaced by a low-loss waveguide. To realise a low-loss SIW in the structure of WGPD (SIW-WGPD), MS has been replaced by SIW and a transition of MS to multilayer SIW considering DC bias of the photodetector has been designed and fabricated. The insertion loss of less than 2 dB/cm up to 40 GHz was measured for SIW-WGPD, while the conventional MS-WGPD have an insertion loss of more than 5 dB/cm. A good agreement between the simulated and measured results has been observed for our circuit.

In addition to use of SIW in photodetector structures, it can be used in the structure of electro-optical phase and amplitude modulators to increase their bandwidth for mmW applications as explained in the second chapter. Band-pass SIW phase modulator based-on $LiNbO_3$ substrate has been designed and realised. In an initial simple design of the modulator, an optical waveguide was considered in the RWG structure. Because of the low interaction between the microwave and optical signals, field overlap integral was obtained as low as 7.4×10^{-3} (applied voltage of 69 V for a 5 cm modulator) at 60 GHz frequency range for the substrate thickness of 10 μm. This substrate thickness has shown the highest overlap integral among the substrate thicknesses of 10 μm, 50 μm and 220 μm. On the other hand, SIW microwave loss that affects the modulator bandwidth was obtained as low as 1 dB/cm at 60 GHz frequency range for the substrate thickness of 220 μm that have the minimum loss among the different specified substrate thicknesses. To improve the design of the SIW phase modulator, modifications such as using optical waveguide array, multimode optical waveguides and multi-layer substrate have been applied to the initial design.

The designed SIW modulator with two layers of $LiNbO_3$ substrates and optical waveguide array has been optimized at 60 GHz frequency range. For the structure with 10 μm of the Z-cut $LiNbO_3$ substrate includes 16 optical waveguides located on X-cut $LiNbO_3$ substrate, an overlap integral of 52.2×10^{-3} (applied voltage of 19.7 V for 5 cm modulator) has been obtained. This overlap integral is seven times more than that of the initial SIW modulator. For the optical part of the SIW modulator, Y-branch angles should be less than one degree to achieve minimum optical loss. In addition to the design of modulation section of the proposed device, the CPW to SIW transition has been designed at 60 GHz frequency range for the measurement purpose. For the fabrication of SIW in $LiNbO_3$ substrate and specially for the drilling of via holes, laser micromachining has been used instead of time-consuming chemical process methods. Among the lasers for micromachining, Excimer laser was used because of the $LiNbO_3$ transparency range. Dicing the $LiNbO_3$ wafer and drilling SIW holes have been carried out by the Excimer laser micromachining in this work. The fabricated SIW waveguide has been measured and about 5 GHz of bandwidth has been obtained at 60 GHz operating frequency range.

After the design of SIW phase modulators, this concept has been extended to propose a band-pass high frequency amplitude modulator. By considering an MZ structure for the optical waveguides in the design of an SIW amplitude modulator, the TE_{20} mode of SIW seems to be a genius choice, which provides a natural 180 degree phase offset for the two arm outputs (TE_{10} modes). The TE_{20} mode of SIW can be excited by the use of MS lines or CPW structures according to the desired frequency for potential optoelectronic devices.

In addition to the proposed modulators based on pure SIW structure, another type of amplitude modulator based on the mode coupling between SIW and CPW has been presented in the third chapter. In this SIW-CPW modulator, the CPW structure of conventional modulators is preserved for its high overlap integral, which is optimized for high frequency applications such as RoF systems. In the conventional $LiNbO_3$ amplitude modulators, the field interaction between the microwave and optical signals is obtained from the cross-section interactions and is always constant along the modulator. In the newly proposed SIW-CPW modulator, the microwave signal intensity is changed gradually along the modulator and becomes maximized in the middle of the device. As a complete integrated system, the microwave signal coming from SIW and then coupled back from SIW to CPW take place in the first half of the modulation path. Subsequently, in the second half, the CPW to SIW mode coupling is used in a reverse manner towards the end.

Bending structure of SIW to separate microwave and optical ports and also fabrication of resistor pads to suppress resonant frequencies as well as broadband transitions for measurement purpose were challenging issues. They have been considered and solved in the proposed modulator. Design and fabrication of the hybrid SIW-CPW modulator have been carried out and about 7 GHz of bandwidth has been measured at 60 GHz frequency range. An MZ optical waveguide using Ti in-diffusion technique has been fabricated and Y-branch optical loss of about one dB was measured at 1550 nm. It should be mentioned that the optical loss of Y-branch is the main source of loss in MZ structures. Good agreements between the simulated and measured results have been observed in the hybrid SIW-CPW structure on $LiNbO_3$ substrate.

In the fourth chapter of this thesis, photodetector has been considered for THz source generation. Surface and edge-type illuminated photodetectors can be used in THz source generators for many different applications such as biomedical imaging devices.

Surface-type photoconductive as a photomixer as well as the integration of this photomixer with spiral antenna have been designed and fabricated. Optical signal from a dual-wavelength laser diode illuminates to interdigitated fingers of the photoconductor. THz signal is radiated from the back side of substrate after detection of the optical signal. Design and optimization of the photodetector, the spiral antenna and multi-layer masks as well as fabrications and measurements of the THz source generator have been carried out and presented. A microwave generated signal around 50 GHz frequency range with the radiation power of -47 dBm has been measured from the fabricated device. It should be point out that the low radiation power of the surface-type THz source generator has been obtained because of the damage threshold of a small photoconductive area as well as high insertion loss of the harmonic mixer. Also, the high-frequency generated signal can be obtained by using fabrication techniques that improve the photoconductor bandwidth.

The problem of conventional low-power surface-type THz generators has been solved by the proposition and integration of the new edged-type photomixer and complementary antenna in the fifth chapter. Long-length TWPD as a photomixer in the proposed THz generator gives the ability of high-power optical input illumination to increase the power of THz source generators. Design and analysis of this high-power large-bandwidth photodetector have been performed. Also, microwave loss of the multilayer CPW part of the TWPD has been analyzed up to 1 THz.

Two bandwidth limitation factors including the velocity mismatch between the optical and microwave signals and carrier drift time have been obtained versus the dimensions of the TWPD. Moreover, new proposed complementary log-periodic antenna has been designed and analyzed up to 1 THz for this high-power broadband THz generator. In this new antenna, the metallic areas and metallic-etched areas of the conventional log-periodic antennas have been changed. In addition, integration of the TWPD and the proposed antenna has been presented.

Future works explained in the following could be considered for different aspects of this thesis work. For the integration of photodetector and low-loss waveguide using the SICs concepts as discussed in Chapter One, the transition of CPW in TWPD to multilayer SIW could be designed by considering DC bias of the photodetector. SIW can be replaced by SINRD for sub-mmW applications. Also, SINRD-based phase and amplitude modulators can be proposed on $LiNbO_3$ substrate. Furthermore thin-film of high electro-optical coefficient materials such as CBN could be utilized to improve the performances of the proposed modulators. In addition, for the long-length section of Y-branches in the MZ structure presented in Chapter Two, other optical coupling techniques such as 1×N MMI splitter could be used. Moreover, measurements of modulator parameters can be carried out by applying optical and microwave signals simultaneously. In Chapter Three, the second section of the device, coupling from CPW to SIW, can be removed and in this condition, the overlap integral can be gradually increased along the modulation path instead of maximizing in the middle of the presented structure. Using SINRD and multilayer substrates, to increase coupling coefficient and bandwidth of this new modulator, could be studied in the future. For the surface-type THz generator, some other fabrication techniques such as low-temperature growing (LTG) can be used to increase the bandwidth of photoconductors. To illuminate high power optical signal, multilayer photoconductive structures can be designed and fabricated. In the last chapter, the presented edge-illuminated THz generator can be integrated with dual-wavelength laser diode and then it can be commercialized for different applications. Also, the SICs concept can be used in the design of principal structures after the detection including the CPW and antenna. In addition, the SICs concept can be applied to other optoelectronic devices such as optically/electrically controlled electrical/optical devices for mmW and sub-mmW applications.

REFERENCES

[1] D. Jager, "Microwave Photonics – From Concepts to Devices and Applications," pp. 1-30, *in the book entitled Microwave Photonics*, edited by Chi H. Lee, CRC Press, 2007.

[2] D. Jager, R. Kremer, and A. Stohr, "Travelling-wave optoelectronic devices for microwave applications," *IEEE, MTT-S International Microwave Symposium Digest*, Vol.1, pp. 163-167, 1995.

[3] K. Kato, S. Hata, A. Kozen, J. Yoshida, and K. Kawano, "High-Efficiency Waveguide InGaAs pin Photodiode with Bandwidth of over 40 GHz," *IEEE, Photonics Technology Letters*, Vol. 3, No. 5, pp. 413-414, 1991.

[4] D. Wake, T. P. Spooner, S. D. Perrin, and I. D. Henning, "50 GHz InGaAs edge-coupled PIN photodetector," *Electronics Letters*, Vol. 27, No. 12, pp. 1073-1075, 1991.

[5] E. Goldfarb and A. Platzker, "Losses in GaAs Microstrip," *IEEE, Transactions on Microwave Theory and Techniques*, Vol. 38, pp. 1957-1962, 1990.

[6] J. P. Thakur, A. K. Pandey, A. Kedar, K. K. Gupta, H. P. Vyas, "Modelling of GaAs-MMIC microstrip line up to 40 GHz," *International Journal of RF and Microwave Computer-Aided Engineering*, Vol.14, pp. 475-482, 2004.

[7] Soon-Cheol Kong, Sang-Jun Yoon, and Young-Wan Choi, Microwave characteristics of long TWPDs for high-power operation, *Microwave and Optical Technology Letters*, Vol. 35, pp. 51-54, 2002.

[8] S. Kong, S. Lee, J. Lee, Y. Choi, "Numerical Analysis of Traveling-Wave Photodetectors Bandwidth Using the Finite-Difference Time-Domain Method," *IEEE, Transactions on Microwave Theory and Techniques*, Vol. 50, No. 11, pp. 2589-2597, 2002.

[9] W. Heinrich, "Full-wave analysis of conductor losses on MMIC transmission lines," *IEEE Transactions on Microwave Theory and Techniques*, Vol. 38, No. 10, pp. 1468-1472, 1990.

[10] W. H. Haydl, Kitazawa, T. J. Braunstein, R. Bosch, M. Schlechtweg, "Millimeterwave coplanar transmission lines on gallium arsenide, indium phosphide and quartz with finite metalization thickness," *IEEE, MTT-S Symposium Digest*, Vol. 2, pp. 691-694, 1991.

[11] M. Zhang, C. Wu, K. Wu and J. Litva, "Losses in GaAS Microstrip and Coplanar Waveguide," *IEEE, MTT-S Symposium Digest*, pp. 971-974, 1992.

[12] W. K. Burns, M. M. Howerton, R. P. Moeller, R. R. Krahenbuhl, W. McElhanon and A. S. Greenblatt, "Low drive voltage, broad-band LiNbO3 modulators with and without etched ridges," *IEEE, Journal of Lightwave Technology*, Vol. 17, No.12, pp. 2551–2555, 1999.

[13] J. M. Liu, Photonic Devices, Cambridge University Press, 2005.

[14] E. L. Wooten, K. M. Kissa, A. Yi-Yan, E. J. Murphy, D. A. Lafaw, P. F. Hallemeier, D. Maack, D. V. Attanasio, D. J. Fritz, G. J. McBrien, and D. E. Bossi, "A review of lithium niobate modulators for fiber-optic communications systems," *IEEE, Journal of Selected Topic in Quantum Electronics*, Vol. 6, pp. 69-82, 2000.

[15] K. Noguchi, O. Mitomi, and H. Miyazawa, "Millimeter-Wave Ti:LiNbO3 Optical Modulators," *IEEE, Journal of Lightwave Technology*, Vol. 16, No. 4, pp. 615-619, 1998.

[16] K. Noguchi, H. Miyazawa, and O. Mitomi, "Frequency-dependent propagation characteristics of coplanar waveguide electrode on 100GHz Ti:LiNbO3 optical modulator," *Electronics Letters*, Vol. 34, No. 7, pp. 661-663, 1998.

[17] B. M. A. Rahman and S. Haxha, "Optimization of Microwave Properties for Ultrahigh-Speed Etched and Unetched Lithium Niobate Electrooptic Modulators," *Journal of Lightwave Technology*, Vol. 20, No. 10, pp. 1856-1863, 2002.

[18] A. Patrovsky, K. Wu, "Substrate Integrated Image Guide (SIIG)—a novel planar dielectric waveguide technology for millimeter-wave applications," *IEEE, Transactions on Microwave Theory and Techniques*, Vol. 54, pp. 2872-2879, June 2006.

[19] K. Wu, D. Deslandes, and Y. Cassivi, "The Substrate Integrated Circuits – A New Concept for High-Frequency Electronics and Optoelectronics," *Proc. 6th Int. Conf. Telecommunications Modern Satellite*, pp. 1-10, Oct. 2003.

[20] K. Wu, "Substrate integrated circuits for radio-frequency and millimeter-wave system applications – status and outlook," *Asia-Pacific Microwave Conf. Proc. (APMC'06)*, pp. 1895-1900, Dec. 2006.

[21] D. Deslandes and K. Wu, "Integrated microstrip and rectangular waveguide in planar form," *IEEE, Microwave and Wireless Components Letters*, Vol. 11, No.2, pp. 68-70, 2001.

[22] D. Deslandes, and K. Wu, "Single-Substrate Integration Technique of Planar Circuits and Waveguide Filters," I*EEE Transactions on Microwave Theory and Techniques*, Vol. 51, pp. 593-596, 2003.

[23] M. Bozzi, M. Pasian, L. Perregrini, and K. Wu, "On the Losses in Substrate Integrated Waveguides," *37th European Microwave Conference 2007 (EuMC 2007)*, pp. 384-387, Oct. 2007.

[24] Y. Cassivi, and K. Wu, "Substrate Integrated Nonradiative Dielectric Waveguide," *IEEE Microwave and Wireless Components Letters*, Vol. 14, No. 3, pp. 89-91, Mar. 2004.

[25] D. Wake, T. P. Spooner, S. D. Perrin, and I. D. Henning, "50 GHz InGaAs edge-coupled PIN photodetector," *Electronics Letters*, Vol. 27, No. 12, pp. 1073-1075, 1991.

[26] E. Goldfarb and A. Platzker, "Losses in GaAs Microstrip," *IEEE, Transactions on Microwave Theory and Techniques*, Vol. 38, pp. 1957 1962, 1990.

[27] J. P. Thakur, A. K. Pandey, A. Kedar, K. K. Gupta, H. P. Vyas, "Modelling of GaAs-MMIC microstrip line up to 40 GHz," *International Journal of RF and Microwave Computer-Aided Engineering*, Vol. 14, pp. 475-482, 2004.

[28] W. Heinrich, "Full-wave analysis of conductor losses on MMIC transmission lines," *IEEE, Transactions on Microwave Theory and Techniques*, Vol. 38, No. 10, pp. 1468-1472, 1990.

[29] W. H. Haydl, Kitazawa, T. J. Braunstein, R. Bosch, M. Schlechtweg, "Millimeterwave coplanar transmission lines on gallium arsenide, indium phosphide and quartz with finite metalization thickness," *IEEE, MTT-S Symposium Digest*, Vol. 2, pp. 691-694, 1991.

[30] M. Zhang, C. Wu, K. Wu and J. Litva, "Losses in GaAS Microstrip and Coplanar Waveguide," *IEEE, MTT-S Symposium Digest*, pp. 971-974, 1992.

[31] K. Noguchi, H. Miyazawa, and O. Mitomi, "Frequency-dependent propagation characteristics of coplanar waveguide electrode on 100GHz Ti:LiNbO3 optical modulator," *Electronics Letters*, Vol. 34, No. 7, pp. 661-663, 1998.

[32] B. M. A. Rahman and S. Haxha, "Optimization of Microwave Properties for Ultrahigh-Speed Etched and Unetched Lithium Niobate Electrooptic Modulators," *Journal of Lightwave Technology*, Vol. 20, No. 10, pp. 1856-1863, 2002.

[33] D. Deslandes and K. Wu, "Accurate modeling, wave mechanisms, and design considerations of a substrate integrated waveguide," *IEEE, Transactions on Microwave Theory and Techniques*, Vol. 54, No. 6, pp. 2516-2526, 2006.

[34] F. Xu and K. Wu, "Guided-wave and leakage characteristics of substrate integrated waveguide," *IEEE, Transactions on Microwave Theory and Techniques*, Vol. 53, No.10, 66-72, 2005.

[35] M. N. Armenise, "Fabrication techniques of lithium niobate waveguides," *IEEE Proceedings*, Vol. 135, No.2, pp. 85-91, 1988.

[36] A. Yariv, Quantum Electronics, John Wiley & Sons Inc., 1989.

[37] H. Chung, W. S. Chung, E. Adler, "Modeling and optimization of traveling-wave LiNbO3 interferometric modulators," *IEEE, Journal of Quantum Electronics,* Vol. 27, No. 3, pp. 608-617, 1991.

[38] H. Chung, W. S. Chung, G. E. Betts, "Microwave properties of traveling-wave electrodes in LiNbO3 electrooptic modulators," *Journal of Lightwave Technology*, Vol. 11, No. 8, pp. 1274-1278, 1993.

[39] K. Noguchi, O. Mitomi, K. Kawano, M. Yanagibashi, "Highly efficient 40-GHz bandwidth Ti:LiNbO3 optical modulator employing ridge structure," *IEEE, Photonics Technology Letters,* Vol. 5, No. 1, pp. 52-54, 1993.

[40] G. K. Gopalakrishnan, C. H. Bulmer, W. K. Burns, R. W. McElhanon, A. S. Greenblatt, "40 GHz, low half-wave voltage Ti:LiNbO3 intensity modulator," *Electronics Letters*, Vol. 28, No. 9, pp. 826-827, 1992.

[41] R. S. Cheng, W. L. Chen, W. S. Wang, "Mach-Zehnder modulators with lithium niobate ridge waveguides fabricated by proton-exchange wet etch and nickel indiffusion," *IEEE, Photonics Technology Letters*, Vol. 7, No.11, pp. 1282-1284, 1995.

[42] N. Anwar, T. Wongchareon, F.A. Katsriku, B. M. A. Rahman, K. T. V. Grattan, "An Accurate Model for a LiNbO3 Electro-optic Modulator," *IEEE, High Performance Electron Devices for Microwave and Optoelectronic Applications Workshop,* pp. 56-61, 1996.

[43] O. Mitomi, K. Noguchi, H. Miyazawa, "Broadband and low driving-voltage LiNbO3 optical modulators," *IEE, Proceedings Optoelectronics*, Vol. 145, No.6, pp. 360-364, 1998.

[44] K. W. Hui, K. S. Chiang, B. Wu, Z. H. Zhang, "Electrode optimization for high-speed traveling-wave integrated optic modulators," *Journal of Lightwave Technology*, Vol. 16, No. 2, pp. 232–238, 1998.

[45] K. Noguchi, H. Miyazawa, O. Mitomi, "LiNbO3 high-speed modulator». Conference on Lasers and Electro-Optics," *Conference on Lasers and Electro-Optics, CLEO 99,* Vol. 4, pp. 1267-1268, 1999.

[46] N. M. Abe, M. A. R. Franco, A. Passaro, "Analysis of a x-cut Ti:LiNbO3 electrooptic modulator with a ridge structure," *International Microwave and Optoelectronics Conference, SBMO/IEEE MTT-S, APS and LEOS – IMOC*, Vol. 1, pp. 144-148, 1999.

[47] K. Higuma, S. Oikawa, Y. Hashimoto, H. Nagata, M. Izutsu, "X-cut lithium niobate optical single-sideband modulator," *Electronics Letters*, Vol. 37, No. 8, pp. 515-516, 2001.

[48] J. Kondo, K. Aoki, A. Kondo, T. Ejiri, Y. Iwata, A. Hamajima, T. Mori, Y. Mizuno, M. Imaeda, Y. Kozuka, O. Mitomi, M. Minakata, "High-speed and low-driving-Voltage thin-sheet X-cut LiNbO3 Modulator with laminated low-dielectric-constant adhesive*," IEEE, Photonics Technology Letters*, Vol. 17, No. 10, pp. 2077-2079, 2005.

[49] I. P. Kaminow and J. Liu, "Propagation characteristics of partially loaded two-conductor transmission line for broadband light modulators," *Proceedings of IEEE*, Vol. 51, No. 1, pp. 132.136, 1963.

[50] M. Izutsu, Y. Yamane, and T. Sueta, "Broad-band traveling-wave modulator using a LiNb03 optical waveguide," *IEEE, Journal of Quantum Electronics*, Vol. QE-13, pp. 287-290, 1977.

[51] M. Rangaraj, T. Hosoi, and M. Kondo, "A Wide-Band Ti:LiNbO, Optical Modulator with a Conventional Coplanar Waveguide Type Electrode," *IEEE, Photonics Technology Letters,* Vol. 4, No. 9, pp. 1020-1022, 1992.

[52] E. Mortazy, F. Xu, M. Meunier and K. Wu, "Millimeter-wave transition of coplanar line to substrate integrated $LiNbO_3$ waveguide for traveling-wave electro-optical modulator," *Microwave and Optical Technology Letters*, Vol. 51, No.4, pp. 1105-1107, 2009.

[53] A. Patrovsky, M. Daigle, and K. Wu, "Millimeter-wave wideband transition from CPW to substrate integrated waveguide on electrically thick high-permittivity substrates," *Proceedings of the 37th European Microwave Conference*, pp. 138-141, 2007.

[54] Y. Cassivi, L. Perregrini, P. Arcioni, M. Bressan, K. Wu, and G. Conciauro, "Dispersion Characteristics of Substrate Integrated Rectangular Waveguide," *IEEE, Microwave and Wireless and Components Letters,* Vol. 12, No. 9, pp. 333-335, 2002.

[55] D.M. Pozar, Microwave Engineering, *John Wiley and Sons Int.,* third edition, 2005.

[56] L. C. Ozcan, F. Guay, R. Kashyap, and L. Martinu, "Fabrication of buried waveguides in planar silica films using a direct CW laser writing technique," *Journal of Non-Crystalline Solids*, Vol. 354, pp. 4833–4839, 2008.

[57] H. W. Chong, A. Mitchell, and M. W. Austin, "Wet etching techniques for the realisation of novel electrode structures on X and Z-cut lithium niobate," *IEEE conference of Optoelectronic and Microelectronic Materials and Devices*, Vol. 1, pp. 194-197, 2000.

[58] J. Greuters and N. Rizvi, "UV laser micromachining of silicon, indium phosphide and lithium niobate for telecommunications applications," *Proc. SPIE-The International Society for Optical Engineering,* Vol. 4876, pp. 479-486, 2003.

[59] M. Meunier, B. Fisette, A. Houle, A.V. Kabashin, S.V. Broude and P. Miller, "Processing of metals and semiconductors by a femtosecond laser-based microfabrication system," *Proc. SPIE-The International Society for Optical Engineering*, Vol. 4978, pp. 169-179, 2003.

[60] L. Gui, B. Xu, and T. Chong, "Microstructure in lithium niobate by use of focused femtosecond laser pulses," *IEEE, Photonics Technology Letters*, Vol. 16, pp. 1337-1339, 2004.

[61] R. R. Thomson, S. Campbell, G. Brown, I. J. Blewett, A. K. Kar and D. T. Reid, "Femtosecond waveguide fabrication in bulk Lithium Niobate (LiNbO3)," *Conference on Lasers and Electro-Optics, CLEO*, Vol. 1, pp. 1918-1920, 2005.

[62] J. Kondo, A. Kondo, K. Aoki, M. Imaeda, T. Mori, Y. Mizuno, S. Takatsuji, Y. Kozuka, O. Mitomi, and M. Minakata, "40-Gb/s X-cut LiNbO3 optical modulator with two-step back-slot structure," *IEEE, Journal of Lightwave Technology*, Vol. 20, No. 12, pp. 2110-2114, 2002.

[63] Resonetics Micromachining Technology, Maestro series Excimer laser workstation, Technical reference, Rev. B, 2002.

[64] M. D. Janezic, and J. A. Jargon, "Complex Permittivity Determination from Propagation Constant Measurements," *IEEE, Microwave and Guided Wave Letters*, Vol. 9, No. 2, pp. 76-78, 1999.

[65] A. Patrovsky, M. Daigle, and K. Wu, "Coupling mechanism in hybrid SIW-CPW forward couplers for millimeter wave substrate integrated circuits," *IEEE Trans. Microwave Theory Tech.*, Vol. 56, pp. 2594-2601, 2008.

[66] S. E. Miller, "Coupled wave theory and waveguide applications," *Bell System Technical Journal,* Vol. 33, pp. 661–719, May 1954.

[67] Z. Ruifeng, L. Jie, W. Qingpu, W. Yurong, W. Aijian, J. Jun, Y. Xiujie, C. Huanchu, and H. Jianru, "Refractive index dispersion and anisotropy in Ca0.28Ba0.72Nb2O6," *Crystal Research and Technology*, Vol. 41, No. 5, pp. 494 – 497, 2006.

[68] Kiyomi Sakai, Terahertz Optoelectronics, *Springer-Verlag Berlin Heidelberg*, 2005.

[69] E. R. Brown, K. A. McIntosh, K. B. Nichols, and C. L. Dennis, "Photomixing up to 3.8 THz in low-temperature-grown GaAs," *Applied Physics Letters*, Vol. 66, No. 3, pp. 285-287, 1995.

[70] K. A. McIntosh, E. R. Brown, K. B. Nichols, O. B. McMahon, W. F. DiNatale, and T. M. Lyszczarz, "Terahertz photomixing with diode lasers in low-temperature-grown GaAs," *Applied Physics Letters*, Vol. 67 No. 26, pp. 3844-3846, 1995.

[71] C. Baker, I. S. Gregory, M. J. Evans, W. R. Tribe, E. H. Linfield, and M. Missous, "All-optoelectronic terahertz system using low temperature-grown InGaAs photomixers," *Optics Express*, Vol. 13, No. 23, pp. 9639-9644, 2005.

[72] E. R. Brown, A. W. M. Lee, B. S. Navi, and J. E. Bjarnason, "Characterization of a planar self-complementary square- spiral antenna in the THz region," *Microwave and Optical Technology Letters*, Vol. 48, No. 3, pp. 524-530, 2006.

[73] N. Chimot, J. Mangeney, P. Crozat, J. M. Lourtioz, K. Blary, J. F. Lampin, G. Mouret, D. Bigourd, and E. Fertein, "Photomixing at 1.55 μm in ion-irradiated In0.53Ga0.47As on InP," *Optics Express*, Vol. 14, No. 5, pp. 1856-1861, 2006.

[74] J. Mangeney, A. Merigault, N. Zerounian, and P. Crozat, "Continuous wave terahertz generation up to 2 THz by photomixing on ion-irradiated In0.53Ga0.47As at 1.55 um wavelengths," *Applied Physics Letters*, Vol. 91, 241102, 2007.

[75] A. Hassani, A. Dupuis, and M. Skorobogatiy, "Low Loss Porous Terahertz Fibers Containing Multiple Subwavelength Holes," *Applied Physics Letters*, Vol. 92, 071101, 2008.

[76] S. Atakaramians, S. Afshar V. , B. M. Fischer , D. Abbott and T. M. Monro, "Low loss, low dispersion and highly birefringent terahertz porous fibers," *Optics communications*, Vol. 282, No.1, pp.36-38, 2009.

[77] E. Brown, F. Smith, K. McIntosh, "Coherent millimeter-wave generation by heterodyne conversion in low-temperature-grown GaAs photoconductors," *Journal of Applied Physics*, Vol. 73, pp. 1480–1484, 1993.

[78] J. E. Bjarnason, T. L. J. Chan, A. W. M. Lee, E. R. Brown, D. C. Driscoll, M. Hanson, A. C. Gossard, and R. E. Muller, "ErAs:GaAs photomixer with two-decade tunability and 12 mW peak output power," *Applied Physics Letters*, Vol. 85, No. 18, pp. 3983-3985, 2004.

[79] J. Shi, S. Chu, M. Tien, C. Sun, Y. Chiu, and J. E. Bowers, "Edge-coupled membrane terahertz photonic transmitters based on metal–semiconductor–metal traveling-wave photodetectors," *Applied Physics Letters*, Vol. 81, pp.5108-5110, 2002.

[80] A. Stöhr, A. Malcoci, A. Sauerwald, I. C. Mayorga, R. Güsten, and D. S. Jäger, "Ultra-Wide-Band Traveling-Wave Photodetectors for Photonic Local Oscillators," *Journal of Lightwave Technology*, Vol. 21, No. 12, pp. 3062-3070, 2003.

[81] A. Stohr, A. Malcoci, D. Jager, " THz photomixing employing travelling-wave photodetectors," *IEEE MTT-S, International Microwave Symposium Digest*, Vol. 1, pp. 275- 278, 2004.

[82] A. Stohr, "Pushing the boundaries," *IEEE Microwave Magazine*, Vol. 10, No. 4, pp. 106 – 115, 2009.

[83] S. Chen, P. Wang, and P. Hsu, "Uniplanar Log-Periodic Slot Antenna Fed by a CPW for UWB Applications," *IEEE Antennas and Wireless Propagation Letters*, Vol. 5, pp. 256-259, 2006.

[84] S. Demiguel, N. Li, X. Li, X. Zheng, J. Kim, J. C. Campbell, H. Lu, and A. Anselm, "Very High-Responsivity Evanescently Coupled Photodiodes Integrating a Short Planar Multimode Waveguide for High-Speed Applications," *IEEE, Photonics Technology Letters*, Vol. 15, No. 12, pp. 1761-1763, 2003.

[85] S. Demiguel, X. Li, N. Li, H. Chen, J. C. Campbell, J. Wei, and A. Anselm, "Analysis of Partially Depleted Absorber Waveguide Photodiodes," *Journal of Lightwave Technology*, Vol. 23, No. 8, pp. 2505-2512, 2005.

[86] A. Beling, H. Bach, G. G. Mekonnen, R. Kunkel, and D. Schmidt, "High-Speed Miniaturized Photodiode and Parallel-Fed Traveling-Wave Photodetectors Based on InP," *IEEE, Journal of Selected Topics in Quantum Electronics*, Vol. 13, No. 1, pp. 15-21, 2007.

[87] H. G. Bach, "Ultrafast Efficient Photodiodes Exceeding 100 GHz Bandwidth," *International Conference on Indium Phosphide and Related Materials*, pp.71-76, 2007.

[88] A. Beling and J. C. Campbell, "InP-Based High-Speed Photodetectors," *Journal of Lightwave Technology*, Vol. 27, No. 3, pp. 343-355, 2009.

[89] K. S. Giboney, M.J.W. Rodwell, J.E: Bowers, "Traveling-wave photodetector theory", *IEEE, Transactions on Microwave Theory and Techniques*, Vol. 45, pp. 1310-1319, 1997.

[90] S. Kong, S. Yoon, and Y. Choi, "Microwave Characteristics of Long TWPDs for High-Power Operation," *Microwave and Optical Technology Letters,* Vol. 35, No. 1, pp. 51-54, 2002.

[91] S. Kong, S. Lee, J. Lee, and Y. Choi, "Numerical Analysis of Traveling-Wave Photodetectors' Bandwidth Using the Finite-Difference Time-Domain Method," *IEEE, Transactions on Microwave Theory and Techniques,* Vol. 50, No. 11, pp. 2589-2597, 2002.

[92] V. M. Hietala, G. A. Vawter, T. M. Brennan, and B. E. Hammons, "Traveling- Wave Photodetectors for High-Power,Large-Bandwidth Applications," *IEEE, Transactions on Microwave Theory and Techniques,* Vol. 43, No. 9, pp. 2291-2298, 1995.

[93] T. A. Milligan, Modern Antenna Design, *John Wiley and Sons Int.,* second edition, 2005.